

Atomistic and Mesoscale Modeling of Dislocation Mobility

by

Wei Cai

Submitted to the Department of Nuclear Engineering
in partial fulfillment of the requirements for the degree of

Doctor of Philosophy of Nuclear Engineering

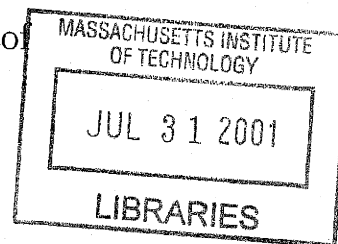
at the

MASSACHUSETTS INSTITUTE OF TECHNOLOGY

May 2001

[June 2001]

© Massachusetts Institute of Technology 2001. All rights reserved.



ARCHIVES

Author

Cai Wei

蔡 巍

Department of Nuclear Engineering

May 4, 2001

Certified by

Sidney Yip

Sidney Yip

Professor of Nuclear Engineering

Thesis Supervisor

Certified by

Al S. Argon

Al S. Argon

Professor of Mechanical Engineering

Thesis Reader

Accepted by

Sow-Hsin Chen

Sow-Hsin Chen

Chairman, Department Committee on Graduate Students

Atomistic and Mesoscale Modeling of Dislocation Mobility

by

Wei Cai

Submitted to the Department of Nuclear Engineering
on May 4, 2001, in partial fulfillment of the
requirements for the degree of
Doctor of Philosophy of Nuclear Engineering

Abstract

Dislocation is a line defect in crystalline materials, and a microscopic carrier of plastic deformation. Because dislocation has both a localized core and a long-range stress field, linking atomistic and meso scales is often the most challenging step in studying its dynamics. This Thesis presents theories and simulations of dislocations in Si and BCC transition metals, with emphasis on the atomistic-mesoscale coupling. Contributions are made in both methods development and mechanistic understanding of dislocation mobility.

For atomistic studies of defects embedded in a mesoscale surrounding, we have given rigorous treatments of two types of boundary effects. A method is derived for quantifying artificial image energies in dislocation simulations with a periodic cell, in which a longstanding conditional convergence problem in lattice summation is resolved. We have also developed a systematic approach based on the linear response theory, which minimizes boundary wave reflections in molecular dynamics simulations without artificial damping.

When predictive models are confronted with experiments at the level of mesoscale kinetics, the challenge is to properly incorporate atomistic details into a coarse-grained simulation. We have investigated dislocation core and kink mechanisms and obtained deeper understandings on the shuffle-glide controversy in Si and edge versus screw dislocations in BCC Mo, with some of these breakthroughs related to a better control of artificial boundary effects.

The atomistic-mesoscale coupling is then manifested in our formulation of a kinetic Monte Carlo description of dislocation glide in Si at the mesoscale, based on kink mechanisms. As a result, the nature of "weak obstacles" to kink propagation, a long-standing postulate for interpreting low stress dislocation mobility data, is clarified. This model is then generalized to incorporate cross slip for modeling screw dislocation motion in a BCC lattice. Lastly, a physically-motivated procedure is derived for removing the stress singularity in mesoscale dislocation dynamics simulations.

Thesis Supervisor: Sidney Yip
Title: Professor of Nuclear Engineering

Acknowledgments

This is an ideal place for me to express my gratefulness to my mentor Professor Sidney Yip. Five years ago, I felt lucky that I was admitted to MIT; now five years later, I feel that I was even more fortunate to have such a wise and caring person as my Thesis advisor. From working with me through my first publication, to giving me advices on how to deliver an insightful presentation, Professor Yip puts his effort in helping me on every small step that I need to make, as I gradually become more experienced in research and start to make a few achievements along the way. I am grateful for having been working with him, and for growing up in our friendly and exciting group that he brought together.

I owe my special thanks to Dr. Vasily Bulatov, whom I have been working with ever since I came to MIT. He guided me hand by hand through my first steps in scientific research, and met my ignorance and inexperience with patience and encouragement. After he joined Lawrence Livermore National Laboratory (LLNL) two years later, he is still deeply involved in my research and has been a constant source of inspiration through our electronic communications. I feel grateful to Livermore Lab for offering me a Postdoctoral Fellowship so that I can work with Vasily again and continue the research that I am excited with.

I want to thank Professor Ali Argon and John Joannopoulos for serving on my thesis committee. The solid mechanics courses that I took from Professor Argon and solid physics courses from Professor Joannopoulos have provided me the theoretical basis for my research, and sitting in their classes was an immensely enjoying learning experience. I am grateful to Professor Argon for always having time to listen to me on my latest research developments, and always giving me his critical assessment. I also want to thank Professor Sow-Hsin Chen for serving as my registration officer and Chair for my thesis defense meeting. He has urged me to take at least one experimental course before I leave MIT, which I find is a very wise thing to do.

My research has been supported by Lawrence Livermore National Laboratory, and in the last three years under an ASCI-Level 2 project. I want to thank our

Department for awarding me the Manson Benedict Fellowship in 2000.

I owe my thanks to Professor Kyeongjae Cho for hosting my summer visit to his group at Stanford University, and to his students Seongjun Park and Panchapakesan Ramanarayanan (Ram) for teaching me how to do electronic structure calculations. I also want to thank Professor Hanchen Huang and his student Averil Liu for making our group's trip to Hong Kong IUMRS symposium a pleasant experience.

I am happy to thank Dr. Maurice de Koning and Dr. João Justo for co-authoring several publications that we are proud of. And my thanks to Dr. Meijie Tang and Dr. Ladislav Kubin for their useful suggestions to my research. I want to thank Dr. Genrich Krasko for his enthusiastic encouragements to me.

My memory of MIT is inseparable from the guys that I have been working and playing with through all these years — Dr. Ju Li, Dongyi Liao and Jinpeng (Elton) Chang. I am grateful to Ju Li for being a role model for me, as a dedicated and passionate researcher, an ingenious and rigorous physicist. I have also benefited a lot from Dongyi's wizardly expertise on computers. I am happy to thank Elton for our team work on Livermore projects, which proved to be a success in each year. Also thanks to other fellow graduate students in our group, my friends Sundararaman (Sundar) Subramanian, Antonino Romano, Jing Wang and Zhiwen Xu.

I want to thank my home university in Wuhan, P. R. China, Huazhong University of Science and Technology (HUST), the program of Special Class for the Gifted Young (SCGY) and the Department of Optoelectronic Engineering, where I acquired the basis of my knowledge as an undergraduate, which will benefit my entire career.

I am grateful to my parents for encouraging and directing my interests in science since I was a boy. Coming to SCGY and later to MIT would be impossible to me, if I were deprived of the guidance and support from my father, who was a physics teacher in high school. Today, I find myself always able to draw strength whenever I think about my father, from his strong sense of responsibility towards family, work, and his students.

I dedicate this Thesis to my dear wife, Bei, for her love, and the happiness that we shared in our little family.

Contents

1	Introduction	33
1.1	Multiscale Modeling of Materials Strength	33
1.2	Scope of Thesis	37
2	Experiments on Dislocations in Si	41
2.1	Mechanical Response: Yield Stress	42
2.2	Dislocation Core Structure: Shuffle-Glide Competition	46
2.3	Dislocation Mobility	51
2.4	Kink Mechanism	58
3	Experiments on Dislocations in BCC Metals	65
3.1	Temperature and Orientation Dependence of Mechanical Response . .	67
3.2	Slip Behavior	71
3.2.1	Slip Systems	71
3.2.2	Slip Asymmetry	74
3.2.3	Anomalous Slip	76
3.3	Dislocation Microstructure	79
3.3.1	Initial Microstructure	79
3.3.2	Screws and Prismatic Loops	82
3.3.3	Anomalous Slip	83
3.3.4	High Temperature Behavior and Cell Structure	87
3.4	Dislocation Mobility	90

4	Atomistic Simulation Methods	95
4.1	Interatomic Potentials	95
4.2	Dislocations in Periodic Boundary Conditions	102
4.2.1	PBC and Conditional Convergence	102
4.2.2	Conventional Methods	105
4.2.3	A Systematic Approach	105
4.2.4	Extracting Core Energy	107
4.2.5	Predicting Elastic Interactions in PBC	110
4.3	Dynamic Domain Coupling	117
4.3.1	Artificial Wave Reflection at Domain Boundary	117
4.3.2	Linear Response Theory	119
4.3.3	Measuring Memory Kernel	121
4.3.4	Reflectivity Tests	123
4.3.5	Application to Static Relaxation	128
5	Atomistic Study of Shuffle Set Dislocation in Si	131
5.1	Core Structure and Peierls Stress	132
5.2	Peierls Energy Barrier	137
5.3	Kink Structure and Energy	139
5.4	Dislocation Motion by Molecular Dynamics	145
6	Atomistic Study of Dislocations in Mo	153
6.1	Core Structure	153
6.2	Peierls Stress	161
6.3	Kink on Screw Dislocation	166
6.4	Dislocation Motion by Molecular Dynamics	169
7	Mesoscale Study of Dislocation in Si	175
7.1	Introduction	175
7.2	Kinetic Monte Carlo Method	177
7.2.1	General Settings	177

7.2.2	Double Kink Nucleation	181
7.2.3	Kink Energies	186
7.3	Dislocation Mobility	188
7.3.1	Extracting Dislocation Velocity	188
7.3.2	Temperature Dependence	190
7.3.3	Stress Dependence	191
8	Mesoscale Study of Dislocation in BCC Metals	197
8.1	KMC Model with Cross Slip	198
8.1.1	General Settings	198
8.1.2	Double-kink Nucleation	199
8.1.3	Kink Migration and KMC Algorithm	201
8.2	Super Jog and Debris Loop	202
8.3	Orientation Dependence of Dislocation Mobility	206
9	Nodal Dislocation Dynamics	209
9.1	Introduction	209
9.2	Equation of Motion	212
9.3	Nodal Driving Force	215
9.4	Prismatic Loop and Super Jog	218
10	Summary and Outlook	221
A	Dislocation Dipole Energy in PBC	225
A.1	Cut-off Radius and Core Energy	225
A.2	Line Energy Divergence at Large Scale Limit	227
A.3	Derivation of Dipole Energy in PBC	230
A.4	Ghost Dipole Correction Term	233
B	More on Dynamic Coupling	237
B.1	Derivation of Generalized Langevin Equation	237
B.2	Symmetry between GLE and Green's Function	239

B.3	Translational Invariance in GLE Approach	243
B.4	Translational Invariance in Greens' Function Approach	246
B.5	GLE Type Coupling in Fourier Space	249
C	Markovian Models for Dislocation Motion	253
C.1	Hirth-Lothe Model	253
C.2	H-L Model with Discrete Kink Jump	257
C.3	Correlated Double Kink Nucleation in Si	262
C.4	Debris Loop Distribution	267
C.5	Lattice Spin Model of Dislocation Motion	272
C.5.1	System Description	272
C.5.2	Verify H-L Model	274
C.5.3	Dislocation Loops and Pinning Points	276
D	Linear Elasticity Theory of Dislocations	281
D.1	Stress in Two-Dimension	281
D.2	Energy in Two-Dimension	283
D.3	Nodal Driving Force	287
D.3.1	Hinge Interaction	287
D.3.2	Interaction Energy between a Finite and a Differential Dislocation Segment	290
D.4	Anisotropic Elasticity	292
	Bibliography	297
	About the Author	320

List of Figures

- 1-1 Ta flow stress as a function of pressure for initial sample thickness of $25\mu\text{m}$ (■) and $50\mu\text{m}$ (◇). The Steinberg-Guinan [3, 4] lower limit estimate of the flow stress and the calculated ideal strength of perfect crystal are shown in solid and dash lines respectively. (Fig. 9 of [5]) 36
- 2-1 Stress-strain curve of Si for strain rate $\dot{\epsilon} = 1.2 \times 10^{-4}$ and initial dislocation density $N_0 = 2 \times 10^{-4}\text{cm}^{-2}$. (1) $T=800$, (2) 850, (3) 900, (4) 950°C . τ_{eff} is the effective stress where the internal dislocation interaction stresses are subtracted out. (Fig. 1 of [14].) 42
- 2-2 Lower yield stress as a function of temperature. Data converted to the same shear strain rate $\dot{\epsilon} = 5 \times 10^{-5}\text{s}^{-1}$. + compression, $N_0 = 10^4\text{cm}^{-2}$, □ compression $N_0 = 0$, • tension $N_0 = 10^4\text{cm}^{-2}$, Δ, ○ compression plus hydrostatic pressure. (Fig. 25(b) of [8], $1\text{kg/mm}^2 = 9.8\text{MPa}$.) 43
- 2-3 Lower yield stress as a function of temperature for dislocation free Si samples. (Fig. 2 of [16].) 44
- 2-4 Yield stress of Si (*), GaAs (□, ◆, △), InP (+, ▲, ×) and InSb (○, ●) as a function of temperature. (Fig. 5 of [18].) 45
- 2-5 Diamond cubic structure of Si lattice. The two interlaced FCC lattices are shown in white and dark atoms respectively. (a) primitive cell of the diamond cubic lattice. (b) Glide and shuffle set of (111) planes. 47

2-6	(a) Dislocation pattern in the primary glide plane Si after a few seconds of deformation at $T = 520^{\circ}\text{C}$ and $\tau = 392\text{MPa}$. (b) Weak beam micrograph of a dissociated loop in Si deformed for 45 min at $T = 420^{\circ}\text{C}$ and $\tau = 256\text{MPa}$. (Fig.2 and 6 of [23], with minor editing.)	48
2-7	(a) Dislocation microstructure at $T = 450^{\circ}$ and 1.5GPa confining pressure, showing large stacking fault areas. (b) Dislocation microstructure at room temperature and 5GPa confining pressure, where the dislocations are mostly aligned along [110] and [123] directions. (Fig. 2 of [18] and Fig. 1 of [39].)	50
2-8	Growth of dislocation half loops in Si revealed by X-ray topography. Dislocations were introduced by scratching the surface followed by uniaxial loading at elevated temperature. Dislocation half loops expanded perpendicular to the scratch direction. (Fig. 6 of [43].)	52
2-9	Expansion of half and full dislocation loops in Si under shear stress, observed by X-ray topography. (Fig. 1 of [44].)	52
2-10	(a) Temperature dependence of velocity of screw (\bullet) and 60° (\circ) dislocations in intrinsic Si at stresses (1) $\tau = 30$, (2) 19, (3) 10, (4) 6, (5) 4 MPa. (b) Stress dependence of velocity of screw (\bullet) and 60° (\circ) dislocations in intrinsic Si at temperatures (1) $T = 800$, (2) 710, (3) 650°C . (Fig. 2 and 3 of [44].)	53
2-11	Stress dependence of activation energy Q (a) and temperature dependence of stress exponent m (b) for screw (\circ) and 60° (\bullet) dislocations in intrinsic Si. (Data from Table 2 and 3 of [44].)	55
2-12	Temperature dependence of dislocation velocity in Si at high temperature. Smooth splines are drawn to guide the eye. (Fig.1 of [51].)	55
2-13	Stress dependence of dislocation velocity in intrinsic Si at low stresses. (Fig.4 of [43].)	56
2-14	Schematic of the Peierls barrier and kink mechanism for dislocation motion. Dislocation is represented as a continuous line, which resides mostly at the bottom of the Peierls energy surface except at kinks.	59

2-15	TEM image of dissociated 60° dislocation in Si, displaying kinks on the two partial dislocations. (Fig. 3 of [61])	61
2-16	The stress pulse sequences in intermittent loading experiment [63].	62
2-17	Dislocation displacement during intermittent loading, at $T = 873\text{K}$ and $\sigma = 7\text{MPa}$, (a) as a function of t_i with $t_p = t_i$ and total loading time $\sum t_i = 7200\text{s}$. Curve 1 (\bullet) and curve 2 (\circ) correspond to the two 60° dislocations respectively; (b) as a function of t_p/t_i at $t_i = 94\text{ms}$. (Fig. 2 and 3 of [63]).	63
3-1	Tensile stress-strain curve of Mo. (a) Uniaxial tension along A direction (inside the standard triangle) at 293 and 493K. (b) Uniaxial tension along $[110]$ and $[100]$ from 77 to 573K. (Fig. 2 of [79] and Fig. 1 of [80].)	68
3-2	Tensile stress-strain curve of Mo along $[101]$, $[010]$, $[111]$ directions under (a) 293K and (b) 77K. (Fig. 1 of [81]. $1\text{kp/mm}^2 = 9.8\text{GPa}$.)	68
3-3	Temperature dependence of the critical resolved shear stress of $[110]$ Mo single crystals for tension (\bullet) and compression (\blacktriangle). (Fig. 1 of [82]. $1\text{kp/mm}^2 = 9.8\text{GPa}$.)	69
3-4	Slip traces of Mo deformed at 353 and 413K under uniaxial tension along the direction near the center of the standard triangle. (a) Slip lines on face 1 after 0.045 tensile strain. (b) Slip lines on face 2 after 0.045 tensile strain. (c) Slip lines on face 2 after 0.175 tensile strain. (Fig. 6 of [92].)	72
3-5	Slip traces of Mo deformed at 293K under uniaxial tension along the direction near the center of the standard triangle. (Fig. 5 of [95].)	73
3-6	Slip band directions of Mo deformed to (a) 0.8% and (b) 20% under same condition as in Fig. 3-5. (Fig. 7 of [95].)	73
3-7	(a) Stress strain curve of Mo under direct shear. (b) Estimated bounds for critical resolved shear stress to nuclear slip on different planes. (Fig. 3 and 4 of [96].)	75

3-8	(a) Cyclic stress-strain curve of Mo under uniaxial deformation at room temperature. (b) Stress asymmetry $\Delta\tau$ between tension and compression as a function of angle χ between MRSS plane and $(1\bar{1}0)$ plane. (Fig. 1 and 2 of [100].)	76
3-9	Orientation of the primary slip plane and the anomalous plane with respect to the tensile axis. (a) Stereographic plot. (b) 3-dimensional plot. (Fig. 1 and 2 of [104].)	77
3-10	Anomalous $(\bar{1}01)$ slip lines in high purity Mo at 77K after 0.46% strain. Secondary slip on (101) plane is also visible. (Fig. 2 of [103].)	78
3-11	(a) Grown-in dislocation loops around inclusion particles. (b) Grown-in dislocations pinned by fine precipitate particles. (c) Grown-in dislocation act as dislocation pinning centers upon deformation. (d) Featureless grown-in dislocation microstructures in high purity Mo. (Fig. 1, 4 and 7 of [114] and Fig. 2 of [115].)	80
3-12	Dislocation structure of Mo under 0.5% tensile strain at 4.2K. Primary Burgers vector along $[11\bar{1}]$. Foil plane on (011) using (a) $(\bar{2}33)$ and (b) $(01\bar{1})$ reflections. (Fig. 5 of [116].)	81
3-13	Dislocation structure of Mo under 2% tensile strain along $[110]$ at 4.2K. (Fig. 6 of [82].)	81
3-14	Dislocation structure of Mo at 293K with (a) 0.3%, (b) 3.5% and (c) 14% strain. (Fig. 2, 5 and 7 of [117].)	84
3-15	Dislocation structure of Mo under 5.8% tensile strain at 293K. (Fig. 5 of [82].)	85
3-16	Dislocation density (a) and debris density (b) in Mo at 293K versus strain. (Fig. 8 and 9 of [117].)	85
3-17	Dislocation structure of Mo with anomalous slip, $T = 77K$, axial strain $\epsilon = 0.46\%$. (a) Straight lamella dislocation bands along anomalous $(\bar{1}01)$ plane. (b) Dislocation arrangement on the anomalous $(\bar{1}01)$ plane. Dislocation junctions (R), dipole trails (D) and dipole loops (L) are observed. (Fig. 3 and 4 of [103].)	86

3-18 Dislocation structure of Mo at 493K with 2.1% strain. (a) Edge dipoles and elongated loops. (b) Long bundle of primary edge dislocations. (Fig. 7 and 8 of [79].)	87
3-19 Cellular structure of dislocations in Mo under tension along [110] at (a) 423K with 12% strain and (b) 573K with 4% strain and (c) along [100] at 423K with 12% strain. (Fig. 5 and 7 of [80].)	88
3-20 Dislocation microstructures in Mo under cyclic deformation along the axis near the center of the standard triangle. (a) Cell structure at plastic strain amplitude $\epsilon_p = 1.04 \times 10^{-3}$ and cumulative strain $\epsilon_c = 5$. (b) Dislocation walls at $\epsilon_p = 1.13 \times 10^{-3}$ and $\epsilon_c = 4.5$. (c) Dislocation bundles linking to form cell structure at high total strain amplitude $\epsilon_T = 3.45 \times 10^{-3}$ and $\epsilon_c = 0.94$. (Fig. 10, 12 and 18 of [115].)	89
3-21 Edge dislocation mobility measurements. (a) Dislocation etch pits from the indenter. (b) Measured dislocation velocity as a function of stress in unit of (kg/mm ²) at different temperatures and slip planes. (Fig. 5 and 6 of [121]. 1kg/mm ² = 9.8MPa.)	91
3-22 Screw dislocation mobility measurements. (a) Etch pits displaying a rosette pattern of dislocations around the indent. (b) Geometries of dislocation line and slip planes near the indent. (c) dislocation velocity of two Mo sample (a,b) as a function of loading stress at three temperatures: 1. 300K, 2. 77K, 3, 4.2K. (Fig.1, 2 of [125] and Fig.2 of [126].)	92
3-23 Comparison of velocities of edge (from Prekel et al.) and screw (from Leiko et al.) dislocations as a function of stress. It is misleading since screw dislocations have a much higher mobility than edges. (Fig. 6.28 of [124].)	92
3-24 Dislocation mobility in Mo by <i>in situ</i> high voltage electron microscopy. (Fig. 1 and 2 of [119].)	93

3-25	Core structure of screw dislocation in Mo by high resolution transmission electron microscopy (a) HRTEM images and (b) Atom position and (in plane) differential displacement map constructed from (a). (Fig. 5 and 6 of [129].)	94
4-1	Schematic of an atomistic simulation cell (solid rectangle) containing a dislocation dipole with Burgers vector $\pm\vec{b}$ and separated by \vec{a} under PBC along \vec{c}_1 , \vec{c}_2 and \vec{c}_3 (out of plane). To facilitate calculation of the image energy, we introduce "ghost" dislocations (in white) at the cell boundaries.	103
4-2	Atomic structure of shuffle set screw dislocation dipole in Si a simulation cell under PBC. The displacement field for these two dislocations are mainly along z direction, which is perpendicular to the paper. The high energy atoms in the dislocation core are plotted in dark color.	108
4-3	(a) Variation of atomistic (\circ) E_{atm} and linear elastic (anisotropic \diamond and isotropic \square) E_{el} energies of a shuffle-set screw dislocation dipole in a PBC cell of Si with \vec{c}_1 at $\vec{c}_2 = 3[111]$. Predictions of $2E_{\text{core}}$ are shown in dashed and dotted line respectively. (b) Variation of E_{atm} with \vec{c}_2 at $\vec{c}_1 = 4[11\bar{2}]$. Atomistic simulation results are shown in \circ , while anisotropic elastic results for E_{el} plus $2E_{\text{core}}$ obtained from (a) are shown in \diamond	108
4-4	Atomic structure of edge dislocation dipole in Mo a simulation cell under PBC. The dipole is created by removing a layer of atoms between the two dislocations. The high energy atoms in the dislocation core are plotted in dark color.	111
4-5	Variation of atomistic (\circ) E_{atm} and linear elastic (anisotropic \diamond and isotropic \square) E_{el} energies of an edge dislocation dipole in a PBC cell of Mo.	112

4-6	(a) Elasticity theory predictions of image energy (in \diamond) for screw dislocation dipole as in Fig. 4-2,4-3. Anisotropic elasticity (in \diamond) predicts $E_{\text{img}} = 0$ at $c_2/c_1 = 0.329$, while isotropic elasticity (in \square) predicts a different zero point at $c_2/c_1 = 0.365$	113
4-7	(a) Schematic of the total energy variation with relative displacement x , ΔE being the maximum. (b) Variation of ΔE with cell aspect ratio c_2/c_1 for edge dislocations in Mo, with the same set up as in Fig. 4-5. Anisotropic elasticity predicts $\Delta E = 0$ at $c_2/c_1 = 2.918$ (\diamond). Isotropic elasticity predicts a monotonic decrease of ΔE with increasing c_2/c_1 (\square). Atomistic simulations with $c_1 = 15, 20$ and $30[111]$ are shown in \times, \circ and $+$ respectively.	114
4-8	Variation of ΔE with cell aspect ratio c_2/c_1 for screw dislocations in Mo. Anisotropic elasticity predicts a reverse of sign at $c_2/c_1 \approx 2.2$ while isotropic elasticity predicts a monotonic increase of ΔE approaching zero.	115
4-9	Variation of total energy E and Virial stress σ , and dislocation displacement X in MD simulations of edge dislocation motion, with cell aspect ratio c_2/c_1 at (a) 3.8 and (b) 1.65. The fluctuation in (a) is small and is mainly due to thermal noise, while the large oscillations in (b) is clearly due to the image interaction artifact.	116
4-10	Elastic wave emitting from the crack tip gets reflected at the boundary of the simulation cell. (From B. L. Holian via S. Yip. Similar results can be found in [182].)	118
4-11	MD region P is the region enclosed by the solid line, surrounded by region Q , which is perfect lattice.	119
4-12	Typical behavior of the memory kernel matrix elements as a function of time (full line). In practice, the response functions are determined within a time interval $[0, t_c]$, with t_c being a cut-off time. For $t > t_c$ they are assumed to remain constant at their cut-off values $\beta_{ij}(t_c)$ (dashed line).	122

4-13	Memory function for one-dimensional harmonic oscillators. MD simulation results (\bullet) agrees closely with analytic solutions $\beta(t) = -J_0(2t) - J_2(2t)$ (in solid line).	123
4-14	Phonon reflectivity as a function of wave vector k for a one-dimensional chain of harmonic oscillators. Inset shows reflectivities associated with the CGMD method [191] for the same problem.	124
4-15	(a) Initial condition of a Gaussian wave packet on a 2D harmonic lattice. (b) Wave packet propagating outwards after 300 timesteps using the boundary condition developed in this section. (c) 450 timesteps. (d) 600 timesteps.	126
4-16	(a) MD simulations after 450 timesteps under free boundary, with the same initial condition as in Fig. 4-15(a). (b) At 600 timesteps, severe boundary reflections are observed.	127
4-17	Reflectivity on a two-dimensional square harmonic lattice as a function of the width σ of initial Gaussian displacements. Inset shows reflectivity results reported in Ref. [188] using another reflection reduction technique for similar Gaussian displacements in a three-dimensional fcc lattice.	127
4-18	(a) Displacements in two-dimensional square harmonic lattice containing a screw dislocation dipole in primary region P . (b) Displacement fields of oscillators along the four edges of the boundary $a-b-c-d-a$; results obtained using conjugate-gradient minimization (full line) and response function relaxation (dotted line).	128
5-1	Core structures of shuffle set screw dislocation in Si. The high energy core atoms are shown in dark color. (a) Core A resides in a hexagonal ring. (b) Core B resides at the boundary between two hexagonal rings.	132

5-2	Simulation cell containing a single dislocation. (a) Front view. The cell is periodic along x (horizontal) and z (out of the plane) axes. Dislocation line is along z axis with core atoms shown in dark color. Two layers of atoms are set fixed (grey) at the top and bottom of the cell. (b) Top view of the upper fixed atom layer. (c) Bottom view of the lower fixed atom layer. The two possible shuffle set slip planes S_1 and S_2 are shown in dash lines.	134
5-3	Initial (B) final (B_1) and intermediate (A) configurations for Peierls stress calculation.	135
5-4	Energy change of system B , B_1 and A as a function of dz the displacement of upper layer of fixed atoms in $-z$ direction.	136
5-5	Energy variation along the transition path between states B and B_1 via A when the displacement of the top fixed layer is at $dz = 0$. The results with $r_{\text{cut}} = 25\text{\AA}$ (\bullet) and $r_{\text{cut}} = 15\text{\AA}$ (\diamond) are indistinguishable. .	138
5-6	Energy variation along the transition path at $dz = 0$ (thick line), $dz = 1.53\text{\AA}$ (thin line) and $dz = 3.33\text{\AA}$ (dash line).	139
5-7	(a) Schematic of (full) kinks (K) between shuffle core B and B_1 . (b) Schematic of dissociation of full kinks into partial kinks (PK) connected with a segment of dislocation in core A	140
5-8	Atomic arrangements of a shuffle set screw dislocation core in Si with length $40b$ having a double kink. The two kinks are separated by (a) $20b$, (b) $19b$, (c) $21b$ respectively. Only atoms with local energy larger than -4.52eV are shown, while the energy per atom in perfect Si lattice is -4.62eV	141
5-9	Energy variation (solid curve) along the transition path of kink migration. The dashed curve is the result after a linear term corresponding to the residual stress effect is subtracted. The peak of the dashed curve gives $W_m = 0.022\text{eV}$	142

5-10	Variation of the internal stress during MD simulations of shuffle set screw dislocation motion at 10K under constant shear strain rate (see text).	146
5-11	Instantaneous dislocation position during MD simulations under the same condition as Fig. 5-10.	147
5-12	(a) Magnified view of stress variation in Fig. 5-10. (b) Magnified view of dislocation displacement along x in Fig. 5-11.	147
5-13	Variation of the internal stress during MD simulations of shuffle set screw dislocation motion at 300K under constant shear strain rate $\dot{\gamma}_{yz} = 4.08 \times 10^{-4} \text{ps}^{-1}$.	149
5-14	Instantaneous dislocation position during MD simulations under the same condition as Fig. 5-13.	149
5-15	Snapshot at 150ps of MD simulation at 300K (see text). Atoms with instantaneous energy higher than -4.5eV are plotted dark. Slip steps are created where the dislocation has pass through the cell for multiple times. (a) Front view. (b) Side view.	151
5-16	Snapshot at 400ps of MD simulation at 300K (see Fig. 5-15). (a) Front view. (b) Side view.	152
6-1	Simulation cell containing a single screw dislocation. (a) Front view. The cell is periodic along x (horizontal) and z (out of the plane) axes. Dislocation line is along z axis. Fixed atoms are plotted in grey. Atoms with energy higher than -6.72eV are shown in dark color. (b) Top view of the upper fixed atom layer. (c) Bottom view of the lower fixed atom layer.	155
6-2	Core structure of screw dislocation with polarity $+1$. (a) 3D view. (b) Top view. (c) Side View.	156
6-3	Core structure of screw dislocation with polarity -1 . (a) 3D view. (b) Top view. (c) Side View.	156

6-4	Simulation cell containing a single mixed 71° dislocation. (a) Front view. Dislocation line is along z axis. Atoms with energy higher than -6.72eV are shown in dark color. (b) Top view. (c) Bottom view.	157
6-5	Core structure of mixed 71° dislocation. (a) 3D view. (b) Top view.	158
6-6	Simulation cell containing a single edge dislocation. (a) Front view. Dislocation line is along z axis. Atoms with energy higher than -6.72eV are shown in dark color. (b) Top view. (c) Bottom view.	159
6-7	Core structure of an edge dislocation. (a) 3D view. (b) Top view.	160
6-8	Total energy variation ΔE of the relaxed structure containing a screw dislocation (Fig. 6-1) as a function of the displacement dz of the upper layer of fixed atoms. The initial dislocation positions are at the origin (solid line), and (b) one repeat distance $h_s = 2\sqrt{2}b/3$ to the right (dash line) respectively.	161
6-9	Total energy variation ΔE of the relaxed structure containing a mixed 71° dislocation (Fig. 6-4) as a function of the displacement dl of the upper layer of fixed atoms.	163
6-10	Total energy variation ΔE of the relaxed structure containing an edge dislocation (Fig. 6-6) as a function of the displacement dz of the upper layer of fixed atoms.	164
6-11	Core structure of a screw dislocation containing a double-kink. (a) 3D view. (b) Front view. (c) Side view. (d) Top view.	167
6-12	Total energy variation ΔE of the relaxed structure containing a double-kinked screw dislocation (Fig. 6-11) as a function of the displacement dz of the upper layer of fixed atoms.	168
6-13	Variation of the internal stress during MD simulations of screw dislocation motion at 10K under constant shear strain rate (see text).	171
6-14	Instantaneous dislocation position during MD simulations under the same condition as Fig. 6-13.	171
6-15	Instantaneous dislocation position during the same MD simulation as in Fig. 6-13.	172

6-16	Instantaneous configurations during MD simulation (see text) showing the atomistic pathway for screw dislocation cross slip.	173
6-17	Variation of the internal stress during MD simulations of screw dislocation motion at 300K under the same strain rate as in Fig. 6-13. . .	174
6-18	Instantaneous dislocation position during the same MD simulation as in Fig. 6-17.	174
7-1	Schematics of kMC model of dislocation in Si. Screw dislocation with Burgers vector \vec{b} is dissociated into leading and trailing 30° partials, with Burgers vector \vec{b}_1 and \vec{b}_2 respectively. Elementary kink width is b , while kink height is $h = \sqrt{3}/2 b$. An embryonic double-kink nucleation event is shown at position I, and a kink migration event is shown at position II, both in dashed lines.	178
7-2	Theoretical dependence of the kink pair energy E_{dk} on its width w are shown as dots. For large width it approaches $2E_k$. At finite width w , E_{dk} is a superposition of $2E_k$ and the kink pair interaction energy $W_{int}(w)$. The solid curve illustrates the energy barrier between the neighboring states. E_{emb} is the barrier for nucleating an embryonic double-kink, i.e. transition from state $w = 0$ to $w = 1$	182
7-3	Schematic representation of the Markov process in the space of discrete kink width w . Transitions are allowed between neighboring states, shown as solid arcs. Every state can be reached from every other state. We draw dashed arcs between states widely separated to denote a collection of different paths. $F(i)$ and $B(i)$ are the forward and backward probabilities from state i . The nucleation rate $j_{dk}(w_c)$ of double-kinks of width w_c is the product of embryonic double nucleation rate $j_{dk}(1)$ with the survival rate $p_s(1 \rightarrow w_c)$	184

7-4	(a) Survival probabilities $p_s(1 \rightarrow n)$ can be broken up as the multiplication of smaller survival probabilities $p_s(i \rightarrow i+1)$. (b) Two possibilities of reaching $i+1$ from i . First, it can jump to $i+1$ directly from the first step. Second, it can choose to jump to $i-1$ in the first step. But then it has to come back to i from $i-1$ before it can reach $i+1$. . .	184
7-5	Profile of the leading 30° partial dislocation during the motion at $T = 1000\text{K}$, $\sigma_{yz} = 50\text{MPa}$. The dislocation length is $5000b = 1.92\mu\text{m}$. Kink energies are $E_k = 0.52\text{eV}$, $W_m = 0.89\text{eV}$	189
7-6	Simulated instantaneous positions of the two partials at $T = 1000\text{K}$, $\sigma_{yz} = 10\text{MPa}$	189
7-7	Temperature-dependent velocities of screw dislocations at stress $\tau = 10\text{MPa}$. Experiments are denoted by \diamond [43] and \circ [54] respectively. \blacksquare and \blacklozenge are kMC predictions using EDIP and TB kink energetics. KMC predictions for the optimized kink parameters, $E_k = 0.7\text{eV}$ and $W_m = 1.2\text{eV}$, are also shown in \times	190
7-8	Velocity of a screw dislocation in Si as a function of stress, at temperature $T = 1000^\circ\text{K}$. kMC prediction for a commensurate case ($X_0 = 10.0h$) is shown as \blacklozenge , with a “starting stress” at about 20MPa . Experimental data from [43] shows similar velocity variation, plotted as \diamond . kMC results for a non-commensurate case ($X_0 = 10.5h$) are plotted as \bullet , demonstrating linear stress-velocity relationship, in agreement with other experiments [54], plotted as \circ	191
7-9	Commensurability between the ideal separation X_0 and the periodicity of Peierls barrier gives rise to two distinct mechanisms of dislocation motion at low stresses (see text).	193
7-10	Dislocation velocity plotted against glide stress σ_{yz} , as \bullet , predicted for a special case when the ratio of the glide stress σ_{yz} to the non-glide stress σ_{xy} is fixed at -0.16 . For comparison, dislocation velocity for a non-commensurate case ($X_0 = 10.5h$) and zero non-glide stress is also shown as the dashed line.	195

8-1	A schematic of dislocation motion in BCC metals examined in the kMC simulations. The dislocation line is mostly aligned along the $1/2\langle 111 \rangle$ Burgers vector. Kink pairs can nucleate on either of the three (110) planes a, b and c , after which kink migration is constrained to the glide plane selected by kink pair nucleation. A kink pair nucleation event is shown at position I, and a kink migration event is shown at position II, both in dashed lines.	198
8-2	(a) Peierls stress τ_p as a function of loading angle χ (see text). (b) Double kink nucleation energy ΔH as a function of loading stress τ at different angle χ . Both predicted by the line tension model [212] taking only a single energy parameter from atomistic calculations, i.e. the core energy difference between hard and easy cores.	200
8-3	Schematic representation of the formation of (a) two kinks forming an elementary super jog (or cross-kink), (b) more kinks joining the super jog, and (c) debris loop L formation with the primary dislocation breaking away from the self-pinning point A	203
8-4	Snapshot of kMC simulation showing debris loops left in the wake of the moving screw dislocation. segments are significantly shrunk compared to the V segments in order to show the entire dislocation line; the total length of the H segments are in fact $27\mu m$ while each V segment is only 2.5\AA . Linear elastic interactions were ignored in this simulation.	204
8-5	Snapshots of kMC simulations of screw dislocation motion at 373K under 320MPa resolved shear stress with different orientations. (a) M.R.S.S. plane bisects the glide plane a and b , with super jogs and debris loops readily observed. (b) M.R.S.S. plane is parallel to glide plane b . The dislocation moves only in this plane. The larger resolved shear stress on the glide plane results in a much higher kink density.	207

9-1	Representation of dislocation as linked nodes. The motion of nodes after each times step gives the dislocation motion.	211
9-2	Velocity distribution on dislocation segment r_i - r_{i+1}	213
9-3	Dislocation discretization into segments.	216
9-4	Introducing semi-infinite segments M and N for nodal force calculation.	217
9-5	A circular prismatic dislocation loop discretized into linear segments connecting a set of equally spaced nodes. Number of nodes $N = 20$	219
9-6	Total energy (o) and nodal driving force (•) of prismatic dislocation loop, as a function of node number N . Both energy and driving force are converging to analytic solutions (solid lines) for large N	219
9-7	Super jog on screw dislocations in BCC metals represented by Nodal Dynamics. (a), (b) and (c) are equilibrium configurations under progressively larger shear stress. In (d) a prismatic loop is formed by joining the two arms of the super jog. Shear stress is removed after the loop forms.	220
A-1	An isolated screw dislocation within a cylinder of radius R . The dislocation line and Burgers vector b are out of the plane. The material within cut-off radius r_c around the dislocation is removed to avoid singularity.	226
A-2	(a) A screw dislocation dipole separated by a . (b) An elongated dislocation loop consisting of two screw segments of length L and two edge segments of length a	228
A-3	Introducing a cut in a perfect lattice at surface \vec{A} and displacing the positive side of \vec{A} by \vec{b} relative to the negative side, to create a dislocation dipole separated by \vec{a}	231
B-1	MD region P is the region enclosed by the solid line, surrounded by region Q , which is perfect lattice. The effect of Q is to exert a force $F_{PQ}(t)$ on atoms in P , as a boundary condition. This boundary is of the Generalized Langevin Equation (GLE) type.	240

B-2	Domain P and Q as systems. (a) $F_{PQ}(t) = Q[x_P(t)]$. (b) $x_P(t) = P[F_{PQ}(t)]$. (c) Coupling between P and Q	241
B-3	MD region P is the region enclosed by the solid line, surrounded by region Q , which is perfect lattice. P will exert forces $F_{QP}(t)$ on atoms in Q , while Q responds to these forces accordingly by moving its atoms $x_Q(t)$. This boundary is of the Time-dependent Green's Function (TGF) type.	242
B-4	Domain P and Q as systems. (a) $x_Q(t) = Q[F_{QP}(t)]$. (b) $F_{QP}(t) = P[x_Q(t)]$. (c) Coupling between P and Q	242
B-5	(a) Replace MD region P with a perfect lattice region L . Define the total region L plus Q to be Ω , which is translationally invariant. Define a Memory Kernel matrix $\hat{\beta}_{\Omega\Omega}(t)$ for Ω , whose element $\hat{\beta}_{ij}(t)$ is the <i>total</i> force $F_i(t)$ on atom i , if atom j is displaced to $x_j = 1$, while $x_i = 0$ for all the other atoms $i \neq j$ in Q (and $v_i = 0$ for all i). $\hat{\beta}_{\Omega\Omega}(t)$ is translationally invariant, i.e. $\hat{\beta}_{ij}(t) = \hat{\beta}(\vec{r}_i - \vec{r}_j, t)$. (b) Representation of Q, L and Ω as systems.	244
B-6	Representing P - Q system in terms of the L - Q system in GLE formulation.	245
B-7	Molecular Dynamics on two sets of coupled systems, P - Q and L - Q' , where Q' behaves the same as Q . We interpret the physical meaning of δx_L , as the amount of external disturbance needed to maintain system Q' the same as Q	246
B-8	(a) Replace MD region P with a perfect lattice region L . Define the total region L plus Q to be Ω , which is translationally invariant. Define a Time-dependent Green's Function matrix $\hat{G}_{\Omega\Omega}(t)$ for Ω , whose element $\hat{G}_{ij}(t)$ is the displacement x_i of atom i in response to an external force $\delta F_j(t) = \delta(t)$ exerted on atom j , while $x_i = 0$ for all atoms at $t = 0$. $\hat{G}_{\Omega\Omega}(t)$ is translationally invariant, i.e. $\hat{G}_{ij}(t) = \hat{\beta}(\vec{r}_i - \vec{r}_j, t)$. (b) Representation of Q, L and Ω as systems.	247

B-9	Representing P - Q system in terms of the L - Q system in TGF formulation.	248
B-10	Molecular Dynamics on two sets of coupled systems, P - Q and L - Q' , where Q' behaves the same as Q . We interpret the physical meaning of δF_Q , as the amount of external force on Q' needed to maintain system Q' the same as Q	248
B-11	One dimensional semi-infinite chain of harmonic oscillators x_1, x_2, x_3, \dots	249
B-12	(a) Real part of the memory kernel function in Fourier space. (b) Phonon dispersion relation of the one-dimensional harmonic oscillator.	251
C-1	Kink pair energy E_{dk} as a function of width w , shown as dots. Elastic interactions of between kinks are ignored. The applied stress creates a tilt in the energy landscape.	258
C-2	Expansion time $t(1, N)$ for successful double-kinks (see text). Kink jump step is set to $a = 1$. (a) $\alpha = 0.01$, $x_d = 24.5$, $v_k = 0.02$. (b) $\alpha = 0.001$, $x_d = 249.5$, $v_k = 0.002$	261
C-3	Two-dimensional lattice representing the width of the double-kinks on the coupled partials.	263
C-4	Energy landscape and contour for double-kinks on the two coupling partials as a function of their width w_1 and w_2 . (a), (b) $X_0 = 5.0$. (c),(d) $X_0 = 5.5$. Kink energy $E_k = 0.25\text{eV}$. Stress $\sigma = 4\text{MPa}$	265
C-5	Rate distribution of double-kink nucleation on two partials with $w_1 + w_2 = w = 50$ at stress $\sigma = 4\text{MPa}$. (a) $X_0 = 5.0$, $E_k = 0.25\text{eV}$. (b) $X_0 = 5.5$, $E_k = 0.25\text{eV}$. (c) $X_0 = 5.0$, $E_k = 0.5\text{eV}$. (d) $X_0 = 5.5$, $E_k = 0.5\text{eV}$	266
C-6	(a) Two random walkers on two dimensional lattice representing the growth of the two arms of the super jog. (b) Coordinate transformation of (a) into a one-dimensional random walk.	268

C-7	Diagram for $F(L, A)$ (solid path) and $G(L, A)$ (wavy path) and their recursive relationships.	269
C-8	Loop half length distribution function $f(L)$ for different values of p	270
C-9	Distribution function $f(L, A)$ for (a) fixed L and (b) fixed A at $p = 0.5$	271
C-10	Contour plot of $f(L, A)$ for $p = 0.5$. $f(L, A)$ is nonzero only for $L^2/4 \leq A \leq L - 1$, and are most prominent along the ridge $A = L^{1.5}/2.3$ (dash line), indicating a “fractal” loop dimension of $D = 1.5$	271
C-11	Lattice points next to a dislocation segment	273
C-12	Local environment of a lattice spin determining whether (a) double-kink nucleation, (b) kink migration, or (c),(d),(e) annihilation is controlling the spin flip.	273
C-13	KMC simulation of dislocation motion with constant double kink nucleation rate J and kink migration rate v_k , only lattice sites neighboring the dislocation are shown. (a) simulation snapshot with $J = 1$, $v_k = 50$. (b) average dislocation displacement as a function of physical time, parameters as in (a). (c) simulation snapshot with $J = 1$, $v_k = 5$, (d) average dislocation displacement, parameters as in (c).	275
C-14	KMC simulation of dislocation motion with constant double kink nucleation rate J and kink migration rate v_k . The dislocation loop overcomes four pinning points during expansion. (a) initial condition containing a dislocation loop. (b-t) snapshots of subsequent simulation steps.	278
C-15	KMC simulation snapshots of dislocation motion and interaction with pinning points. The effect of dislocation self stress is included.	279
D-1	Stress calculation of dislocation segment for the points on the glide plane.	281
D-2	Dislocation segment interactions (a) between horizontal (H) segments, (b) between horizontal (H) and vertical (V) segments.	284

D-3	Dislocation segment interactions (a) between horizontal (H) segments, (b) between horizontal (H) and vertical (V) segments, when two segments share a common node.	285
D-4	Interaction between an infinitely long H segment ($a \rightarrow \infty$) with (a) an H dipole, (b) a V dipole.	286
D-5	Two dislocation segments sharing a common node form a hinge structure.	288
D-6	Interaction between a finite and a differential dislocation segment. . .	290
D-7	Integration path of the second dislocation in the stress field of the first dislocation at the origin to compute interaction energy . (a) The second dislocation moves along x axis. (b) The second dislocation moves along a circle.	295

List of Tables

2.1	Stress dependence of activation energy Q and temperature dependence of stress exponent m for screw and 60° dislocations in intrinsic Si. (Table 2 and 3 of [44].)	54
3.1	Bulk properties of BCC transition metals [68, 69, 30, 70]. Elastic constants C_{11}, C_{12}, C_{44} in GPa, melting temperature in K, cohesive energy E_{coh} in eV, and thermal conductivity κ in $\text{Wm}^{-1}\text{K}^{-1}$. Note that VIB metals Cr, Mo and W generally have a larger shear modulus C_{44} and thermal conductivity κ than VB metals V, Nb and Ta.	66
3.2	Resolved yield stress τ_0 (in MPa) for Mo and Ta below 4.2K. χ is the angle between the maximum resolved shear stress plane and the (110) slip plane.	70
3.3	Orientation dependence of the CRSS (in MPa, resolved on the M.R.S.S. plane) for BCC metals at 77K. $[uvw]$ represent directions near the corner or the center of the standard triangle. (Table 1 of [11].)	70
4.1	Reconstruction energy (in eV/b) of 90° and 30° partials in Si by SW, Tersoff (T3), and EDIP potentials, as well as by DFT calculations. (Table 1 of [150])	100
7.1	Formation energies, E_k , and migration barriers, W_m , of kinks on 30° partials in silicon, obtained from atomistic calculations using EDIP and TB, in eV. Underlined values are selected for use in kMC simulation.	187

7.2 Kink's formation energy E_k and migration barrier W_m (in eV) on 30° and 90° partials in silicon obtained from atomistic calculations using EDIP potential, tight-binding (TB) and density functional theory (DFT), and experimental measurements using transmission electron microscopy (TEM) and high resolution electron microscopy (HREM). 187

Chapter 1

Introduction

1.1 Multiscale Modeling of Materials Strength

From ancient metals making to the invention of plastics in the early 20th century, from silicon based microelectronics today to nano-engineered diamondoid devices of tomorrow, the technology of processing and making use of new materials continuously influences our everyday life, with our history often marked by the revolutionary material of its time. While conventional materials research was largely an experimental science, computer modeling quickly becomes established as another effective tool during the past decade. With the continuous doubling of computing power of microprocessors in every 18 months over the past 30 years, known as the Moore's law, computer modeling and simulations are now playing an increasingly important role in scientific research and engineering applications in all disciplines, such as DNA sequencing, weather forecasting, and flight simulators. Computational materials science, the application of high performance computing on materials research, quickly emerges as a new discipline of itself. Different from the conventional trial and error approach in looking for new materials with desired properties, the goal of computational materials science is materials by *design*. Through numerical modeling at the most fundamental level, a computational materials scientist seeks *understanding* of materials behavior in terms of underlying mechanisms, which would then allow him to make reliable *predictions* in a wide range of the parameter space, and to arrive at

new material *designs* with improved performance.

While simulations can be regarded as “virtual” experiments running in the numerical space inside the computer, they offer a set of unique advantages over conventional or “real” experiments. Firstly, high performance computing is now becoming available at an increasingly lower cost, with negligible safety concerns and environmental effects. As the researcher has ultimate control over the simulation setup, extreme conditions such as high temperature, high pressure and high strain rate can easily “achieved” in computer simulations. From a theoretical point view, the most important advantage is perhaps the enormous amount of microscopic information retained after the simulation, allowing detailed *post mortem* data analysis to retrieve mechanistic understanding on the process of interest. However, this is by no means to say that simulations would eventually replace all the experiments. Aside from some serious limitations on computer modeling which we will discuss below, the validity of a prediction from simulations will ultimately be judged by experiments, and its significance would depend on whether or not it helps to create a new product which functions in the “real” world that we live in.

The major limitations of computer simulations in materials research are, in short, on the length and time scales of the processes that can be studied. For example, materials models that do not rely on any experimental inputs, thus staying “purely predictive”, are called *ab initio*, or first principles, which uses quantum mechanics of electrons to describe bonding and interaction between atoms. Unfortunately, the computational load of these *ab initio* models are extremely intensive, capable of handling systems with at most a few hundred atoms to date. While this is sufficient to determine certain properties such as elastic constants, electric conductance or transparency to light for a perfect crystal, most material properties of interest, such as mechanical strength, are the result of the collective behavior of a large number of atoms, exceeding the capacity of direct *ab initio* simulations by tens of orders of magnitude. In a sense, this is the challenge that is met by all frontiers of science of our century, that is, how does one take the universal laws of “elementary” particles — the triumph of the last century, and start to comprehend the immense complexity

of real world, such as order arising from disorder, and life from non-life [1]. Faster computers will help, but will definitely not be sufficient, if used blindly.

To describe materials behavior at larger scales, numerical models with different levels of coarse graining are necessary, such as molecular dynamics simulations in which atoms interact through a given potential function, and finite element methods describing the material as a continuum. The time and length scale limit of first principles methods would then be eliminated if the theories and models at different scales can be connected, so that macroscopic materials behaviors can be understood through fundamental physics. This is the so called multiscale approach [2], and this Thesis is concerned with applying it towards modeling materials strength against deformation and failure.

A lot of technological breakthroughs, from high temperature turbine blades to durable biomedical implants, rely on a better understanding on how materials fail and how to improve their mechanical strength. However, understanding materials strength in terms of atomic-level interactions is a long-standing challenge, because strength is sensitively dependent on material microstructures, whose complexity is beyond reach of any single theory. These microstructures can be the result of biological processes, or be intentionally engineered, or organize themselves automatically as deformation proceeds. In crystalline materials such as metals, the microstructures are made up of lattice defects with a whole range of dimensions, from point defects, dislocations, grain boundaries, to voids, twins and cracks. The complexity of this problem is obvious since one will need to study not only the behavior of each type of defect individually, but also their interactions with each other. Being a daunting task, understanding the microstructural details seems to be the only approach to achieve reliable predictions. We intend to illustrate this point by Fig. 1-1, in which a large discrepancy is shown between experiments and model predictions on the flow stress of tantalum under ultrahigh pressure. Because the model was not constructed based on microstructural effects, but was fitted with low pressure experiments instead, there is no surprise that it cannot make new predictions beyond the conditions that it was fitted to.

In this Thesis we will focus on a particular microstructural effect, the dynamics of

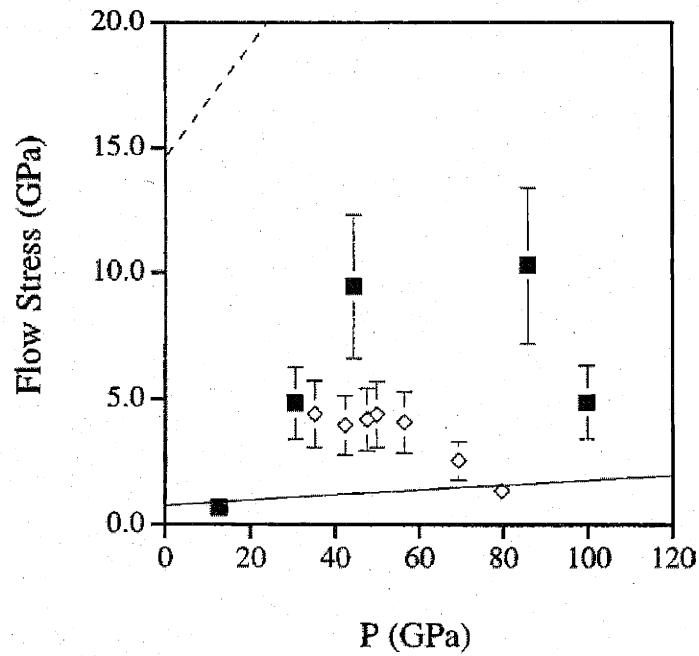


Figure 1-1: Ta flow stress as a function of pressure for initial sample thickness of 25 μm (■) and 50 μm (◇). The Steinberg-Guinan [3, 4] lower limit estimate of the flow stress and the calculated ideal strength of perfect crystal are shown in solid and dash lines respectively. (Fig. 9 of [5])

dislocations. Being a line defect in the lattice, dislocation becomes dominant in low temperature plastic deformation of a pure single crystal, where other defects such as vacancies and cracks can be neglected. While the initial yield stress is controlled by the lattice resistance to dislocation motion, the strain hardening behavior is the result of mutual dislocation interactions and intersections, which give rise to spontaneous formation of complex dislocation microstructures that can be either planar, cellular or fractal, depending on the mode and history of loading. Therefore, even in this highly idealized situation, where we can allow ourselves to focus on dislocations alone, to construct a predictive strength model for single crystals still remains as a great challenge to the field of computational materials science. This Thesis is intended to make contributions at the fundamental levels of this problem, with the objective to understand the mobility individual dislocations through interatomic interactions.

1.2 Scope of Thesis

This Thesis is focused on the mobility of single dislocations in semiconductor Si and BCC transition metals such as Mo, and on how it is affected by temperature and external stress. Atomistic simulations using empirical potential models are applied to investigate the underlying atomistic modes, while new methods such as the kinetic Monte Carlo model are developed to study dislocation motion at mesoscale. Because dislocation has both a localized core and a long-range stress field, we find that linking atomistic and meso scales is the most critical step in our study. In this Thesis, we present five contributions in the context of atomistic-mesoscale coupling, which may be regarded as advances in both methods development and mechanistic understanding of dislocation mobility.

Generally speaking, atomistic-mesoscale coupling can be of two forms for the same physical problem. This is because in practice the coupling allows one to eliminate one scale or the other. If one wants to probe a local defect on the atomistic level, then the coupling appears in the form of defect-surrounding interaction or a boundary condition. On the other hand, if one is interested in the mesoscale behavior of the

defect where atomic degrees of freedom are not treated, then the coupling can manifest in terms of an energy (or a stress or cutoff parameter) which has to be determined by microscopic considerations. For the purpose of this Thesis, we will refer to these two forms of coupling as types (a) and (b) respectively. Contributions to atomistic-mesoscale modeling of dislocation mobility of both types will be presented.

For the problem of simulation of dislocation core in a periodic cell, we derived a rigorous treatment of summing up image interaction energies (Chapter 4.2) by an elastic energy argument. As a consequence, a longstanding problem of conditional convergence of the lattice summation is resolved. This is an example of coupling of type (a). A second example is the derivation using linear response theory of a boundary condition for dynamically coupling an atomistic domain to its elastic surrounding (Chapter 4.3). In this case, the result is a method for which unphysical wave reflections at the boundary are minimized.

Problems of type (b) coupling are inherent in mesoscale simulations whenever atomistic effects cannot be ignored. In this context, we have investigated atomistic modes for dislocation motion in Si and BCC Mo (Chapter 5, 6). We calculated the Peierls stress and kink formation and migration energies for shuffle set screw dislocation in Si, which provide new evidences on the shuffle-glide controversy in Si, and raises questions on a previous interpretation based on kink mechanisms. We have also studied the core structure and Peierls barrier for edge, screw and mixed dislocations in BCC Mo, and found a much smaller Peierls stress for edge dislocations than previously reported values. This new result naturally explains the experimentally observed high mobility of edge dislocations, and suggests the inadequacy of the boundary condition used in the previous investigation.

The atomistic-mesoscale coupling is then most directly seen in our formulation of a kinetic Monte Carlo description of single dislocation motion in terms of displacement of line segments (Chapter 7, 8), where we invoke explicitly the mechanism of kink nucleation and migration. The result is a method to simulate dislocation velocity in response to applied stress and temperature on the time and length scale of experiments. Our model in Si was found to be able to explain a longstanding

controversial behavior of dislocation mobility at low stresses without introducing any *ad hoc* assumptions, by taking in account the coupling between the split partials. In the study of screw dislocation moving in a BCC lattice, we found that a simple mechanistic treatment of cross slip naturally gives rise to several new mechanisms leading to super jog (cusp) and debris loop formation, a microstructure that resembles experimental observations.

The last contribution, a more subtle form of type (b) coupling, is a formulation of interaction of dislocation nodes (Chapter 9), where we make use of the concept of local energy to remove the stress singularity in the current elasticity treatment of dislocation dynamics.

Before presenting these results, we start our discussions with a review of current experimental knowledge on dislocations in Si and BCC metals in Chapter 2 and 3 respectively. The purpose is to provide a general background on the observed properties of dislocations and their relationship with macroscopic deformation behaviors. We hope that by familiarizing ourselves with what is known and more importantly, what remains unknown from experiments, we can better appreciate the most relevant problems that awaits theoretical understandings. In this sense, Chapter 2 and 3 forms an extended introduction to the following Chapters (4 to 9), which contain our specific contributions. A brief summary is given in Chapter 10, which discusses the future work directions beyond single dislocation mobility. More technical details and extended discussions are given in four Appendixes for interested readers.

Chapter 2

Experiments on Dislocations in Si

The experimental and theoretical study of dislocations in Si has been an active field of study for 40 years, and is attracting ever more interests of researchers all over the world. The research in this area is clearly driven by the need for a better understanding of mechanical properties of Si, under various temperature, stress and electrical conditions, as this material is becoming the base material in the semiconductor industry. At the same time, two other driving forces of the research deserve to be pointed out. First, the relative easiness to grow high purity single crystal Si with zero dislocation content makes it convenient to measure the properties of a single dislocation, which can be introduced into the crystal one by one. Consequently, Si becomes the ideal test bed material for theory and modeling of dislocations. Second, it is observed that dislocations in Si contain in-gap local states at the core, so that a dislocation line could conduct electric current and short-cut the micro-electrical circuits. A primary concern in the semiconductor industry is then to control the dislocation mobility so that they do not migrate to the sensitive zones of electric circuits [6].

The experiments on dislocations in semiconductors has been reviewed extensively by Louchet and George (in 1983) [7], Alexander (in 1986) [8], George and Rabier [9, 10] (in 1987), and Duesbery and Richardson (in 1991) [11]. The purpose of this Chapter is to summarize the experimental results that are particularly relevant to this Thesis, with special interests on new experiments that have not been discussed in these reviews. It is hoped that through the discussion of the known facts as well

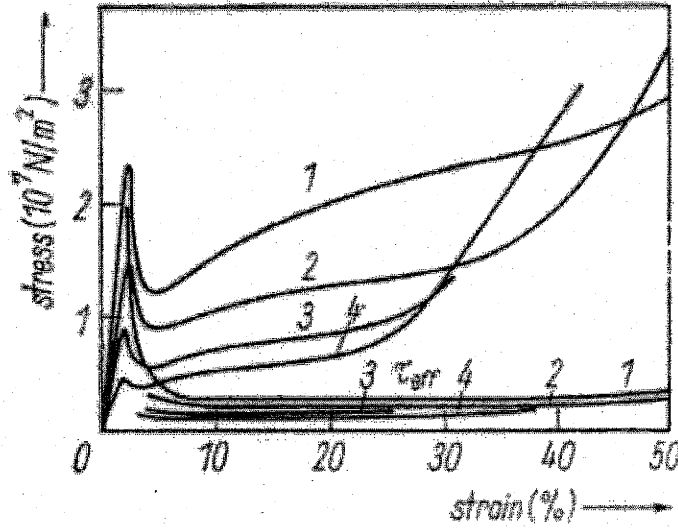


Figure 2-1: Stress-strain curve of Si for strain rate $\dot{\epsilon} = 1.2 \times 10^{-4}$ and initial dislocation density $N_0 = 2 \times 10^{-4} \text{cm}^{-2}$. (1) $T=800$, (2) 850, (3) 900, (4) 950°C. τ_{eff} is the effective stress where the internal dislocation interaction stresses are subtracted out. (Fig. 1 of [14].)

as remaining unresolved issues from experiments, one can form a clear view on where and how theories and modeling at the fundamental scale could make the most impact. The contents of this Chapter do not follow the chronological order of the experimental findings, but are organized to reflect a progressively more detailed picture concerning the dislocation mobility. The following four sections will discuss the macroscopic yield behavior of Si, dislocation core structures, dislocation mobility measurements, and properties of kinks, respectively.

2.1 Mechanical Response: Yield Stress

Due to the strong covalent bonding between Si atoms, dislocations in Si are more difficult to move than those in metals. This leads to the brittleness of Si under normal temperatures. A very sharp brittle-to-ductile transition (BDT) occurs in Si at $T_c \sim 873\text{K}$ [12], which is higher than half of its melting temperature $T_m = 1693\text{K}$ [9]. The cubic elastic constants of Si are $C_{11} = 161\text{GPa}$, $C_{12} = 81.6\text{GPa}$, $C_{44} = 60.3\text{GPa}$ [13].

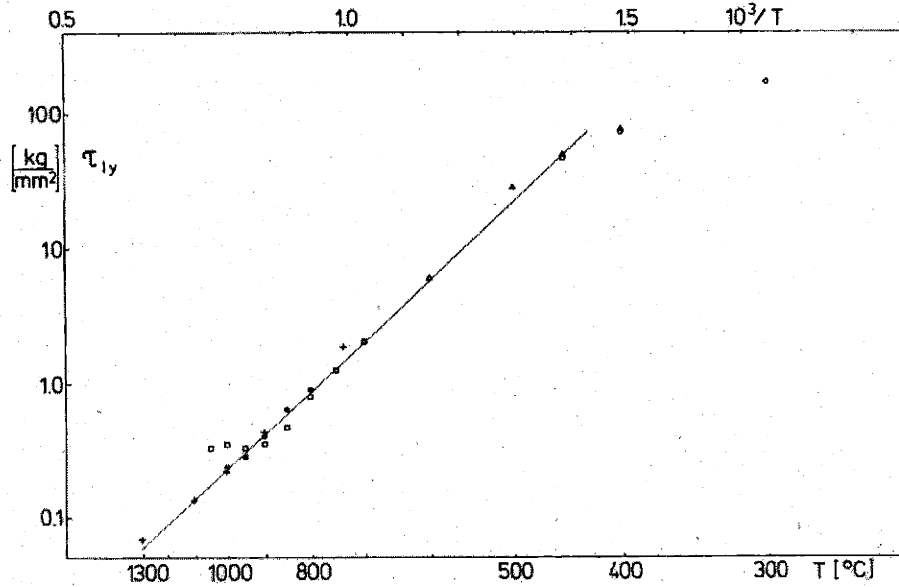


Figure 2-2: Lower yield stress as a function of temperature. Data converted to the same shear strain rate $\dot{\epsilon} = 5 \times 10^{-5} s^{-1}$. + compression, $N_0 = 10^4 cm^{-2}$, \square compression $N_0 = 0$, \bullet tension $N_0 = 10^4 cm^{-2}$, Δ, \circ compression plus hydrostatic pressure. (Fig. 25(b) of [8], $1 kg/mm^2 = 9.8 MPa$.)

Fig. 2-1 shows typical relationships between resolved shear stress and strain of Si deformed at different temperatures [14]. The distinctive feature here is the existence of a stress peak at the onset of yield, which is defined as the *upper yield stress*. The adjacent stress minimum is defined as the *lower yield stress*. The existence of the upper yield stress is the consequence of the exceptionally low dislocation density in the Si sample prior to deformation. The dislocation density remains low until the *upper yield stress* is reached, at which point a large number of dislocations are generated via multiplication, providing a rapid relief of the resolved shear stress.

At larger strains, Si also exhibits different stages of hardening, similar to face-centered cubic (FCC) metals. After the lower yield stresses, a region of easy glide and subsequent stage II hardening can be found in Fig. 2-1. Stage III dynamic recovery has also been reported, and some researchers [15] have even detected further stages (IV and V) of hardening and softening in semiconductors in a certain range of temperature. Please refer to Alexander [8] for more details.

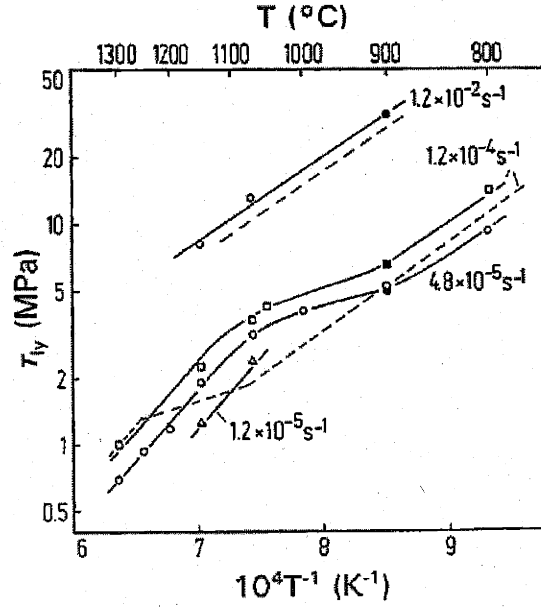


Figure 2-3: Lower yield stress as a function of temperature for dislocation free Si samples. (Fig. 2 of [16].)

Since the lower yield stress τ_{ly} is the minimum stress to deform the material plastically, it represents a lower bound of the materials strength. It is found in Si that τ_{ly} depends on temperature T and strain rate $\dot{\epsilon}$ in the following manner [8],

$$\tau_{ly} = C_{ly} \dot{\epsilon}^n \exp\left(\frac{Q}{nk_B T}\right), \quad (2.1)$$

where C_{ly} and n are constants independent of T and $\dot{\epsilon}$, and Q is an effective activation energy. The values of Q and n in yield stress measurements are related with the Q and m ($m = n - 2$) obtained from dislocation mobility measurements (see Section 3). In Fig. 2-2 τ_{ly} is plotted as a function of temperatures T with data converted to the same shear strain rate of $\dot{\epsilon} = 5 \times 10^{-5} \text{ s}^{-1}$. It is fair to conclude that Eq. (2.1) holds very well for a wide range of temperatures ($400 \sim 1300^\circ\text{C}$), except for the dislocation free samples at high temperatures.

Recent measurements of lower yield stress of dislocation free Si in high temperatures [16], see Fig. 2-3, have shown a transitional behavior at temperatures above

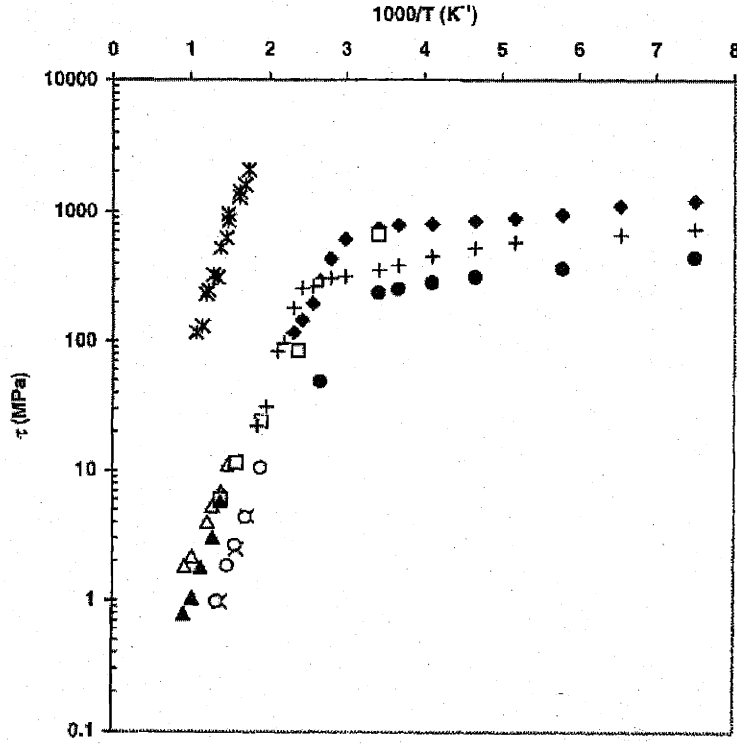


Figure 2-4: Yield stress of Si (*), GaAs (\square , \blacklozenge , \triangle), InP (+, \blacktriangle , \times) and InSb (\circ , \bullet) as a function of temperature. (Fig. 5 of [18].)

900°C at low strain rates ($\sim 10^{-5}\text{s}^{-1}$). Samples with nonzero initial dislocation concentration show similar trends, with the transition temperature pushed to higher values. It has been postulated [16] that this transition is due to the change of self diffusion mechanism (from vacancy to interstitial) in Si at elevated temperatures, a topic that has been recently studied by atomistic simulations [17]. It was also noted that [16] dislocation mobility (see Section 3) also exhibits similar transition at high temperatures. At the same time, the effect of dislocation-dislocation interactions has also been postulated [10] to account for this transition. Therefore, the explanation for the high temperature yield stress behavior of Si is still a matter of controversy.

At the same time, recent experiments on the yield stress of semiconductors under high confining pressure suggests that the linear behavior between $\ln \tau_y$ and $1/T$ may change at the low temperature limit. As shown in Fig. 2-4, the $\ln \tau_c$ and $1/T$

curve¹ turns into a much smaller slope for III-V semiconductors below a critical temperature [19, 20, 21]. TEM and slip trace analysis indicate that a different type of dislocation (from glide to shuffle set) is responsible for the plastic deformation for semiconductors at low temperature. Recent experiments in Si at room temperature also shows a similar dislocation microstructure change. Unfortunately, the shear stress at such conditions are unknown, so that a direct observation on the transition of yield stress behavior is not available in Si so far, as shown in Fig. 2-4. Previous theoretical analysis[22] on double kink nucleations has anticipated such a transition at about 500MPa. But the experimental results show that the transition does not occur at 500MPa, if it occurs at all. It is clear that more questions remain to be answered to reach a complete understanding of this low temperature transition. The two types of dislocation core structures in Si, i.e. glide and shuffle sets, is discussed in more detail in the next section.

2.2 Dislocation Core Structure: Shuffle-Glide Competition

The structures of the dislocations are determined, to a large extent, by the structure and symmetry of the crystal lattice. Fig. 2-5 shows the diamond cubic lattice of Si viewed in two different perspectives. The diamond cubic lattice can be considered as the super-position of two face-centered cubic (FCC) lattices, offset by $\frac{1}{4}[111]$ from each other, as shown in Fig. 2-5(a). The slip systems of Si are then similar to that of FCC metals, i.e. they are on (111) planes and in $[110]$ directions. However, the co-existence of two sub-FCC lattices complicates the situation in Si. As shown in Fig. 2-5(b), dislocations can glide on two different sets of (111) planes. The closely spaced set, e.g. between C and b , is called the *glide* set, while the widely spaced set, e.g. between b and B is called the *shuffle* set. On which set of the (111) planes do dislocations in Si exist or move has been a controversy for some forty years. Although

¹At low temperatures, the stress peak at the yield region ceases to exist, and the onset of yield is designated as the critical resolved shear stress τ_c .

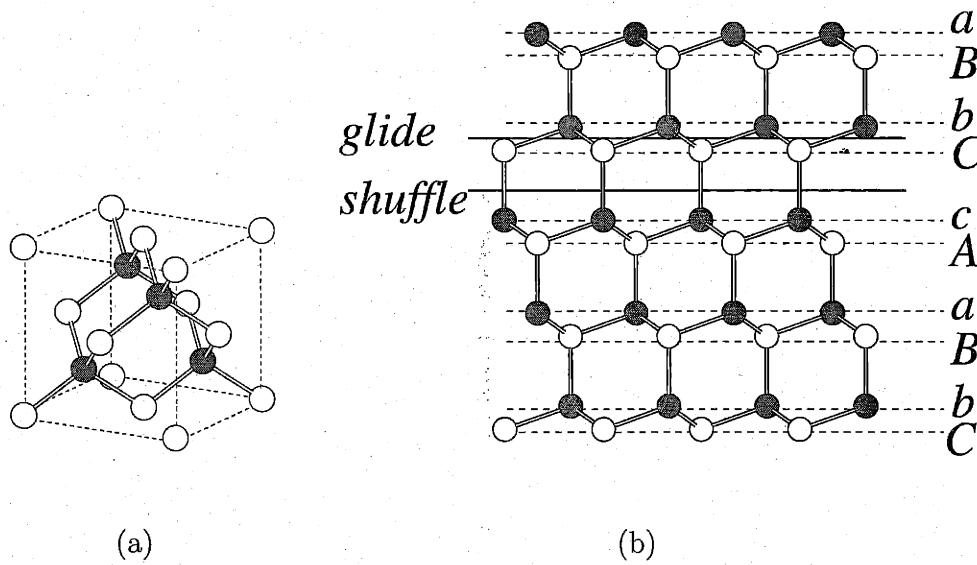


Figure 2-5: Diamond cubic structure of Si lattice. The two interlaced FCC lattices are shown in white and dark atoms respectively. (a) primitive cell of the diamond cubic lattice. (b) Glide and shuffle set of (111) planes.

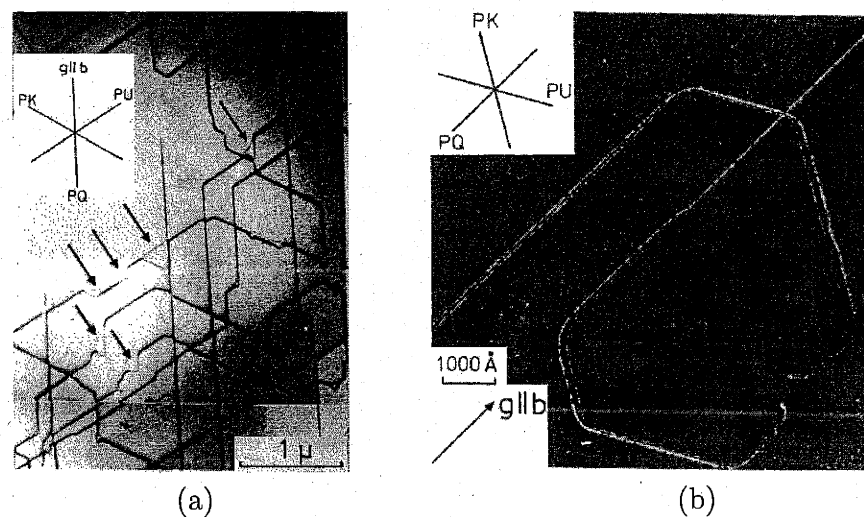


Figure 2-6: (a) Dislocation pattern in the primary glide plane Si after a few seconds of deformation at $T = 520^\circ\text{C}$ and $\tau = 392\text{MPa}$. (b) Weak beam micrograph of a dissociated loop in Si deformed for 45 min at $T = 420^\circ\text{C}$ and $\tau = 256\text{MPa}$. (Fig.2 and 6 of [23], with minor editing.)

it is now widely accepted that dislocations in tetrahedrally bonded semiconductors are located and move on the *glide* set, this is perhaps only true within a certain stress ($< 1\text{GPa}$) and temperature range ($800 \sim 1100\text{K}$). Experiments at higher stress and lower temperature suggests that plastic deformation could be carried by the motion of dislocations on shuffle set planes.

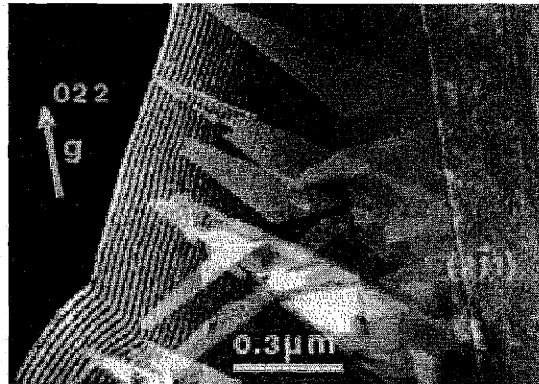
Because stacking fault can exist on *glide* set planes, glide set dislocations can dissociate into *partial* dislocations and lower their elastic energies, while dissociation is impossible on the *shuffle* set plane. Therefore, attempts toward resolving the “shuffle-glide” controversy has been focused in determining whether or not dislocations in Si are dissociated. Using the weak beam technique, it is found that almost all dislocations in Si [24, 25] and Ge [26] are dissociated into partials, and are mobile in the dissociated form [27, 28].

The dislocation dissociation in Si is clearly illustrated in the observation of widely separated partial under high external stress[23], as shown in Fig. 2-6(a). In this experiment, the Si sample has been deformed for a few seconds at $T = 520^\circ\text{C}$ and $\tau = 392\text{MPa}$. The dislocation lines are observed to be parallel to three $[110]$ directions,

which is a general feature in diamond cubic semiconductors. The Peierls barrier for the glide set planes force the dislocation to become either screw or mixed 60° (the angle between the dislocation line and the Burgers vector). The arrows in Fig. 2-6(a) indicate places where the leading partial is well separated from the trailing partial. At smaller stress, the dislocation is usually weakly dissociated, as revealed by the weak beam method, shown in Fig. 2-6(b). The separation between partials are on the order of 30\AA , and the measurements of this separation are used to determine the stacking fault energy of semiconductors. A recent experiment [29] found the stacking fault energy to be $\gamma_{SF} = 55 \pm 7\text{mJ/m}^2 = 3.4 \pm 0.4\text{meV/\AA}^2$ for Si, $\gamma_{SF} = 60 \pm 10\text{mJ/m}^2 = 3.8 \pm 0.6\text{meV/\AA}^2$ for Ge, and $\gamma_{SF} = 285 \pm 40\text{mJ/m}^2 = 17.8 \pm 2.5\text{meV/\AA}^2$ for diamond.

Although the dissociation of dislocations in Si is well established, the “shuffle-glide” controversy remains open. This is because a partial dislocation can also exist in the shuffle set plane [30], by absorbing a linear chain of point defects into its core. In other words, a glide partial can transform into a shuffle vacancy (S_v) or into a shuffle interstitial (S_i) partial by climb [31]. This possibility seems to be necessary in order to explain electron paramagnetic resonance (EPR) [32, 33, 34, 35] measurements on deformed Si samples. Plastic deformation of Si within a certain temperature range is accompanied by an large increase of the density of paramagnetic centers, which are identified as point defects from the symmetry of their signal [32]. As dislocation intersecting processes seems to play no role in generating these point defects, it was speculated [36] that a complex interaction between the core of the partial dislocation and intrinsic point defects is responsible, with the end result of releasing point defects when the partial starts to move. Although the dislocation interactions with intrinsic point defects have been the subject of recent theoretical studies [37, 38], no direct experimental evidence exists so far to support this mechanism.

Lowering the temperature will change the dislocation microstructure significantly. In these experiments a hydrostatic confining pressure is applied to suppress fracture. Deformation of Si under 1.5GPa pressure [40, 18] has resulted in large number of free partial dislocations and stacking fault areas. Recent experiments [39] at room temperature with 5GPa confining pressure have found that dislocations are mainly



(a)



(b)

Figure 2-7: (a) Dislocation microstructure at $T = 450^\circ$ and 1.5 GPa confining pressure, showing large stacking fault areas. (b) Dislocation microstructure at room temperature and 5 GPa confining pressure, where the dislocations are mostly aligned along [110] and [123] directions. (Fig. 2 of [18] and Fig. 1 of [39].)

undissociated and aligned along $[110]$ (screw) and $[123]$ (mixed 41°) directions, suggesting that they are on the shuffle set planes. Similar behavior is also recently found in III-V compounds [19, 20, 21], where the transition into shuffle occurs at a much smaller stress ($\sim 1\text{GPa}$) so that the experiments are easier to perform. It is also found [18] to be very difficult for the preexisting dissociated dislocation to recombine into the undissociated form, so that the shuffle set dislocations at low temperatures are most likely newly nucleated, possibly from internal crack tips. Fig. 2-7(a) and (b) show the dislocation microstructures at 1.5GPa and 5GPa confining pressure respectively.

2.3 Dislocation Mobility

In the context of this Thesis, it is a fortunate fact that a great wealth of experimental data are available on the dislocation mobility in Si. Among the different approaches to observe dislocation motion, X-ray topography method used by A. George [41] in 1972 is still one of the most popular ways to investigate the *intrinsic* behavior of dislocations, with the advantage that artificial effects on dislocation motion are relatively small. In comparison, in the “double-etching” method [42], where the positions of the dislocations are revealed by chemical etching before and after applying the loading stress, dislocations could be pinned by impurity atoms segregating on the etching surface. As a result, a starting stress at $5 \sim 10\text{MPa}$ was reported in experiments [42] using the etching method, below which no dislocation motion is found, while this is not the case in X-ray topography experiments.

In the experiments of George [45], dislocations were introduced into initially dislocation free Si samples by scratching the surface with a diamond needle, along the direction perpendicular to that of the anticipated slip lines on this surface. Uniaxial loading is then applied to the sample at an elevated temperature.² As shown in Fig. 2-8, dislocation half loops emerge and expand in the direction perpendicular to

²The process of dislocation nucleation at the scratch surface during annealing was investigated by Puttick et al. [46, 47, 48]. Other methods of introducing dislocations also exist, such as indentation by a micro-hardness machine [49].

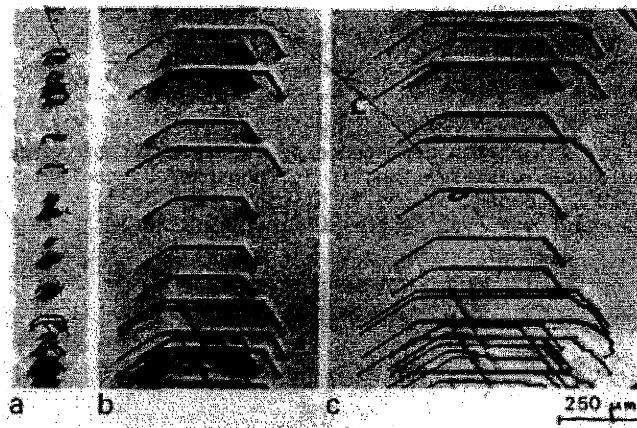


Figure 2-8: Growth of dislocation half loops in Si revealed by X-ray topography. Dislocations were introduced by scratching the surface followed by uniaxial loading at elevated temperature. Dislocation half loops expanded perpendicular to the scratch direction. (Fig. 6 of [43].)

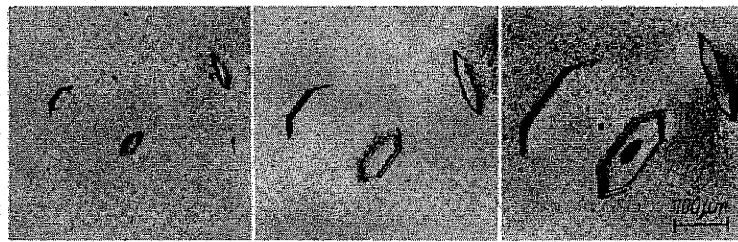


Figure 2-9: Expansion of half and full dislocation loops in Si under shear stress, observed by X-ray topography. (Fig. 1 of [44].)

the scratch direction. The dislocation segments parallel to the free surface were found to be screw while the two arms intersecting the surface were 60° dislocations. These dislocation half loops as well as some complete hexagonal loops inside the sample [44] continued to expand upon further loading, as shown in Fig. 2-9. The velocities of both screw and 60° dislocations were then obtained by measuring the size of these loops at different times. Fig. 2-10(a) and (b) show the measured dislocation velocity at different temperature and stress respectively [44]. Before discussing the temperature and stress dependences, some microscopic details are worth mentioning.

First, the two 60° dislocation segments moved with slightly different velocities. In

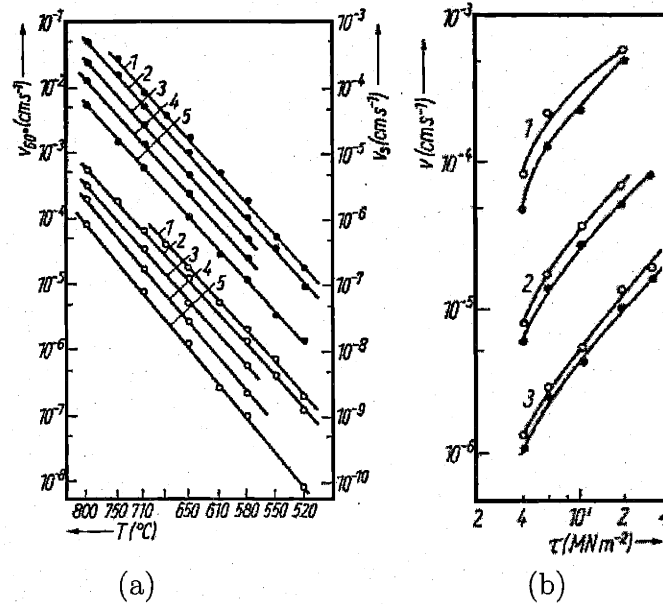


Figure 2-10: (a) Temperature dependence of velocity of screw (●) and 60° (○) dislocations in intrinsic Si at stresses (1) $\tau = 30$, (2) 19, (3) 10, (4) 6, (5) 4 MPa. (b) Stress dependence of velocity of screw (●) and 60° (○) dislocations in intrinsic Si at temperatures (1) $T = 800$, (2) 710, (3) 650 °C. (Fig. 2 and 3 of [44].)

one case [43], the relative velocities of the three segments were found to be: screw 1, 60°₁₁₀ 1.1, 60°₀₁₁ 1.5. This may be attributed to the different order of the partials in these two 60° dislocations. There is however, a more puzzling phenomenon, that is, the faster moving 60° dislocation seems to be subjected to a “glide instability”, where part of the segment can suddenly increase its velocity by 40% with other parts moving at the same speed as the other 60° segment, resulting in a “zig-zaged” shape, see Fig. 2-8(c). George [43] suggested that this could be due to some changes in the dislocation core structure resulting from a climb mechanism. The velocity of 60° dislocations in the following discussion refer to the average values of the left and right segments.

Dislocation velocity v as a function of temperature T and resolved shear stress τ were usually fitted with the following empirical formula [41],

$$v = C\tau^m \exp\left(-\frac{Q}{k_B T}\right), \quad (2.2)$$

Table 2.1: Stress dependence of activation energy Q and temperature dependence of stress exponent m for screw and 60° dislocations in intrinsic Si. (Table 2 and 3 of [44].)

$\tau(\text{MPa})$	$Q_s(\text{eV})$	$Q_{60^\circ}(\text{eV})$
240	1.9	1.9 [50]
30	2.17	2.16
19	2.19	2.22
10	2.22	2.28
6	2.23	2.42
4	2.17	2.43
$T(^{\circ}\text{C})$	m_s	m_{60°
800	1.15	0.8
710	1.1	1.2
650	1.15	1.2
580	1.2	1.4
550	1.3	1.8
520	1.2	1.6

where m is called the stress exponent, Q is the effective activation energy, k_B is the Boltzmann's constant and C is a constant. However, it is clear that a power law stress dependence of velocity is only obeyed for stress larger than 6MPa (see Fig. 2-10(b)), and m increases at lower stresses. The stress exponent m is also temperature dependent and the activation energy has stress dependence as well. This dependence is more pronounced for 60° dislocations than for screws. The fitted values for Q and m at different temperature and stresses are listed in Table. 2.1 and plotted in Fig. 2-11.

It was known that the description of dislocation mobility by Eq. (2.2) is valid only in the so called "central range" ([9], p.955) of temperature ($750 \sim 1100\text{K}$) and stress ($6 \sim 100\text{MPa}$). In the rest of this section, we will discuss dislocation mobility at high and low extremes of stress and temperature. As discussed in the previous section, the majority of dislocations below a transition temperature will glide on the shuffle set planes, hence they are expected to have a very different mobility. At the same time, the simple linear temperature dependence as shown in Fig.2-11(a) is also found to change at higher temperatures [7, 51, 52].

In the double-etching experiment, Farber et al. [51] measured temperature depen-

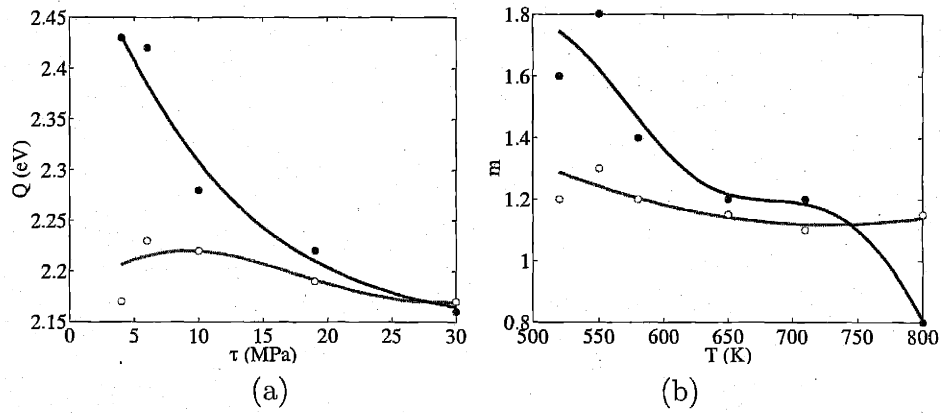


Figure 2-11: Stress dependence of activation energy Q (a) and temperature dependence of stress exponent m (b) for screw (\circ) and 60° (\bullet) dislocations in intrinsic Si. (Data from Table 2 and 3 of [44].)

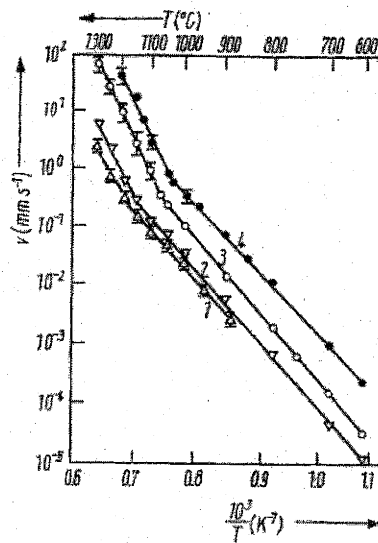


Figure 2-12: Temperature dependence of dislocation velocity in Si at high temperature. Smooth splines are drawn to guide the eye. (Fig.1 of [51].)

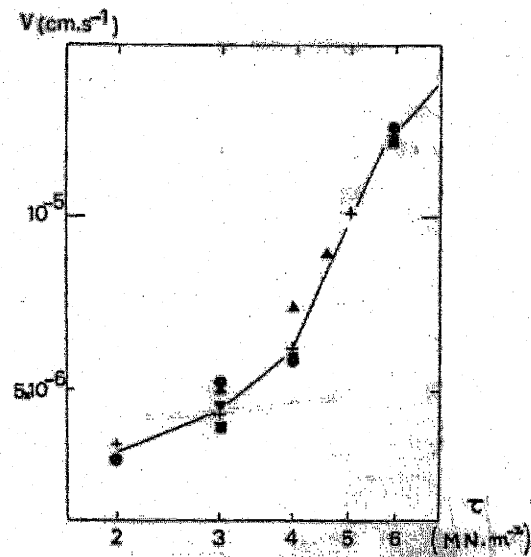


Figure 2-13: Stress dependence of dislocation velocity in intrinsic Si at low stresses. (Fig.4 of [43].)

dence of 60° dislocation velocity up to 1600K ($0.9T_m$), as shown in Fig. 2-12. At temperatures higher than 1323K, the dislocation velocity becomes higher than the low temperature extrapolation, and the effective activation energy nearly doubles, i.e. $Q = 4 \pm 0.1\text{eV}$. Parenthetically, similar measurements in Ge showed either decreased or unchanged velocity and activation energy at high temperatures, depending on the loading stress [53]. Farber postulated that dislocation-point defect interaction could be responsible, and it could be related with the possible transition from equilibrium vacancies to equilibrium interstitials at elevated temperatures. Recent atomistic calculations [17] and high temperature yield point measurements [16] seem to support this view.

The behavior of dislocation mobility at low stress regime still remains as a matter of controversy to date. As shown in Fig. 2-13, there seems to be a “threshold stress” [43] (around 6MPa), below which dislocation velocity drops much more rapidly with decreasing stress than at higher stresses. The effect of phosphorus concentration was investigated, but no effect was found for contents ranging from 10^{14} to $1.2 \times 10^{18}\text{at.cm}^{-3}$. It was then argued [43] that the “threshold stress” behavior is

intrinsic to dislocations in Si, although it cannot be explained by the well known kink diffusion model of Hirth and Lothe (H-L), which predicts linear relationship between velocity and stress. At the same time, *in situ* X-ray topography study by Imai et al. [54] reported linear stress-velocity relationship in high purity Si throughout the stress range of 1.2 ~ 40MPa, in contradiction with George. In Chapter 7, we present a possible resolution of this controversy by considering the coupling effect [55] between the two partial dislocations.

In the high stress limit (30 ~ 300MPa), the stress dependence of dislocation velocity can be well described by the power-law equation $v = v_0(\tau/\tau_0)^m$ [7, 9, 56]. However, it was found that the stress exponent m depends not only on the dislocation character, but also on the relative orientation of Burgers vector (\vec{b}) with respect to the loading axis (\vec{c}), along which uniaxial compression is applied. An empirical expression for this relation was found to be,

$$m = -7.2(1 - |\vec{b} \cdot \vec{c}|)^2 F_n / b\sigma + m_1, \quad (2.3)$$

where F_n is the normal component of the force on the dislocation, and σ is the nominal compression stress. The fact that dislocation mobility depends on F_n is a violation of the so called *Schmid* law, which states that dislocation velocity should only depend on the glide component of the resolved shear stress on the slip plane. Although no serious attempts have been made so far to explain this non-Schmid effect in Si, it may be due to the coupling between partial dislocations again. Although F_n cannot exert a net glide force on the perfect dislocation, it exerts opposite forces on the two partials, thus can alter the separation between the two partials. The effect of the partial separation width and the dislocation mobility will be investigated in Chapter 7.

Before closing this Section, let us take another look at the asymmetry of 60° dislocation mobility. Differently from the findings of George [43] for the slight symmetry on the mobility of the small difference of the two 60° dislocations both moving forward, the mobility difference of the same 60° dislocation in the forward forward and

backward direction was found to be more than one order of magnitude [57, 58]. Care must be taken to understand these results, because they could easily come from the surface effect rather than the intrinsic properties of Si. Since the dislocation lines are inclined at 60° with the free surface, image forces would tend to shrink the dislocation half loops. Louchet [7] also suggested that surface effect should be responsible by noticing the shape of the etch pits of these experiments. However, Nikitenko et al [57] argued that since dislocation half loops did not undergo spontaneous shrinkage under annealing, the surface (or image) effect is negligible. Instead, a long time annealing at $T > 700^\circ\text{C}$ resulted in disappearance of the mobility asymmetry effect. The authors argued that this effect can only be explained by the change of the “states” of point defects or impurity complexes after the passage of dislocation. To account for the asymmetry effect, the authors had to assume the defect complexes have an “order orientation” such that they impede dislocation coming from one direction while enhance their motion for those coming from the other side. Such an explanation sounds a little far-fetched, since no such anisotropic defect complexes has ever been found before. Here we discuss an alternative explanation. Notice that the motion of surface etch pit does not necessarily imply the uniform motion of the entire 60° dislocation segment beneath the surface. Part of the dislocation could be slowed down by point defects and have not moved as far ahead as the etch pit during the forward motion. This could result in the faster backward motion of the etch pit upon reversed loading. Annealing could make the entire dislocation catch up with the surface etch pit and thus removing the asymmetry effect. In this sense, it looks important to repeat such experiments with X-ray topography where the entire dislocation line can be observed.

2.4 Kink Mechanism

To date it is widely accepted that³ dislocations in Si moves by double-kink mechanism [30] on the two partials, although point defect interactions are also important. The double-kink mechanism is illustrated in Fig. 2-14. Due to the strong Peierls bar-

³at least in the temperature range of $750 \sim 1100\text{K}$

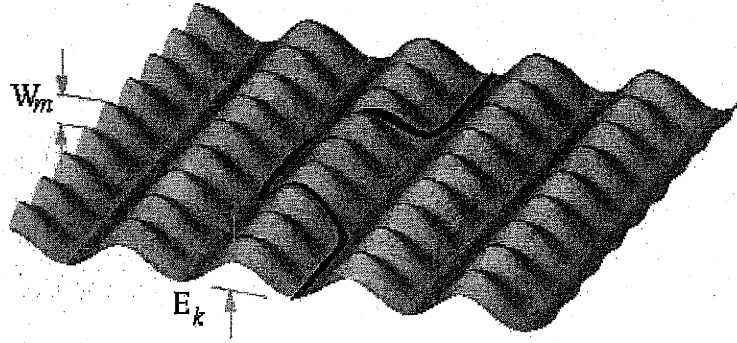


Figure 2-14: Schematic of the Peierls barrier and kink mechanism for dislocation motion. Dislocation is represented as a continuous line, which resides mostly at the bottom of the Peierls energy surface except at kinks.

rier, each (partial) dislocation moves forward by advancing only a segment of itself to the next Peierls relief, thus creating a “double-kink”, followed by the migration of the two kinks in opposite directions. Thus two energy barriers control the dislocation motion, one for the double-kink nucleation ($E_{dk} \approx 2E_k$, E_k for single kink self energy), and the other for the kink migration(W_m).

This Section discusses various experimental approaches to determine the values for E_k and W_m . This would be impossible without at least a brief introduction on the theoretical model which relates these energy parameters with the dislocation velocity.

A complete description of dislocation motion has to consider possibly correlated kink mechanisms on the two partials, which will be the subject of in Chapter 7. On the other hand, a lot of insight can be obtained in the Hirth-Lothe (H-L) model [30], which studies a simplified scenario of undissociated dislocation motion. In the H-L model, kink migration is assumed to be at a constant velocity v_k and the double kink nucleation rate is assumed to be at a constant J per atomic site along the dislocation. As will be discussed in more detail in Appendix C.1, H-L model predicts the dislocation velocity to be,

$$v = \sqrt{2v_k J} = \omega_0 \sqrt{2h} \frac{\tau b h a}{k_B T} \exp \left(-\frac{E_k + W_m}{k_B T} \right), \quad (2.4)$$

in the limit of infinitely long dislocations. Therefore, the effective activation energy Q fitted from the temperature dependence of dislocation velocity is related with the kink energies through $Q = E_k + W_m$. For screw and 60° dislocations in $800 \sim 1100\text{K}$, $Q \sim 2.2\text{eV}$. Therefore, conventional experiments on dislocation mobility gives $E_k + W_m = 2.2\text{eV}$, but cannot differentiate the relative contribution of E_k and W_m .

For dislocations with length L much shorter than the mean free path of kinks, their motion becomes nucleation controlled and their velocities exhibit a linear dependence on L with a different temperature dependence,

$$v = hLJ = \omega_0 \frac{\tau b h^2 L}{k_B T} D_k \exp \left(-\frac{2E_k + W_m}{k_B T} \right). \quad (2.5)$$

In this case, $Q = 2E_k + W_m$. Therefore, by studying the length dependence of dislocation velocity, one can extract E_k and W_m separately.

The experiments of this type requires a much higher resolution than X-ray topography and are usually carried out in a high-voltage electron microscope. For example, Louchet [50] found that the mobilities of both screw and 60° dislocations are independent of their length down to about $X = 0.4\mu\text{m}$ at $\tau = 90\text{MPa}$, $T = 873\text{K}$, while at a higher stress ($\tau = 550\text{MPa}$, $T = 813\text{K}$), $X = 0.1\mu\text{m}$ [7]. Hirsch [59] estimated that this critical length to be $0.2\mu\text{m}$ (to within a factor of 2 or 3) at $\tau = 280\text{MPa}$, $T = 593\text{K}$, which gives

$$W_m \leq 1.2\text{eV}. \quad (2.6)$$

Gottschalk [60] measured W_m by studying mobility of individual partials at very low temperature in high stress deformed specimens, which contains an over saturation of kinks. The dislocation mobility in this experiment is then controlled only by migration of these pre-existing kinks. Assuming the kink migration to be equal for 30° and 90° partials, W_m is found to be between 1 and 1.2eV , which is consistent with the above result of Hirsch. Assuming $E_k + W_m \approx 2.0\text{eV}$, kink formation energy was found to be

$$E_k \approx 0.8\text{eV}. \quad (2.7)$$

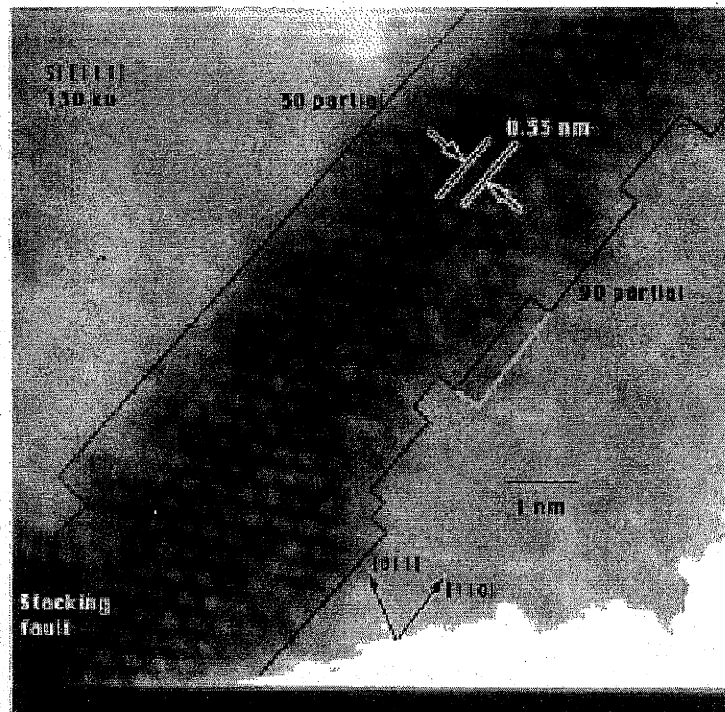


Figure 2-15: TEM image of dissociated 60° dislocation in Si, displaying kinks on the two partial dislocations. (Fig. 3 of [61])

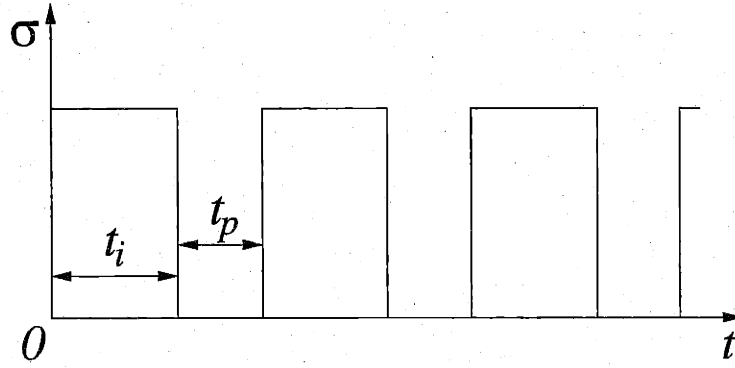


Figure 2-16: The stress pulse sequences in intermittent loading experiment [63].

Recently Kolar et al. [61, 62] used the so called atomic resolution electron microscopy to study dislocations in Si, where individual kinks on the partials are visible, as shown in Fig. 2-15. The kink density was obtained by simply counting the kinks along the partials. Assuming the mobility of the partials is determined solely by the migration of these kinks, the kink migration barrier is estimated to be $W_m = 1.24 \pm 0.07\text{eV}$ for both 30° and 90° partials. Assuming the kink density is at thermal equilibrium, kink formation energy is estimated to be $E_k = 0.797 \pm 0.15\text{eV}$ for 30° partial and $E_k = 0.73 \pm 0.15\text{eV}$ for 90° partial. These give an estimation of the effective activation energy of dislocation mobility at $Q = E_k + W_m = 1.97 \pm 0.2\text{eV}$, which is consistent with direct mobility measurements ($Q = 2.2\text{eV}$) [44].

Estimation of E_k and W_m can also be obtained by applying an intermittent loading⁴ [63, 65, 66], i.e. a constant external stress is applied during load pulse t_i while zero load is applied during pause period t_p , as shown in Fig. 2-16. The total time with stress exerted on the specimen $\sum t_i$ is kept constant at 7200s. Mobility of 60° dislocations as a function of t_i and t_p were investigated by etch-pit method, with $t_p = 0$ corresponding to the conventional static loading condition. Fig. 2-17 shows the average dislocation displacement with different choices of t_i and t_p . In (a), t_p is kept equal to t_i , and dislocation displacement increases with increasing t_i , and the

⁴Sinusoidal stress oscillation has also been applied in the so called internal friction experiments [64]. But it has not been successful in determining kink energies.

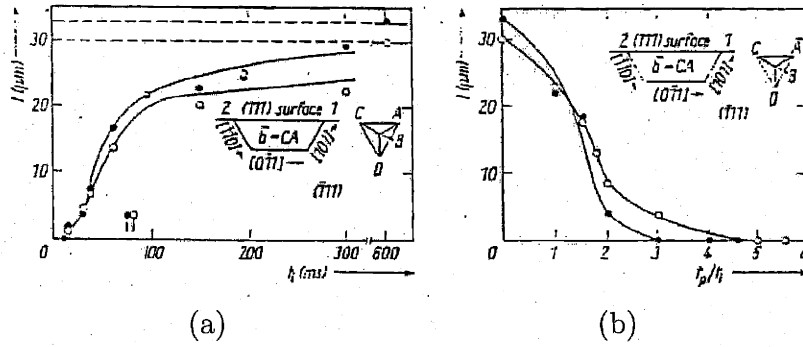


Figure 2-17: Dislocation displacement during intermittent loading, at $T = 873\text{K}$ and $\sigma = 7\text{MPa}$, (a) as a function of t_i with $t_p = t_i$ and total loading time $\sum t_i = 7200\text{s}$. Curve 1 (\bullet) and curve 2 (\circ) correspond to the two 60° dislocations respectively; (b) as a function of t_p/t_i at $t_i = 94\text{ms}$. (Fig. 2 and 3 of [63]).

dislocation did not move at all if $t_i \leq 10\text{ms}$. In (b), t_i is kept at 94ms , and dislocation displacement decreases with t_p/t_i . Dislocation displacement vanishes altogether at $t_p/t_i \approx 3$ to 5 . By comparing these results with the kink model of dislocation mobility, the energy factors are found [63] to be $W_m = 1.58\text{eV}$ and $E_k = 0.62\text{eV}$. A comparison between kink energies from experimental measurements and those from atomistic calculations will be presented in Chapter 7.2.3.

Chapter 3

Experiments on Dislocations in BCC Metals

The start of making and utilization of metals (copper, iron) and alloys (bronze) was a huge technological advance in the human history. Today 86 metals has become known [67], and they can be characterized either by their structure or by their chemical properties. The different structures of metals were revealed by the X-ray diffraction method, the invention of which by von Laue in 1912 had simultaneously proved the wave nature of X-ray and the periodic arrangement of atoms in crystals. Common crystal structure of metals include face-centered cubic (FCC), such as Cu and Al, body-centered cubic (BCC), such as Fe, W, Mo and Ta, and hexagonal close packed (HCP), such as Zn and Mg, etc. Metals can also be divided into representative metals, including groups 1(IA), 2(IIA), 13(IIIA), 14(IVA) and 15(VA), and transition metals, including groups 3(IIIB) to 10(IIIB), which are in the center region of the periodic table.¹ The common feature of transition metals is that they all have partially filled *d*-orbits. Transition metals in group 5(VB), such as V, Nb, Ta, and group 6(VIB) such as Cr, Mo, W, and Fe in group 8 (VIII) are of primary interest in this Thesis, and they all have BCC structure. Some important bulk properties of these metals are listed in Table 3.1. In the following sections, we will mainly focus

¹For simplicity, we have ignored lanthanides and actinides, which are also called inner transition metals.

Table 3.1: Bulk properties of BCC transition metals [68, 69, 30, 70]. Elastic constants C_{11}, C_{12}, C_{44} in GPa, melting temperature in K, cohesive energy E_{coh} in eV, and thermal conductivity κ in $\text{Wm}^{-1}\text{K}^{-1}$. Note that VIB metals Cr, Mo and W generally have a larger shear modulus C_{44} and thermal conductivity κ than VB metals V, Nb and Ta.

	Z	ele. conf.	C_{11}	C_{12}	C_{44}	T_m	E_{coh}	κ
V	23	$3d^34s^2$	227.9	118.7	42.6	2163	5.31	30.7
Nb	41	$4d^45s^1$	246.6	133.2	28.1	2742	7.57	53.7
Ta	73	$5d^36s^2$	266.0	161.2	82.4	3293	8.10	57.5
Cr	24	$3d^54s^1$	387.1	103.5	100.8	2130	4.10	93.7
Mo	42	$4d^55s^1$	464.7	161.5	108.9	2896	6.82	138
W	74	$5d^46s^2$	522.4	204.4	160.6	3695	8.90	174
Fe	26	$3d^64s^2$	242	146.5	112	1808	4.29	80.2

on the properties of Mo, as a representative of BCC transition metals.

BCC metals are generally strong and have high melting points, so that are widely used in structural applications, such as iron, and under high temperature conditions, such as tungsten filament. Experimental studies on strength and plasticity of BCC metals and their relation with dislocation activities were initiated around 1960's, and they are still attracting the interests of numerous researchers today. Besides the need for high temperature high strength materials, to understand the plasticity of BCC system is an immensely intellectually challenging problem. The yield strength of BCC metals exhibits strong temperature and orientation dependence as well as asymmetry with respect to tension and compression. Unexpected slip systems are found to be operating at low temperatures, and were referred to as "anomalous slip" due to the lack of a convincing explanation. At the same time, the intrinsic lattice resistance to dislocation motion is found to be large, and capable to explain a number of distinctive behavior of BCC metals. This allows atomistic modeling to make direct contact with macroscopic deformation behaviors of these materials. However, for a complete understanding of the plastic strength of BCC metals one has to take into account the collective behavior of a large number of dislocations, giving rise to their own microstructures, at the so called "meso" scale, which is between the atomistic and the macroscopic. In this Chapter, we summarize the current experimental knowledge

on dislocations in BCC metals, in hoping to provide a general background for the theories and numerical modeling in the following Chapters.

The experiments on the temperature and orientation dependence of plasticity of BCC metals, as well as their relationship with the core structure of screw dislocations have been discussed in great detail by Duesbery and Vitek et al. (from 1969 to 1998) [71, 72, 73, 74, 75, 76, 11, 68], as well as Kubin [77]. While these topics will be the focus of this Chapter as well, we will also discuss anomalous slip, dislocation microstructure and individual dislocation mobility measurements.

3.1 Temperature and Orientation Dependence of Mechanical Response

The differences in the mechanical response of BCC metals from that of FCC metals mainly come from the stronger lattice resistance to dislocation motion in the former. As a result, the yield stress of BCC metals rises dramatically as temperature approaches zero. In comparison, the resistance to plastic deformation in FCC metals mainly comes from dislocation interactions with impurities or other dislocations (work hardening), with intrinsic lattice resistance to dislocation motion being vanishingly small (see for example the stress-strain curve of Cu [78]). In addition, slip in BCC metals also exhibit strong orientation dependence, most of which can be accounted for by the anisotropy of intrinsic lattice resistance to dislocations.

Fig. 3-1(a) shows stress-strain curves of Mo at two different temperatures [79]. The sample was under uniaxial tension along the direction marked as *A* inside the standard triangle. This loading condition favors single slip on $(101)[11\bar{1}]$ system² with Schmid factor ≈ 0.5 . While at 493K three-stage hardening was observed, the crystal at 293K is much stronger and exhibits parabolic hardening. Fig. 3-1(b) shows the stress-strain curves at high symmetry tensile directions [80] such as [110] and [100], where multiple slip systems are favored. The increase of yield stress with decreasing

²The slip systems in BCC metals will be discussed in the next Section.

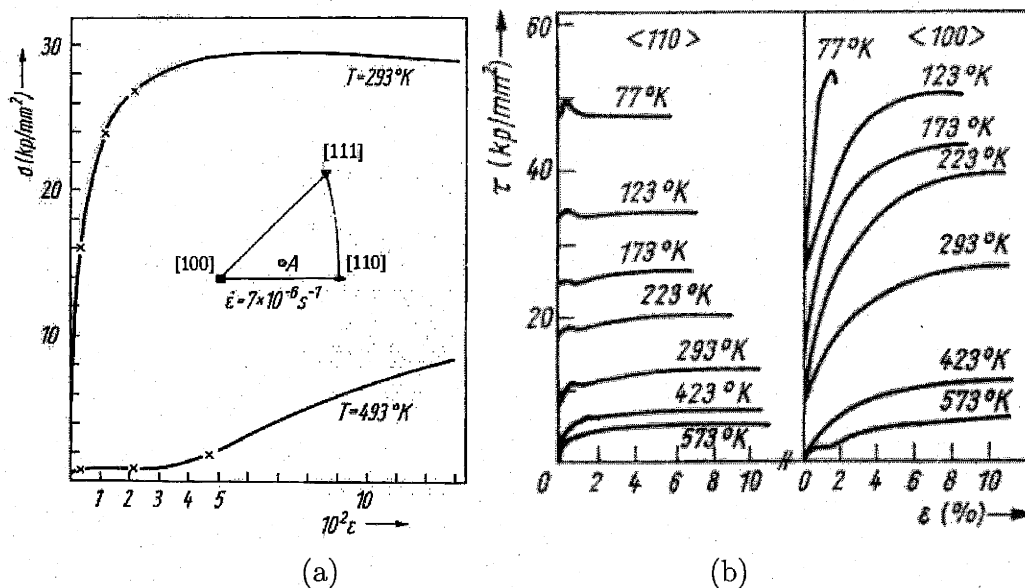


Figure 3-1: Tensile stress-strain curve of Mo. (a) Uniaxial tension along A direction (inside the standard triangle) at 293 and 493K. (b) Uniaxial tension along $[110]$ and $[100]$ from 77 to 573K. (Fig. 2 of [79] and Fig. 1 of [80].)

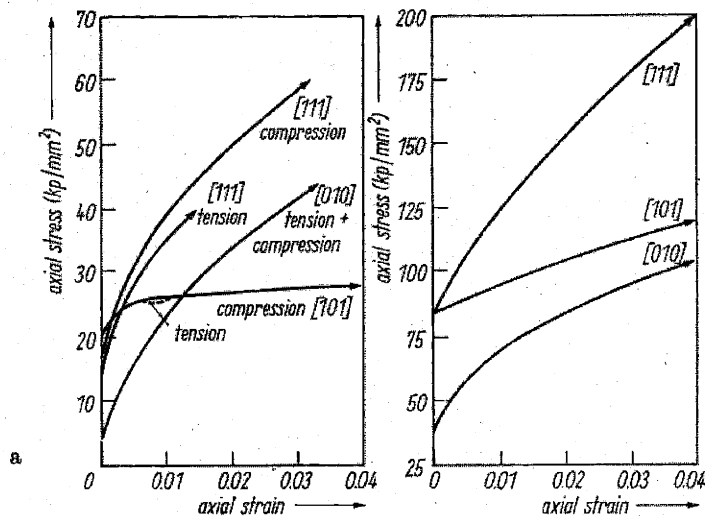


Figure 3-2: Tensile stress-strain curve of Mo along $[101]$, $[010]$, $[111]$ directions under (a) 293°K and (b) 77°K . (Fig. 1 of [81]. $1 \text{ kp/mm}^2 = 9.8 \text{ GPa}$.)

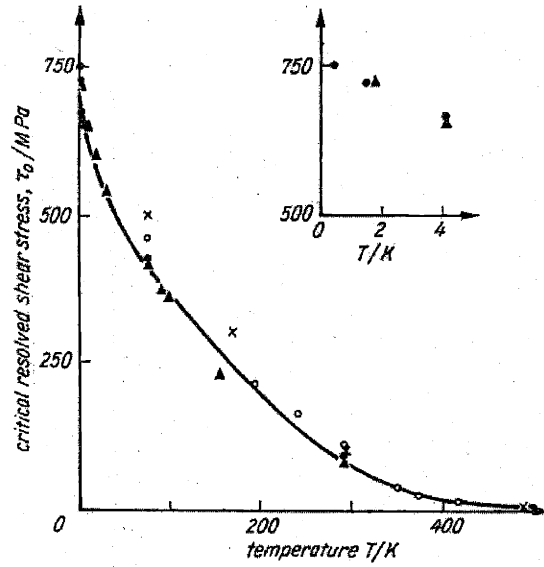


Figure 3-3: Temperature dependence of the critical resolved shear stress of [110] Mo single crystals for tension (\bullet) and compression (\blacktriangle). (Fig. 1 of [82]. $1\text{kp/mm}^2 = 9.8\text{GPa}$.)

temperature is also clearly seen in multiple slip orientations. As shown in Fig. 3-2, a slight asymmetry in stress between tension and compression is found at low temperature (77K) but not at higher temperature (293K).

The critical resolved shear stress (CRSS) τ_0 for Mo single crystals as a function of temperature was compiled by Kaufmann et al. [82], which is reproduced in Fig. 3-3. We observe that as temperature approaches zero, the CRSS goes to 750MPa. The low temperature limit of CRSS for Mo and Ta are listed in Table 3.2. This value is usually regarded as the experimental indication of the minimum stress to move the dislocation across the lattice, namely the Peierls stress, and can be compared with atomistic calculations such as in Chapter 6.

Stress-strain relations have also been measured for other BCC metals, such as Nb [93], W[85], Fe[94], etc, and strong temperature and orientation dependence of yield stress has been found as a general behavior. The orientation dependence of CRSS for several BCC metals at 77K are compiled by Duesbery et al. [11], which is reproduced here in Table 3.3.

Table 3.2: Resolved yield stress τ_0 (in MPa) for Mo and Ta below 4.2K. χ is the angle between the maximum resolved shear stress plane and the (110) slip plane.

	τ_0	T	deformation mode	Ref.
Mo	750	0.5K	[110] tension	[82]
Mo	666	4.2K	[110] tension/compression	[82]
Ta	364	0.7K	$\chi = +10^\circ$ tension	[83]
Ta	350	4.2K	$\chi = +10^\circ$ tension	[83]

Table 3.3: Orientation dependence of the CRSS (in MPa, resolved on the M.R.S.S. plane) for BCC metals at 77K. [uvw] represent directions near the corner or the center of the standard triangle. (Table 1 of [11].)

	Tension				Compression				Ref.
	[110]	[100]	[111]	[uvw]	[110]	[100]	[111]	[uvw]	
W	730	353	416	485					[84]
W	584	283	255						[85]
Ta	323	179			172	273			[86]
Ta	353	283			264	221			[87]
Ta	406	297	337	338					[88]
Ta	400	278	293	275	259	221	309	300	[89]
Fe	270		200						[90]
Mo	471	151			393	137			[86]
Mo					577	214	647	320	[91]
Mo	500	170		250					[92]
Nb	254	165			108	214			[86]

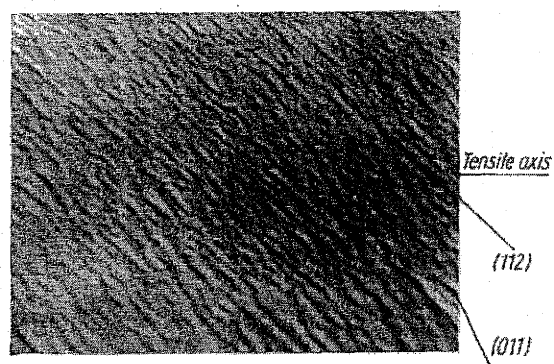
3.2 Slip Behavior

3.2.1 Slip Systems

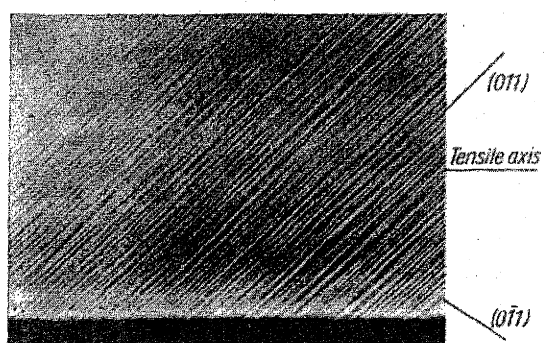
FCC and BCC lattices are reciprocals of each other, so that the slip systems in BCC metals are the “conjugate” of those in Si as discussed in the previous Chapter. While slip in FCC lattice occurs on (111) planes and along [110] directions, the most common slip planes in BCC lattice are (110) with slip directions along [111]. Slip on (112) planes is also observed in BCC metals.

The planes on which slip occurs can be determined by observing the slip traces on the surface of the specimen after deformation. A general feature in BCC metals is that multiple slip systems tend to operate simultaneously. Fig. 3-4 shows the slip lines on (0 $\bar{1}$ 0) (face 1) and (201) (face 2) surfaces [92] for Mo deformed at 353 and 413K, under uniaxial tension along a direction near the center of the standard triangle. This condition favors single slip with the stress-strain curve exhibiting three-stage hardening. Slip traces on face 1 were short wavy segments corresponding to (112) and (011) slip planes, both containing $[\bar{1}11]$ direction. The waviness of the slip traces can be interpreted as the result of cross slip of $[\bar{1}11]$ screw dislocations between these two planes. While at small strain slip traces on face 2 indicate single slip on (011) planes, both primary slip on (011) planes and secondary slip on (1 $\bar{1}$ 2) are observed at larger strain. For tension along [110] and [100] directions slip lines were very difficult to resolve, because multiple slip systems are equally favored.

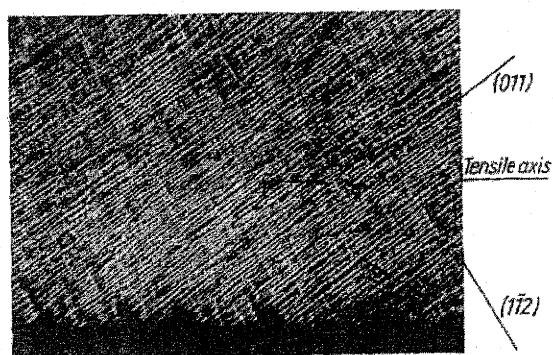
Vesely carried out more systematic studies of slip traces of Mo, both at 293K (parabolic hardening) and 400K (three-stage hardening), with tensile axis inside the standard triangle. The slip traces at 400K were dominated by ($\bar{1}$ 01)[111] primary system, similar to the results discussed above [92]. At 293K however, the slip traces of both the primary slip system ($\bar{1}$ 01)[111] and conjugate system (101) $[\bar{1}11]$ were visible, as shown in Fig. 3-5. Vesely noticed that at very small strains (0.8%), the slip lines did not correspond to the primary slip system, which become dominant only after the strain reached a few percent. This is clearly shown by plotting the slip bands on the stereographic projection, as in Fig. 3-6. The fact that the overall



(a)



(b)



(c)

Figure 3-4: Slip traces of Mo deformed at 353 and 413K under uniaxial tension along the direction near the center of the standard triangle. (a) Slip lines on face 1 after 0.045 tensile strain. (b) Slip lines on face 2 after 0.045 tensile strain. (c) Slip lines on face 2 after 0.175 tensile strain. (Fig. 6 of [92].)



Figure 3-5: Slip traces of Mo deformed at 293K under uniaxial tension along the direction near the center of the standard triangle. (Fig. 5 of [95].)

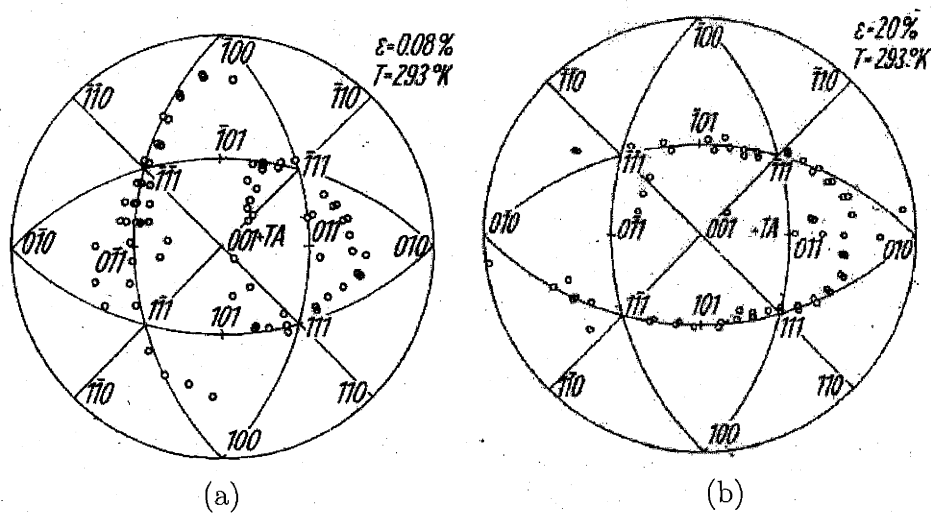


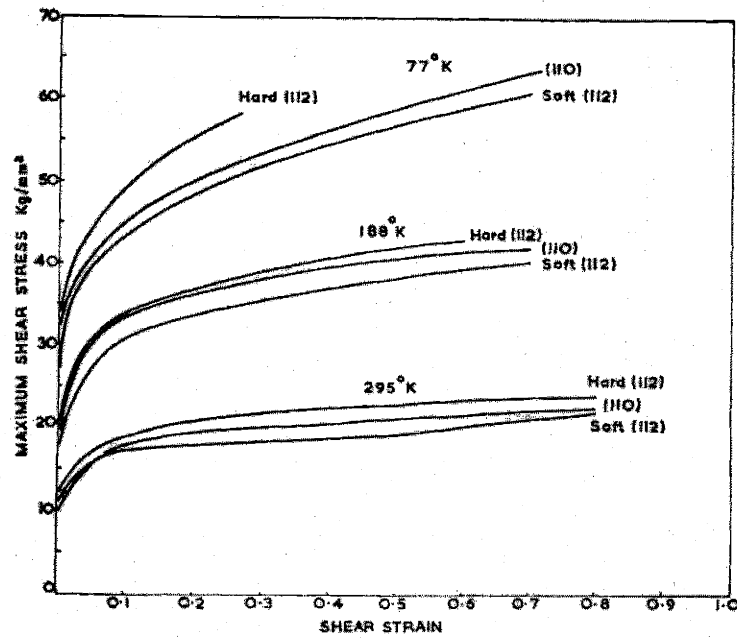
Figure 3-6: Slip band directions of Mo deformed to (a) 0.8% and (b) 20% under same condition as in Fig. 3-5. (Fig. 7 of [95].)

picture of slip bands changes with deformation and that multiple slip systems operate at the initial stage of deformation were noted as surprising [95], because processes like dislocation intersections should not play an important role in such conditions. Veselý argued that there must be a temperature dependent criterion responsible for the choice of slip systems at low temperature and low stresses, which determines the condition for the primary slip system to become fully operative. The origin of this criterion may come from the temperature dependent intrinsic lattice resistance to screw dislocation motion, which can be studied by atomistic methods (see Chapter 6). It was noted that surface effect could also play an important role at the initial stage of deformation, because of the enhanced mobility of screw dislocations near the surface due to image forces.

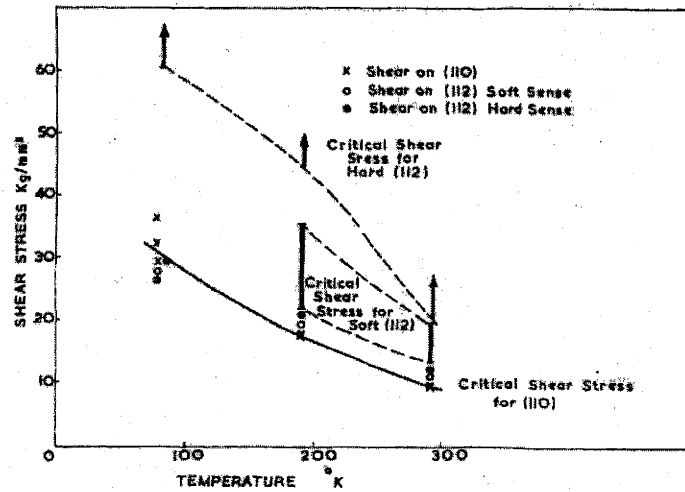
3.2.2 Slip Asymmetry

Slip analysis was also carried out in Mo deformed by pure shear [96] at temperatures between 77 and 293K. The shearing direction was always along [111], but shear on both (112) and (110) planes were studied. Similar to the tension-compression asymmetry under uniaxial loading (see Fig. 3-2), shearing along two opposite directions on (112) planes have different responses as well, and are labeled “soft” (favorable for twinning) and “hard” (anti-twinning) respectively. Fig. 3-7(a) shows the stress-strain curves for three different shear orientations at three different temperatures. The estimated CRSS of different slip systems is shown in Fig. 3-7(b), which is compatible with uniaxial deformation experiments [82] (see Fig. 3-3).

Slip asymmetry in BCC metals becomes even more pronounced in cyclic deformations. A dramatic consequence is the shape change of the sample, with its cross section turning from circular to elliptic [97, 98, 99, 100] during cyclic tensile-compressive deformation. In Mo this effect is most pronounced at around 400K [101]. The shape change is the result of the operation of different slip systems during tension and compression respectively [102]. This also leads to the difference in the response stress for compression and tension at the same strain amplitude, as shown in the cyclic stress strain (c.s.s) curve of Fig. 3-8 [100]. Stress asymmetry ($\Delta\tau$) is plotted in Fig. 3-8(b)



(a)



(b)

Figure 3-7: (a) Stress strain curve of Mo under direct shear. (b) Estimated bounds for critical resolved shear stress to nuclear slip on different planes. (Fig. 3 and 4 of [96].)

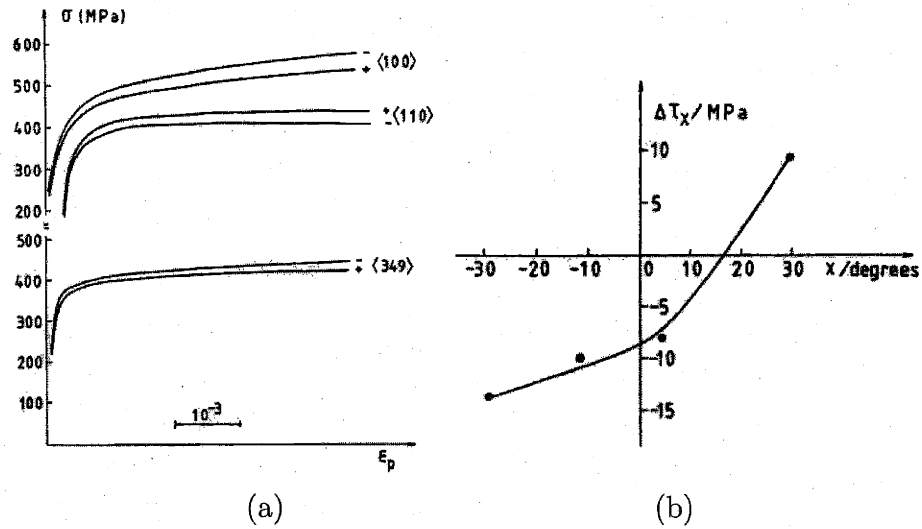


Figure 3-8: (a) Cyclic stress-strain curve of Mo under uniaxial deformation at room temperature. (b) Stress asymmetry $\Delta\tau$ between tension and compression as a function of angle χ between MRSS plane and $(1\bar{1}0)$ plane. (Fig. 1 and 2 of [100].)

as a function of angle χ between the maximum resolved shear stress (MRSS) plane and the $(1\bar{1}0)$ plane. As noted by Anglada et al. [100], $\Delta\tau(\chi)$ would be symmetrical, i.e. $\Delta\tau(\chi) = -\Delta\tau(-\chi)$, if the tensile-compressive asymmetry were induced solely by the shear asymmetry in the twinning-antitwining (or soft-hard) sense on the (112) planes (see Fig. 3-7). The fact that $\Delta\tau(\chi)$ is not symmetrical indicates that normal stress components also affects the lattice resistance to dislocation motion. This is in agreement with some atomistic simulations of screw dislocations [74].

3.2.3 Anomalous Slip

“Anomalous” slip [103] occurs at low temperature in high purity BCC metals, and derives its name from the fact that its Schmid factor is much lower than that of the primary slip system, so that its occurrence is “unexpected”. As shown in Fig. 3-9, for the specified tensile direction, the Schmid factor on the primary slip plane (011) is about 0.5, while that on the anomalous slip plane $(\bar{1}01)$ is only $0.25 \sim 0.3$ [104]. Yet in VB transition metals such as Nb, anomalous slip can even be the dominant

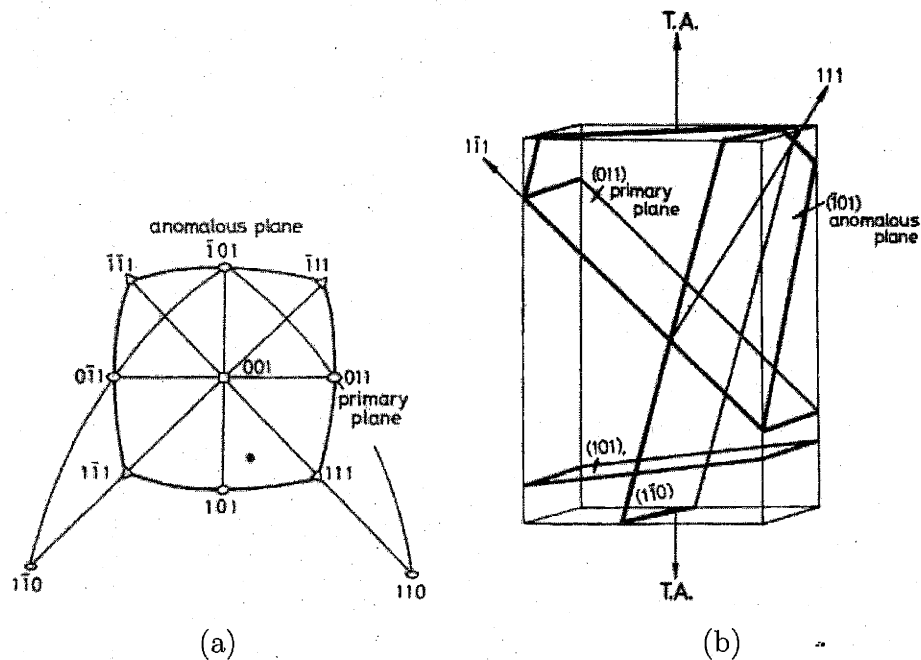


Figure 3-9: Orientation of the primary slip plane and the anomalous plane with respect to the tensile axis. (a) Stereographic plot. (b) 3-dimensional plot. (Fig. 1 and 2 of [104].)

slip system, carrying as much as 70% of the total plastic strength [105]. Furthermore, anomalous slip lines are coarse and crystallographic, as shown in Fig. 3-10, in contrary to the wavy ones of normal slip, such as in Fig. 3-4(a). To distinguish the anomalous slip from other secondary slips, Matsui named it anomalous $(\bar{1}01)$ slip.

Anomalous $(\bar{1}01)$ slip was first discovered only in VB metals, such as Nb and Ta [105, 106, 107], and it was not clearly identified in VIB metals such as Mo and W. In the latter case multiple slip systems were found at the beginning of the deformation but primary slip system quickly become dominant [95], as shown in Fig. 3-6. However, Matsui and Kimura [103] later observed anomalous $(\bar{1}01)$ slip lines in high purity Mo, where for the first time the anomalous slip lines appear to be the most prominent. Although anomalous $(\bar{1}01)$ slip lines are eventually replaced by primary slip lines at larger strains, Matsui et al. argued that anomalous slip in VB metals and in Mo are essentially the same effect, with the persistence of the anomalous slip bands affected by the mobility ratio of the edge and screw dislocations.

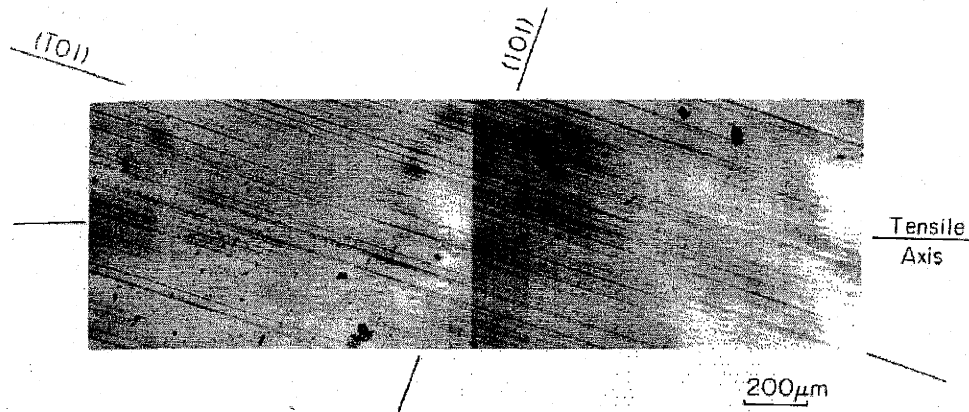


Figure 3-10: Anomalous $(\bar{1}01)$ slip lines in high purity Mo at 77K after 0.46% strain. Secondary slip on (101) plane is also visible. (Fig. 2 of [103].)

Several mechanisms were proposed to explain the anomalous slip in BCC metals. The early theory based on the core effects of screw dislocation by Takeuchi et al. [108] did not seem to be able to explain a lot of the observed properties of anomalous slip, and the proposed planarly split core structure is not consistent with later atomistic simulations. Vitek and Taylor [109] argued that anomalous slip can only be explained by incorporating extra features, such as a free surface, dislocation interactions, or normal stress components, in order to overcome the symmetry restrictions of a theory based only on intrinsic dislocation core properties. A later model proposed by Matsui and Kimura does incorporate both the free surface effect [110, 111, 112] and the dislocation interactions, i.e. the so called coplanar double slip mechanism (CDS) [113]. In their model, it is postulated that the image force of a free surface bends intersecting screw dislocations towards a mixed orientation, making them mobile at a much lower stress than straight screws. Two sets of screw dislocations activated through this or other processes (such as from internal defects) will then intersect with each other and form a lamellar network structure in the anomalous slip plane, which moves as a whole. Some microstructural evidence of this mechanism will be presented in the next section. It is argued by Matsui et al. that the dominance of primary slip over anomalous slip in Mo at larger strain is due to the relative unstableness of the lamellar

network.

3.3 Dislocation Microstructure

Macroscopic properties of materials are largely determined by their microstructures. For plastic deformation of a single crystal, the controlling microstructure is formed by dislocations. In this section we discuss transmission electron microscopy (TEM) observations of dislocation microstructures in deformed Mo samples, and their correlation with the macroscopic strain hardening behavior.

3.3.1 Initial Microstructure

The microstructure of grown-in dislocations in single crystal Mo (with 13 p.p.m. carbon) were observed before any deformation [114]. Dislocations either take the form of prismatic loops emitting from inclusion (most probably Mo_2C) particles, see Fig. 3-11(a), or as lines pinned by fine impurity segregations, as in Fig. 3-11(b). The stress near an inclusion are usually compressive and the loops are mostly of interstitial type. Upon deformation, these grown-in dislocations act as internal dislocation pinning centers where dislocation entanglement occurs and dislocation network starts to form, as shown in Fig. 3-11(c). Therefore the materials hardening rate may be sensitive to the initial dislocation structure and sample purity. On the other hand, grown-in dislocations in high purity Mo were found to be featureless, as shown in Fig. 3-11(d).

During tensile loading, the dislocation density increases, with higher multiplication rate at lower temperatures. Lawley et al. [116] found that a linear relationship is well obeyed between the flow stress τ_f and the square root of dislocation density ρ , i.e. $\tau_f = \tau_0 + K\sqrt{\rho}$. As the temperature dependence of τ_0 is much weaker than τ_f , Lawley et al. argued that a large portion of the apparent temperature dependence on the macroscopic yield stress mainly comes from the more pronounced work hardening rate at low temperatures, although the intrinsic lattice resistance for dislocation is temperature dependent as well.

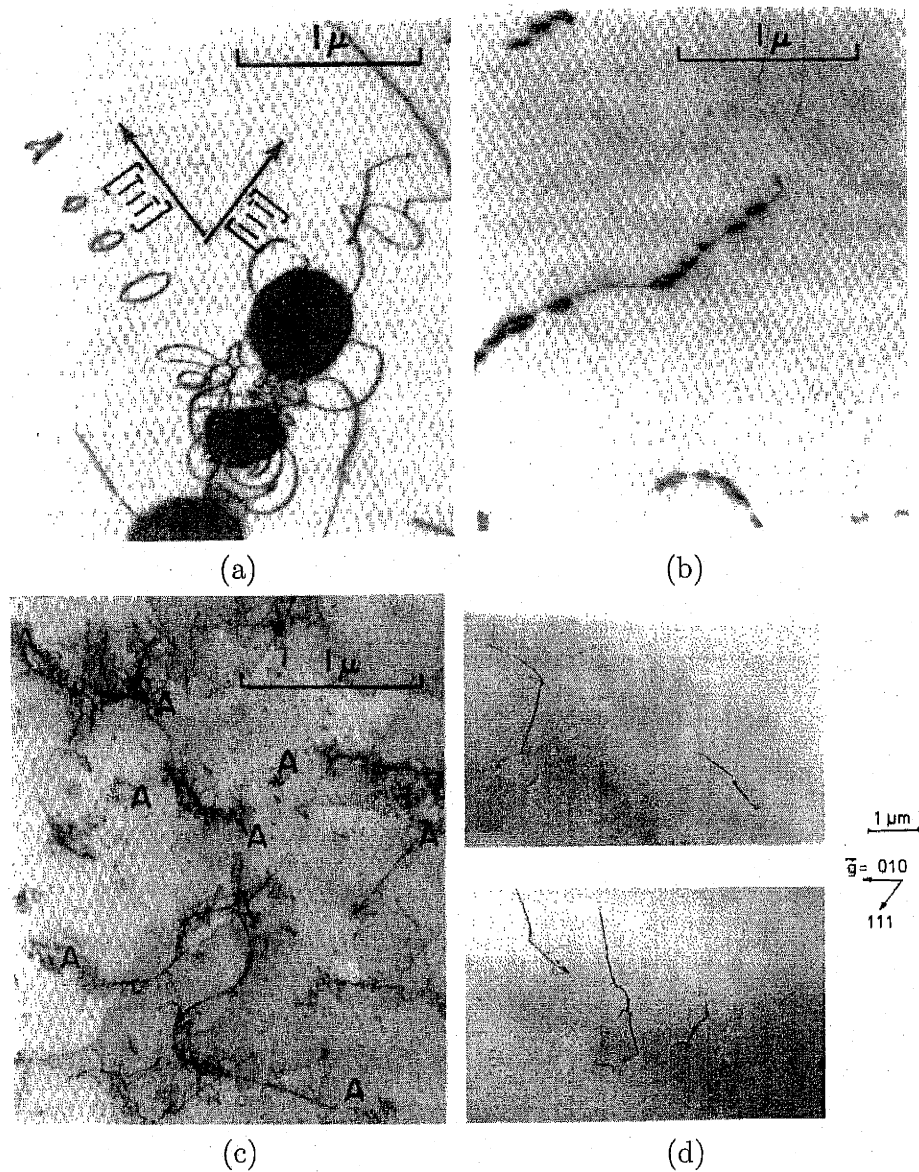


Figure 3-11: (a) Grown-in dislocation loops around inclusion particles. (b) Grown-in dislocations pinned by fine precipitate particles. (c) Grown-in dislocation act as dislocation pinning centers upon deformation. (d) Featureless grown-in dislocation microstructures in high purity Mo. (Fig. 1, 4 and 7 of [114] and Fig. 2 of [115].)

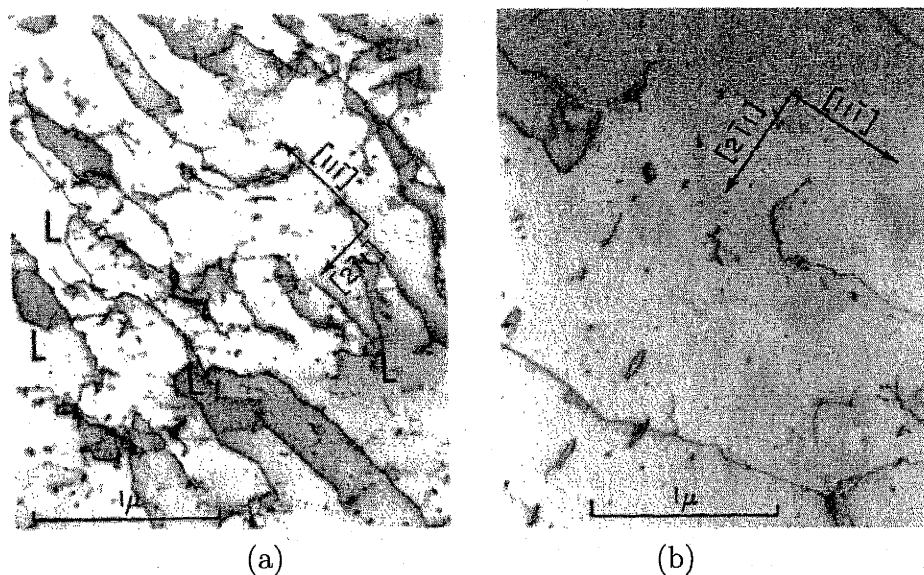


Figure 3-12: Dislocation structure of Mo under 0.5% tensile strain at 4.2K. Primary Burgers vector along $[11\bar{1}]$. Foil plane on (011) using (a) (233) and (b) $(01\bar{1})$ reflections. (Fig. 5 of [116].)

3.3.2 Screws and Prismatic Loops

Fig. 3-12 shows a typical dislocation microstructure in Mo deformed by tension at 4.2K [116]. The tensile axis is near the center of the standard triangle so that single slip on $(011)[11\bar{1}]$ is favored. Dislocation lines are observed to lie largely along $[11\bar{1}]$ direction, and have the primary Burgers vector $[11\bar{1}]$, i.e. they are mainly screw dislocations. The large number screws than edges indicating the much smaller mobility of the former. The velocity ratio for edge and screw are estimated as 40 : 1. The diffraction contrast between two adjacent screw dislocations are often dark grey; this indicates that the two screws have opposite Burgers vector, i.e. they form a dipole. These microstructures are away from any inclusions or immobile grown-in dislocations, so that even though dislocation density is quite high, dislocation distribution is remarkably uniform and entanglements are not observed. Numerous cusps are found on screw dislocation segments. Short straight secondary dislocation segments were observed to run completely through the foil, which are postulated to act as obstacles and create jogs on the gliding primary screw dislocation. It is estimated that

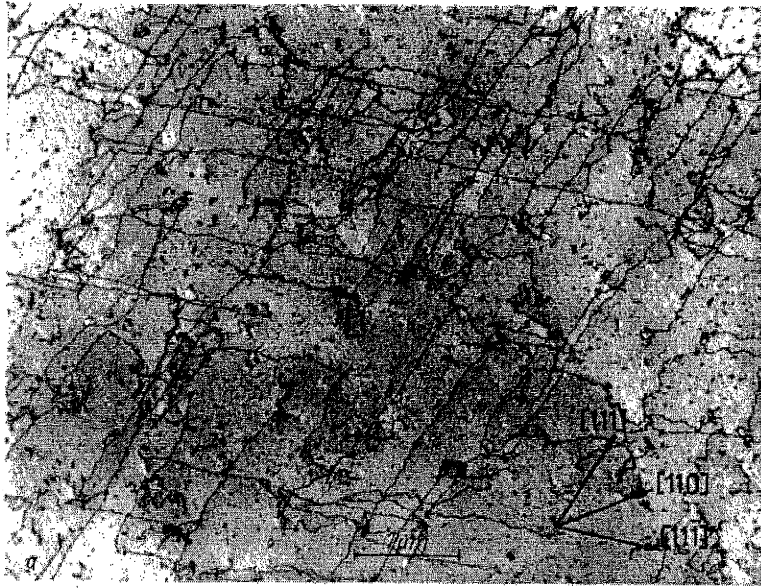


Figure 3-13: Dislocation structure of Mo under 2% tensile strain along $[110]$ at 4.2K. (Fig. 6 of [82].)

the jogs created by dislocation intersection can exert a substantial dragging stress on the screw dislocation, which contributes significantly to the macroscopic yield stress. Therefore, the temperature dependence of macroscopic yield stress was regarded to be mostly due to work hardening by cutting through secondary dislocations, instead of the intrinsic lattice resistance. Interestingly, it was realized later that the emergence of secondary slip itself at the onset of plastic deformation (even when the loading direction favors single slip) is related to the large intrinsic lattice resistance to screw dislocation. Secondary screw dislocations appear because the stress to move secondary edge dislocations are smaller than that to move the primary screw dislocation.

Round or elongated prismatic³ loops with length to ratio of $\leq 5 : 1$ are found in the wake of the glide screw dislocations. The maximum loop length is around 2200\AA and their average length is 900\AA . While the length and distribution of loops larger than 500\AA did not change significantly with temperature for a given strain, the

³Burgers vector normal to the loop plane.

density of small loops increased with decreasing temperature for a given strain. A large number of dislocation debris was also present in the form of unresolvable spots. Since the debris was not present in undeformed material, they are most probably small prismatic loops.

For tensile axis along high symmetry directions such as $[110]$, multiple slip systems are favored. The dislocation structures under such conditions consist of the uniform distribution of two sets of long screw dislocations with a high density of small prismatic loops, as shown in Fig. 3-13.

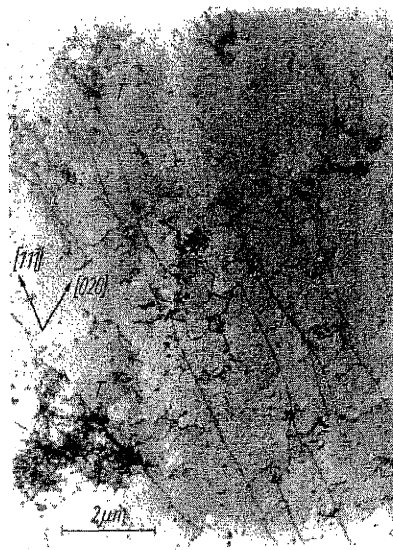
Similar dislocation microstructures are found at 293K, where the tensile stress-strain curve is still parabolic, i.e. it belongs to the low temperature regime, see Fig. 3-1(a). Fig. 3-14 shows the change of dislocation microstructures with increasing strain, with tensile orientation favoring single $(101)[11\bar{1}]$ slip $[117]$. In (a) at 0.3% strain long and jogged screw dislocations were observed, as well as attractive dislocation junctions (R) and prismatic loops. In (b) at 3.5% strain, dense dislocation entanglement starts to appear, which are not necessarily around grown-in dislocations, while the distribution of screws and debris loops remain unchanged. Qualitatively the same feature was observed for tension along $[110]$ axis, as shown in Fig. 3-15. For strains above 5% where the stress-strain curve reaches plateau (see Fig. 3-1(a)), the size of entanglements as well as the dislocation density within them continue to increase, while density of long screw dislocations keeps nearly constant. Dislocation junctions formed at earlier stages should be important for the formation of these entanglement. Dislocation density and debris density as a function of strain are shown in Fig. 3-16.

3.3.3 Anomalous Slip

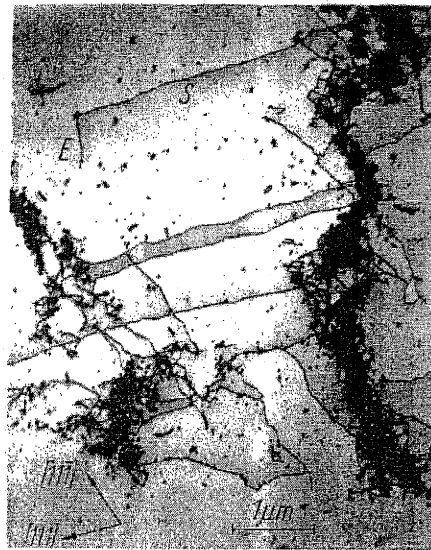
In high purity Mo, anomalous slip was observed under low temperature at small strains (see Section 2). As shown in Fig. 3-17, the dislocation microstructure corresponding to anomalous slip exhibits straight, lamellar structure of slip bands on the anomalous $(\bar{1}01)$ slip plane. The lamellar structure are seen to consist of two sets of screw dislocations, in accordance with the model of Matsui et al. [113].



(a)



(b)



(c)

Figure 3-14: Dislocation structure of Mo at 293K with (a) 0.3%, (b) 3.5% and (c) 14% strain. (Fig. 2, 5 and 7 of [117].)

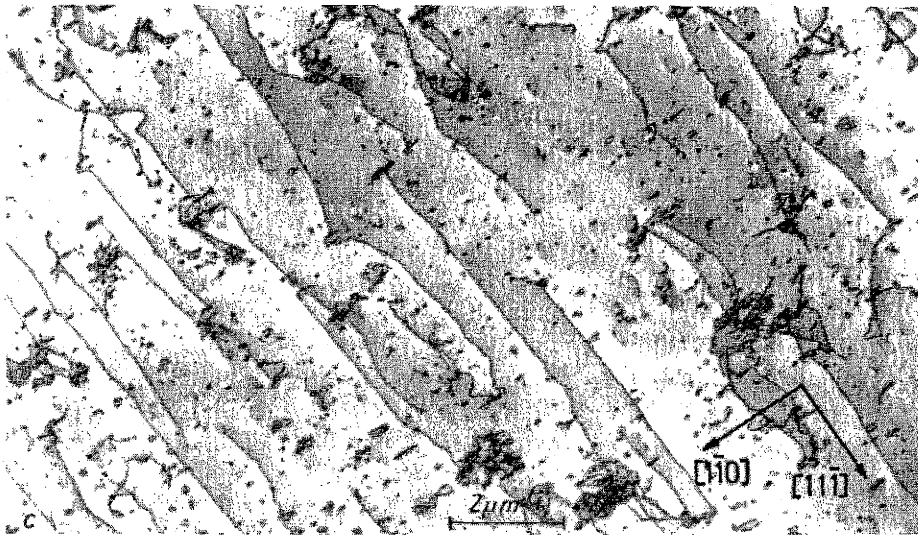


Figure 3-15: Dislocation structure of Mo under 5.8% tensile strain at 293K. (Fig. 5 of [82].)

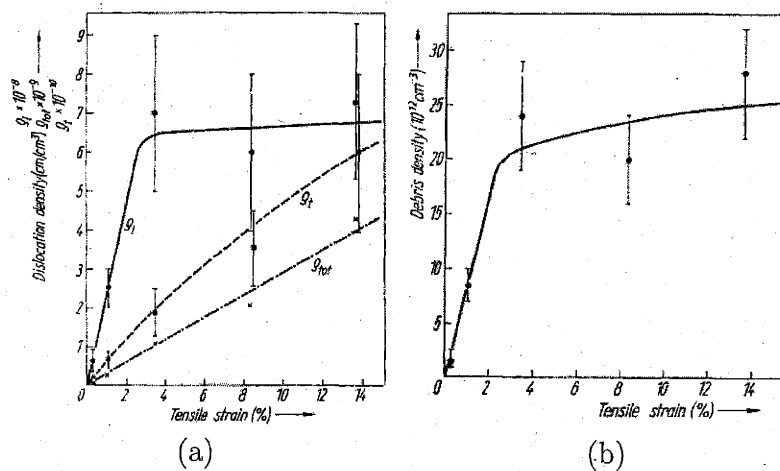
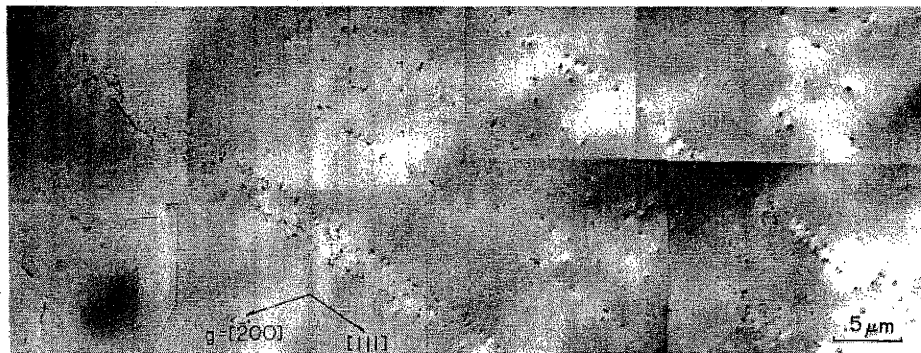
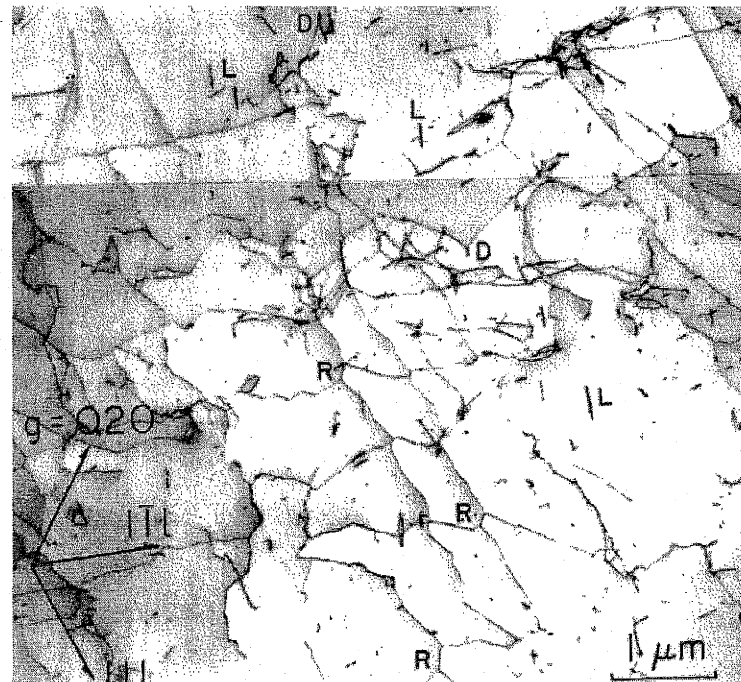


Figure 3-16: Dislocation density (a) and debris density (b) in Mo at 293K versus strain. (Fig. 8 and 9 of [117].)



(a)



(b)

Figure 3-17: Dislocation structure of Mo with anomalous slip, $T = 77\text{K}$, axial strain $\epsilon = 0.46\%$. (a) Straight lamella dislocation bands along anomalous $(\bar{1}01)$ plane. (b) Dislocation arrangement on the anomalous $(\bar{1}01)$ plane. Dislocation junctions (R), dipole trails (D) and dipole loops (L) are observed. (Fig. 3 and 4 of [103].)

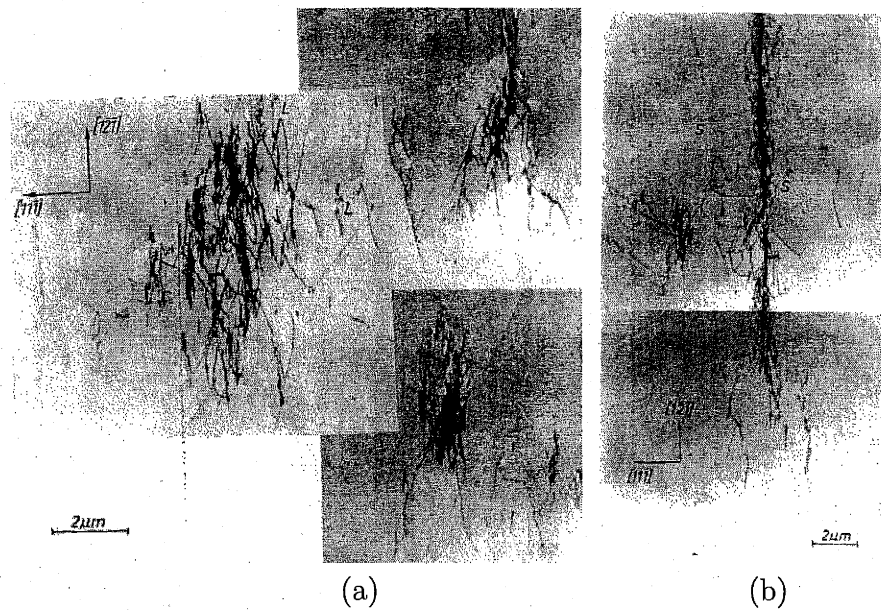


Figure 3-18: Dislocation structure of Mo at 493K with 2.1% strain. (a) Edge dipoles and elongated loops. (b) Long bundle of primary edge dislocations. (Fig. 7 and 8 of [79].)

3.3.4 High Temperature Behavior and Cell Structure

At 493K the dislocation microstructure changes substantially [79] from that at 293K, and is accompanied by the three-stage hardening in the stress-strain curve (Fig. 3-1). As shown in Fig. 3-18, dislocation structures consist mainly of edge dipoles and elongated loops widely varying in size and distribution, with screw dislocations no longer found. This is due to the high mobility of screw dislocations at elevated temperatures and their capability to cross slip and annihilate with each other. At 2.1% strain which is in the middle of stage I, dislocations are organized into long bundles which are not connected with each other. The remaining region in the materials is nearly dislocation free.

When the tensile axis is along high symmetry directions, such as $[110]$ and $[100]$, multiple slip is favored, which leads to the formation of cellular structures at high temperature and large strains. Fig. 3-19 shows cell structures in Mo under tension at 423K and 573K respectively. Cellular structures and dislocation walls were also

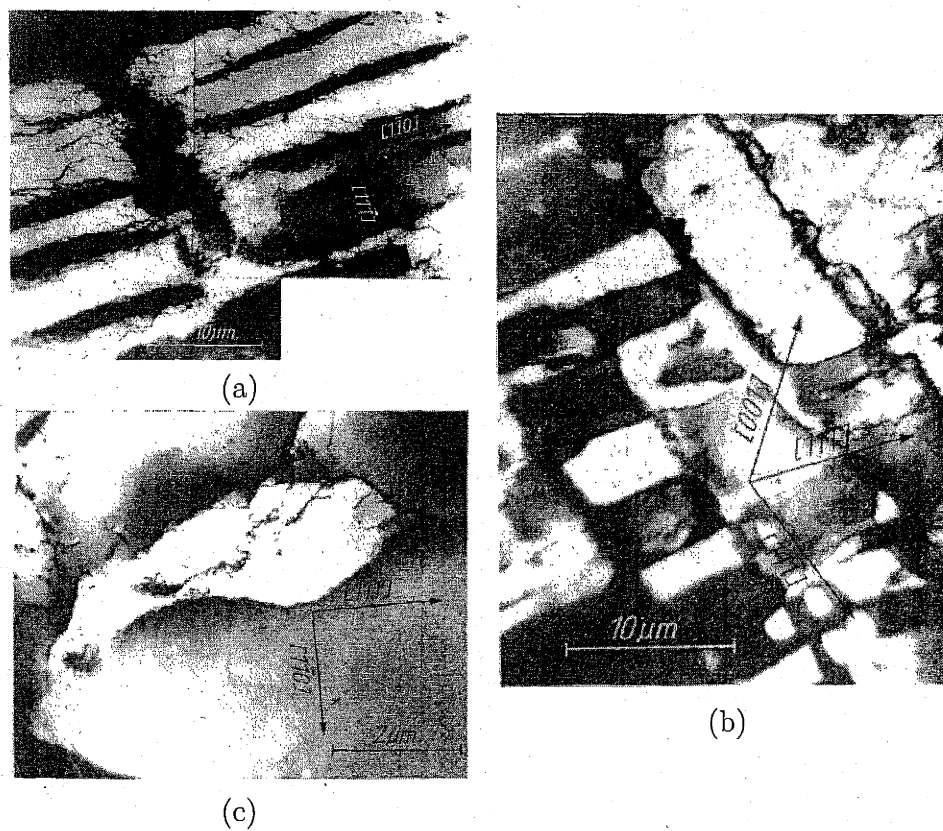


Figure 3-19: Cellular structure of dislocations in Mo under tension along $[110]$ at (a) 423K with 12% strain and (b) 573K with 4% strain and (c) along $[100]$ at 423K with 12% strain. (Fig. 5 and 7 of [80].)

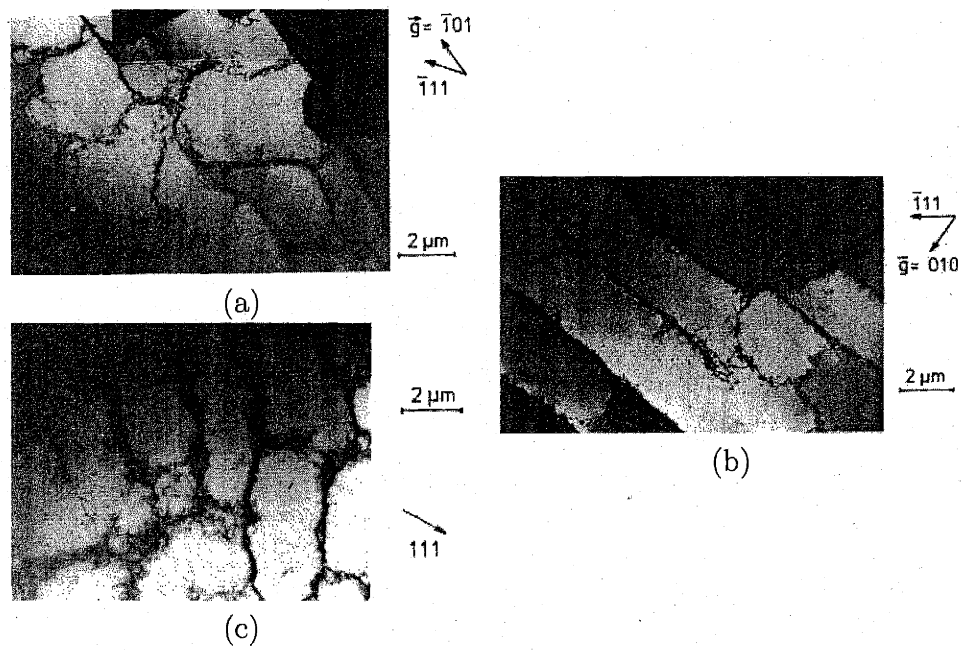


Figure 3-20: Dislocation microstructures in Mo under cyclic deformation along the axis near the center of the standard triangle. (a) Cell structure at plastic strain amplitude $\epsilon_p = 1.04 \times 10^{-3}$ and cumulative strain $\epsilon_c = 5$. (b) Dislocation walls at $\epsilon_p = 1.13 \times 10^{-3}$ and $\epsilon_c = 4.5$. (c) Dislocation bundles linking to form cell structure at high total strain amplitude $\epsilon_T = 3.45 \times 10^{-3}$ and $\epsilon_c = 0.94$. (Fig. 10, 12 and 18 of [115].)

found in cyclic deformations, as shown in Fig. 3-20.

3.4 Dislocation Mobility

Measurements of individual dislocation mobility could provide information on the most fundamental aspect of mechanical strength, and serve as a reference point to check the validity of atomistic models of dislocations. Unfortunately, not much data is available for single dislocation mobility in BCC metals, such as Mo, as compared with the case of Si. This is mainly due to the difficulty in obtaining dislocation free samples as well as in introducing single dislocations from the surface. Early experimental results using etch pit techniques might be contaminated by the interaction of observed dislocations with grown-in dislocations and the free surface [118]. In comparison, a recent *in situ* TEM study [119] seems to be more reliable. However, a more systematic *in situ* study of dislocation mobility in Mo is still lacking [120]. In this section, the early measurements of dislocation mobility will be discussed. We will see that, while today it is believed that edge dislocation moves much faster than screw dislocations, early experiments seem to show the contrary, most probably due to various surface artifacts.

One of the earliest measurements on the mobility of individual dislocations was performed by Prekel et al. [121]. Edge dislocations were introduced by indenting the surface using a sharp sapphire stylus. Indentation was used instead of surface scratching [122] because dislocations nucleated near the scratch surface were previously found to be not moving, unless stress is so high that grown-in dislocations move as well. Dislocation positions are revealed by etch pits, as shown in Fig. 3-21(a). Dislocation velocity as a function of resolved shear stress are shown in Fig. 3-21(b) for 77 and 300K and on (110) and (112) planes. Edge dislocations were found to be more mobile on (112) planes and the mobility increases with temperature. The dislocation velocity data was found to support kink mechanism with kink energy fitted to be 0.63eV. However, the kink mechanism on edge dislocation are not consistent with more recent atomistic calculations. As will be discussed in Chapter 6, edge

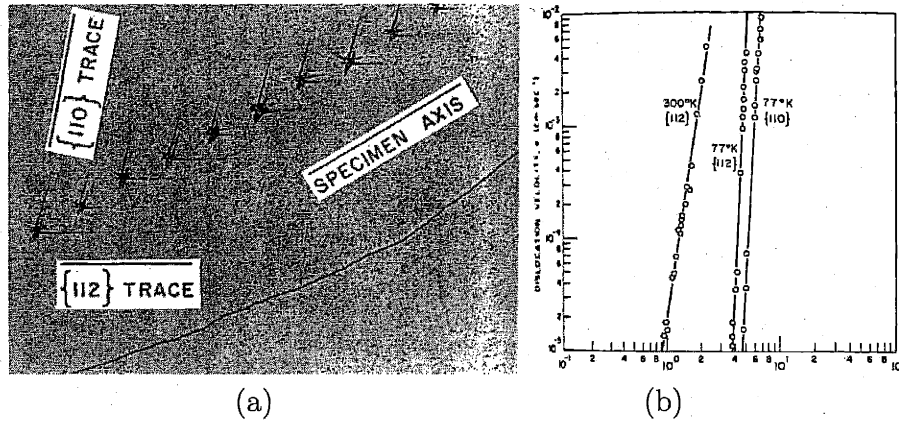


Figure 3-21: Edge dislocation mobility measurements. (a) Dislocation etch pits from the indenter. (b) Measured dislocation velocity as a function of stress in unit of (kg/mm²) at different temperatures and slip planes. (Fig. 5 and 6 of [121]. 1kg/mm² = 9.8MPa.)

dislocation experiences a very small lattice resistance and are ready to move without forming kinks. Prekel's conclusion that the results agree with Peierls-Nabarro model was also criticized by Stein [123] for the failure to account for the temperature dependence of yield strength. The apparently strong resistance to dislocation motion in this experiment may come from interactions with grown-in dislocations, point defects or the surface. It was found later [124] that a thin surface film always appeared on etched Mo sample and strongly impeded dislocation motion.

On the other hand, early experiments by Leiko [125, 126, 127, 128] reported an unexpectedly high mobility of screw dislocations. This had lead Nadgornyi [124] to conclude that kink mechanism does not play a role in screw dislocations, which is also inconsistent with current understandings.⁴ Dislocations are introduced by indentation and revealed by etching, as shown in Fig. 3-22(a). The geometry of dislocations are illustrated in (b) and the velocity data are shown in (c). Leiko [125] observed that screw dislocations start to move at very low stress $\tau \approx 2\text{MPa}$ with very high velocity $v \approx 0.1\text{m/s}$. When plotting the results from Leiko (for screw)

⁴Atomistic simulations show that the critical stress for screw dislocation is around 2GPa and it has to move via kink mechanism when stress is below this critical value.

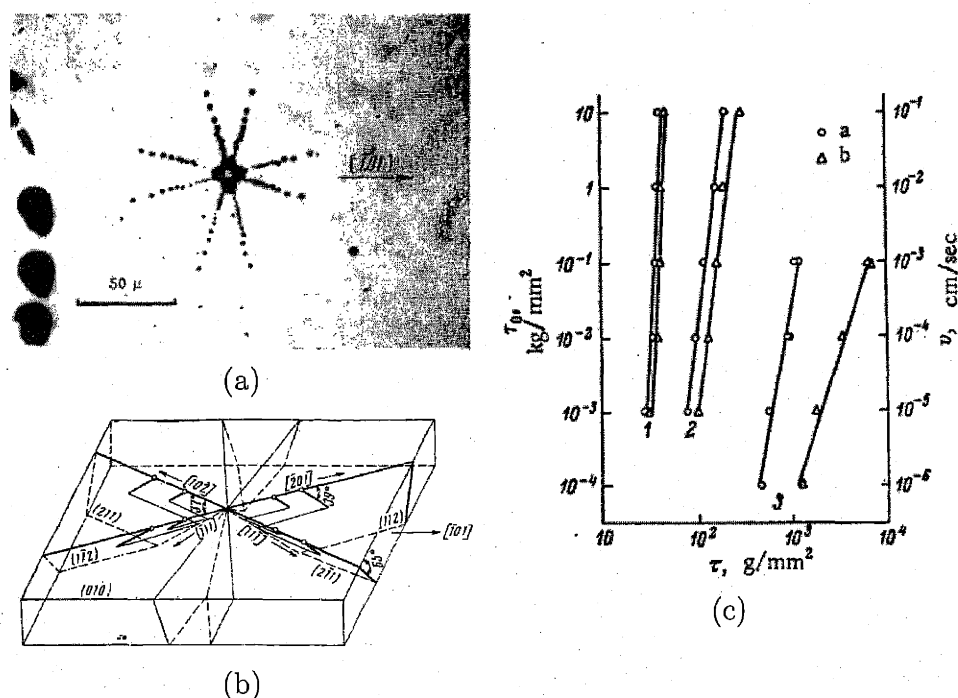


Figure 3-22: Screw dislocation mobility measurements. (a) Etch pits displaying a rosette pattern of dislocations around the indent. (b) Geometries of dislocation line and slip planes near the indent. (c) dislocation velocity of two Mo sample (a,b) as a function of loading stress at three temperatures: 1. 300K, 2. 77K, 3, 4.2K. (Fig.1, 2 of [125] and Fig.2 of [126].)

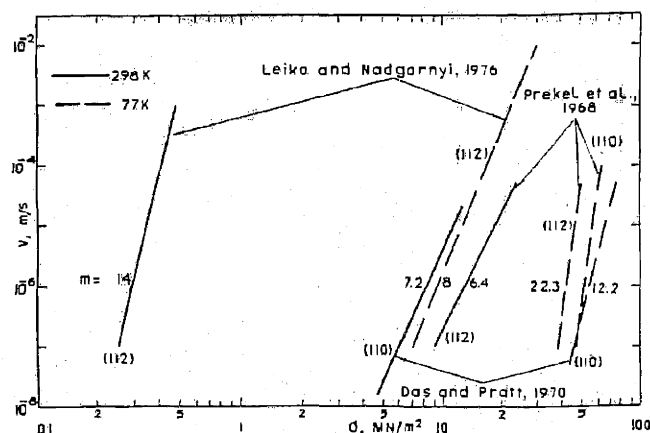


Figure 3-23: Comparison of velocities of edge (from Prekel et al.) and screw (from Leiko et al.) dislocations as a function of stress. It is misleading since screw dislocations have a much higher mobility than edges. (Fig. 6.28 of [124].)

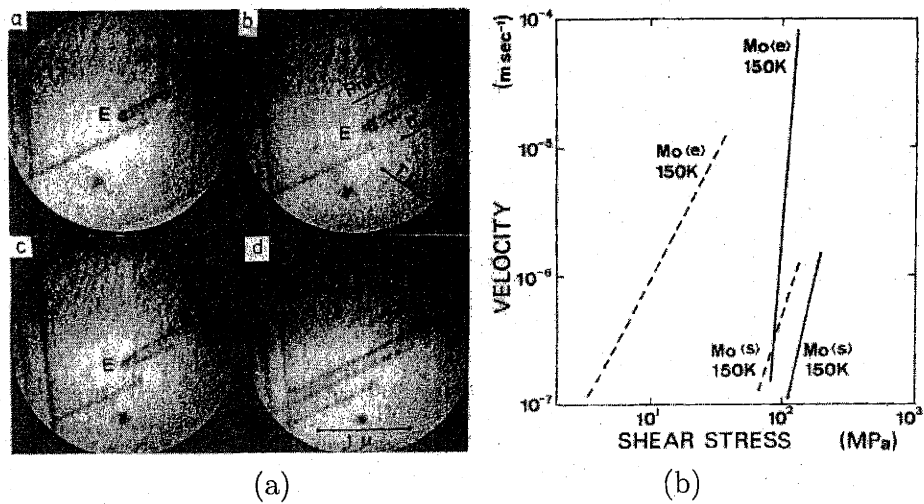


Figure 3-24: Dislocation mobility in Mo by *in situ* high voltage electron microscopy. (Fig. 1 and 2 of [119].)

and Prekel (for edge) as did by Nadgornyi [124], see Fig. 3-23, it is confusing to see screw dislocations to have a much higher mobility than edges. It is very likely that a surface effect mechanism suggested by Matsui [110] (to explain anomalous slip, see Section 2) could be responsible, where screw dislocations intersecting with the free surface may be forced to bend toward a mixed configuration thus substantially increase their mobility. In this respect, both the early results on edge [121] and screw [125] dislocation mobility could be contaminated by surface effects and should not be trusted as an accurate measure of the intrinsic behavior of dislocations mobility in Mo.

Fortunately, more recent *in situ* TEM observations seemed to provide convincing results [119]. As shown in Fig. 3-24(a), edge dislocations are observed to move faster than screws. Their velocity as a function of applied stress and effective stress (corrected for mutual elastic interactions) are plotted in Fig. 3-24(b). Unfortunately, no systematic investigation of dislocation mobility at different temperatures and on different planes are available so far. New experiments similar to this one that are sufficiently free from artificial surface effects are critically needed.

To conclude this section, let us examine some evidence on the core structure of

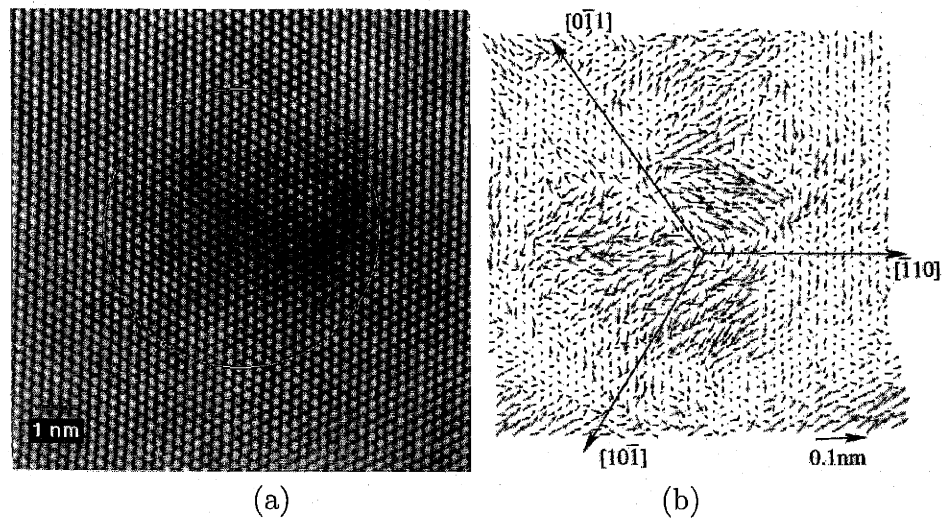


Figure 3-25: Core structure of screw dislocation in Mo by high resolution transmission electron microscopy (a) HRTEM images and (b) Atom position and (in plane) differential displacement map constructed from (a). (Fig. 5 and 6 of [129].)

screw dislocations. It is now widely accepted that the low mobility of screw dislocations in BCC metals compared with non-screw segments are due to the three fold splitting of the screw dislocation core, first proposed by Hirsch [130], and later confirmed by various atomistic simulations. The recent high resolution transmission electron microscopy (HRTEM) [129] observation of screw dislocation core also seemed to support the core splitting picture. As shown in Fig. 3-25, the observed in-plane displacement field, corresponding to edge Burgers vector components, does seem to show a 3 way extended pattern.

Chapter 4

Atomistic Simulation Methods

In this Chapter, we discuss several methodological issues on atomistic simulations, which will become useful for the dislocation studies on Si and Mo in later Chapters. For a more comprehensive treatment of atomistic simulation methods, such as Molecular Dynamics and Monte Carlo, the reader is referred to several well written books [131, 132, 133, 134].

In the first section, we will discuss and compare several interatomic potentials for Si and Mo that will be used in our simulations. We will then present two recent contributions on the study of boundary effects in atomistic simulations. According to Chapter 1, the discussions in Section 2 and 3 are two examples of type (a) coupling between atomistic and meso scales, and address the static and dynamic effect, respectively, of a mesoscale surrounding to an atomistic domain.

4.1 Interatomic Potentials

Atomistic simulations study the energetics and dynamics of a collection of interacting atoms following classical dynamics. For a system containing N atoms with position \vec{r}_i and velocity $\vec{v}_i = d\vec{r}_i/dt$, $i = 1, \dots, N$, the total Hamiltonian is,

$$H(\{\vec{r}_i\}) = T + V = \sum_{i=1}^N \frac{1}{2} m_i \vec{v}_i^2 + V(\{\vec{r}_i\}), \quad (4.1)$$

where T and V represent kinetic and potential energy respectively, and m_i is the mass of atom i . Molecular Dynamics (MD) simulation is then the numerical integration of Newton's equation of motion,¹

$$m \frac{d^2}{dt^2} \vec{r}_i = \vec{F}_i = -\frac{\partial}{\partial \vec{r}_i} V(\{\vec{r}_i\}), \quad i = 1, \dots, N \quad (4.2)$$

which produces the trajectory $\vec{r}_i(t)$ of all N atoms. Here \vec{F}_i represents the force on atom i due to its interaction with other atoms. Most of the thermodynamic properties can then be calculated as the time average along the atomic trajectories. Transport properties, on the other hand, can be calculated from the time correlation functions [131, 132].

Another widely used method is static structure relaxation, or the search for a local minimum² of the potential energy for a given microstructure,

$$E_0 = \min_{\{\vec{r}_i\}} V(\{\vec{r}_i\}). \quad (4.3)$$

For example, one can compute the excess energy of a particular defect by comparing the relaxed energy of the same atomic system with and without this defect.

The validity of atomistic simulation results thus depends critically on how well the potential energy function $V(\{\vec{r}_i\})$ describes the interactions between the atoms in the real material. For empirical potential functions constructed by fitting with experimentally measured properties, their predictive power is quite limited, although they are still useful in interpolating or extrapolating known properties and in constructing reasonable atomic structures for unknown defects. Many of the interatomic potentials nowadays are semi-empirical, because their functional forms are constructed based on first-principles theory and their parameters are fitted with *ab initio* calculation results

¹Several most widely used numerical integration schemes in MD can be found in [131].

²The "locality" of the energy minimum is usually not rigorously defined. It refers to the energy minimum within the phase space which preserves a given microstructure. For example, the true global energy for a simulation cell containing a dislocation dipole could be a perfect lattice where the two dislocations have annihilated with each other, but it is not the energy minimum of interest.

as well as experiments. This type of potential is expected to be more transferable and to have higher predictive capability.

Most of the atomistic simulations on Si in this Thesis used the so called Stillinger-Weber (SW) potential [135]. The more recent (and more complex) Environmentally Dependent Interatomic Potential (EDIP) [136] is also used occasionally. Tersoff [137] potential is another widely used potential in Si, which will be discussed here as well. On the other hand, our simulations on BCC metals are mostly based on the Embedded Atom Method (EAM) type Finnis-Sinclair (FS) [138] potential. The more sophisticated and more computationally expensive potential based on the Multi-ion Generalized Pseudopotential Theory (MGPT) is also applied for comparison.

The oldest interatomic potential used in MD simulations is the Lennard-Jones (LJ) [139, 140] potential, where the total potential energy of the system is pairwise additive and takes the form of $v(r) = 4\epsilon[(\sigma/r)^6 - (\sigma/r)^{12}]$ for each pair of atoms separated by r . The LJ potential well describes the interactions between atoms in noble gas solids, such as Ar, which form a close packed structure. However this potential is found not adequate to describe Si atoms. It became quite obvious that no reasonable pairwise potentials can even stabilize a diamond cubic structure.

Stillinger-Weber potential [135] was constructed to overcome this difficulty. It stabilizes the diamond cubic structure by explicitly putting in three-body interactions, favoring the tetrahedra bonding structure. Furthermore, its parameters chosen to best reproduce the liquid structure of Si as well as its melting point. Therefore, the SW potential is expect to be more transferable, i.e. more accurate in describing different local structures such as defects, surfaces, as compared with the Keating potential [141] which is constructed only to reproduce small perturbative responses from the perfect lattice

The functional form of SW potential is reproduced below,

$$V(\{\vec{r}_i\}) = \sum_{i < j} v_2(\vec{r}_i, \vec{r}_j) + \sum_{i < j < k} v_3(\vec{r}_i, \vec{r}_j, \vec{r}_k), \quad (4.4)$$

$$v_2(\vec{r}_i, \vec{r}_j) = \epsilon f_2(r_{ij}/\sigma), \quad (4.5)$$

$$v_3(\vec{r}_i, \vec{r}_j, \vec{r}_k) = \epsilon f_3(\vec{r}_i/\sigma, \vec{r}_j/\sigma, \vec{r}_k/\sigma), \quad (4.6)$$

$$f_2(r) = \begin{cases} A(Br^{-p} - r^{-q}) \exp[(r - a)^{-1}], & r < a \\ 0, & r \geq a \end{cases} \quad (4.7)$$

$$f_3(\vec{r}_i/\sigma, \vec{r}_j/\sigma, \vec{r}_k/\sigma) = h(r_{ij}, r_{ik}, \theta_{jik}) + h(r_{ji}, r_{jk}, \theta_{ijk}) + h(r_{ki}, r_{kj}, \theta_{ikj}), \quad (4.8)$$

$$h(r_{ij}, r_{ik}, \theta_{jik}) = \lambda \exp[\gamma(r_{ij} - a)^{-1} + \gamma(r_{ik} - a)^{-1}](\cos \theta_{jik} + 1/3)^2 \quad (4.9)$$

The term $(\cos \theta_{jik} + 1/3)^2$ in the three body interaction v_3 explicitly favors the tetrahedra bonding structure, whose bonding angle satisfies $\cos \theta = -1/3$. The interaction vanishes whenever the separation between two atoms exceeds the cut-off radius a . A common cut-off scheme is use here, by the $\exp[(r - a)^{-1}]$ term, which ensures that all the derivatives of the potential function vanishes smoothly at the cut-off radius.

Broughton et al. [142] applied SW potential to calculate the melting point of Si and obtained $T_m = 1691 \pm 20\text{K}$ which is very close to the experimental value of 1683K .³ However, SW behaves poorly in describing amorphous phase of Si. The cut-off radius of SW potential is also very short — it only includes first nearest neighbor interactions, therefore it cannot differentiate FCC from HCP packing (which are different only in second nearest neighbors) and leads to zero stacking fault energy.

A very different approach to describe bonding was proposed by Tersoff [137, 143], which utilized the notion of bond order.⁴ The Tersoff potential was subsequently improved both in functional forms and parameter values, and its three versions are also known as T1 [137], T2 [143] and T3 [145]. The functional form of T3 is reproduced below,

$$V(\{\vec{r}_i\}) = \frac{1}{2} \sum_{i,j,i \neq j} V_{ij}, \quad (4.10)$$

$$V_{ij} = f_c(r_{ij})[a_{ij}A \exp(-\lambda_1 r_{ij}) - b_{ij}B \exp(-\lambda_2 r_{ij})], \quad (4.11)$$

$$b_{ij} = (1 + \beta^n \zeta_{ij}^n)^{-1/2n}, \quad (4.12)$$

$$\zeta_{ij} = \sum_{k \neq i,j} f_c(r_{ik})g(\theta_{ijk}) \exp[\lambda_3^3(r_{ij} - r_{ik})^3], \quad (4.13)$$

$$g(\theta) = 1 + c^2/d^2 - c^2/[d^2 + (h - \cos \theta)^2], \quad (4.14)$$

³This could be considered as fortuitous as one usually does not expect empirical potentials to have such high accuracy.

⁴An elementary introduction to bond order can be found in the book of Sutton [144].

$$a_{ij} = (1 + \alpha^n \eta_{ij}^n)^{-1/2n}, \quad (4.15)$$

$$\eta_{ij} = \sum_{k \neq i,j} f_c(r_{ik}) \exp[\lambda_3^3 (r_{ij} - r_{ik})^3], \quad (4.16)$$

where $f_c(r)$ is a cut-off function. Bond order is included in b_{ij} term, which depends on the local environment of atom i . It is a decreasing function of the number of competing bonds, the strength of the competing bonds and the cosine of the angles with competing bonds. In this formulation, $V_{ij} \neq V_{ji}$, meaning that the energy of a bond is not equally distributed to the two atoms. The Tersoff potential was also generalized to describe carbon [146] as well as multicomponent systems such as SiC, SiGe [147].

A comparative study of SW, T3 along with several other proposed potentials for Si was performed by Balamane et al.[13], which concluded that all these potentials do a relatively poor job on modeling the energetics of small clusters as well as various constructions of the Si (111) surface. Interestingly, SW and T3 potentials predict different behavior of atomic relaxation around a single vacancy — SW leads to inward relaxation of first nearest neighbor atoms, and T3 gives outward relaxation. While the direction of relaxation was still a controversy at the time when this comparison was made [13], recent DFT calculations showed quite convincingly that the nearest-neighbor atoms relax inwards, decreasing the open volume, in agreement with the SW potential.

A newly developed potential, named Environmentally Dependent Interatomic Potential (EDIP) [136] seems to out-perform both the SW and T3 potentials in describing interactions between Si atoms in a wide range of environments, especially in the dislocation core. Surprisingly, the better performance comes with no extra computational cost, in that the computing time of EDIP is comparable with both these two potentials. The functional form of EDIP is given below,

$$V(\{\vec{r}_i\}) = \sum_i E_i, \quad (4.17)$$

$$E_i = \sum_{j \neq i} V_2(r_{ij}, Z_i) + \sum_{j \neq i} \sum_{k \neq i, k > j} V_3(\vec{r}_{ij}, \vec{r}_{ik}, Z_i), \quad (4.18)$$

Table 4.1: Reconstruction energy (in eV/b) of 90° and 30° partials in Si by SW, Tersoff (T3), and EDIP potentials, as well as by DFT calculations. (Table 1 of [150])

	DFT [151, 152]	SW [153]	Tersoff [150]	EDIP [152]
90°	0.87	—	0.86	0.80
30°	0.43	0.81	0.45	0.36

$$Z_i = \sum_{m \neq i} f(r_{im}), \quad (4.19)$$

where $f(r)$ equals to 1 at small r and smoothly goes to zero at large r . Z_i describes the coordination number of atom i . The theoretical justification of the potential form is given in [148, 149]. Intuitively, one can appreciate EDIP as a combination of both the merits of SW and Tersoff, i.e. having both explicit three-body interactions and an environmentally dependent bond order effect.

As this Thesis mostly concerns dislocation properties, a comparison of the performance of the different potentials discussed so far would be highly relevant. We reproduce here the data from [150] in Table 4.1, which lists the core reconstruction energies for 90° and 30° partial dislocations in Si. SW potential does not predict the correct reconstruction at all on the 90° partial, while both Tersoff and EDIP give comparable predictions with first-principle density function theory (DFT) calculations.

Similar to the case of Si, atomistic simulations on BCC transition metals cannot employ pair potentials either. An obvious drawback for pair potential here is that the resulting elastic constants for cubic crystals must satisfy the so called Cauchy relation $C_{12} = C_{44}$, which is never obeyed by real metals. A simple potential is proposed by Finnis and Sinclair [138], which describes the metallic bonding following a second-moment approximation to the tight-binding model [154, 144]. The function form of the FS potential is given below,

$$V(\{\vec{r}_i\}) = V_N + V_P, \quad (4.20)$$

$$V_N = -A \sum_i \sqrt{\rho_i}, \quad (4.21)$$

$$\rho_i = \sum_j \phi(r_{ij}), \quad (4.22)$$

$$V_P = \frac{1}{2} \sum_{ij} v(r_{ij}) + v_c(r_{ij}), \quad (4.23)$$

$$\phi(r) = \begin{cases} (r-d)^2 + \beta(r-d)^3/d, & r \leq d \\ 0, & r > d \end{cases} \quad (4.24)$$

$$v(r) = \begin{cases} (r-c)^2(c_0 + c_1r + c_2r^2), & r \leq c \\ 0, & r > c \end{cases} \quad (4.25)$$

$$v_c(r) = B(b_0 - r)^3 \exp(-\alpha r), \quad (4.26)$$

where V_P represents a pairwise repulsive interaction accounting for the core electron overlap and V_N describes metallic cohesive energy. The cohesive energy per atom varies as the square root of the effective electron charge density ρ_i . Although the theoretical justification of the functional form of FS potential was thought to be valid only for metals with nearly half filled d band, such as VIB metals Mo, W, etc, it was later shown by Ackland et al. [154] that it is applicable for all band fillings after charge neutrality of each atom is considered, so that the square root form can be used for noble metals and Ni as well.

FS potentials were constructed for seven BCC metals, V, Nb, Ta, Cr, Mo, W, Fe, with parameters fitted with experimental data on lattice constants, cohesive energy, elastic constants. The v_c term in the pair potential term Eq.(4.23) was later revised by Ackland et al. [155] to correct the unphysical behavior of short range interactions of the original FS potential.

Although widely used, FS potential has its limitations. It is found [156] that it results in low thermal expansions and describes surfaces poorly. Later on, it became quite clear that angular terms need to be introduced explicitly into potential functions [157]. This is done in the MGPT potential of Moriarty [158] based on the Generalized Pseudopotential Theory [159, 160, 161]. This potential was explicitly tailored for central transition metals, i.e. metals with half filled d band, such as Mo. In MGPT, the total energy of the system is rigorously expanded in real space into

two-, three-, and four- body interactions, i.e.

$$V(\{\vec{r}_i\}) = NE_{\text{vol}}(\Omega) + \frac{1}{2} \sum_{i \neq j} v_2(ij) + \frac{1}{6} \sum_{i \neq j \neq k} v_3(ijk) + \frac{1}{24} \sum_{i \neq j \neq k \neq l} v_4(ijkl), \quad (4.27)$$

where Ω denotes atomic volume. While MGPT potential is supposed to be more accurate than FS potential, it is much more computationally intensive as well. Both potentials are used in the atomistic simulation of dislocations in BCC metals in current literature [162, 163].

4.2 Dislocations in Periodic Boundary Conditions

It is fair to say that, besides the interatomic potential, the treatment of boundary conditions is the single most important aspect for atomistic simulations. In this Section and the next, we will discuss two specific contributions on the study of static and dynamic effects of a mesoscale surrounding to atomistic simulations.

Periodic boundary conditions (PBC) are ubiquitous in describing crystalline states theoretically and computationally, its fundamental appeal being that translational invariance of the infinite crystal is naturally preserved. However, when applied to study dislocation core energies and structures, it also introduces an artificial effect as if the dislocations are embedded in an infinite periodic array of their own images. Because of the long-range stress fields of dislocations, the summation of image interactions is only conditionally convergent. While existing methods of summation [164, 165, 166, 165, 167] are applicable to isotropic media only, we present here a new treatment [168] that is applicable to general anisotropic media.

4.2.1 PBC and Conditional Convergence

Consider an atomistic simulation cell for dislocation core energy calculations that is periodic along \vec{c}_1, \vec{c}_2 and \vec{c}_3 directions, and contains a dislocation dipole with Burgers vector $\pm \vec{b}$, as shown in Fig. 4-1. The dislocation lines are parallel to \vec{c}_3 and are separated from each other by \vec{a} . The total energy E_{atm} , in excess of that of the

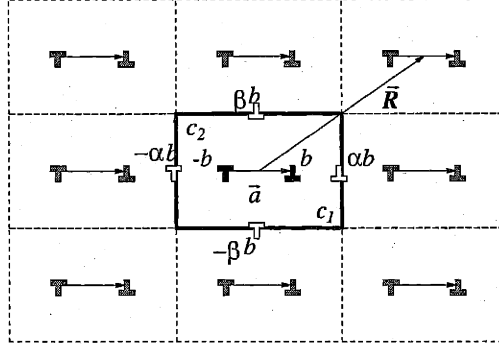


Figure 4-1: Schematic of an atomistic simulation cell (solid rectangle) containing a dislocation dipole with Burgers vector $\pm \vec{b}$ and separated by \vec{a} under PBC along \vec{c}_1 , \vec{c}_2 and \vec{c}_3 (out of plane). To facilitate calculation of the image energy, we introduce “ghost” dislocations (in white) at the cell boundaries.

perfect periodic lattice, obtained from a fully relaxed atomistic calculation can be separated into core and elastic contributions [169],

$$E_{\text{atm}} = 2E_{\text{core}} + E_{\text{prm}} + E_{\text{img}} , \quad (4.28)$$

where E_{core} is the core energy of each dislocation, E_{prm} represents the linear elastic interaction between the two dislocations in the primary simulation cell, and E_{img} represents the interaction between the primary dipole and all the periodic images. The sum of E_{prm} and E_{img} constitute the elastic interactions, E_{el} . For the sake of simplicity, we assume \vec{c}_3 has length unity, so that all the energies are normalized per unit length of dislocation.

For a screw dipole and assuming isotropic elasticity E_{prm} is known [30], $E_{\text{prm}} = \mu b^2 / (2\pi) \ln(|\vec{a}|/r_c)$, where μ is the shear modulus and r_c is the core cut-off radius.⁵ The problem of extracting E_{core} from E_{atm} therefore reduces to determining E_{img} . Following current practice [169, 170] one regards the effect of PBC as introducing an infinite array of image cells (see Fig. 4-1), and treats E_{img} as the total interaction

⁵A more detailed discussion of linear elasticity theory of dislocations and cut-off radius is given in Appendix A.

between the primary dipole and all the image dipoles,

$$E'_{\text{img}} = \frac{1}{2} \sum_{\vec{R}}' E_{\text{dd}}(\vec{R}) \quad (4.29)$$

where the summation runs over $\vec{R} = m\vec{c}_1 + n\vec{c}_2$, m and n being integers, and $\vec{R} \neq 0$. $E_{\text{dd}}(\vec{R})$ denotes the interaction between the primary dipole and an image dipole at position \vec{R} . The interaction between two dipoles is just the superposition of four dislocation-dislocation interactions. For screw dislocations in isotropic medium,

$$E_{\text{dd}}(\vec{R}) = \frac{\mu b^2}{2\pi} \ln(|\vec{R} + \vec{a}| \cdot |\vec{R} - \vec{a}|/R^2). \quad (4.30)$$

The factor of $\frac{1}{2}$ in Eq. (4.29) appears because only half of each interaction term should be attributed to the primary dipole. This factor also appears naturally in our more systematic treatment below.⁶

We denote Eq. (4.29) as E'_{img} to indicate that this summation is not *absolutely convergent*, since $E_{\text{dd}} \sim R^{-2}$ for large R . The lack of absolute convergence can be seen (by definition) by the *divergence* of the series if absolute values of each summand is summed, i.e.

$$\begin{aligned} \sum_{\vec{R}} E_{\text{dd}}(\vec{R}) &\sim \int^{\infty} dR \cdot 2\pi R \cdot R^{-2} \\ &\sim \int^{\infty} \frac{dR}{R} \\ &\sim [\ln R]^{\infty} \rightarrow \infty \end{aligned} \quad (4.31)$$

The cancellation of terms having opposite signs makes the original summation *conditionally convergent* [166], with its value depending on the ordering of the summand. Similar problems arise in summing Coulomb interactions of dipole lattices, e.g. the cohesive energy of NaCl crystal. They are called Madelung summation [171, 172], and are typically treated using the Ewald method [173, 174].

⁶Eq. (4.28) and (4.29) are equivalent to Eq.(1) and (2) of [169], except that the factor 1/2 is absent in [169], which is probably a typo.

4.2.2 Conventional Methods

Naive summation of Eq. (4.29) clearly will give the wrong estimation of E_{img} , which would lead to incorrect core energies E_{core} , if the summation is arbitrarily cut-off. This is because no matter how large the cut-off radius is chosen, the summation result still varies from scheme to scheme, depending on the detailed shape and morphology of the cut-off surface. One can show that by “maliciously” choosing different cut-off schemes, the summation can “converge” to any real number from minus to plus infinity [175].

Current approaches to resolve the conditional convergence problem include summing dislocation walls for edge dislocations [164, 165, 166] and performing fast multipole calculations [165] or Ewald-like summations for screw dislocations [167]. However, all the proposed methods are applicable only to isotropic media, leaving the effects of anisotropy without scrutiny.

4.2.3 A Systematic Approach

In our systematic treatment of the elastic interactions, the issue of conditional convergence does not arise. By evaluating the reversible work to create a dislocation dipole in the periodic cell, we obtain an expression for the elastic energy of the dipole, expressed in terms of its stress field $\sigma(\vec{r})$ in the PBC cell.

$$E_{\text{el}} = -\frac{1}{2} \int dA_j b_i \sigma_{ij}^0(\vec{r}) + \frac{1}{2} S \bar{\sigma}^2 V, \quad (4.32)$$

where the integral extends over the area enclosed by the dislocation dipole, $\bar{\sigma} = \langle \sigma(\vec{r}) \rangle_V$ is the stress averaged over the cell volume V , $\sigma^0(\vec{r}) = \sigma(\vec{r}) - \bar{\sigma}$, and S is the elastic compliance tensor.

Eq. (4.32) is our central result; it follows from the combination of two steps, first creating a perfect lattice under a uniform stress field and then creating a dislocation dipole by making a cut on a surface (under stress) and displacing the two sides of the surface relative to each other. A detailed derivation of Eq. (4.32) is given in Appendix A. The elastic energy is therefore composed of a defect contribution,

which depends only on the stress field variation $\sigma^0(\vec{r})$, and a bulk contribution varying quadratically with the average stress $\bar{\sigma}$.

One can express $\sigma^0(\vec{r})$ as the summation of variations in the stress due to the individual dislocation dipoles. Denote the stress field of a dipole at \vec{R} by $\sigma_{ij}^{\text{dipole}}(\vec{r} - \vec{R})$; this summation is absolutely convergent since the stress difference between two field points decays like R^{-3} . To connect with the existing approach mentioned above, we note that the integral of the stress field of one dipole over the region enclosed by the primary dipole equals to minus the interaction between the two dipoles, so that

$$E_{\text{prm}} = -\frac{1}{2} \int dA_j b_i \sigma_{ij}^{\text{dipole}}(\vec{r}) \quad (4.33)$$

and

$$E_{\text{dd}}(\vec{R}) = - \int dA_j b_i \sigma_{ij}^{\text{dipole}}(\vec{r} - \vec{R}). \quad (4.34)$$

It then follows that E_{img} can be rigorously written as

$$E_{\text{img}} = \frac{1}{2} \sum_{\vec{R}}' E_{\text{dd}}(\vec{R}) + \frac{1}{2} A_j b_i \sigma_{ij}^{\text{err}} + \frac{1}{2} S \bar{\sigma}^2 V, \quad (4.35)$$

where $\sigma_{ij}^{\text{err}} = \left\langle \sum_{\vec{R}} \sigma_{ij}^{\text{dipole}}(\vec{r} - \vec{R}) \right\rangle_V$, and the summation here involves the same collection of image dipoles as in the first term of Eq. (4.35) plus the primary dipole contribution ($\vec{R} = 0$). Eq. (4.35) shows that what is missing in Eq.(2), besides a term describing the bulk stress effect, $\frac{1}{2} S \bar{\sigma}^2 V$, is a dipole correction $\frac{1}{2} A_j b_i \sigma_{ij}^{\text{err}}$, which is $-1/2$ of the interaction between the primary dipole and the average stress introduced by the primary and image dipoles. This is similar to that derived by Wolf [176] in treating Coulomb interaction summations in electric dipole lattices. The correction is non-zero only if the primary cell contains a nonzero dipole moment [177]. If one can group every two neighboring cells to form a dislocation quadrupole array [151], its image summation is then free from this dipole correction. It is important to note the difference between σ^{err} and $\bar{\sigma}$. The former is average stress arbitrarily introduced into the PBC cell when summing the image dislocations, whose effect has to be subtracted out completely. On the other hand, $\bar{\sigma}$ is the “physical” average

stress determined by atomistic simulations, whose contribution to the total energy is expressed in the quadratic term in Eq. (4.32).

One can show that the dipole correction can be exactly canceled by introducing a set of specially chosen “ghost” dislocations to interact with all the dipoles, see Appendix A for details. This is analogous to the fictitious charges introduced in [178] to cancel the dipole correction in the lattice of electric dipoles. As shown in Fig. 4-1, “ghost” dislocation with Burgers vector $\alpha\vec{b}$ can be placed at $\vec{c}_1/2$, $-\alpha\vec{b}$ at $-\vec{c}_1/2$, $\beta\vec{b}$ at $\vec{c}_2/2$, and $-\beta\vec{b}$ at $-\vec{c}_2/2$, with α, β satisfying $\vec{a} = \alpha\vec{c}_1 + \beta\vec{c}_2$. In this way E_{img} becomes,

$$E_{\text{img}} = \frac{1}{2} \sum_{\vec{R}} (E_{\text{dd}}(\vec{R}) - E_{\text{dg}}(\vec{R})) - \frac{1}{2} E_{\text{dg}}(0) + \frac{1}{2} S \bar{\sigma}^2 V, \quad (4.36)$$

where $E_{\text{dg}}(\vec{R})$ represents the interaction energy between a dislocation dipole (at offset \vec{R}) and the “ghost” dislocations. The summation in Eq. (4.36) is absolutely convergent because the “ghost” dislocations have exactly the same dipole moment as the primary dipole, so that $E_{\text{dd}}(\vec{R}) - E_{\text{dg}}(\vec{R}) \sim R^{-3}$ for large R . Since Eq. (4.36) does not depend on the explicit form of dislocation interactions, our method is applicable to dislocations of any character in a general anisotropic elastic medium.

4.2.4 Extracting Core Energy

We apply our method to extract the core energy of a shuffle-set screw dislocation in Si from atomistic calculations using the Stillinger-Weber (SW) [135] potential. The basis vectors $\vec{c}_1, \vec{c}_2, \vec{c}_3$ of the simulation cell are along $[11\bar{2}], [111]$ and $[1\bar{1}0]$ directions respectively. The two dislocations have Burgers vector $\vec{b} = \pm[1\bar{1}0]/2$, and are separated by $\vec{a} = \vec{c}_1/2$. The cell is given an overall strain to accommodate the plastic strain introduced by the dislocation dipole, so that it has zero average stress and the last term in Eq. (4.36) vanishes. A typical atomic structure in these simulations are shown in Fig. 4-2. Fig. 4-3(a) shows the variation of the total energy per unit dislocation length (E_{atm}) with cell dimension \vec{c}_1 , while \vec{c}_2 is fixed at $3[111]$. For a given simulation cell, we calculate the corresponding elastic energy $E_{\text{prm}} + E_{\text{img}}$ through Eq. (4.36) and use sextic anisotropic elasticity theory for individual dislocation inter-

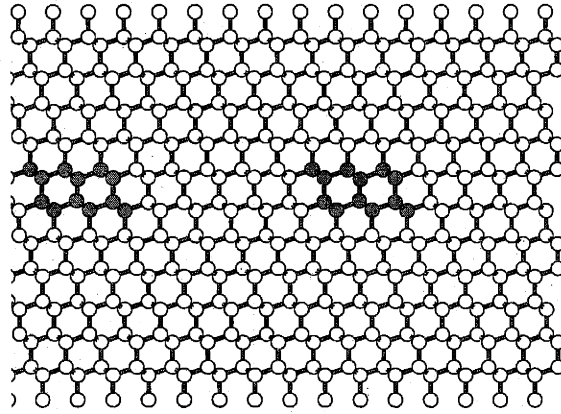


Figure 4-2: Atomic structure of shuffle set screw dislocation dipole in Si a simulation cell under PBC. The displacement field for these two dislocations are mainly along z direction, which is perpendicular to the paper. The high energy atoms in the dislocation core are plotted in dark color.

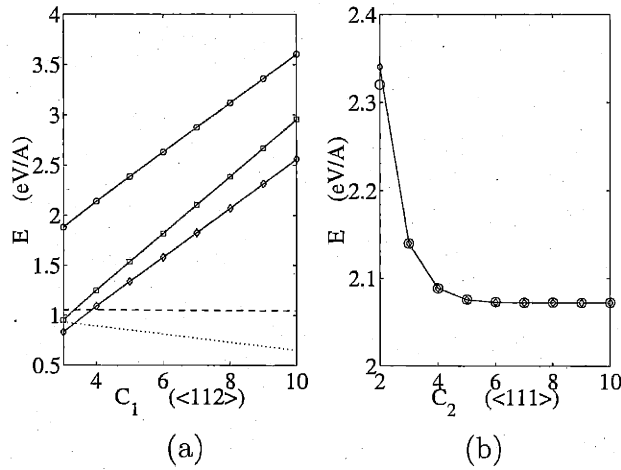


Figure 4-3: (a) Variation of atomistic (o) E_{atm} and linear elastic (anisotropic \diamond and isotropic \square) E_{el} energies of a shuffle-set screw dislocation dipole in a PBC cell of Si with \vec{c}_1 at $\vec{c}_2 = 3[111]$. Predictions of $2E_{\text{core}}$ are shown in dashed and dotted line respectively. (b) Variation of E_{atm} with \vec{c}_2 at $\vec{c}_1 = 4[11\bar{2}]$. Atomistic simulation results are shown in o, while anisotropic elastic results for E_{el} plus $2E_{\text{core}}$ obtained from (a) are shown in \diamond .

action energies. The expression for the interaction energy are obtained by integration of the stress expression from [30]. For two parallel dislocations separated by (x, y) , their interaction takes the form $E \sim \ln(x + p_\alpha y)$, with p_α being roots of a sixth order polynomial. More details on dislocation interactions in anisotropic elastic medium are presented in Appendix D. The elastic constants used for elasticity calculations are taken from the reported values [13] for the SW potential, which are $C_{11} = 161\text{GPa}$, $C_{12} = 81.6\text{GPa}$, $C_{44} = 60.3\text{GPa}$.

The anisotropic elasticity results, Eq. (4.32), are seen to fall on a straight line with a slope that agrees with the atomistic result to within 0.5%. This agreement between atomistic and anisotropic linear elasticity results is significant because there are no adjustable parameters in either calculation, in contrast to previous studies [166, 169]. The difference between the two gives the core energy $E_{\text{core}} = 0.526 \pm 0.002\text{eV}/\text{\AA}$, at $r_c = b = 3.84\text{\AA}$, which is manifestly independent of \bar{c}_1 . As discussed in Appendix A.1, this result can also be expressed in terms of a cut-off radius $r_c = b/\alpha$ for which $E_{\text{core}} = 0$. In this case, $\alpha = 4.31$. A previous calculation using first principles method and isotropic elasticity theory [169] has given $E_{\text{core}} = 0.56 \pm 0.21\text{eV}/\text{\AA}$ using the same r_c , (corresponding to $\alpha = 4.73$). First principles method is supposed to be more accurate than empirical potentials in obtaining the atomistic energy, while anisotropic elasticity is more accurate than isotropic elasticity in estimating the image energy. In view of this and considering the large error bar in the previous work, one cannot conclude much at this stage.

In Fig. 4-3(b) we directly compare the two sides of Eq. (4.28) by fixing \bar{c}_1 at $4[11\bar{2}]$ and varying \bar{c}_2 from 2 to $10[111]$. The atomistic result agrees very well with the sum of anisotropic elasticity results plus $2E_{\text{core}}$ obtained from Fig. 4-3(a), except at the smallest \bar{c}_2 ($2[111]$), where the dislocation cores overlap with their own image and linear elasticity is expected to break down. This is a direct confirmation of Eq. (4.28) as the proper way of define the core energy of a dislocation.

To bring out the effects of elastic anisotropy, we repeat our calculation by assuming elastic isotropy. The shear modulus and Possion ratio for isotropic elasticity calculations are obtained by Voigt averaging [30] of the cubic elastic constants

C_{11}, C_{12}, C_{44} , which yields $\mu = 52.18\text{GPa}$ and $\nu = 0.2924$ for Stillinger-Weber Si. The results, shown in Fig. 4-3(a), also follow a linear variation with a slope that is now 14% larger than the atomistic calculation. One could try “improving” the isotropic elasticity estimate by replacing the shear modulus μ by an energy prefactor K [167], with K taken from an anisotropic expression of screw dislocation self energies. In this case, $K = (C_{44}(C_{11} - C_{12})/2)^{1/2} = 49.11\text{GPa}$. Yet the resulting slope is still too large by 8%. Alternatively one could treat μ as a free parameter [166, 169] to obtain a best fit with atomistic data. Such a procedure leads to a core energy of $E_{\text{core}} = 0.532 \pm 0.002\text{eV}/\text{\AA}$ (corresponding to $\alpha = 4.38$).

We have also performed similar calculations for edge dislocations in a BCC metal Mo. We use a simulation cell with $\vec{c}_1, \vec{c}_2, \vec{c}_3$ along $[111], [\bar{1}01], [1\bar{2}1]$ directions respectively, with $\vec{a} = \vec{c}_2/2$ and $\vec{b} = \pm[111]/2$. A typical atomic structure is shown in Fig. 4-4. The dislocation dipole is created by removing a layer of atoms followed by relaxing the configuration to zero stress. We adopt the Finnis-Sinclair (FS) [138] potential, for which $C_{11} = 464.7\text{GPa}$, $C_{12} = 161.5\text{GPa}$, $C_{44} = 108.9\text{GPa}$, and Voigt average values are $\mu = 125.98\text{GPa}$, $\nu = 0.2932$. As shown in Fig. 4-5, the behaviors are found to be similar to that of Si. The core energy predicted by anisotropic elasticity is $E_{\text{core}} = 0.324 \pm 0.002\text{eV}/\text{\AA}$, at $r_c = b = 2.7256\text{\AA}$, (corresponding to $\alpha = 1.66$). On the other hand, using μ as a free parameter, isotropic elasticity gives $E_{\text{core}} = 0.382 \pm 0.002\text{eV}/\text{\AA}$, (corresponding to $\alpha = 1.81$), significantly different from anisotropic results. Thus dislocation core energies obtained under the assumption of elastic isotropy can be in appreciable error even when the energy prefactor is fitted to atomistic data. This error seems to be more pronounced in edge dislocations.

4.2.5 Predicting Elastic Interactions in PBC

The foregoing analysis indicates that elastic isotropy should not be assumed in determining the elastic interaction results toward which atomistic calculations should converge in the limit of large simulation cells. An issue of practical concern then is whether there exists an optimum cell geometry for atomistic simulation studies of dislocations. Linear elasticity predicts that when \vec{a} is kept at $\vec{c}_1/2$, E_{img} is only

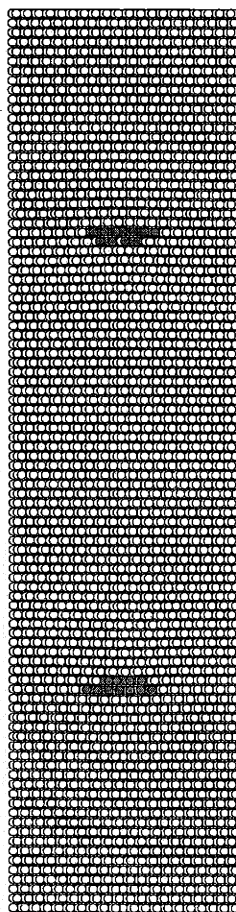


Figure 4-4: Atomic structure of edge dislocation dipole in Mo a simulation cell under PBC. The dipole is created by removing a layer of atoms between the two dislocations. The high energy atoms in the dislocation core are plotted in dark color.

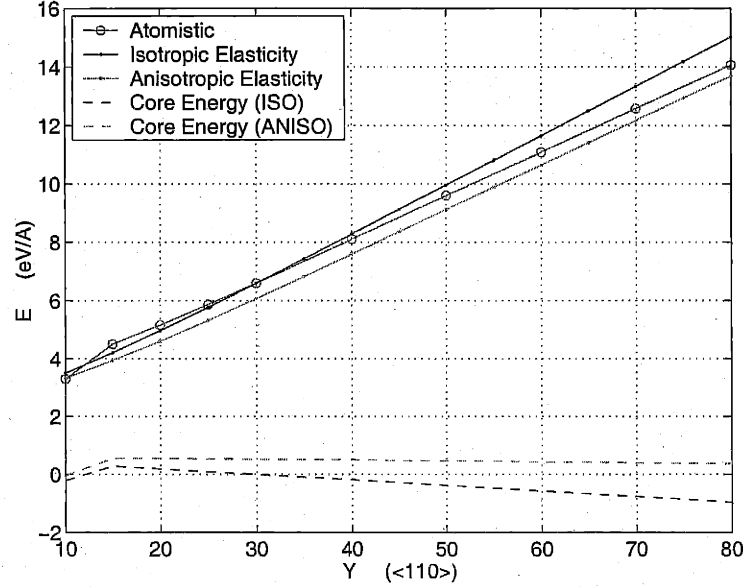


Figure 4-5: Variation of atomistic (\circ) E_{atm} and linear elastic (anisotropic \diamond and isotropic \square) E_{el} energies of an edge dislocation dipole in a PBC cell of Mo.

dependent on the cell aspect ratio. Fig. 4-6 shows the predicted image interactions not only decrease with increasing aspect ratio, as one would expect, with anisotropy effects reducing the magnitude, but also the energies can change sign. This information is noteworthy because a simulation cell with small magnitude of image energy E_{img} would have higher accuracy in determining the core energy.

Proceeding further, we can ask how cell geometry generally affects the total elastic interactions and hence the dynamics of dislocations in atomistic simulations. A question of practical interest is whether there exists an optimum cell geometry for which the elastic interactions are minimized. Consider a simulation cell (Fig. 4-7(a)) containing an edge dislocation dipole at separation $\vec{a} = \vec{c}_2/2$ which can only glide along \vec{c}_1 . The system energy is then a periodic function of their relative displacement x along \vec{c}_1 direction, the energy barrier being a result of an oscillatory image stress field superimposed on any applied external stress. Linear elastic considerations show that the energy variation has extrema at $x = 0$ and $x = c_1/2$, so that $\Delta E = E(x = 0) - E(x = c_1/2)$, a function only of the cell aspect ratio, is an ap-

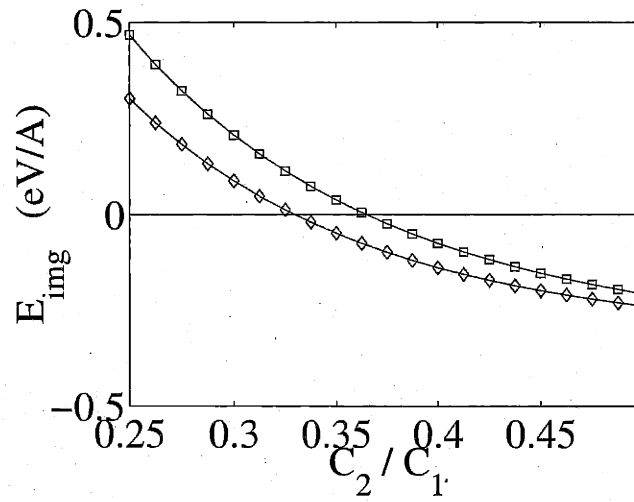


Figure 4-6: (a) Elasticity theory predictions of image energy (in \diamond) for screw dislocation dipole as in Fig. 4-2,4-3. Anisotropic elasticity (in \diamond) predicts $E_{\text{img}} = 0$ at $c_2/c_1 = 0.329$, while isotropic elasticity (in \square) predicts a different zero point at $c_2/c_1 = 0.365$.

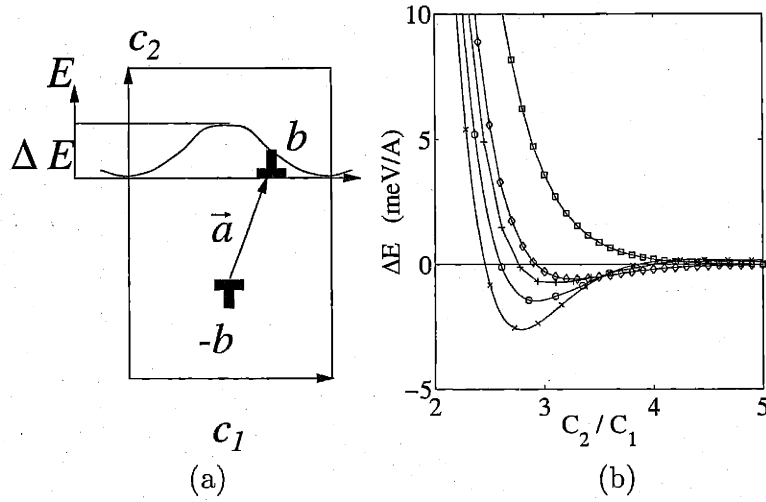


Figure 4-7: (a) Schematic of the total energy variation with relative displacement x , ΔE being the maximum. (b) Variation of ΔE with cell aspect ratio c_2/c_1 for edge dislocations in Mo, with the same set up as in Fig. 4-5. Anisotropic elasticity predicts $\Delta E = 0$ at $c_2/c_1 = 2.918$ (\diamond). Isotropic elasticity predicts a monotonic decrease of ΔE with increasing c_2/c_1 (\square). Atomistic simulations with $c_1 = 15, 20$ and $30[111]$ are shown in \times , \circ and $+$ respectively.

appropriate measure of the internal dislocation interaction. For dislocation mobility simulations [179] a minimum value ΔE is desirable for obtaining an accurate relation between the dislocation velocity and the applied stress.

Results for the energy barrier determined separately by isotropic and anisotropic elasticity calculations are compared in Fig. 4-7(b). One sees the former clearly decreases monotonically with increasing aspect ratio without becoming negative, whereas the latter vanishes at the value of $c_2/c_1 = 2.918$. Also shown in Fig. 4-7(b) are direct atomistic simulation results for the energy barrier for three cell sizes, showing a converging behavior toward the elasticity result.

The vanishing of the energy barrier at the special aspect ratio implies a complete cancellation among the primary and image interactions, thus allowing unhindered dislocation glide in the PBC simulation cell. Direct atomistic simulations confirm that ΔE indeed is greatly reduced at a cell geometry close to the predicted c_2/c_1 . For example, at $\bar{c}_1 = 20[111]$ and $\bar{c}_2 = 64[101]$, simulation gives $\Delta E = 0.091 \text{ meV}/\text{\AA}$,

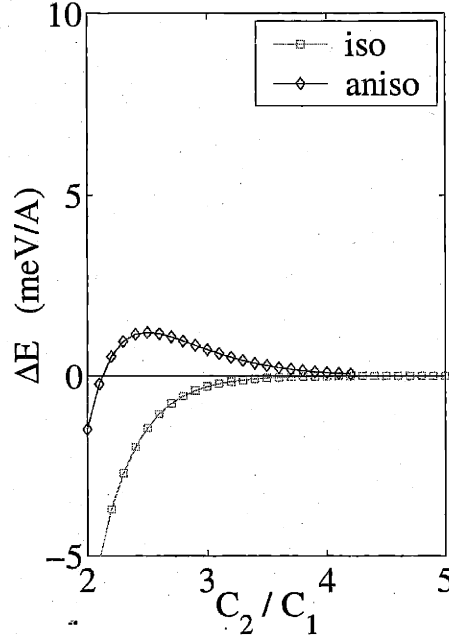
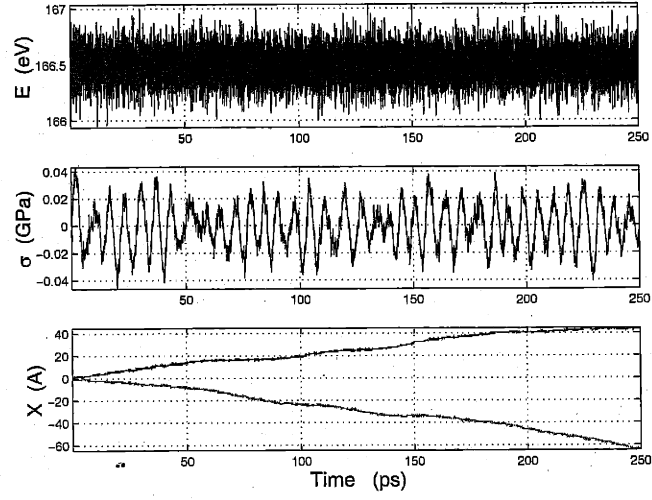


Figure 4-8: Variation of ΔE with cell aspect ratio c_2/c_1 for screw dislocations in Mo. Anisotropic elasticity predicts a reverse of sign at $c_2/c_1 \approx 2.2$ while isotropic elasticity predicts a monotonic increase of ΔE approaching zero.

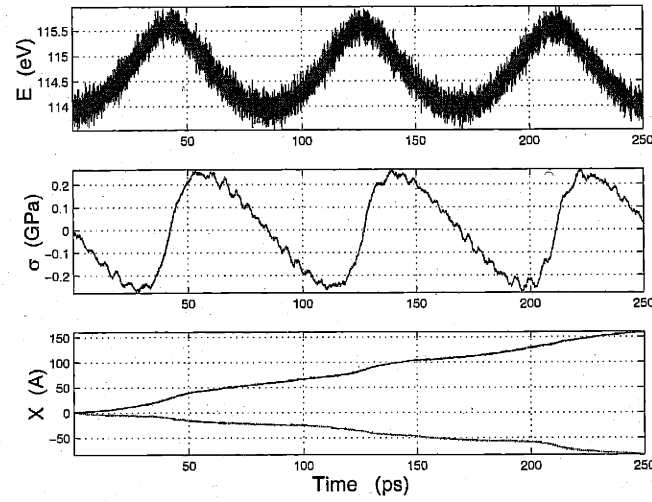
corresponding to a maximum internal stress of about 0.3MPa. In contrast, typical stresses applied in mobility simulations are in the range of 10 – 1000MPa [179].

It may appear that the atomistic results in Fig. 4-7(b) indicate a significant size dependence. Indeed, a contributing factor could be the higher order (e.g. $\sim 1/r$) terms in the elastic interactions. On the other hand, it should be noted that the energy scale in this figure is about 2 orders of magnitude smaller than typical values for migration barriers for dislocations, so the effect here is rather small. Nevertheless we believe the existence of special geometries, arising from elastic anisotropy, for which $\Delta E = 0$ is quite general, and it is indeed confirmed by our results for a screw dislocation in Mo, as shown in Fig. 4-8.

According to Fig. 4-7(b), for edge dislocation mobility simulations in Mo using periodic boundary conditions, the aspect ratio c_2/c_1 of the simulation cell need to be larger than 3 ~ 4 to make image interaction effects negligibly small. This prediction



(a)



(b)

Figure 4-9: Variation of total energy E and Virial stress σ , and dislocation displacement X in MD simulations of edge dislocation motion, with cell aspect ratio c_2/c_1 at (a) 3.8 and (b) 1.65. The fluctuation in (a) is small and is mainly due to thermal noise, while the large oscillations in (b) is clearly due to the image interaction artifact.

is confirmed by direct Molecular Dynamics simulations. Fig. 4-9 shows the Virial stress oscillation during MD simulations of moving edge dislocation dipoles with cell aspect ratio at 3.8 and 1.65 respectively [180]. The simulations are performed at 20K with a constant shear rate of $0.4 \times 10^{-9} \text{s}^{-1}$. The Virial stress oscillation for the large aspect ratio is very small and mainly comes from thermal fluctuation, while that for the small aspect ratio clearly shows a sinusoidal pattern, which is an artifact due to the image interactions.

4.3 Dynamic Domain Coupling

In this section, we study an even more clear-cut case of type (a) coupling (see Chapter 1), where an atomistic region is embedded in an elastic continuum surrounding. We will present a systematic approach [181] which couples a discrete atomistic simulation domain with a linear elastic surrounding where the artificial wave reflection at the interface is minimized.

4.3.1 Artificial Wave Reflection at Domain Boundary

A general problem in the domain decomposition approach to modeling discrete systems with localized inhomogeneities (defects) is the spurious reflection of elastic waves due to a change in system description across a domain boundary. Such effects are seen in, for example, the atomistic modeling of dislocation motion [183], crack propagation [184, 185, 182, 186], and energetic particle-solid collisions [187, 188], while they are also of concern in the recent development of hybrid techniques involving multiple length and/or time scales [189, 190, 191, 192]. Fig. 4-10 illustrates such reflections of elastic waves emitted from the crack tip in an MD simulation (from B. L. Holian). Such an reflection is inherently due to the change of system description across the domain boundary. For example, fixed boundary conditions are usually used for crack simulations [185, 182], and the wave gets reflected at the rigid boundary surfaces. In coupled MD-Finite Element method (FEM) simulations, wave reflection also occurs, because elastic wave modes with short wavelengths simply do not exist in the

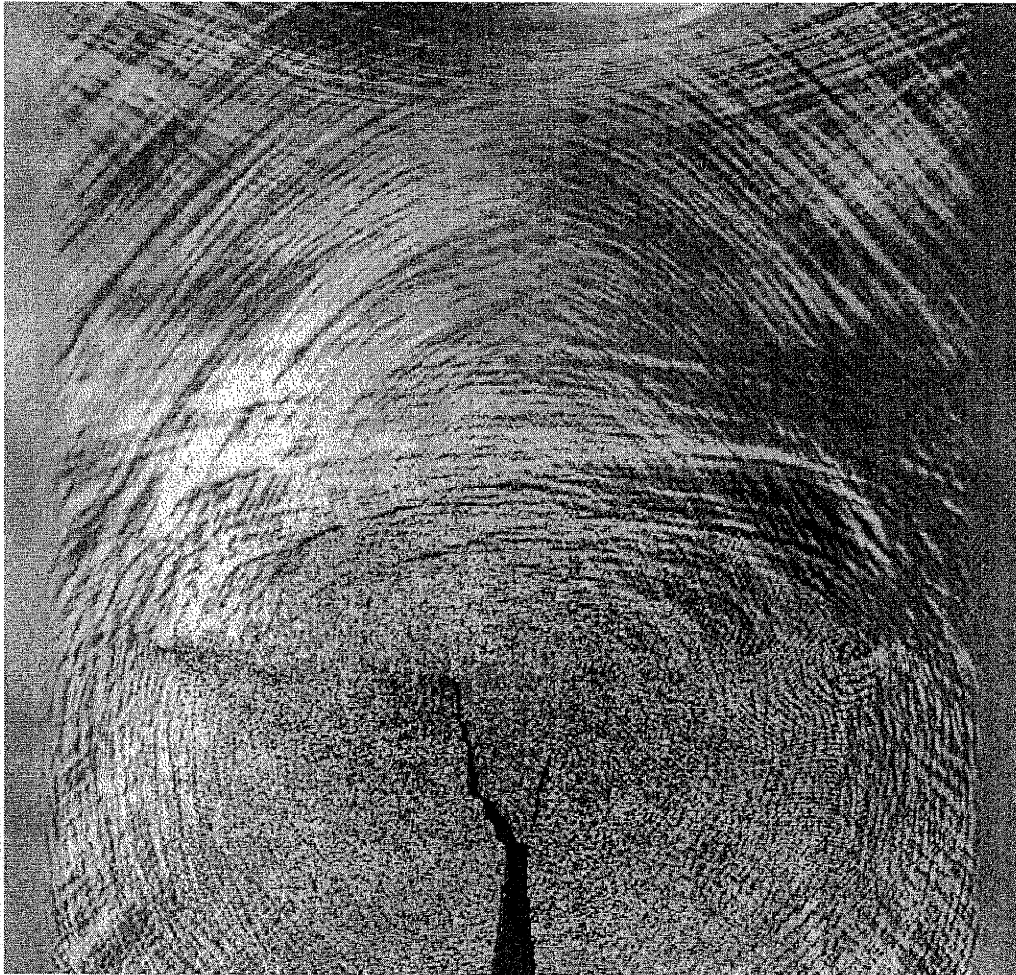


Figure 4-10: Elastic wave emitting from the crack tip gets reflected at the boundary of the simulation cell. (From B. L. Holian via S. Yip. Similar results can be found in [182].)

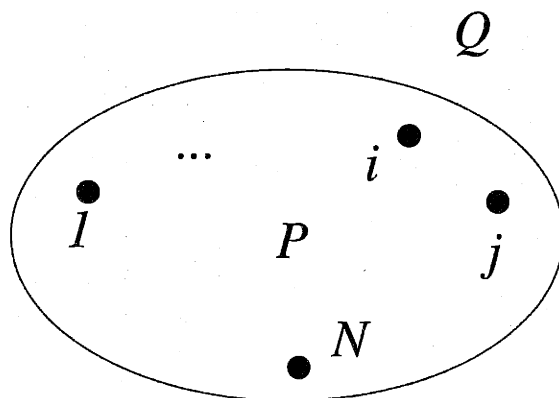


Figure 4-11: MD region P is the region enclosed by the solid line, surrounded by region Q , which is perfect lattice.

coarse grained FEM region. Minimizing boundary reflection is therefore equivalent to minimizing the difference between the dynamic responses of the two domains. Ideally the reflection will disappear if the two domains are identical, both being fully resolved by Molecular Dynamics, in which case there is no physical interface at all. However, the very reason that a domain coupling problem arises in the first place is the computational limitation of MD simulations. It is common practice to simulate only a small portion of the real system and treat the remaining region as a boundary condition, which can be usually regarded as infinitely large compared with the MD region. A number of coupling schemes or boundary conditions have been proposed in order to minimize such reflections, such as *ad hoc* viscous damping [185, 182, 186] and the more physically motivated use of an approximate description of coupling across a domain boundary [188]. To date, however, none can claim to be free from empiricism and the attendant limitation on general applicability. In the following subsections, we will present our systematic solution to this problem based on the linear response theory.

4.3.2 Linear Response Theory

Consider a crystalline P - Q system in which region of interest P may contain inhomogeneities, while medium Q consists of defect-free material only, see Fig. 4-11. For sufficiently large P and moderate temperatures it is appropriate to describe the P - Q and Q - Q interactions as harmonic. One can then obtain an equation for P from which the explicit degrees of freedom associated with medium Q have been eliminated and replaced by an implicit formulation [193, 194]:

$$\begin{aligned}
 m\ddot{x}_i(t) = & -\frac{\partial V}{\partial x_i} + \int_0^t d\tau \sum_{j=1}^N \beta_{ij}(\tau) \dot{x}_j(t-\tau) + \\
 & + \sum_{j=1}^N \beta_{ij}(t) x_j(0) + R_i(t).
 \end{aligned} \tag{4.37}$$

Here, the x_i represent the N degrees of freedom in P , $V = V(\{x_j\})$ is the potential energy of the entire system with the atoms in Q fixed at their equilibrium positions, $\beta_{ij}(t)$ denote the N^2 elements of the time-dependent memory kernel matrix $\beta(t)$, and $R_i(t)$ is a linear function of the initial displacements and velocities in domain Q . Eq. (4.37) is generally referred to as the generalized Langevin equation (GLE) [193, 194, 195], in which the functions $\beta_{ij}(t)$ describe the response of medium Q to disturbances in region P in the form of P -to- P correlation. The $R_i(t)$ represent the effects on P due to any initial disturbance in Q and are usually treated as random forces to describe the effects of statistical fluctuations in region Q at a nonzero temperature [188, 193, 194]. A detailed derivation of GLE will be presented in Appendix B.

Eq. (4.37) provides the equation of motion for MD simulations with the region P , while all the effects of Q atoms are accurately represented by the memory kernel functions $\beta_{ij}(t)$ as a time-dependent boundary condition. In principle, such a simulation should not give any boundary reflections, since no approximate was made at this stage other than the linearity assumption for the P - Q and Q - Q interactions. Although this equation has been derived for a long time, it did not result in a systematic solution

of the boundary reflection problem, because the functional form of the memory functions are not known for an general system with an arbitrarily complex Hamiltonian. Analytical solutions of the memory kernel only exist for very idealized systems, such as one-dimensional harmonic lattices [196] (see Appendix B.5 for more details). For more realistic systems, approximations to the memory kernels were made [188], which can be shown to be equivalent to introduce a viscous damping force on boundary layer atoms.

4.3.3 Measuring Memory Kernel

In this work, we found that the memory kernel functions can be rigorously determined, albeit numerically, through a series of MD simulation. This is done by regarding the Q region as a linear system and the memory functions as its response functions. More discussion on this analogy are presented in Appendix B.

Suppose the system is at equilibrium with the atoms in P and Q all at rest. At $t = 0$ one of the atoms in P is given a displacement ϵ , after which all atoms in P are frozen in their initial positions:

$$x_j(t) = x_j(0) = \epsilon \delta_{jk}. \quad (4.38)$$

Allowing the atoms in Q to relax after $t = 0$, the time-dependent forces acting on the atoms in P are given by the right-hand side of Eq. (4.37),

$$F_i(t) = -\frac{\partial V}{\partial x_i} + \epsilon \beta_{ik}(t), \quad (4.39)$$

where the convolution terms and the $R_i(t)$ have vanished due to Eq. (4.38) and the fact that region Q is initially in equilibrium, respectively.

The first term in Eq. (4.39) represents the static force exerted on x_i if all atoms in Q were to be held fixed in their initial positions (i.e. fixed boundary conditions), while the second term is the time-dependent component arising from the motion of the Q atoms after $t = 0$. It is clear that the response functions $\beta_{ik}(t)$ completely specify

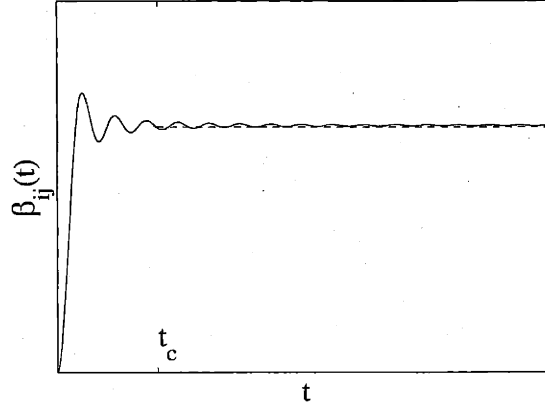


Figure 4-12: Typical behavior of the memory kernel matrix elements as a function of time (full line). In practice, the response functions are determined within a time interval $[0, t_c]$, with t_c being a cut-off time. For $t > t_c$ they are assumed to remain constant at their cut-off values $\beta_{ij}(t_c)$ (dashed line).

the P - Q coupling as a space-time dependent P -to- P correlation through medium Q .

Equations (4.38) and (4.39) constitute the basis for an algorithm to compute $\beta_{ik}(t)$ from a series of test simulations. Each simulation would start with the perturbation of an x_k according to Eq. (4.38), followed by an MD run that measures the subsequent response of the atoms in Q under the constraint of fixed positions in P . During each run the forces $F_i(t)$ are recorded as a function of time, giving directly the N response functions $\beta_{ik}(t)$, $i = 1 \dots N$, after subtraction of the static force components $-\partial V/\partial x_i$.

In practice, the test simulations are performed over a finite time interval, so that the $\beta_{ij}(t)$ are determined only within a time interval $[0, t_c]$, with t_c being a cut-off time. Given the typical behavior of the matrix elements as a function of time, shown in Fig. 4-12, it is reasonable to disregard any further variations in the response functions for $t > t_c$, and assume they remain constant at their cut-off values $\beta_{ij}(t_c)$, provided that t_c is sufficiently large. To be internally consistent, temporal truncation should be accompanied by a spatial cut-off. This means one should neglect all matrix elements that involve atoms separated by a distance larger than a cut-off radius $r_c \sim ct_c$, where c is the sound velocity in Q . In many cases, the number of relevant response

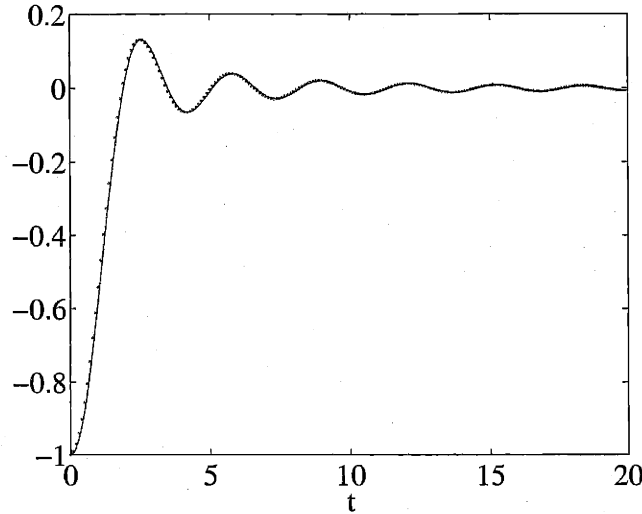


Figure 4-13: Memory function for one-dimensional harmonic oscillators. MD simulation results (\bullet) agrees closely with analytic solutions $\beta(t) = -J_0(2t) - J_2(2t)$ (in solid line).

functions can be further reduced if the interatomic potential model is finite-ranged and the number of degrees of freedom in P that interact directly with those in Q is considerably smaller than N .

4.3.4 Reflectivity Tests

As a first demonstration of the effectiveness of the response function boundary condition we are proposing, we apply Eq. (4.37) to simulate the dynamics in a small section of a linear chain of identical harmonic oscillators with nearest-neighbor interactions. The masses, spring constants and equilibrium distances are set equal to unity. 50 oscillators are assigned to a region P which is bracketed by two semi-infinite chains Q_1 and Q_2 . Because of the configurational symmetry there is only one relevant memory kernel in this problem, describing the response of a semi-infinite chain to a displacement in the corresponding boundary oscillator. The test simulation, carried out using a time step $\Delta t = 0.1$, is truncated after a cut-off time $t_c = 50$, when the force fluctuations in the response function have decayed to within approximately 0.15% of the

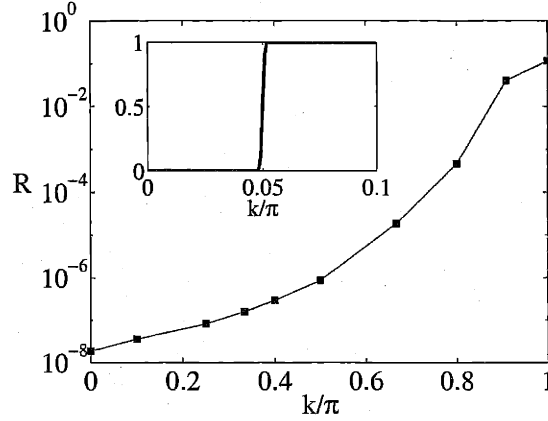


Figure 4-14: Phonon reflectivity as a function of wave vector k for a one-dimensional chain of harmonic oscillators. Inset shows reflectivities associated with the CGMD method [191] for the same problem.

asymptotic value. The numerically computed response function is essentially indistinguishable from the analytical solution $\beta(t) = -J_0(2t) - J_2(2t)$ [196], as shown in Fig. 4-13.

Using the numerically computed response function in (4.37), an MD simulation is performed to study the time evolution in P after introducing initial displacements $x_i(0)$ according to the wave packet

$$x_i(0) = \cos[k(X_i^0 - b)] \exp[-(X_i^0 - b)^2/2\sigma^2].$$

Here, X_i^0 denotes the equilibrium position of oscillator i and $X = b$ is the position in the center of domain P . As a reference, the motion is also monitored using a full MD simulation in which the oscillators in Q_1 and Q_2 are treated explicitly and no boundary is present. As a measure of the effectiveness of our response function approach, we evaluate the wave reflection at the boundaries between domain P and the chains Q_1 and Q_2 . The reflectivity R is defined as the maximum difference between the instantaneous energies stored in region P during the response function simulation and the full MD run, divided by the initial energy in region P .

In Fig. 4.3.4 R is plotted as a function of wave vector k with $\sigma = 5$. The results

show that the response function approach provides an excellent description of the dynamics in P , featuring a reflectivity below 10^{-3} for approximately 80% of the Brillouin zone, and of the order of only 10^{-1} for k -values at the zone boundary. For comparison, the reflectivity results obtained in a coarse-grained molecular dynamics (CGMD) simulation for the same system [191] are shown in the inset. It can be seen that the coupling method in the latter work is much less effective, as only the lower 5% of the Brillouin zone is treated correctly while the components with higher values of k are totally reflected due to the fact that such modes cannot exist in the coarse-grained region.

As a second demonstration we study wave reflectivity in a two-dimensional version of the previous system, a square lattice of harmonic oscillators with the same specifications. The oscillators are allowed to move only in the direction perpendicular to the plane of the lattice. The primary domain P is defined as a square region containing 3600 lattice sites. Given the symmetry of the configuration and the short range of the interactions, the total number of test simulations required to fully specify the memory kernel matrix is 30. Each simulation is carried out using a time step $\Delta t = 0.1$ and is truncated after a cut-off time $t_c = 50$. Furthermore, an additional spatial truncation is introduced; all matrix elements that involve oscillators separated by a distance larger than a cut-off radius $r_c = 30$ are disregarded. In this case, the storage of the total memory function matrix takes about 56Mega-bytes.

In order to compare to existing reflectivity results [188] we study the boundary reflectivity as a function of the width of the wave packets. The initial displacements in P are set according to a symmetric two-dimensional Gaussian function of width σ , centered in the middle of domain P . Following the procedure described previously, the reflectivity R is evaluated by comparing the energies stored in domain P during the full MD run and the response function simulation.

Fig. 4-15 shows four snapshots of the simulation with the memory kernel method. The initial Gaussian wave packet smoothly passes through the simulation cell boundary leaving no residual oscillation behind. As a comparison, simulation snapshots using a free boundary are shown in Fig. 4-16. We notice the severe wave reflection

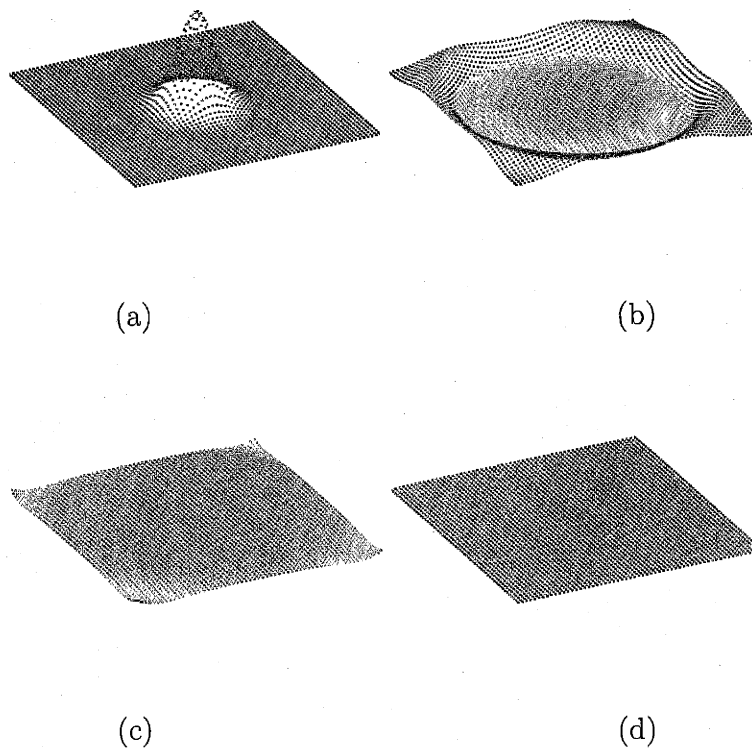


Figure 4-15: (a) Initial condition of a Gaussian wave packet on a 2D harmonic lattice. (b) Wave packet propagating outwards after 300 timesteps using the boundary condition developed in this section. (c) 450 timesteps. (d) 600 timesteps.

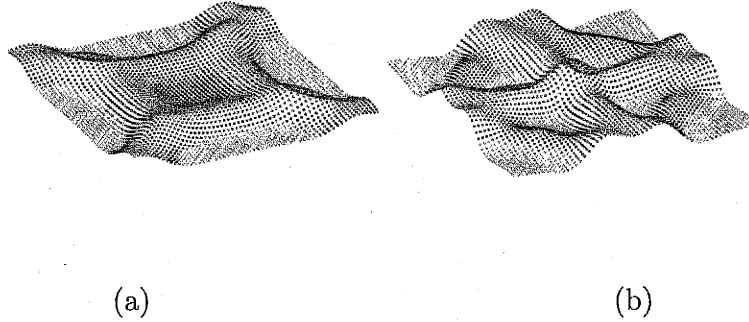


Figure 4-16: (a) MD simulations after 450 timesteps under free boundary, with the same initial condition as in Fig. 4-15(a). (b) At 600 timesteps, severe boundary reflections are observed.

at the boundary. In this case, reflection is inevitable because the total energy of the system is conserved.

Fig. 4.3.4 shows the reflectivity R as a function of the width σ . Our method provides an accurate description of the response of medium Q , showing reflectivity between 10^{-3} and 10^{-5} across a wide range of values for σ . The inset shows reported reflectivity results for similar initial Gaussian displacements in a three-dimensional study using another reflection reduction method [188]; the different curves correspond to different values of the empirical damping coefficient in this scheme. Even though these results and ours do not refer to identical simulations, nonetheless, we believe it is significant that the reflectivity given by our treatment is some two orders of magnitude lower. Moreover, the reflectivity of our method can be systematically reduced even further by increasing the cut-off values for t_c and r_c .

4.3.5 Application to Static Relaxation

In addition to minimizing boundary reflection, the response function framework is also useful in the context of static relaxation of displacement fields associated with a defect embedded in domain P . This is because the long time limit of the memory kernel functions $\beta(\infty)$ is related with the static lattice Green's function. The relationship

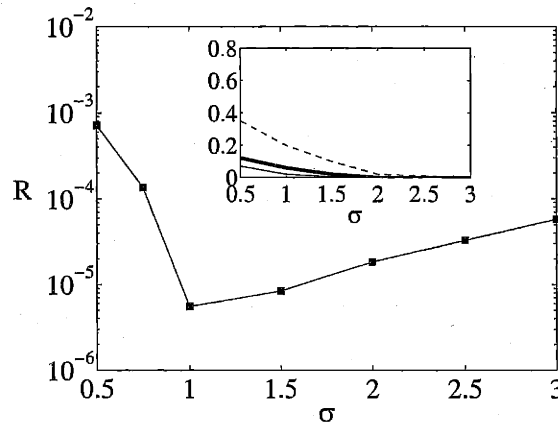


Figure 4-17: Reflectivity on a two-dimensional square harmonic lattice as a function of the width σ of initial Gaussian displacements. Inset shows reflectivity results reported in Ref. [188] using another reflection reduction technique for similar Gaussian displacements in a three-dimensional fcc lattice.

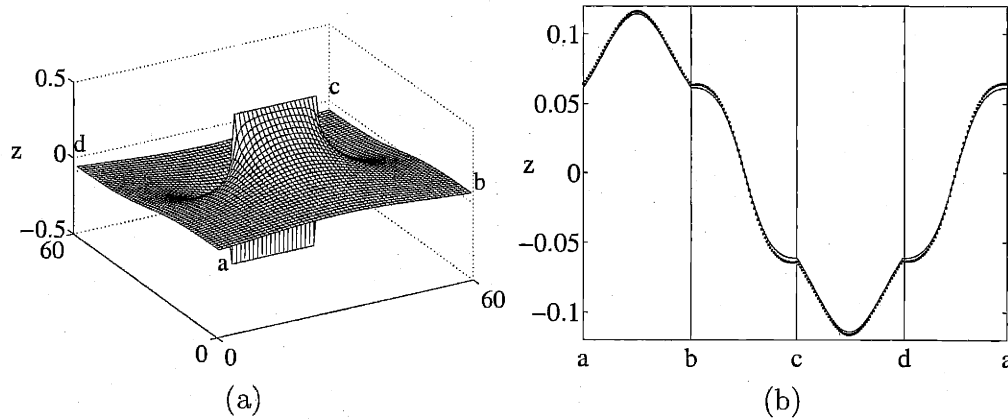


Figure 4-18: (a) Displacements in two-dimensional square harmonic lattice containing a screw dislocation dipole in primary region P . (b) Displacement fields of oscillators along the four edges of the boundary $a-b-c-d-a$; results obtained using conjugate-gradient minimization (full line) and response function relaxation (dotted line).

between the memory functions and the Green's function is discussed in more detail in Appendix B.

As a demonstration, we introduce a model screw dislocation dipole at the center of the previously described two-dimensional square harmonic lattice. The dipole is created by fixing the displacements of a row of atoms in P to $+0.5$, while constraining those in the adjacent row to -0.5 , as shown in Fig. 4.3.4(a). To obtain the reference static displacement fields for this configuration, we first perform a conjugate-gradient (CG) energy minimization procedure on the entire system employing a sufficiently large Q region to achieve satisfactory convergence.

In order to obtain the relaxed displacement field using the response function method one may directly integrate the equations of motion (4.37) until all kinetic energy has dissipated. Using the response functions and cut-off parameters determined in the second application the static displacement field is thus obtained after about 10^5 MD steps. However, since we are interested only in the static response of medium Q in this application, the same result may be obtained more effectively by neglecting the specific time-dependence of the response functions and using only their long-time asymptotic values. In addition, one may also disregard the force components that arise from a particular initial condition. In this manner, the same relaxed displacement fields can be obtained by relaxing the static forces

$$F_i(\{x_j\}) = -\frac{\partial V}{\partial x_i} + \sum_{j=1}^N \beta_{ij}(t_c) x_j, \quad (4.40)$$

using the cut-off values $\beta_{ij}(t_c)$ for the asymptotic values of the response functions.

Fig. 4.3.4(b) shows a comparison between the results obtained with the reference CG procedure (full line) and our response function approach (dotted line). The curves describe the relaxed displacement fields as a function of the oscillator position along the four edges $a-b-c-d-a$ of the $P-Q$ boundary, as indicated in Fig. 4(a). The indicated agreement is satisfactory, while the small discrepancies originate from the errors introduced by the temporal and spatial truncations of the response functions. These errors can be systematically reduced by increasing the values of the cut-off

parameters t_c and r_c .

In summary, we have shown how the response of a linear medium surrounding an atomistic simulation system can be treated in a systematic and numerically tractable manner requiring no assumptions beyond linear response theory. The method is found to be optimal in reducing artificial boundary reflections in dynamical simulations, as well as effective in the context of the static relaxation of displacement fields associated with embedded inhomogeneities.

Chapter 5

Atomistic Study of Shuffle Set Dislocation in Si

The type (b) coupling between atomistic and meso scales that we discussed in Chapter 1 refers to the extraction of mechanistic understandings based on atomistic studies and use them as inputs in the mesoscale models. In this Chapter and the next, we present several findings on the atomistic modes of dislocation motion in semiconductor Si and BCC metal Mo respectively.

As discussed in Chapter 2, controversy still remains on whether the dislocations in Si moves on the glide or the shuffle set (111) planes. After experiments showed that dislocations in Si move in dissociated form at high temperatures ($> 800K$), it became widely accepted that dislocations should move on the glide set planes at these temperatures. Consequently, atomistic calculations has been focused on the core structure, kink energies of partial dislocations on the glide set. However, recent experiments on Si [39, 18] and III-V semiconductors [20, 19, 21] under high confining pressure suggest that the deformation mechanisms could change from glide set dislocations to shuffle set dislocations below a critical temperature.

At the same time, earlier analysis based on a quasi-elastic Peierls-Nabarro model [22] suggested that such a transition could indeed be possible, when shuffle set dislocations becoming more mobile than their glide set counterparts at higher stresses. However, a conclusive answer to the shuffle-glide competition problem requires a systematic

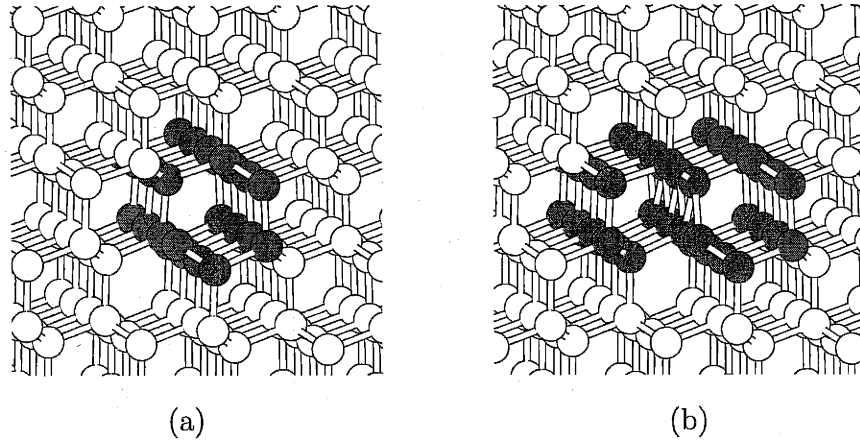


Figure 5-1: Core structures of shuffle set screw dislocation in Si. The high energy core atoms are shown in dark color. (a) Core A resides in a hexagonal ring. (b) Core B resides at the boundary between two hexagonal rings.

atomistic study of shuffle set dislocations [169, 197, 198], as well as on glide set dislocations. In this section, we will present several recent studies on the core and kink energies of shuffle set screw dislocation in Si, as well as direct Molecular Dynamics simulations of its motion. Our results suggest that the mobility of shuffle set dislocations is always higher than that of glide set dislocations, both at low and at high stresses, which is in contradiction with the prediction of previous analysis [22]. A explanation is then proposed to reconcile this finding with the predominance of glide set dislocations in high temperature plastic deformations of Si, by considering the multiplication and dissociation rate of a perfect shuffle set dislocation.

5.1 Core Structure and Peierls Stress

The core properties of shuffle set dislocation in Si was first studied by Arias and Joannopoulos using first principles method [169]. The predicted core structure is shown in Fig. 5-1(a), where the core centers in a hexagonal ring of Si atoms. The core energy was found to be $E_{\text{core}} = 0.56 \pm 0.21 \text{ eV}/\text{\AA}$ at cut-off radius $r_c = b = 3.84 \text{\AA}$. More recent atomistic simulations [198] using Stillinger-Weber (SW) potential model with a much larger number of atoms finds that there are two core structures. SW potential

predicts that the core A, which is similar to the ground state found in first principles calculations, is only metastable, and that in its ground state the core centers at the intersection of two neighboring hexagonal rings, as shown in Fig. 5-1(b). As discussed in Chapter 4.2, using SW potential, we found the core energy of structure B to be $0.526 \pm 0.002 \text{ eV}/\text{\AA}$, at $r_c = b = 3.84 \text{\AA}$. The core energy of structure A is found to be $0.04 \text{ eV}/\text{\AA}$ higher. Because SW potential and first principles calculation gave different predictions on the ground state core structure, it would be worthwhile to study the relative stability and energy difference between the two core structures using more sophisticated potentials, such as EDIP, as well as more first principles calculations. The core energy calculations here used periodic boundary conditions, whose effect were discussed in Chapter 4.2. In the following calculations of Peierls barrier, kink energy and dynamic simulations of dislocation motion, a different boundary condition is applied.

Fig. 5-2(a) shows the simulation cell containing 1920 Si atoms, with cell vectors being $4[11\bar{2}]$ (x , horizontal), $10[111]$ (y , vertical) and $[1\bar{1}0]$ (z , out of plane) respectively. The dislocation Burgers vector is $1/2[1\bar{1}0]$. The cell is periodic along the dislocation line direction z and its glide direction x . Two layers of atoms are fixed at perfect lattice positions at the two ends of the cell in y direction, and a step is created by the dislocation at the bottom layer, as shown in Fig. 5-2(b) and (c). Different from periodic boundary conditions, the simulation cell here contains only one dislocation. Obviously, the fixed layer of atoms present some artificial effect on the dislocation, since the atoms are fixed at perfect lattice positions which is evidently different from the strain field of a dislocation in an infinite medium. On the other hand, this boundary condition makes the system invariant with respect to a translation of the dislocation core, provided the fixed layer of atoms are displaced uniformly to accommodate the plastic strain. The translational invariance property makes this set up suitable for studying the energy barriers and transition paths of dislocation glide.

We will first discuss the Peierls stress τ_P of the shuffle set screw dislocation, which is defined as the minimum stress needed to move a straight dislocation line at zero

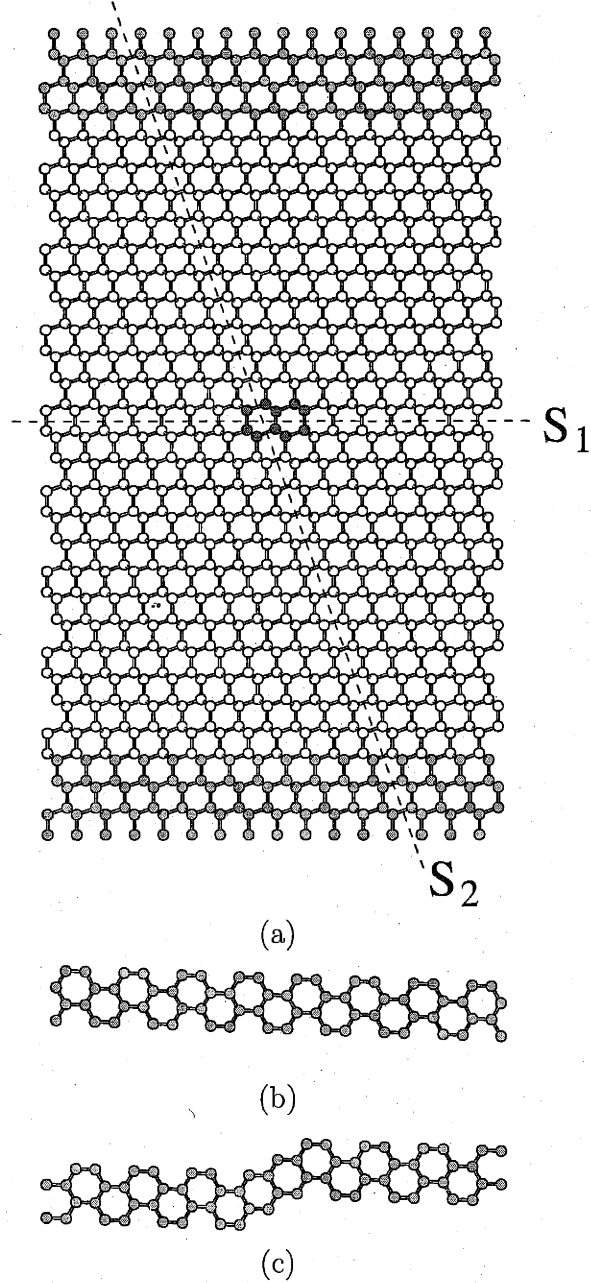


Figure 5-2: Simulation cell containing a single dislocation. (a) Front view. The cell is periodic along x (horizontal) and z (out of the plane) axes. Dislocation line is along z axis with core atoms shown in dark color. Two layers of atoms are set fixed (grey) at the top and bottom of the cell. (b) Top view of the upper fixed atom layer. (c) Bottom view of the lower fixed atom layer. The two possible shuffle set slip planes S_1 and S_2 are shown in dash lines.

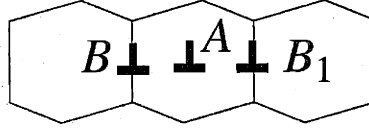


Figure 5-3: Initial (B) final (B_1) and intermediate (A) configurations for Peierls stress calculation.

temperature, against the resistance from the crystal lattice. Previous calculations of Peierls stress of shuffle set screw dislocation in Si using the same (SW) potential yields surprisingly different results. While Ren et al. [197] predicted $\tau_P = 0.086G = 4.0\text{GPa}$, more recent calculations by Koizumi et al. predicted $\tau_P = 0.044G = 2.0\text{GPa}$, with shear modulus $G = 46\text{GPa}$. The fact that two calculations with the same interatomic potential yield drastically different results suggests that there is ambiguity in the simulation set up and boundary effects. Peierls stress is usually determined by recording the Virial stress in the simulation cell where the dislocation starts to move. However, as shown recently by J. Li [199], the Virial stress is not an invariant measure of the dislocation driving force because the boundary condition or other microstructures in the simulation cell usually exert a significant force on the dislocation. Instead, Li [199] showed that the change of Gibbs free energy in a domain containing a single dislocation (without any other defects) after a unit translation of the dislocation is a invariant measure of the dislocation driving force. The Gibbs free energy change include the energy change within the domain (separated from the outside by a “ring” of atoms) plus a work term that equals to the sum of forces on the “ring” atoms times their displacement during the dislocation motion. It was shown that the free energy change defined in this way is invariant with respect to the size of the domain that contains the dislocation, as long as its boundary is $1 \sim 2\text{nm}$ away from the dislocation core.

In this work, we choose entire simulation cell as the domain to measure the dislocation driving force. If we do not allow the boundary atoms to move during the dislocation core translation, the Gibbs energy change is then simply equal to the total energy change of the system. We label the initial configuration as B , which contains

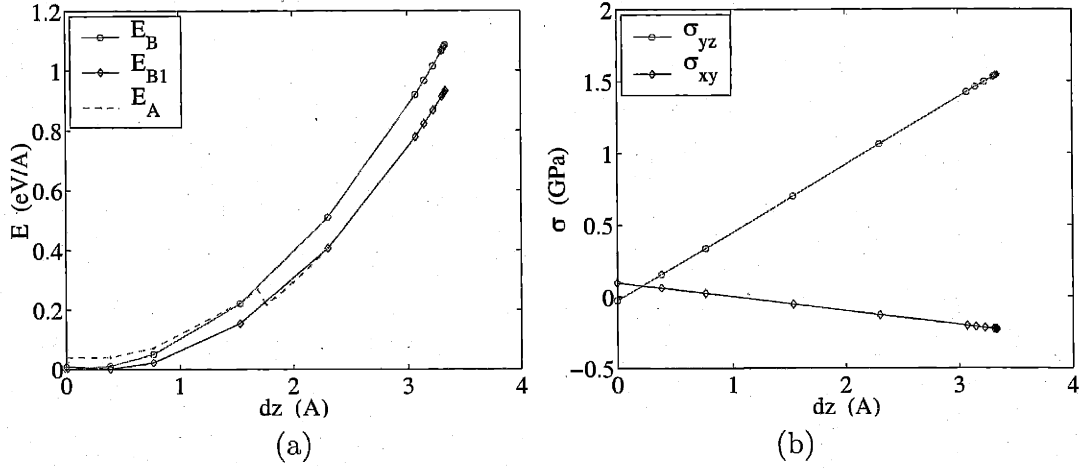


Figure 5-4: Energy change of system B , B_1 and A as a function of dz the displacement of upper layer of fixed atoms in $-z$ direction.

an B-type dislocation core at the cell center, and the final configuration B_1 , where the dislocation core is displaced by one repeat distance to the right. An intermediate configuration is also created, which contains a dislocation of core type A , as illustrated in Fig. 5-3. We then displace the upper layer of fixed atoms in B and B_1 simultaneously in the $-z$ direction by dz . The relaxed energy and internal Virial stress of the two systems are plotted in Fig. 5-4, in which we use the energy of B at $dz = 0$ as a reference. The maximum value of dz in Fig. 5-4 corresponds to the critical condition, at which point a further increase of dz by 0.01\AA will result in a spontaneous motion of dislocation core in B . It is also observed that at $dz = 1.77\text{\AA}$, core A becomes unstable and relaxed to B_1 . This is consistent with the finding the core A becomes unstable at 1GPa stress in the previous study [198].

At the critical displacement $dz = 3.33\text{\AA}$, the energy difference between B and B_1 is $\Delta E_c = E_B - E_{B1} = 0.1529\text{eV/\AA}$, which is an invariant [199] measure of critical driving force to move the dislocation through the lattice. One can convert ΔE_c into the traditionally used Peierls stress through,

$$\tau_P = \frac{\Delta E_c}{bh} = 1.92\text{GPa} , \quad (5.1)$$

where $b = 3.84\text{\AA}$ is the Burgers vector, $h = b\sqrt{3}/2 = 3.33\text{\AA}$ is the lattice repeat distance along the direction of dislocation glide. This result is consistent with that from Koizumi [198] of $\tau_P = 2\text{GPa}$. It is obvious that this stress is not exactly the same as the Virial stress values at the critical condition, which are $\sigma_{yz} = 1.54\text{GPa}$, $\sigma_{xz} = -0.225\text{GPa}$, as shown in Fig. 5-4(b). In fact, for inhomogeneous systems (e.g. in this case having a border), the Virial stress is only an approximate measure of the average stress [200]. Similar calculations for dissociated screw dislocation on the glide set lead to the preliminary prediction of $\tau_P = 5\text{GPa}$ for 30° partials.

5.2 Peierls Energy Barrier

At stresses below the Peierls stress, the dislocation is still possible to move through the lattice at finite temperature, with the help of thermal activation to overcome the so called Peierls energy barrier E_p . In this section, we compute the Peierls barrier E_p at different stresses by identifying the saddle point configuration for dislocation glide at stresses below τ_P .

We used the Nudged-Elastic-Band (NEB) method [201, 202, 203] to determine a minimum energy transition path from state B and state B_1 , which are defined in the previous section. Because it is already known that an intermediate state A exists between B and B_1 at small stress, we search for the transition path between B and A , and between A and B_1 separately under such conditions.

In the NEB method, one relaxes the energy of a series of intermediate states connected by artificial “elastic bands”, corresponding to a low energy transition path between the initial and final states of interest, e.g. B and A . Because the relaxation can easily be “trapped” in a local energy minimum, one should perform simulated annealing technique to search for the global energy minimum of the transition path. For simplicity however, steepest descend relaxation is used in this work, so that the relaxed transition path depends critically on the choice of the initial guess. Nonetheless, the result we obtained can be regarded as an upper bound of the true energy barrier, and it can be a close approximation to the latter when the initial guess is

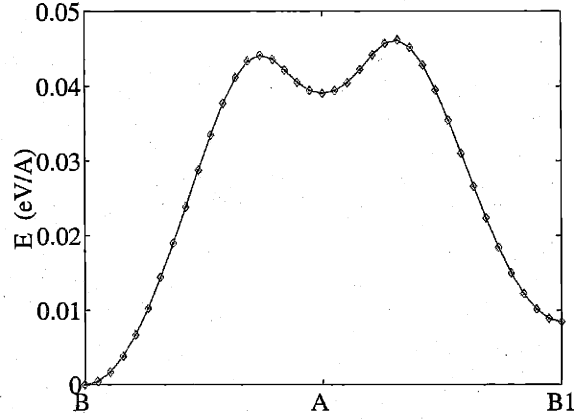


Figure 5-5: Energy variation along the transition path between states B and B_1 via A when the displacement of the top fixed layer is at $dz = 0$. The results with $r_{\text{cut}} = 25\text{\AA}$ (●) and $r_{\text{cut}} = 15\text{\AA}$ (◊) are indistinguishable.

reasonable.

Similar to the approach in [204], only a limited number of degrees of freedom are included in the search for the minimum energy transition path. In this work, only the atoms that are within a cut-off radius r_{cut} around the dislocation core are included. When $r_{\text{cut}} = 25\text{\AA}$, 784 atoms are included, as compared with 1920 atoms in the entire cell. The position of the surrounding atoms in the intermediate states are set to the linear interpolation values between those in the initial (B) and final (B_1) states. Fig. 5-5 shows the energy variation along the relaxed transition path with $r_{\text{cut}} = 25\text{\AA}$ and $r_{\text{cut}} = 15\text{\AA}$ (288 atoms). The results from these two cut-off radius are indistinguishable, indicating that convergence is reached. The energy barrier for core transformation from B to A is about $45\text{meV}/\text{\AA}$, while the barrier for the reverse transformation is about $5\text{meV}/\text{\AA}$. In the following discussions, $r_{\text{cut}} = 25\text{\AA}$ is always used. Fig. 5-6 shows the energy variation along the transition path corresponding to different displacements of boundary layer atoms. At the critical condition of $dz = 3.33\text{\AA}$, the energy barrier vanishes, confirming the calculation of Peierls stress in the previous section. One can also observe that at $dz = 1.53\text{\AA}$, the energy barrier for stabilizing core A becomes very small, and core A is no longer a metastable state at

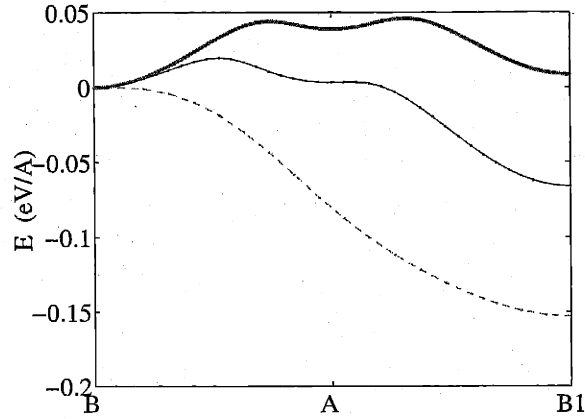


Figure 5-6: Energy variation along the transition path at $dz = 0$ (thick line), $dz = 1.53\text{\AA}$ (thin line) and $dz = 3.33\text{\AA}$ (dash line).

larger strains.

5.3 Kink Structure and Energy

The energy barriers calculated in the previous section are for rigid translation of straight dislocations, with the results expressed in unit of $\text{eV}/\text{\AA}$. In reality, the dislocation does not move as a perfectly straight line, but through a double-kink mechanism. As illustrated in Fig.2-14, a segment of the dislocation moves forward first, creating two kinks, which then moves laterally away from each other. The two energy parameters controlling this process are the kink formation energy E_k and kink migration barrier W_m . One can give a rough estimate of the dislocation velocity based on these two parameters using the Hirth-Lothe model [30] of kink diffusion (for more details see Appendix C). In this section, we calculate E_k and W_m of shuffle set screw dislocation in Si using the SW potential.

Given the small energy difference between core A and B , in principle one would need to consider the possibility of dissociation of kinks into partial kinks [205] connected by a segment of core A , as shown in Fig. 5-7. This would be analogous to the dissociation of glide set dislocations into partial dislocations enclosing an area of

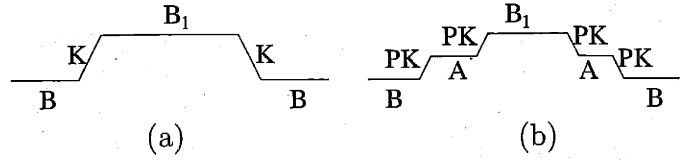


Figure 5-7: (a) Schematic of (full) kinks (K) between shuffle core B and B_1 . (b) Schematic of dissociation of full kinks into partial kinks (PK) connected with a segment of dislocation in core A .

stacking fault. However, for the sake of simplicity, we will ignore such complication in this section and assume that the kinks are not dissociated.

Fig. 5-8 shows the atomic arrangements around a shuffle set screw dislocation with a double-kink. It is created by pasting two atomic configurations with dislocations at B and B_1 states (as defined in the previous section) respectively, followed by static relaxation using the conjugate gradient method. The upper layer of fixed atoms are displaced in $-z$ direction by $b/32$ to accommodate the internal plastic strain caused by double-kinked segment. In Fig. 5-8(a) the two kinks are separated by $20b$, while in (b) and (c), the left kink is displaced with respect to the right kink by $+b$ and $-b$, so that the kinks are separated by $19b$ and $20b$ respectively. According to the kink classification method based on dislocation symmetry [206], the left and right kinks on shuffle set screw dislocation in Si are degenerate, provided that there are no core reconstruction. The kink pair energy is then twice the energy of a single kink, and is calculated by the difference between the relaxed energy of the double-kink configuration in Fig. 5-8(a) and that of the straight dislocation configuration. The result is $2E_k = 1.456 \pm 0.1\text{eV}$, i.e. $E_k = 0.728 \pm 0.05\text{eV}$, with the uncertainty residing in the estimation of the elastic energy difference between the straight and kinked dislocation configurations.

As shown in Fig. 5-8, the kinks on shuffle set screw dislocations in Si are very narrow, similar to those on the partial dislocations on the glide set plane. Since all three configurations in Fig. 5-8 are (meta-) stable, there must exist an energy barrier W_m to kinks to migrate. Again, we calculate W_m using the Nudged-Elastic-Band method. A cut-off radius $r_{\text{cut}} = 15\text{\AA}$ is chosen and only the 968 atoms within r_{cut}

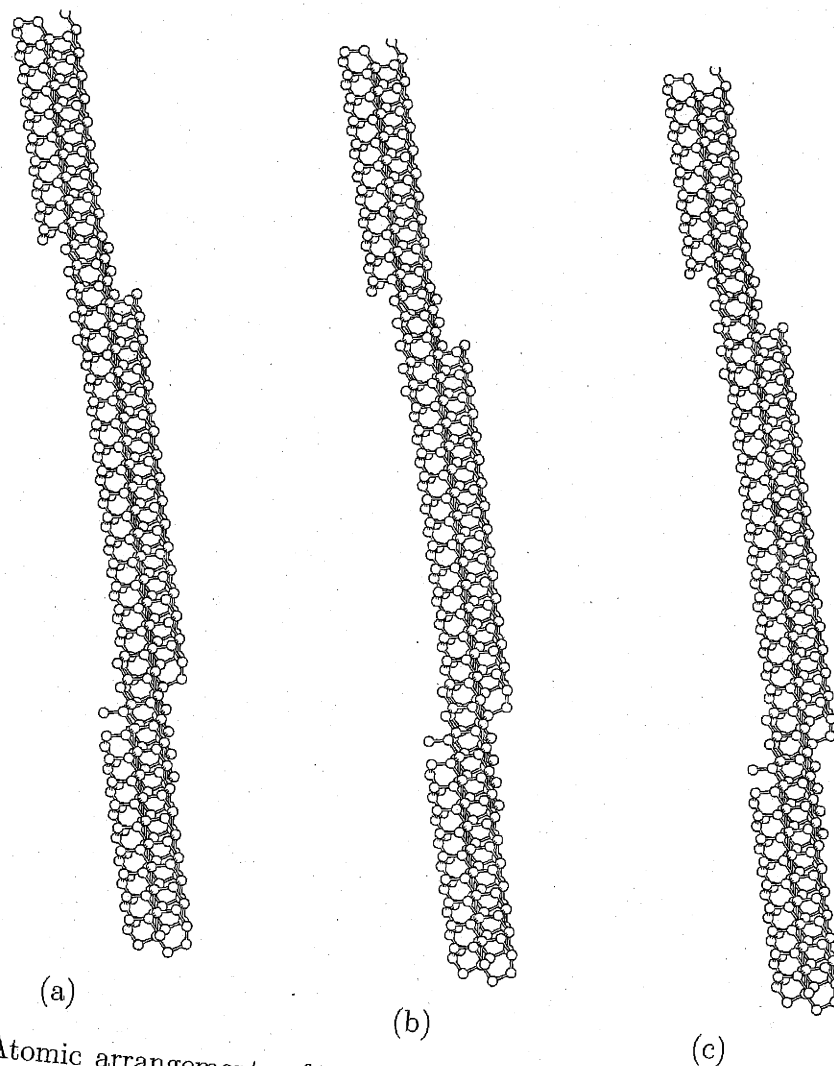


Figure 5-8: Atomic arrangements of a shuffle set screw dislocation core in Si with length $40b$ having a double kink. The two kinks are separated by (a) $20b$, (b) $19b$, (c) $21b$ respectively. Only atoms with local energy larger than -4.52eV are shown, while the energy per atom in perfect Si lattice is -4.62eV .

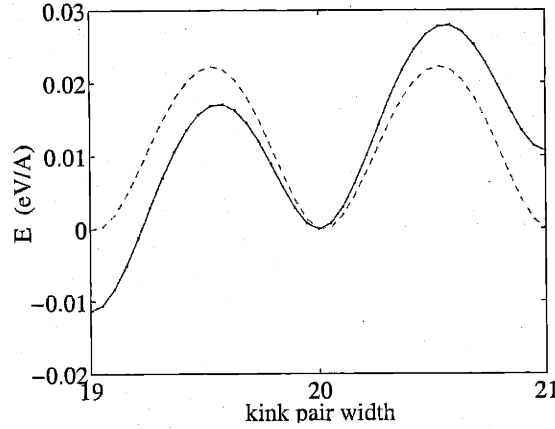


Figure 5-9: Energy variation (solid curve) along the transition path of kink migration. The dashed curve is the result after a linear term corresponding to the residual stress effect is subtracted. The peak of the dashed curve gives $W_m = 0.022\text{eV}$.

around the left kink are included in the path relaxation, while the total number of atoms in this cell is 38400. Fig. 5-9 shows the energy variation along the transition path in changing the kink pair width from $19b$ to $21b$. The overall slope of the energy curve indicates the existence of a residual stress in this simulation setup. If one subtracts off a linear term to counter balance this effect, one obtain the kink migration barrier of $W_m = 0.022 \pm .001\text{eV}$, from the peak of the dashed curve in Fig. 5-9.

As will be discussed in Chapter 7.2.3, the kink energy and migration barrier for 30° partials on the glide set is roughly $E_k = 0.7\text{eV}$ and $W_m = 1.2\text{eV}$. Therefore, the above calculation using SW potential indicates that the kink energy for shuffle and glide set dislocations are about the same, while shuffle set perfect dislocations have a much smaller kink migration energy than glide set partials. This is related to the large atomic spacing across the shuffle set plane, which also gives rise to the much smaller Peierls stress (2GPa) on the shuffle set plane than that on the glide set plane ($\sim 5\text{GPa}$).

The above results do not agree with previous analysis using a quasi-elastic Peierls-Nabarro model [22], where the double-kink nucleation energy barrier for shuffle set screw dislocation at zero stress is around 2.4eV, higher than that for glide set partials

(2.1eV). It was argued that [22] the higher energy barrier for double-kink nucleation is due to the larger Burgers vector of the perfect shuffle dislocation. On the other hand, the Hirth-Lothe model [30] predicts the effective activation energy for double-kink nucleation as $Q_{\text{nuc}} = 2E_k + W_m$ ¹. So that the atomistic calculation here predicts $Q_{\text{nuc}} \approx 1.5\text{eV}$ for perfect shuffle set screw, much smaller than the $Q_{\text{nuc}} \approx 2.6\text{eV}$ for 30° partial on glide set plane. Although the SW potential may not necessarily describe the atomic interactions in the dislocation core region very accurately, the results in this section still cast doubts on the conclusions reached in the previous quasi-elastic analysis. If later calculations using more sophisticated interatomic potential or first-principles methods confirm that W_m for shuffle set dislocations are very small, it would then be reasonably safe to conclude that, shuffle set dislocations always move faster than glide set dislocations, under *all* temperature and stress conditions.

With the above arguments made, we feel obliged to give an explanation on the predominance of glide set dislocations under usual experimental conditions (e.g. without confining pressure), because one would expect the shuffle set dislocations to be dominant if they are much easier to move and hence to operate. This apparent paradox would be resolved, without resorting to a reverse of the relative mobilities of glide and shuffle dislocation, if one notices that by dissociation on the glide plane the dislocation lowers its core energy, thus making perfect shuffle set dislocations thermodynamically unstable. One can envision that all the shuffle set dislocation segments are irreversibly becoming dissociated on the glide set plane. Define the density of shuffle set and glide set dislocations as ρ_s and ρ_g respectively, one can write down the following equation,

$$\dot{\rho}_s = M_s(\tau, v_s)\rho_s - j_{\text{diss}}\rho_s \quad (5.2)$$

$$\dot{\rho}_g = M_g(\tau, v_g)\rho_g + j_{\text{diss}}\rho_s \quad (5.3)$$

$$\dot{\epsilon} = \rho_s v_s b + \rho_g v_g b, \quad (5.4)$$

¹The effective activation energy for the dislocation velocity is the average of Q_{nuc} and W_m , which is $Q = E_k + W_m$. For more details see Appendix C.

where τ is the shear stress and $\dot{\epsilon}$ is the strain rate, v_s and v_g are the velocities of shuffle and glide set dislocations respectively. j_{diss} is the dissociation rate of the shuffle set dislocation. $M_s(\tau, v_s)$ and $M_g(\tau, v_g)$ are the multiplication rates for shuffle and glide set dislocations, and one may use $M_s(\tau, v_s) = C\tau v_s$ and $M_g(\tau, v_g) = C\tau v_g$, with a constant C , following Alexander [8]. In this picture, whether or not the shuffle set dislocation will become the dominant carrier of the plastic deformation depends critically on the relative magnitude of the multiplication rate $M_s(\tau, v_s)$ and dissociation rate j_{diss} .

The situation would become even more unfavorable for shuffle set dislocations if one consider the situation where only a fraction of the dislocation population are moving at any instant of time, while the stresses on other dislocations are not large enough to break them away from their interactions with surrounding defects. For glide set dislocations, one would expect the remaining dislocations to become mobile at higher stresses (strain hardening). But for shuffle set dislocations, they would be irreversibly converted into dissociated glide set dislocations during the waiting period. Although a quantitative model incorporating these effects are still lacking so far, we believe that for a conclusive explanation on which type of dislocation is dominant, one has to account for the relative magnitude of multiplication and annihilation rate of shuffle set dislocations. In this sense, it is inherently a multi-dislocation problem and could not be explained by the mobility change of individual dislocations.

Therefore the shuffle-glide controversy still remains open. The situation would look even more complicated than what has been discussed above, if in addition to the competition between perfect shuffle and dissociated glide dislocations, one consider partial dislocations on the shuffle set plane — a glide set partial would climb to the shuffle set plane by absorbing a row of vacancies or interstitials. A recent study by Justo et al. [37] on the free energy of vacancies in the core of 30° partial has showed that the vacancy concentration in the core is very low at thermal equilibrium. However, the possibility of shuffle set partials has not been ruled out yet because the dislocation processes during deformation are by definition under the condition that is far away from equilibrium.

5.4 Dislocation Motion by Molecular Dynamics

Similar to what we discussed in the previous sections, current works on atomistic studies of dislocations have been mainly focused on static relaxations, in trying to determine zero temperature structure and ground state energies, as well as transition energy barriers for dislocations and kinks. In comparison, direct modeling of dislocation motion at finite temperature by Molecular Dynamics (MD) has not, unfortunately, been applied extensively. The importance of finite temperature dynamical simulations, however, can hardly be overstated. Logically, one should perform dynamical simulations *first*, and after having identified the controlling atomic mechanisms of the process, *then* use refined static relaxation method to pinpoint the key energy parameters. However, it seems to be common practice to initiate static relaxation calculations to determine energy parameters for postulated atomic mechanisms. It is part of the purpose of this Thesis to provide a reminder that in the end, the validity or relevance of such static calculations should be double-checked by either putting them into a mechanistic mesoscopic model (e.g. Chapter 7, 8) that can connect with experiments, or, by comparing zero temperature results with direct dynamical simulations. Only after the static and dynamic studies start to form a coherent theory can one be confident to claim a complete understanding of the atomic mechanisms of the process of interest.

Comparing with static relaxation methods, the main limitations of conventional MD method is on the time scale of the processes that it can follow. Typical physical times in MD simulations are between 10^{-12} s and 10^{-9} s, leaving direct simulations of the so called “rare events” happening on the scale of $10^{-3} \sim 1$ s out of the question. On the other hand, MD simulations on dislocation mobility problems are usually hindered by other technical difficulties that are definitely not insurmountable, such as the setup of boundary conditions and the automatic identification of dislocations during the simulation. In this section, we discuss a set of MD simulations on the motion of shuffle set screw dislocations in Si, in trying to demonstrate the capability of MD simulations on uncovering atomistic details and bringing new understandings

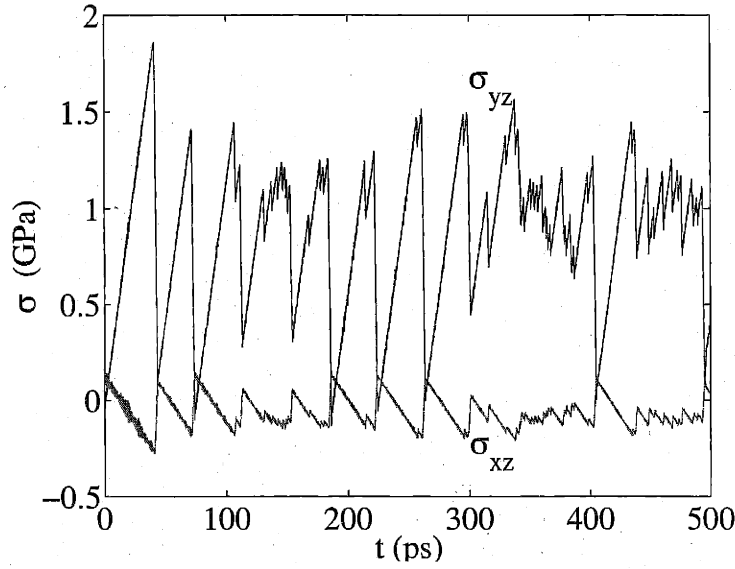


Figure 5-10: Variation of the internal stress during MD simulations of shuffle set screw dislocation motion at 10K under constant shear strain rate (see text).

that are not apparent from zero temperature results alone.

The MD simulations in this section used the same atomic cell and boundary conditions as shown in Fig. 5-2, consisting of 1920 atoms. The Newton's equation of motion for the atoms are integrated by Gear's 6th order predictor-corrector method [131], using a timestep of 5×10^{-16} s. The simulation starts with 1000 equilibration steps where the velocities are rescaled to maintain the desired temperature. After that, the temperature is controlled by the Nose-Hoover thermostat [207, 132]. The two layers of fixed atoms are displaced with respect to each other in z direction at each timestep with a speed of $0.02b/\text{ps}$. Under this constant shear strain rate loading condition, the average dislocation velocity is maintained as $0.32h_s/\text{ps} \approx 106\text{m/s}$, where $h_s = b\sqrt{3}/2 = 3.33\text{\AA}$ is the lattice repeat distance along the glide direction of the screw dislocation.

Following Chang [208], the dislocation core position is identified automatically during the simulation in the following way. First, a time average (over 100 timesteps in this case) of the energy for each atom is calculated and the atom with the largest energy is selected. The dislocation core is identified as the average positions of atoms

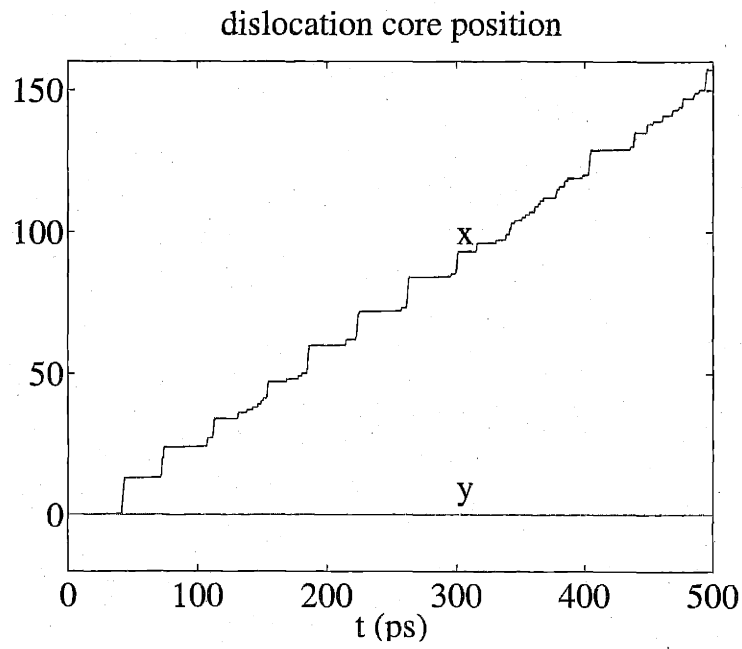


Figure 5-11: Instantaneous dislocation position during MD simulations under the same condition as Fig. 5-10.

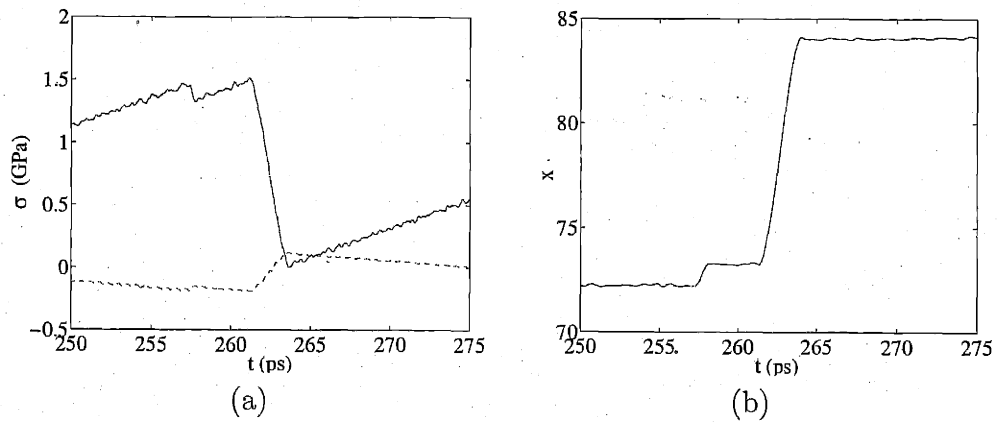


Figure 5-12: (a) Magnified view of stress variation in Fig. 5-10. (b) Magnified view of dislocation displacement along x in Fig. 5-11.

within a cut-off radius (4\AA in this case), weighted by their time averaged energies.

Fig.5-10 shows the internal stress variation during the simulation. σ_{yz} exerts force on the dislocation in the x direction, and is called glide stress, while σ_{xz} exerts force in the $-y$ direction and is called non-glide stress. Although only glide strain is applied, non-glide stress component arises due to the elastic anisotropy of the crystal. As shown in Fig.5-11, the dislocation moves by pure glide. Here the displacement in x direction is plotted in unit of h_s , the lattice repeat distance along x , and that in y direction is plotted in unit of $h_y = [111]/3$, the minimum separation between equivalent shuffle set slip planes. The dislocation glide seems to be highly inhomogeneous in time. As shown in Fig.5-12, the dislocation suddenly moves over $10h_s$ during a period of 2.4ps, and relieves stress σ_{yz} from 1.5GPa to 0. The instantaneous dislocation velocity during this period is then 1400m/s, comparable with the sound speed 2200m/s. The fact that the dislocation can stay mobile till the glide stress drops to essentially zero is a very surprising behavior, especially in Si where the lattice resistance is expected to be large. This is different from the screw dislocations in Mo that will be discussed in the next Chapter, where the glide stress needs to be maintained close to the Peierls stress (also about 2GPa) to keep the dislocation moving. The origin for this exceptionally high mobility of shuffle set dislocation in Si (once the motion starts) could be either due to a different core structure for a moving dislocation, or due to the extremely low radiation loss when the dislocation overcomes a Peierls barrier. Further study to identify the underlying mechanism is necessary. At this point, it is interesting to note that a direct Molecular Dynamics simulation on a single dislocation can give rise to pronounced plasticity instabilities in a constant strain rate deformation, which resembles the Portevin-Le Chatelier effect in real experiments [209, 210].

Fig. 5-13 and 5-14 show the internal stress variation and the instantaneous dislocation position during the simulation at 300K. The dislocation starts to move at a much smaller stress, below 1GPa, although the internal stress occasionally exceeds 1.5GPa. Sudden dislocation jumps over large distances are still observed, while jumps over small distances are more frequent than in the case of 10K. The major difference of

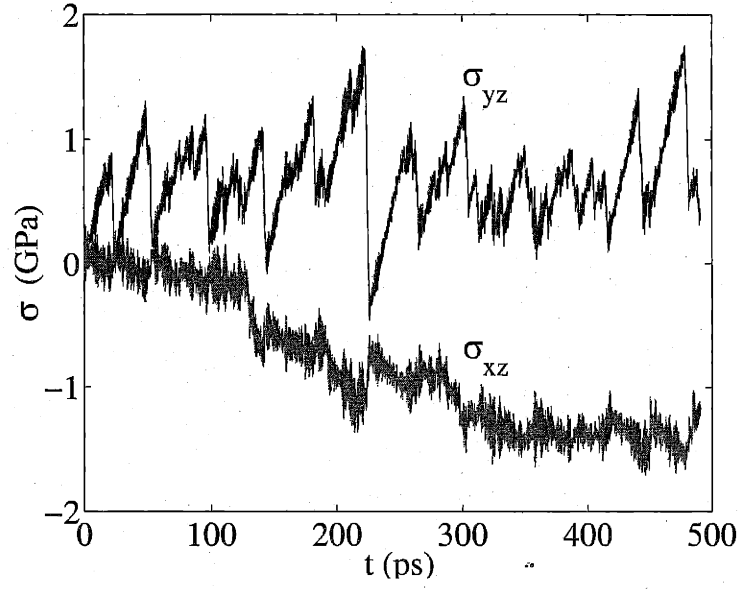


Figure 5-13: Variation of the internal stress during MD simulations of shuffle set screw dislocation motion at 300K under constant shear strain rate $\dot{\gamma}_{yz} = 4.08 \times 10^{-4} \text{ps}^{-1}$.

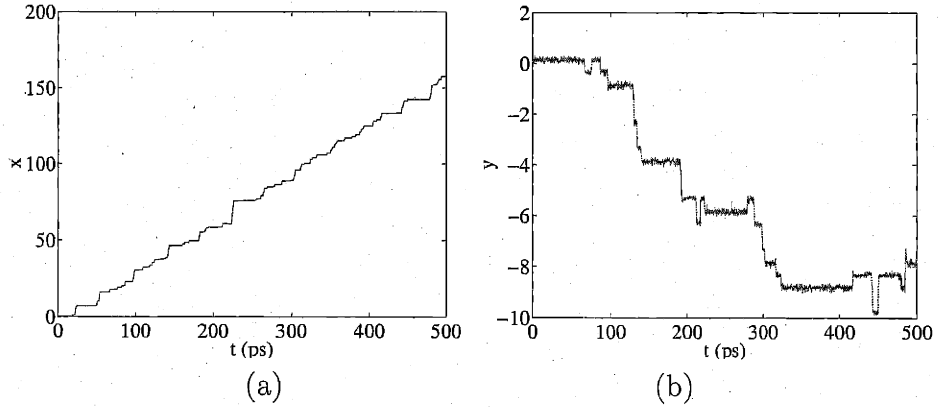


Figure 5-14: Instantaneous dislocation position during MD simulations under the same condition as Fig. 5-13.

dislocation motion at this temperature from that in 10K is that it also cross slips in the $-y$ direction. In response, the boundary atoms automatically generates a back stress σ_{xz} , exerting a force on the dislocation in the $+y$ direction, trying to suppress further cross slip. At the end of the simulation, the dislocation has cross slipped for 9 planes below its original plane.

Fig. 5-15 and 5-16 show the instantaneous atomic positions at 150ps and 400ps during the MD simulation. It is clear that the dislocation has cross slipped for 4 and 9 planes downwards respectively. Slip traces are also created in the crystal where the dislocation has passed for multiple times through the simulation cell. The reason that cross slip only occurs downwards is due to the slip geometry of Si. As illustrated in Fig.5-2(a), there are only two types of shuffle set plane, S_1 and S_2 , on which the dislocation can glide. When the dislocation moves to the right, it is likely to cross slip downwards. One would expect that when the loading stress is reversed, the dislocation would move to the left and is likely to cross slip upwards at high temperatures. We are performing more MD simulations to test this claim.

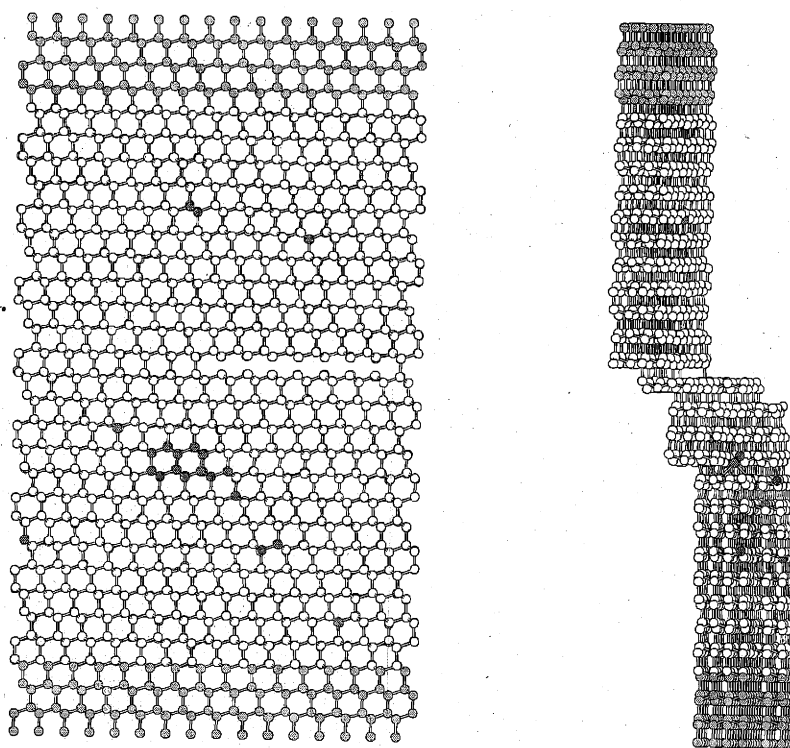


Figure 5-15: Snapshot at 150ps of MD simulation at 300K (see text). Atoms with instantaneous energy higher than -4.5eV are plotted dark. Slip steps are created where the dislocation has pass through the cell for multiple times. (a) Front view. (b) Side view.

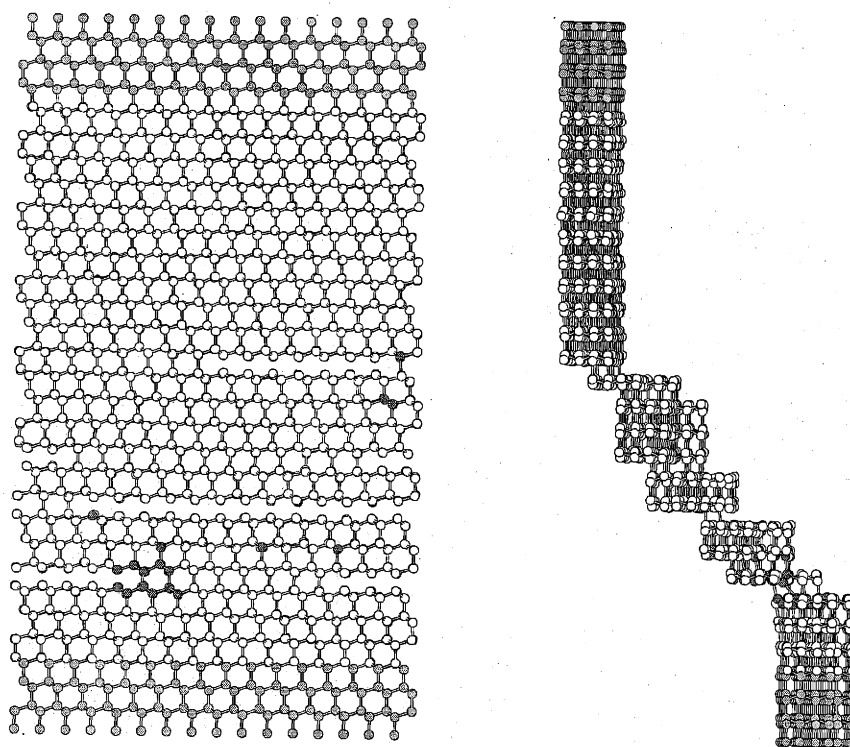


Figure 5-16: Snapshot at 400ps of MD simulation at 300K (see Fig. 5-15). (a) Front view. (b) Side view.

Chapter 6

Atomistic Study of Dislocations in Mo

This Chapter presents atomistic studies of screw, edge and mixed 71° dislocations in BCC metal Mo, using the Finnis-Sinclair (FS) potential. It is found that the Peierls barrier varies significantly for these dislocations, and that it seems to be closely related with the dislocation core structure. The compactness of mixed 71° dislocation core results in much higher Peierls stress than that of edge dislocation. The non-planar shape screw dislocation core leads to a further increase of the Peierls stress. Direct Molecular Dynamics (MD) simulations are carried out to study the glide and cross slip of straight screw dislocation under high stresses at two different temperatures.

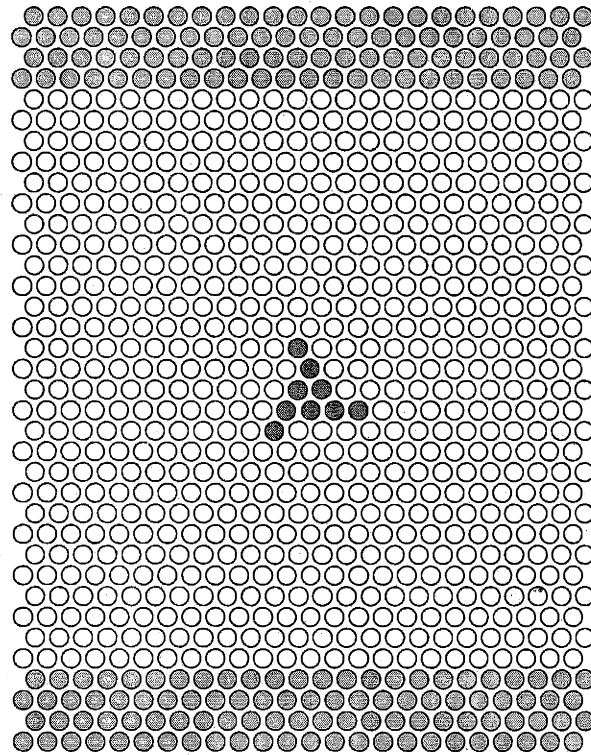
6.1 Core Structure

Fig. 6-1 shows the atomistic simulation cell containing a single screw dislocation under periodic boundary conditions (pbc) in two directions (x, z) and fixed boundary in y direction, similar to the one used in the previous Chapter. The cell dimensions are $8[11\bar{2}]$ along x , $18[1\bar{1}0]$ along y and $5[111]/2$ along z , containing 4320 Mo atoms. The dislocation Burgers vector is $\vec{b} = [111]/2$. A step of size b presences in the crystal below the dislocation, as can be seen in bottom view of the lower fixed layer in Fig. 6-1(c). Atoms with energy higher than -6.72eV are plotted in dark color, to indicate

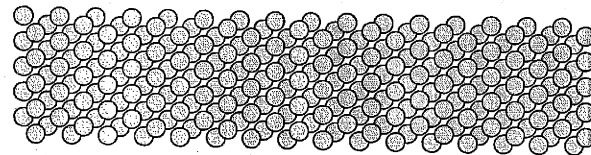
the region of the dislocation core. In comparison, the energy per atom in perfect lattice is -6.82eV . The screw dislocation is observed to undergo spontaneous core reconstruction, leading to two energetically degenerate but topologically distinct core structure, each having only three fold symmetry. The two possible core structures are shown in detail in Fig.6-2 and Fig.6-3, and are defined to have polarity $+1$ and -1 respectively. Obviously, the screw dislocation core is non-planar, which leads to the exceptionally high Peierls barrier as compared with other dislocations.

Fig. 6-4 shows the simulation cell containing a single mixed dislocation, with cell dimensions being $10[121]$ along x , $24[\bar{1}01]$ along y and $5[1\bar{1}1]/2$ along z , containing 7080 atoms. The dislocation Burgers vector is $\vec{b} = [111]/2$. Since its line direction is at 71° degree with respect to the Burgers vector, it is called mixed 71° degree dislocation. Mixed 71° and screw dislocations are the only two dislocations on the (110) (y) slip plane whose line direction lies along the close packed $\langle 111 \rangle$ direction. Because the Burgers vector has edge component, atoms are removed in a half plane below the dislocation, so that the upper and lower fixed layer have different number of atoms. As shown in Fig.6-5, the core structure of mixed 71° dislocation is planar, and has a well defined center, where the two layers of atoms (above and below the glide plane) are perfectly aligned.

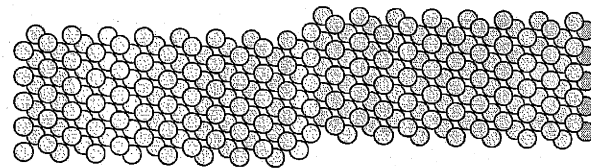
Fig. 6-6 shows the simulation cell containing a single edge dislocation. In this case, the cell has length $20[111]/2$ along x , $24[\bar{1}01]$ along y and $3[1\bar{2}1]$ along z , containing 8424 atoms. The dislocation Burgers vector is $\vec{b} = [111]/2$, along x direction. Because the Burgers vector is purely edge, more atoms are removed in a half plane below the dislocation. The crystal below the dislocation only 19 repeat distances along x direction. As shown in Fig.6-7, the edge dislocation core is also planar. In contrast to that of mixed 71° dislocation, the edge core does not seem to have a well defined center region, i.e. its Burgers vector seems to be more diffused. As will be discussed in the next section, this leads to an exceptionally low Peierls barrier for edge dislocation.



(a)



(b)



(c)

Figure 6-1: Simulation cell containing a single screw dislocation. (a) Front view. The cell is periodic along x (horizontal) and z (out of the plane) axes. Dislocation line is along z axis. Fixed atoms are plotted in grey. Atoms with energy higher than -6.72eV are shown in dark color. (b) Top view of the upper fixed atom layer. (c) Bottom view of the lower fixed atom layer.

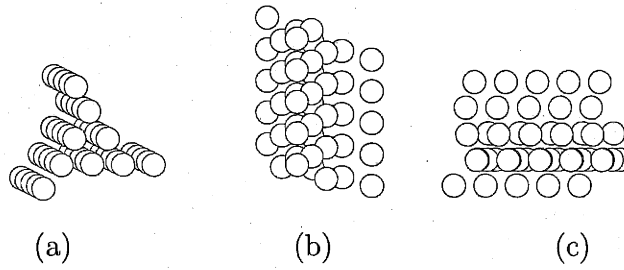


Figure 6-2: Core structure of screw dislocation with polarity +1. (a) 3D view. (b) Top view. (c) Side View.

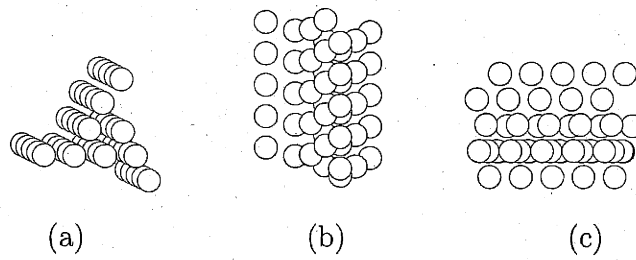
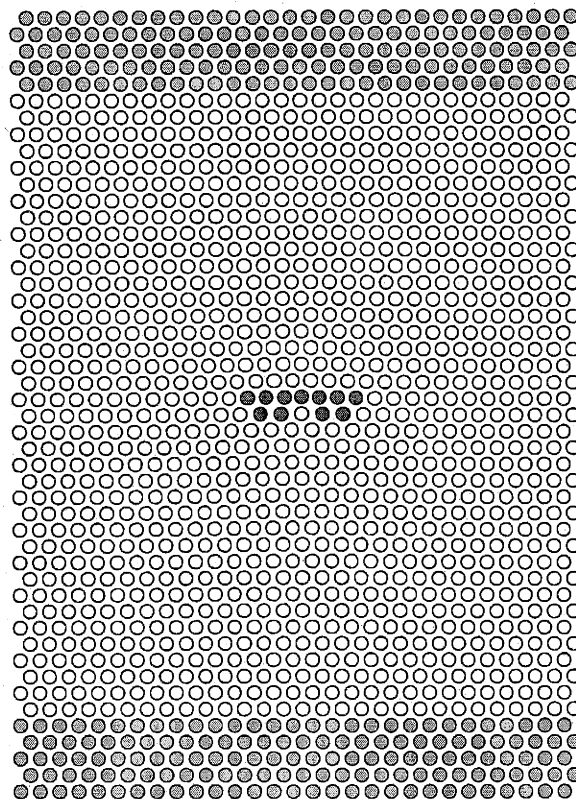
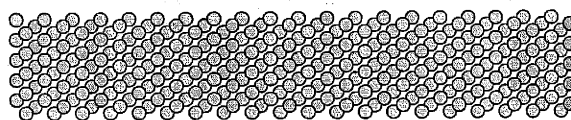


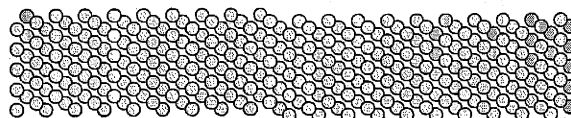
Figure 6-3: Core structure of screw dislocation with polarity -1. (a) 3D view. (b) Top view. (c) Side View.



(a)

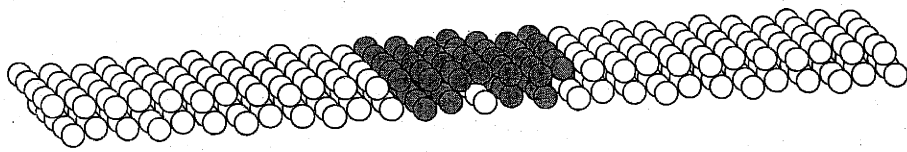


(b)

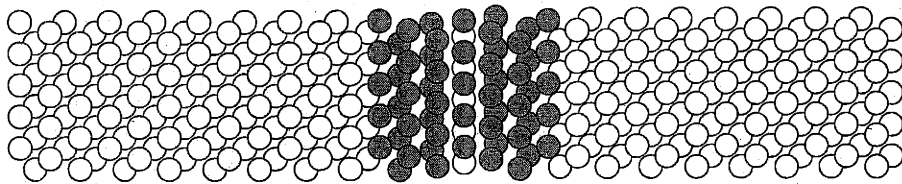


(c)

Figure 6-4: Simulation cell containing a single mixed 71° dislocation. (a) Front view. Dislocation line is along z axis. Atoms with energy higher than -6.72eV are shown in dark color. (b) Top view. (c) Bottom view.

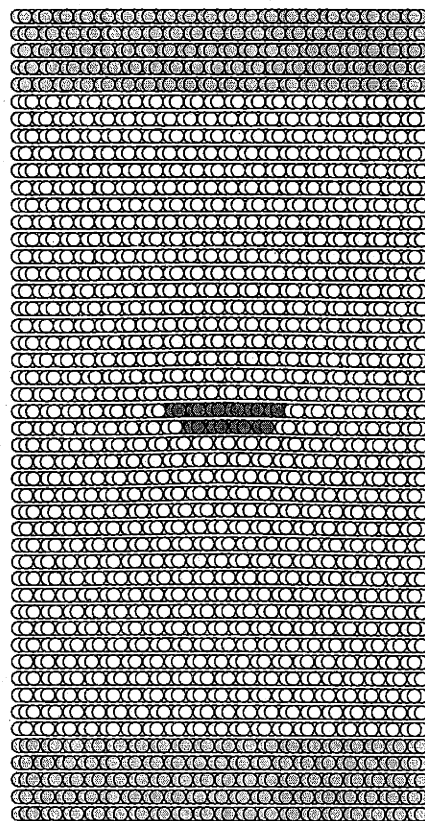


(a)

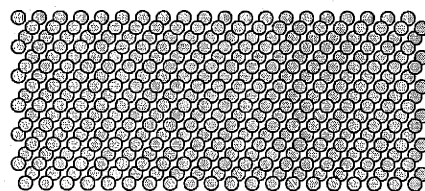


(b)

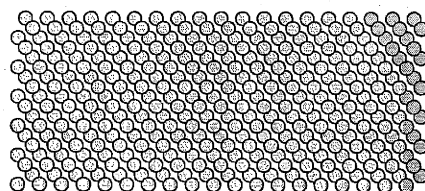
Figure 6-5: Core structure of mixed 71° dislocation. (a) 3D view. (b) Top view.



(a)

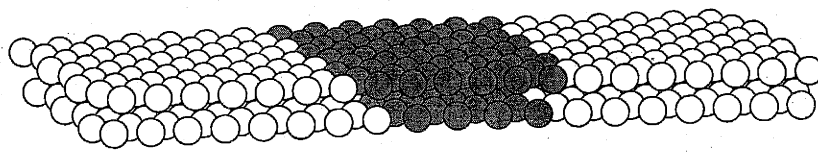


(b)

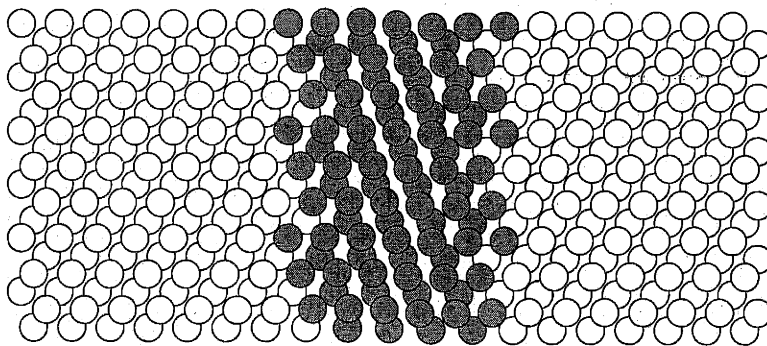


(c)

Figure 6-6: Simulation cell containing a single edge dislocation. (a) Front view. Dislocation line is along z axis. Atoms with energy higher than -6.72eV are shown in dark color. (b) Top view. (c) Bottom view.



(a)



(b)

Figure 6-7: Core structure of an edge dislocation. (a) 3D view. (b) Top view.

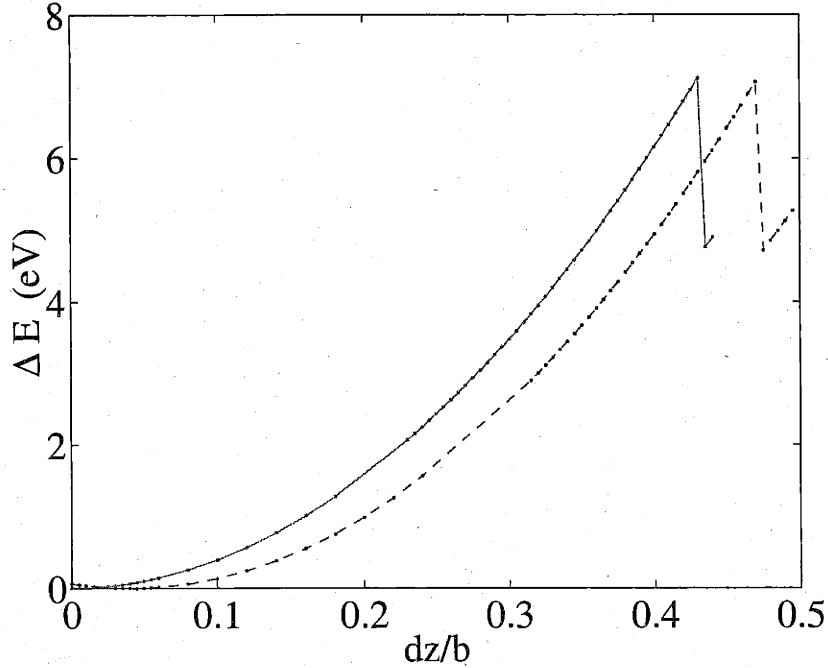


Figure 6-8: Total energy variation ΔE of the relaxed structure containing a screw dislocation (Fig. 6-1) as a function of the displacement dz of the upper layer of fixed atoms. The initial dislocation positions are at the origin (solid line), and (b) one repeat distance $h_s = 2\sqrt{2}b/3$ to the right (dash line) respectively.

6.2 Peierls Stress

In this section, we present results on the Peierls stress for the above three types of dislocation, using similar approaches as in the previous Chapter. Specifically, the relative displacement $d\vec{l} = (dx, 0, dz)$ between the upper and lower layer of fixed atoms is changed in small steps along the Burgers vector, until dislocation motion is observed. The Peierls stress (and sometimes the Peierls energy barrier) is obtained by monitoring the relaxed total energy of the cell as a function of $d\vec{l}$.

In the case of screw dislocation, the Burgers vector is along z direction, i.e. $d\vec{l} = dz$. Fig. 6-8 shows the variation of the total energy after relaxation at each dz . The solid line, defined as E_0 , represents the case where the dislocation is initially at origin. The dash line, defined as E_1 , correspond to the dislocation initially at one repeat distance $h_s = 2\sqrt{2}b/3 = 2.57\text{\AA}$ to the right. At the critical displacement of

$dz \approx 0.43b$, the dislocation in state E_0 becomes unstable. It moves forward in x direction by $2h_s$ (as checked by the atomic structures) and suddenly relieves the total energy.¹ At even larger dz , the dislocations in state E_1 starts to move as well. The system is translationally invariant with respect to the initial dislocation position, as can be seen from the same shape of E_0 and E_1 curves. The measure of the critical driving force is defined [199] as the maximum difference between E_0 and E_1 , and is $\Delta E_c = 1.30 \pm 0.01\text{eV}$. This can be converted to the usually used Peierls stress as

$$\tau_p(\text{screw}) = \Delta E_c / (bh_s L_z) = 2.18 \pm 0.02\text{GPa}, \quad (6.1)$$

where L_z is the cell length in the z direction. This is smaller than the previous result [162] using MGPT potential, which gives $\tau_p(\text{screw}) = 3.4\text{GPa}$. The average Virial stress in the cell can be estimated from the derivative of ΔE against dz , i.e. $\tau = d(\Delta E)/dz/L_x/L_z$, where L_x is the cell length in the x direction. Near the critical region, the critical average stress is found to be $\tau_c = 2.31 \pm 0.02\text{GPa}$, within 6% of the Peierls stress τ_p from the energy criteria.

Since the microstructure of BCC metals at low temperature mainly consists of screw dislocations, the Peierls stress of screw computed from atomistic simulations is usually compared with the experimentally measured yield stress, or critical resolved shear stress (CRSS) at near zero temperature. From Chapter 2, the CRSS for Mo at the zero temperature limit is 750MPa , which is about 3 times smaller than the $\tau_p = 2.18\text{GPa}$ from the above calculation. This factor of 3 difference between atomistic and experiments results are common for most BCC metals, whose origin is not clear so far. It was argued that the experimentally observed CRSS could be the result of the collective behavior of an ensemble of dislocations, and hence may not correspond to the critical stress to move a single dislocation [211, 70].

Similar results for mixed 71° dislocation are shown in Fig. 6-9. The dislocation is initially at the origin. When a critical displacement dl is reached, it suddenly

¹The fact that the dislocation moves forward by two repeat distances whenever the system becomes unstable is related with the system size and the relaxation algorithm; it is not an intrinsic property of the dislocation.

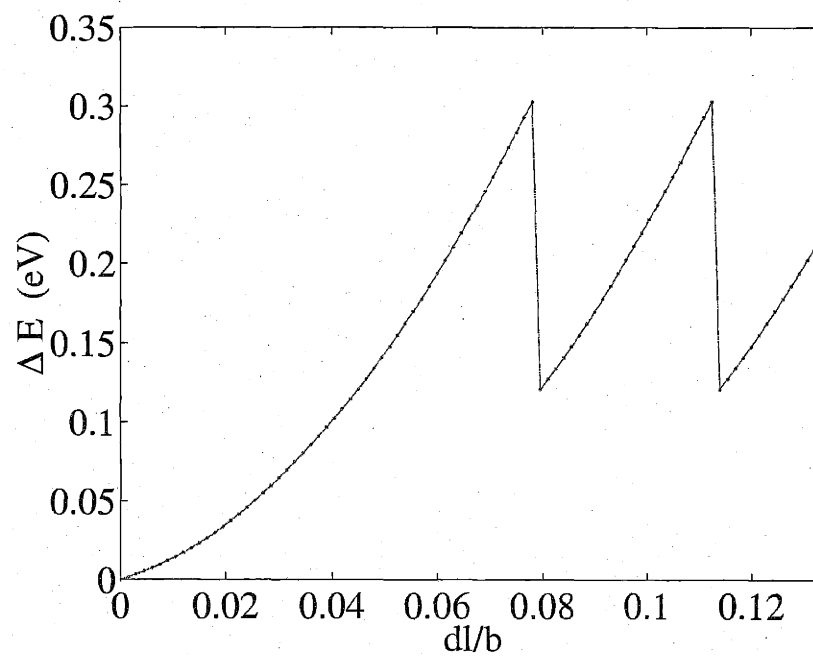


Figure 6-9: Total energy variation ΔE of the relaxed structure containing a mixed 71° dislocation (Fig. 6-4) as a function of the displacement dl of the upper layer of fixed atoms.

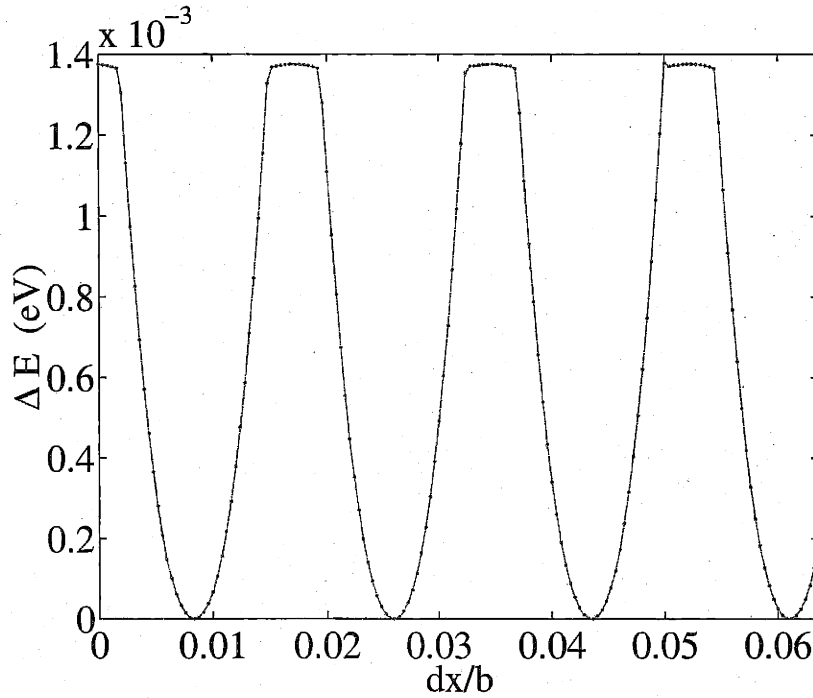


Figure 6-10: Total energy variation ΔE of the relaxed structure containing an edge dislocation (Fig. 6-6) as a function of the displacement dz of the upper layer of fixed atoms.

moves to the next lattice site and relieves the total energy. By checking the atomic configurations, it is found that the dislocation moves by exactly one lattice repeat distance $h_m = h_s$. The critical energy can then be deduced from the single curve as the magnitude of the energy drop at the discontinuity, $\Delta E_c = 0.19 \pm 0.003 \text{ eV}$. The corresponding Peierls stress is then

$$\tau_p(71^\circ) = \Delta E_c / (bh_m L_z) = 320 \pm 5 \text{ MPa}, \quad (6.2)$$

The average stress of the cell at the critical condition is estimated to be $\tau_c = d(\Delta E)/dl/L_x/L_z = 375 \pm 5 \text{ MPa}$, which is within 20% of the estimation based on the energy criteria.

In the above two calculations, the screw and mixed 71° dislocations behave similarly. However, the results on edge dislocation seems to be qualitatively different.

As shown in Fig. 6-10, the total energy changes smoothly from one minimum to another, without any discontinuity or instability. By analyzing the atomic configurations, it is found that each of the energy minimum corresponds to a equilibrium position of the dislocation separating from neighboring ones by exactly the lattice repeat distance $h_e = b/3$ in x direction. The appearance of the smooth transition is the result of the exceedingly small lattice resistance to the dislocation motion. The lattice energy barrier is estimated to be the largest energy increase in Fig. 6-10, i.e. $E_p(\text{edge}) = 1.38 \times 10^{-3} \text{eV}$. The Peierls stress is estimated from the maximum average stress, i.e.

$$\tau_p(\text{edge}) = \Delta E_c / (bh_e L_z) = 20 \pm 4 \text{MPa}. \quad (6.3)$$

The choice of error bar is base on the previous estimation (on 71° dislocation) that the maximum Virial stress could be 20% off the “true” value of the Peierls stress. It should be emphasized that the determination of Peierls stress for edge dislocation is beyond the accuracy limit of empirical potential models, because the total energy variation is below 2meV as shown in Fig. 6-10.

The edge dislocation Peierls stress estimated here is considerably smaller than the previous prediction [163] of $\tau_p(\text{edge}) = 0.003 \sim 0.005\mu = 400 \sim 700 \text{MPa}$, if one takes shear modulus $\mu = 137 \text{GPa}$ [162]. If the present calculation is correct, it is then unnecessary to rely on kink mechanism to explain the large mobility difference between edge and screw dislocations, as did in [163]. As the loading stress can easily exceed the Peierls stress, kinks may not even be stable on edge dislocations, which would move more like a smooth spring than a series of kinked segments. The large “Peierls stress” in the previous calculation is very likely to be contaminated by artificial image stresses from the boundary, which can easily be on the order of 100MPa. In the present calculation, such artifacts do not exist, because the boundary conditions are manifestly translational invariant on the dislocation glide plane. As a result, we are able to capture the periodic energy variation due to the lattice resistance on the scale of 0.001eV.

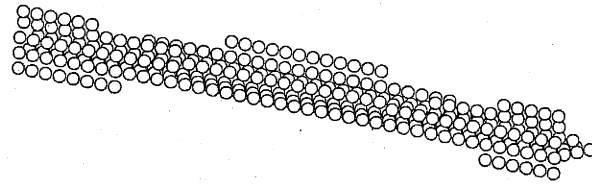
6.3 Kink on Screw Dislocation

Due to the high Peierls stress of screw dislocations, their motion under normal stress conditions is through the double-kink mechanism. The activation energies for double-kink nucleation at different stress are then the material parameter that controls the rate of plastic flow. Recently, such energy barriers are calculated [70] by the Nudged-Elastic-Band method using the Embedded Atom Method (EAM) potential for Fe. In this section, we present the results of a less ambitious calculation, on the formation energy E_{kp} of a widely separated kink pair and the energy barrier W_m for the kink pair expansion. The dislocation velocity can be estimated once these two energy parameters are known, based on the Hirth-Lothe [30] model of kink diffusion (see Appendix C for details).

Fig. 6-11 shows the atomic core structure of the screw dislocation with a double kink. Only the atoms with local energy exceeding -6.72eV are shown. This configuration is created by pasting together two configurations with offset dislocation positions (by one lattice repeat distance h_s), followed by energy minimization. The upper layer of the fixed atoms are displaced by $b/48$ in z direction to accommodate the plastic strain due to the double-kink. Previous calculations such as [70] have shown that double-kink nucleation is the easiest when it is accompanied by a change of polarity from $p = +1$ to $p = -1$. The configuration created here corresponds to this case. It is obvious that the left and the right kink are topologically different, which can be seen most easily in Fig. 6-11(d). This is because the 180° rotation around the $[111]$ axis is not a symmetry operation in the BCC host lattice [206]. The two kinks are also different because they are combined with different core reconstruction defects (RD) due to the change of polarity across the kink. The kink pair energy is estimated as the excess energy of the kinked structure with respect to that of the straight dislocation, which is

$$E_{kp} = 1.63\text{eV} . \quad (6.4)$$

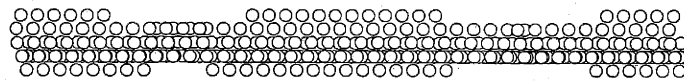
This is somewhat smaller than the previous prediction [162] using MGPT potential,



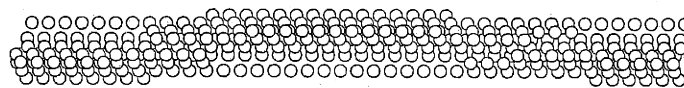
(a)



(b)



(c)



(d)

Figure 6-11: Core structure of a screw dislocation containing a double-kink. (a) 3D view. (b) Front view. (c) Side view. (d) Top view.

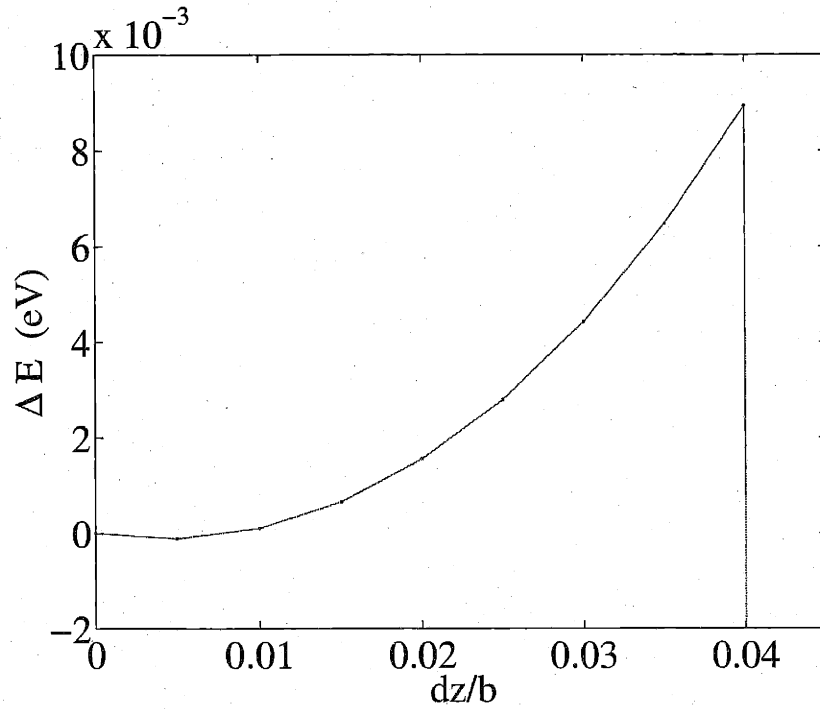


Figure 6-12: Total energy variation ΔE of the relaxed structure containing a double-kinked screw dislocation (Fig. 6-11) as a function of the displacement dz of the upper layer of fixed atoms.

which gives $E_{kp} = 2\text{eV}$. Recalling the comparison on Peierls stress calculations in the previous section, it is reasonable to say that the MGPT potential predicts a “stiffer” dislocation core than FS potential, most probably due to the explicit angular term for directional bonding in MGPT.

The secondary Peierls barrier, i.e. the energy barrier to move kinks, are calculated by displacing the upper layer of the fixed atoms in small steps and recording the relaxed energy. As shown in Fig.6-12, the structure becomes unstable (due to the mutual attraction between the two kinks) at $dz > 0.04b$. The maximum energy increase is taken as an estimation of the kink migration barrier, i.e. $W_m \approx 0.009\text{eV}$. The secondary Peierls stress, i.e. the critical stress for kink migration is estimated from the maximum Virial stress as $\tau_m \approx 27\text{MPa}$. Thus the Peierls stress for kink migration on screw dislocation is on the same scale as that for the edge dislocation,

both being very small.

6.4 Dislocation Motion by Molecular Dynamics

In this section, we explore the dynamical behavior of a screw dislocation under high stress at finite temperature. For simplicity, the simulation cell is rather thin (5b) along the dislocation line, so that kink processes are artificially suppressed and the system is essentially 2-dimensional. The same simulation cell as in Fig. 6-1 is used and the two boundary layers are displaced with each other at every timestep with a speed of $0.01b/\text{ps}$ in z direction. Under this constant shear strain rate loading, the average dislocation velocity is maintained at $0.24h_s/\text{ps} \approx 62\text{m/s}$. The integrator, timestep, equilibration and temperature control methods are the same as in the previous Chapter.

Fig. 6-13 shows the internal stress variation during the simulation at 10K. The glide stress σ_{yz} is observed to oscillate violently around the Peierls stress (2GPa). Even though only glide strain is applied, non-glide stress σ_{xz} , which exerts forces on the dislocation in the y direction was maintained at a small negative value due to elastic anisotropy. Fig. 6-14 shows the instantaneous dislocation core position in x and y direction as a function of time, in units of the h_s and h_y respectively, where $h_s = [11\bar{2}]/3$ is the lattice repeat distance along the (screw) dislocation glide direction and $h_y = [1\bar{1}0]/2$ is the minimum separation between equivalent $(1\bar{1}0)$ slip planes.

The dislocation starts to glide in x direction after the stress reached Peierls stress at around 50ps. The glide continues on the $y = 0$ plane until at around 380ps, when the dislocation cross slipped in the $+y$ direction. The fixed boundary then automatically created a large stress of $\sigma_{xz} \approx 1.2\text{GPa}$ in response, which acted a force on the dislocation in the $-y$ direction. Downward ($-y$ direction) cross slip did not occur and σ_{xz} remains near a constant till the end of the simulation.

Although in the current simulation setup, the dislocation is allowed to cross slip in both the $+y$ and $-y$ direction, the former is always preferred. This is the manifestation of the twinning-antitwinning asymmetry of the BCC lattice. The fact that the

cross slip preference in Mo (this Chapter) and that in Si (previous Chapter) comes from different origin can be appreciated in the following experiment. In the case of Si, a reverse of loading direction would result in a reverse of the cross slip preference, as well as the dislocation glide direction. In the case of Mo here, the reverse of loading direction only changes the dislocation glide direction but the upward cross slip preference remains. This preference is consistent with the previous prediction by the line tension model [212], favoring the double-kink nucleation in the upward direction against the downward direction, in the limit of large glide stress. The dislocation glide seems to be non-homogeneous in time, consisting of hibernation periods of about 5-10ps and sudden jumps over a few lattice repeat distances. A detailed plot of this jerky motion is shown in Fig. 6-15(a). The same seems to be true for cross slip as well, as shown in Fig. 6-15(b).

The dislocation core during glide seems to take a planar structure, as shown in Fig. 6-16(a) and (g). Cross slips are initiated when the planar core becomes bifurcated, as shown in Fig. 6-16(b) and (c), most probably due to the scattering with random phonon waves. It is observed that after some initial oscillations over the upper and lower bifurcation branches, the upper branch always become dominant in the end, and the dislocation cross slips upwards. Due to the back stress of the fixed boundary, the dislocation is then forced to glide on the horizontal plane after moving upward for a few lattice distances. The instantaneous configurations during 367.5ps to 395.0ps are shown in Fig. 6-16 to illustrate the atomistic pathway of cross slip. Atoms with local energy higher than -6.72eV are plotted dark representing dislocation core.

At 300K, the dislocation starts to move a much lower stress (around 1.4GPa), as shown in Fig.6-17. Cross slip also occurred earlier and more frequently than in the case of 10K. As a result, the stress component σ_{xx} quickly reaches an equilibrium of around 1.7GPa, exerting a force in $-y$ direction suppressing further cross slip. The dislocation was then oscillating between slip planes $y = 4$ and $y = 5$, as shown in Fig. 6-18.

In summary, our MD simulations of a straight screw dislocation in Mo have re-

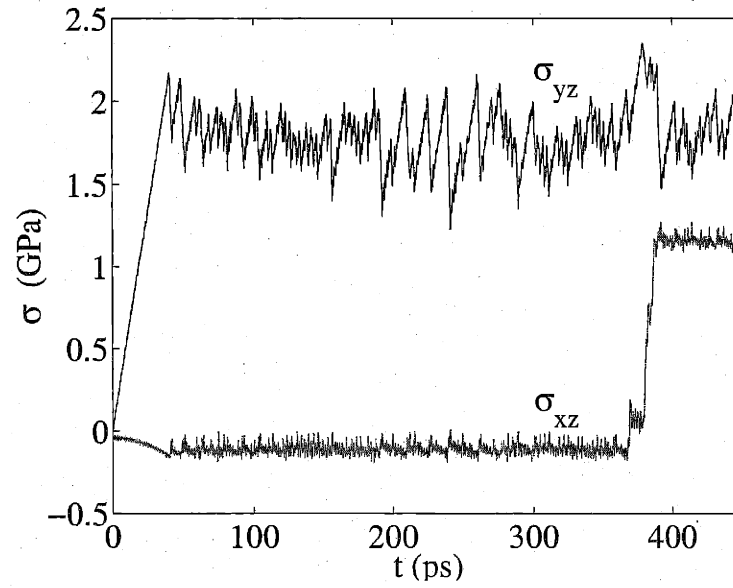


Figure 6-13: Variation of the internal stress during MD simulations of screw dislocation motion at 10K under constant shear strain rate (see text).

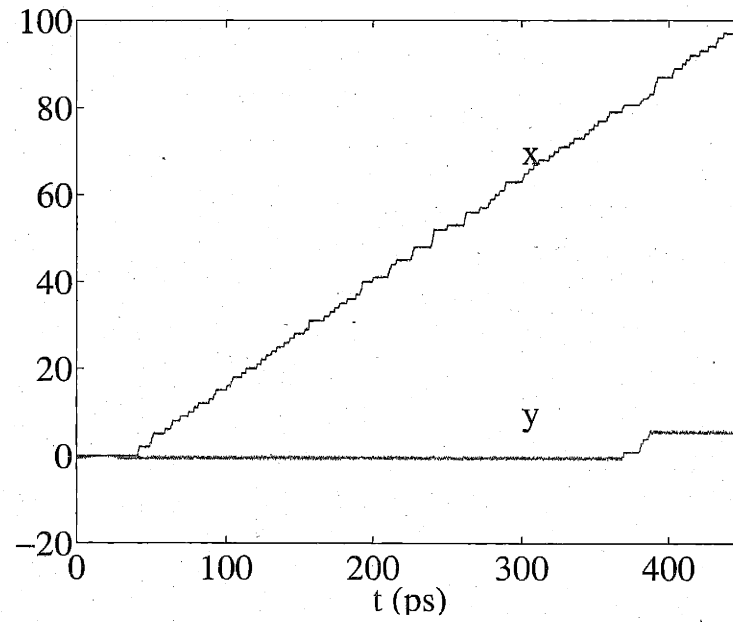


Figure 6-14: Instantaneous dislocation position during MD simulations under the same condition as Fig. 6-13.

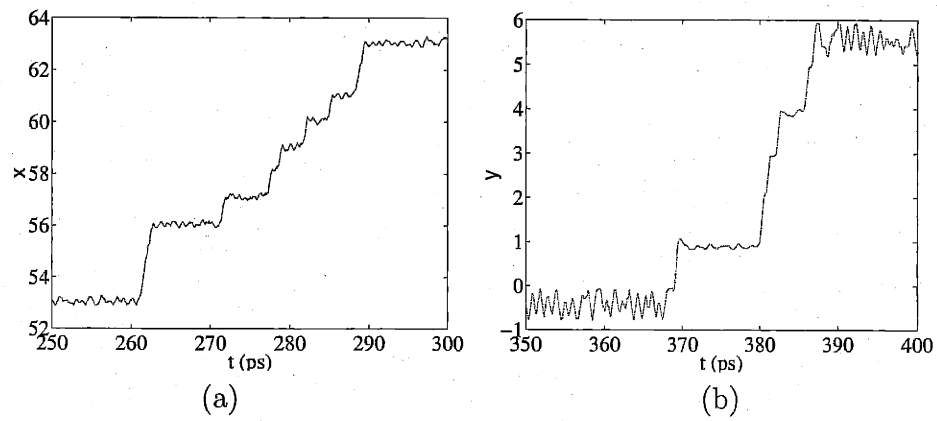


Figure 6-15: Instantaneous dislocation position during the same MD simulation as in Fig. 6-13.

vealed its jerky mode of motion, as well as a cross slip asymmetry. The dislocation core also assumes a more planar shape during the motion. It would be worthwhile to see how much of these behaviors still remains when dislocations are long enough to allow kink nucleation and migration.

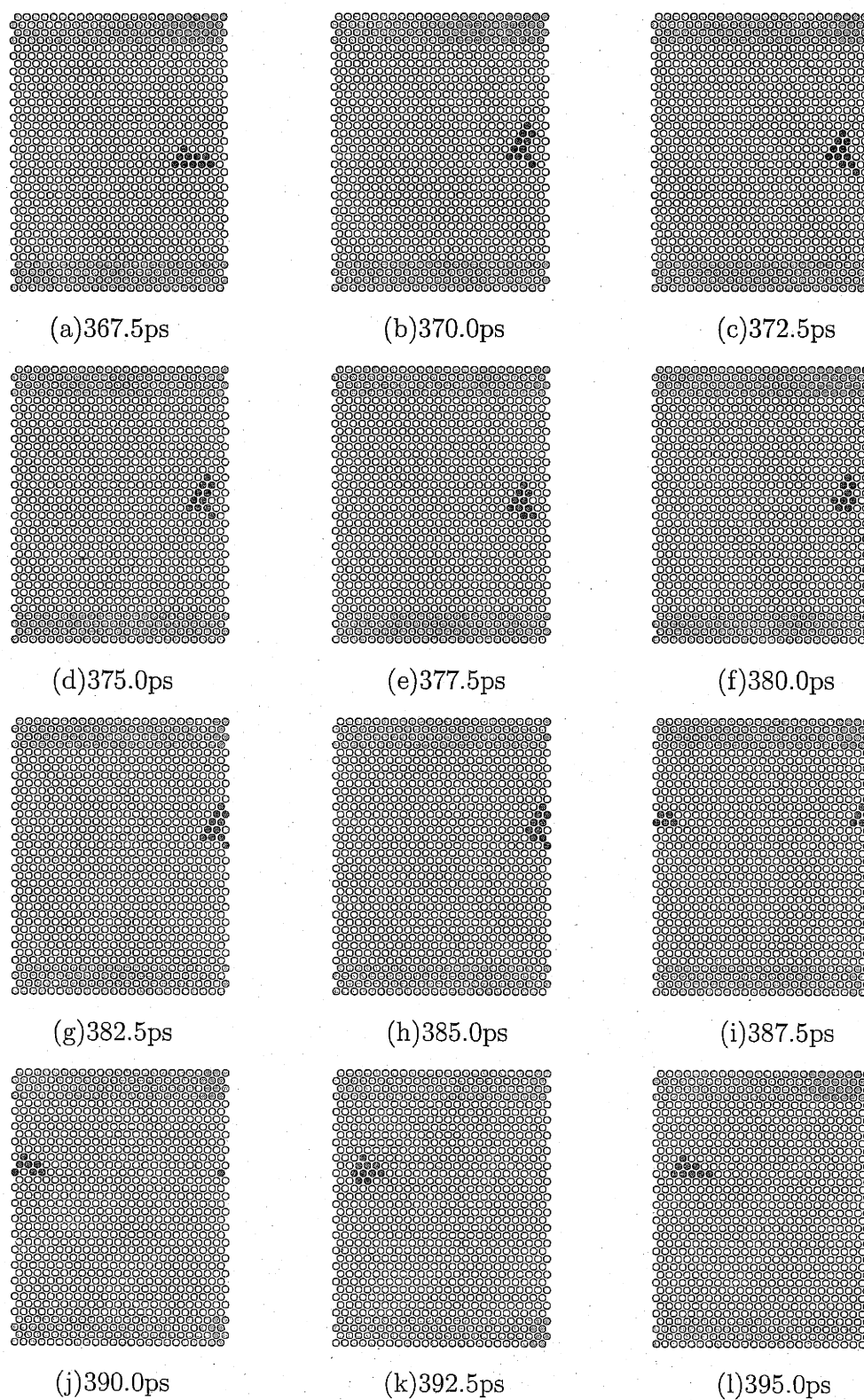


Figure 6-16: Instantaneous configurations during MD simulation (see text) showing the atomistic pathway for screw dislocation cross slip.

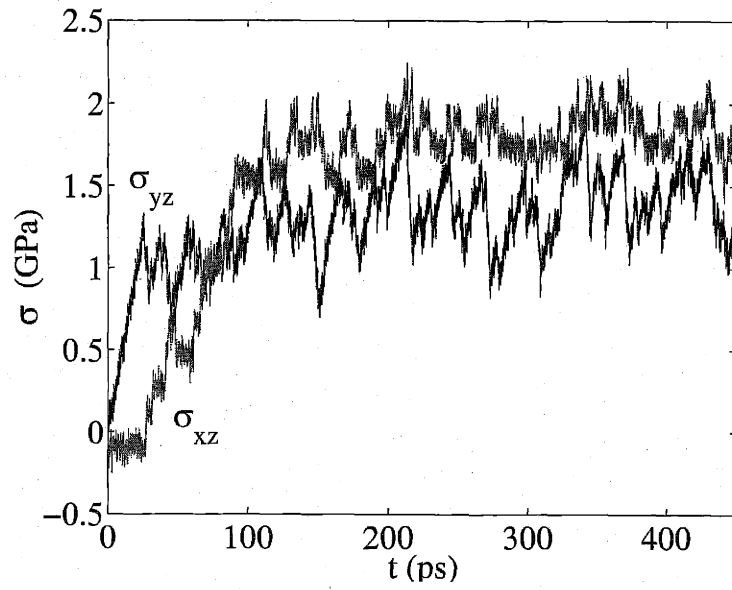


Figure 6-17: Variation of the internal stress during MD simulations of screw dislocation motion at 300K under the same strain rate as in Fig. 6-13.

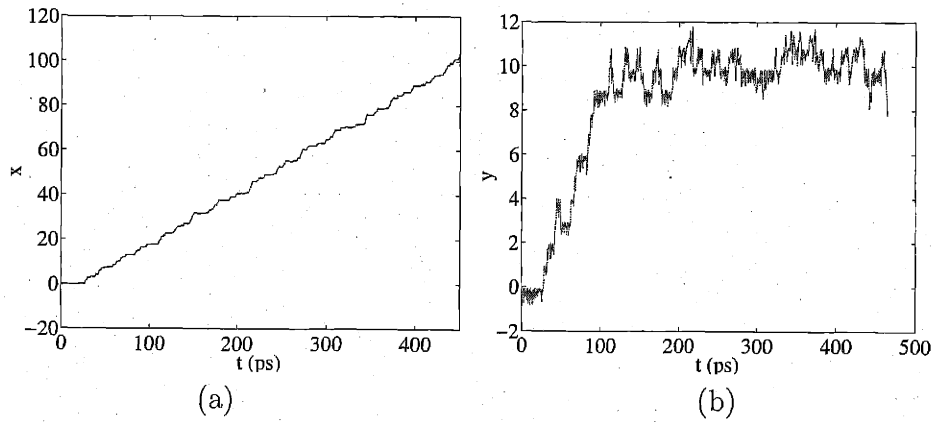


Figure 6-18: Instantaneous dislocation position during the same MD simulation as in Fig. 6-17.

Chapter 7

Mesoscale Study of Dislocation in Si

7.1 Introduction

As we have seen from Chapter 5 and 6, the study of dislocation motion by direct Molecular Dynamics simulations is limited in both length and time scales. Dislocations in MD are typically 100\AA in length, while in experiments they are usually over $100\mu\text{m}$ [44]. At the same time, typical MD simulation timesteps are on the order of 1fs (10^{-15}s), so that a million timesteps would only reach 1ns (10^{-9}s). However, the average displacement of the fastest dislocation over 1ns in a typical experiment [44] would only be 10^{-2}\AA . This simply means that no dislocation motion will be observed at all during the MD simulation, if the temperature and stress conditions are comparable with those in experiments, since the lattice spacing in Si is around 3\AA . Therefore, it is obvious that direct MD is not able to produce dislocation mobility data on the same scale as where typical experiments are performed.

On the other hand, we have seen from previous Chapters that dislocations do start to move in MD simulations, whenever the applied shear stress reaches the Peierls stress (around 2GPa). But this stress is too high compared with that in typical experiments, which is around 1-100MPa, and the mechanisms of dislocation motion in these two stress regimes are different too. In the high stress regime, phonon

radiation loss and dislocation-phonon scattering are the speed limiting mechanisms. Dislocation velocity in this regime are typically higher than 1m/s, and can become comparable with sound velocity (2200m/s). In the low stress regime, where most experiments are performed, dislocations move by nucleation and migration of kinks with the aid of thermal fluctuation. Each elementary kink process is an rare event with an energy barrier of $1 \sim 2\text{eV}$. Due to the fundamental difference in their mechanisms, dislocation mobility data by MD simulations are usually not directly comparable with experimental results.

As the dislocation dissociation and kink mechanisms became well established in Si (see Chapter 2 for details), much theoretical effort has been spent on obtaining accurate activation parameters for kink nucleation and migration on 30° and 90° partials by energy minimization [204, 213, 214, 215, 216]. The kink energies are usually compared with the effective activation energy Q obtained from an Arrhenius fit of the experimental velocity-temperature curve. Such a comparison is heretofore based on the generic kink diffusion model by Hirth and Lothe [30] (from here on referred to as the H-L model). However, it was evident that the H-L model is not able to explain a number of observed mobility behaviors, such as the nonlinear velocity stress dependence at low stresses, and has to rely on additional *ad hoc* assumptions such as “weak obstacles” to fit with experiments. Such difficulties are mostly due to the idealization in the H-L model, where non-interacting kinks nucleate and migrate on a single dislocation line (more details in Appendix C). It ignores a number of important physical mechanisms, such as the elastic interaction between kinks, and more importantly, the coupling between the two partials.

Considering the limitations of existing methods as discussed above, what is lacking so far is a theoretical description which is sufficiently free of *ad hoc* assumptions and capable of relating dislocation mobility behavior to the underlying kink mechanisms. In this section, we present such a description by adopting a kinetic Monte Carlo (kMC) treatment kink nucleation, migration and annihilation processes along with full elastic interactions between the dissociated partial dislocations. The formulation is designed to produce the overall dislocation movement as the cumulative effect of a

large number of individual kink events, requiring for input only the kink formation and migration energies from atomistic calculations. This is a typical type (b) coupling between the atomistic and meso scales as we have discussed in Chapter 1.

In Section 1, we present the implementation details of the kMC method, focusing on the treatment of double-kink nucleation processes and the choice of kink energies. Theoretical predictions on the temperature and stress dependence of dislocation velocities, and their comparison with experiments are discussed in Section 2. In focusing on the stress dependence of dislocation velocity, we show that it is strongly affected by the compatibility between the averaged separation between the partials and the period of the Peierls barrier, and can lead to a sublinear behavior when they are compatible. As a result, the nature of “weak obstacles” to kink propagation, a longstanding postulate in previous data interpretation, is clarified. This also leads to a prediction of non-monotonic oscillatory behavior of dislocation velocity with increasing stress for a particular loading direction, which we offer for experimental verification.

7.2 Kinetic Monte Carlo Method

7.2.1 General Settings

Kinetic Monte Carlo (kMC) method is generally used to simulate the evolution of a physical system through numerical sampling of (Markovian) stochastic processes. While the traditional Monte Carlo (MC) method is applied to sample systems in or close to the thermal equilibrium, kMC has a “kinetic” character, in that it also evolves the system in real physical time making it possible to study non-equilibrium processes [133]. A connection between Monte Carlo timesteps and the real physical time has been discussed within the theory of Poisson processes [217]. The appeal of the kMC method is that it can treat large length- and long time-scale kinetic response while incorporating atomistic information, through appropriately determined transition rates. For example, it is widely used to simulate surface diffusion and growth

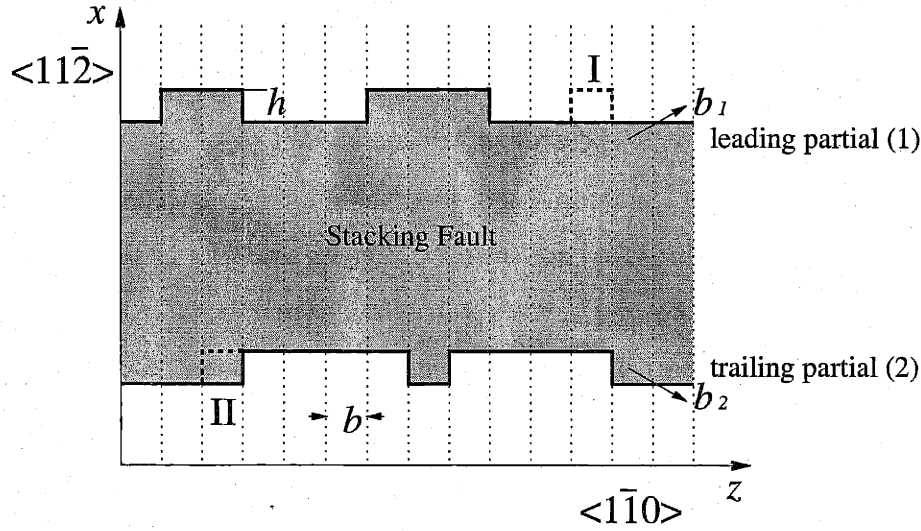


Figure 7-1: Schematics of kMC model of dislocation in Si. Screw dislocation with Burgers vector \vec{b} is dissociated into leading and trailing 30° partials, with Burgers vector \vec{b}_1 and \vec{b}_2 respectively. Elementary kink width is b , while kink height is $h = \sqrt{3}/2 b$. An embryonic double-kink nucleation event is shown at position I, and a kink migration event is shown at position II, both in dashed lines.

processes [218], in which the energy barriers for the atomic mechanisms are obtained from atomistic calculations.

However, the kMC study of dislocation motion has a fundamental difference from that of the surface growth processes. Due to the lower dimensionality of dislocation line, the surrounding elastic medium transmit stress fields which couples different parts of the dislocation line. Therefore, kMC model of dislocation motion needs to incorporate long range elastic interactions, in contrast to the case of surface growth where only local rules are necessary.

Fig. 7-1 shows a schematic representation of a screw dislocation in Si that we study in our kinetic Monte Carlo model. The dislocation line is lying mostly along the $\langle 1\bar{1}0 \rangle$ direction (z axis), dissociated into two 30° partials, with Burgers vectors b_1 and b_2 , respectively. Each partial consists is represented by a series of horizontal (H) and vertical (V) segments. H segments have length in multiple of b , the Burgers vector and the V segments have length $h = \sqrt{3}b/2$, the kink height. The area enclosed by the two partials (shaded) is the stacking fault, whose width is always a multiple of h . Each partial can migrate upward or downward along $\langle 11\bar{2} \rangle$ (x axis) through a series

of segmental events. On the H-segment double-kinks can nucleate in the upward or downward directions, while the V-segment can migrate to the left or right (indicated by the dashed lines).

The choice of x and z as the axis of this planar model (instead of x and y) may need some justification. It is to ensure that the dislocation line is along z direction and that its motion is along x direction, so as to be consistent with our atomistic models (see Chapter 5, 6), as well as the convention used by Duesbery [163].

The dislocation is represented in the computer by two *kink lists*, together with x_1 and x_2 specifying the location of the two partials at $z = 0$. Each entry in the *kink list* contains the position z_i and sense v_i of a kink, with $v_i = +1$ or -1 for left or right kinks respectively. Either one of the *kink lists* is updated at every simulation step as a result of the occurrence of an elementary kink event, e.g. double-kink nucleation, kink migration or kink annihilation on the corresponding partial. The choice of which event to occur is made as follows. At each simulation step, an *event list* is generated containing all possible kink pair nucleation events on each and every horizontal segment of the two partials, and all possible lateral displacements (migration to the left or the right) of the existing kinks. A kinetic Monte Carlo algorithm [219] is then applied to select a particular entry from the *event list*, with the probability of selecting each event proportional to its occurrence rate. The physical time increment is then evaluated as the inverse of the total (sum) rate of all the events in the current list and the simulation continues to the next step.¹

The rate of each event is calculated within the transition state theory [220]. Similar to the surface growth studies [218], the activation energy barriers for each transformation contain terms that are imported from atomistic calculations. However, since the dislocation segments can interact both with external stress and with each other, there is an additional energy term in the activation energy, defined by the local stress at the transformation site. This local stress is evaluated as a sum of the external stress

¹Strictly speaking, the physical time increment should be a random number satisfying exponential distribution with its mean as calculated above. However, if only the average dislocation velocity is to be extracted from the kMC simulation, the above procedure provides the same result but with smaller statistical fluctuation, provided that steady state dislocation motion is reached.

and the internal stress due to all other dislocation segments. For example, the rate for kink migration on partial p ($p = 1, 2$ for leading and trailing partials respectively) is calculated as,

$$j_m = \omega_0 \exp \left(-\frac{W_m - TS - (\pm\gamma_{SF} - \sigma_{yz}b_{p,z} - \sigma_{yx}b_{p,x})A/2}{k_B T} \right), \quad (7.1)$$

where ω_0 is the pre-exponential “frequency” factor that we set equal to the *Debye frequency* ($\omega_0 = 1.3544 \times 10^{13}\text{Hz}$), W_m is the kink migration energy barrier which can be calculated by atomistic methods, S is the vibrational entropy, which is set to $3k_B$, according to earlier theoretical and experimental estimates [221, 50]. γ_{SF} is the stacking fault energy, with “+” or “−” signs for the leading and trailing partial respectively, σ is the stress tensor, $A = \pm bh$ is the area swept out by the dislocation during kink migration, with “+” or “−” sign corresponding to the dislocation moving upward (e.g. left kink move left) or downward (e.g. left kink move right), respectively, k_B is the Boltzmann’s constant and T is the temperature.

The factor of $1/2$ appears in Eq. (7.1) because we assume that the dislocation has swept out half of the total area A at the saddle point configuration. This assumption is valid for the small stresses, where the work done by the stress is much smaller than the energy barrier itself. In this paper the criterion becomes $\tau \ll W_m/b^3$ and simple calculations show that it is satisfied in the normal range of stresses. Kinks may annihilate as a result of their migration, so we do not calculate the kink annihilation rate separately. A similar expression exists for double-kink nucleation, with W_m replaced by the corresponding activation energy, e.g. E_{emb} for embryonic (width one b) double-kink nucleation. The situation for double-kink nucleation is more complicated due to the mutual interactions between the two kinks at small separations, which we discuss in more detail in Section 7.2.2. The stress in Eq. (7.1) is the value at the center of the V-segment². The stress formula simplified for 2-dimension is given in Appendix D. For the newly emerged dislocation segment at each simulation step, stress contributions from all other segments will to be calculated at its center point.

²also at the center of the nucleation site on the H-segment for double-kink nucleations

The stress field on all other segments, on the other hand, can be updated simply by superimposing the stress field of a small dislocation loop. The choice of kink energies from various sets of atomistic data are discussed in Section 7.2.3.

The approach described above where the dislocation is represented as H and V segments are not the only way of performing kMC simulation of dislocation motion. Recently, a lattice spin model of dislocation is implemented by C. Deo and the author; it has advantages in treating dislocation multiplication and annihilations, as will be discussed in Appendix C.4.

7.2.2 Double Kink Nucleation

Our experience is that the major bottle-neck of kMC simulations in general, including kMC simulations of dislocation motion, is an efficient treatment of fast events that consume most of the computing time but do not contribute appreciably to the overall evolution. It is a general feature of *all* kMC simulations that they lack any natural dynamic or kinetic constraint. Unlike Molecular Dynamics in which dynamics is naturally defined by the interatomic potentials, kinetic Monte Carlo method will sample all and every process from its current event catalog. As is often the case, the catalog may contain a number of very fast events that are repetitive or otherwise uninteresting. It is up to the researcher to help such an ill-behaved simulation by integrating out, one way or another, such uninteresting events from the event catalog.

In the case of Si, a vast majority of fresh kink pairs (with kink pair separation b) recombine almost immediately after their formation. Unless specially treated, almost all of the kMC cycles are wasted on sampling these fast but unimportant processes, resulting in a very inefficient simulation unable to advance the dislocation over an appreciable distance within a reasonable amount of simulation time. To remedy such an unwanted behavior we studied kink pair nucleation and propagation as an isolated (Markov) stochastic process. Specifically, we examined a one-dimensional random walk with one absorbing end and derived a recursive formula that allows to compute the effective rate of formation of *sustainable* kink pairs of width w_s , i.e. kink pairs that have considerable probability to expand further without recombination [222]. Based

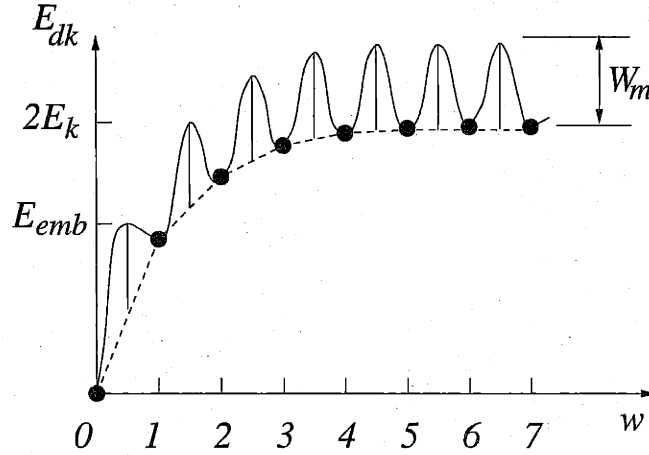


Figure 7-2: Theoretical dependence of the kink pair energy E_{dk} on its width w are shown as dots. For large width it approaches $2E_k$. At finite width w , E_{dk} is a superposition of $2E_k$ and the kink pair interaction energy $W_{int}(w)$. The solid curve illustrates the energy barrier between the neighboring states. E_{emb} is the barrier for nucleating an embryonic double-kink, i.e. transition from state $w = 0$ to $w = 1$.

on this result, it became possible to speed up our kMC simulations by allowing only kink pairs of width w_s to nucleate. Parameter w_s was chosen as a compromise between efficiency and accuracy: a larger w_s means a higher probability for the nucleated kink pairs to survive, while a smaller w_s means a more detailed and realistic sampling of the kink pair propagation processes. In this section, we discuss the calculation of the nucleation rate of kink pairs with an arbitrary width w on an isolated dislocation. A close form solution of this problem also exist, if the elastic interaction between kinks is ignored, which will be presented in Appendix C.2. The result shows that the fast kink pair recombination rate is not only due to mutual kink attractions, but also due to the randomness of kink diffusion. Generalization of this method to study the correlated double-kink nucleation on two partial dislocations will be discussed in Appendix C.3.

We plot in Fig. 7-2 the profile of an energy E_{dk} showing the variation of the double-kink energy with its width w . For large width this quantity approaches $2E_k$. At finite width w , $E_{dk}(w)$ is a superposition of $2E_k$ and the interaction energy W_{int} between the kink pair, as indicated by the dots in Fig. 7-2. From linear elastic theory

we have [30],

$$E_{dk}(w) = 2E_k + W_{int}(w), \quad (w \geq 1) \quad (7.2)$$

$$W_{int}(w) = -\frac{\mu h^2}{8\pi w b} \left(b_z^2 \frac{1+\nu}{1-\nu} + b_x^2 \frac{1-2\nu}{1-\nu} \right), \quad (7.3)$$

where $b_z = b/2$, $b_x = b\sqrt{3}/6$.

Given that W_m is the energy barrier separating two neighboring states of the double-kink in the limit of large width (c.f. Fig. 7-2), we will assume that at finite width including a width of one b , the barrier between adjacent states is still given by placing W_m at the midpoint between the two states. This leads to the following expressions for the transition barriers of each state

$$W^+(i) = \frac{1}{2} [E_{dk}(i+1) - E_{dk}(i)] + W_m, \quad (7.4)$$

$$W^-(i) = \frac{1}{2} [E_{dk}(i-1) - E_{dk}(i)] + W_m, \quad (7.5)$$

where $W^+(i)$ and $W^-(i)$ are the energy barriers for the forward ($i \rightarrow i+1$) and backward ($i \rightarrow i-1$) transitions respectively. Specifically, for a width of one b we obtain

$$E_{emb} = W^+(0) = \frac{1}{2} [2E_k + W_{int}(1)] + W_m. \quad (7.6)$$

The nucleation rate of a double-kink of width w_c can be written as

$$j_{dk}(w_c) = j_{dk}(1) \cdot p_s(1 \rightarrow w_c), \quad (7.7)$$

$$j_{dk}(1) = \omega_0 \exp \left(-\frac{E_{emb} - TS - (\pm \gamma_{SF} - \sigma_{yz} b_{p,z} - \sigma_{yx} b_{p,x}) A/2}{k_B T} \right), \quad (7.8)$$

where $j_{dk}(1)$ is embryonic double-kink nucleation rate and the various terms in Eq (7.8) assume the same meaning as in Eq. (7.1). p_s is the *survival probability* that an embryonic double-kink successfully reaches a width w_c before it is annihilated.

More rigorously, we define p_s as follows. Consider the double-kink nucleation and expansion process as a Markov process in the discrete space of kink width w , $w = 0, 1, 2, \dots$, see Fig. 7-3. The state $w = 0$ corresponds to the situation where

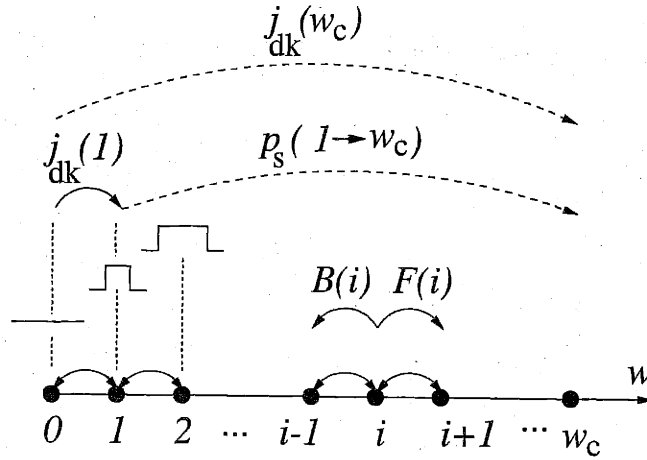


Figure 7-3: Schematic representation of the Markov process in the space of discrete kink width w . Transitions are allowed between neighboring states, shown as solid arcs. Every state can be reached from every other state. We draw dashed arcs between states widely separated to denote a collection of different paths. $F(i)$ and $B(i)$ are the forward and backward probabilities from state i . The nucleation rate $j_{dk}(w_c)$ of double-kinks of width w_c is the product of embryonic double nucleation rate $j_{dk}(1)$ with the survival rate $p_s(1 \rightarrow w_c)$.

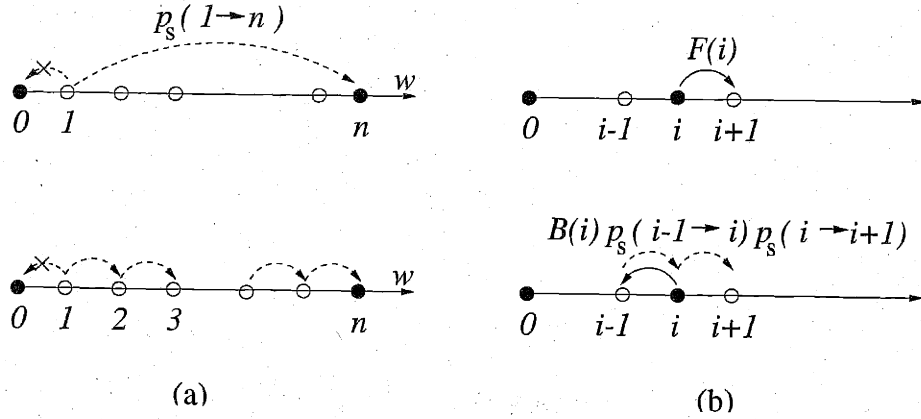


Figure 7-4: (a) Survival probabilities $p_s(1 \rightarrow n)$ can be broken up as the multiplication of smaller survival probabilities $p_s(i \rightarrow i+1)$. (b) Two possibilities of reaching $i+1$ from i . First, it can jump to $i+1$ directly from the first step. Second, it can choose to jump to $i-1$ in the first step. But then it has to come back to i from $i-1$ before it can reach $i+1$.

there is no kink pair. Then $p_s(i \rightarrow n)$ is the probability of reaching state n by starting from state i without ever reaching state 0. The condition of $i < n$ is always assumed.

Because of the connectivity of the 1-D Markov chain, we observe that starting from state 1, the system has to reach $n - 1$ before n , and it has to reach $n - 2$ before it reaches $n - 1$, and so on. Therefore, we can express the *survival probability* $p_s(1 \rightarrow n)$ as the product of the elementary ones, see Fig. 7-4(a).

$$p_s(1 \rightarrow n) = \prod_{i=1}^{n-1} p_s(i \rightarrow i+1) . \quad (7.9)$$

To evaluate $p_s(i \rightarrow i+1)$, we note that there are two possibilities of reaching $i+1$ from i , as shown in Fig. 7-4(b). First, the system can go to $i+1$ upon the first jump from state i . That has the probability of $F(i)$, which we will give explicit expression below. Second, the system can choose to go to $i-1$ upon the first jump from i . This has the probability of $B(i) = 1 - F(i)$. Since it makes the “wrong” move in its first step, it has to correct itself sometime later by coming back to i before it can reach $i+1$. The probability of coming back to i from $i-1$ is $p_s(i-1 \rightarrow i)$. After that, the situation is exactly the same as the initial stage, when the system starts off from state i . The probability of reaching $i+1$ now is $p_s(i \rightarrow i+1)$ again. Therefore we have the recursive equation

$$p_s(i \rightarrow i+1) = F(i) + B(i)p_s(i-1 \rightarrow i)p_s(i \rightarrow i+1) . \quad (7.10)$$

Solving for $p_s(i \rightarrow i+1)$ in terms of $p_s(i-1 \rightarrow i)$ we have,

$$p_s(i \rightarrow i+1) = \frac{F(i)}{1 - B(i)p_s(i-1 \rightarrow i)} , i \geq 1. \quad (7.11)$$

With the initial condition of $p_s(0 \rightarrow 1) = 0$ we can solve for $p_s(i \rightarrow i+1)$ for all $i = 1, \dots, n$. The $F(i)$ in Eq (9-10) is defined as the *forward probability* of state i — the probability of going to $i+1$ instead of $i-1$ upon leaving i . $B(i)$ is defined as the *backward probability* which is just $1 - F(i)$. In terms of the transition barriers given

in Eq. (7.47.5), the expression for $F(i)$ is

$$F(i) = \left[1 + \exp \left(\frac{W^+(i) - W^-(i)}{k_B T} \right) \right]^{-1}, \quad i \geq 1, \quad (7.12)$$

where $W^+(i)$ and $W^-(i)$ are the transition barriers given in equations (4) and (5). At finite stress and in the presence of the stacking fault, the expression of $F(i)$ becomes

$$F(i) = \left[1 + \exp \left(\frac{W^+(i) - W^-(i) - (\pm \gamma_{SF} - \vec{\tau} \cdot \vec{b}_\alpha) A}{k_B T} \right) \right]^{-1}, \quad (7.13)$$

where the additional terms have the same meaning as in Eq. (7.1). The rate $j_{dk}(w_c)$ of nucleating double-kink of width w_c is now fully specified in Eqs. (7.1) through (7.13).

In practice, we found that any value of w_s between 10 and 20 was sufficient to generate reasonably large statics of kink pair nucleation events (survival probability $1 \sim 10\%$) and that specific choice of w_c from this interval had no detectable effect on the final result of dislocation velocity. It turns out that for these choices of w_c the nucleation rate is not sensitive to the exact value of E_{emb} either and is largely determined by E_k and W_m .

7.2.3 Kink Energies

As we have emphasized we will rely on atomistic calculations to provide values for the kink formation and migration energies. It was first found in [204] and then rationalized in [206] that for 30° partials four topologically distinct types of kinks can be distinguished, if one neglects the reconstruction defect and its complexes with the four primary kinks. Table 7.1 shows formation (E_k) and migration (W_m) energies for all four kinks obtained using the environment-dependent interatomic potential (EDIP) [223] and the tight-binding approximation (TB) [215]. Although kink multiplicity can be readily incorporated into our model, in the present work we opted for a simpler parameter space and set representative values for E_k and W_m as follows. Considering that the greatest contribution to dislocation motion comes from kinks that nucleate and migrate at the fastest rates, the value of E_k is taken as the

Table 7.1: Formation energies, E_k , and migration barriers, W_m , of kinks on 30° partials in silicon, obtained from atomistic calculations using EDIP and TB, in eV. Underlined values are selected for use in kMC simulation.

	E_k		W_m	
	EDIP	TB	EDIP	TB
LK	<u>0.65</u>	<u>0.35</u>	1.46	<u>1.52</u>
RK	0.72	<u>1.24</u>	0.56	2.03
LK'	1.49	0.76	0.62	1.11
RK'	<u>0.39</u>	1.85	<u>0.89</u>	1.42

Table 7.2: Kink's formation energy E_k and migration barrier W_m (in eV) on 30° and 90° partials in silicon obtained from atomistic calculations using EDIP potential, tight-binding (TB) and density functional theory (DFT), and experimental measurements using transmission electron microscopy (TEM) and high resolution electron microscopy (HREM).

		30°		90°	
		E_k	W_m	E_k	W_m
EDIP	[223]	0.52	0.89	0.70	0.62
TB	[215]	0.82	1.52	0.12	1.62
DFT	[224]	2.1			
DFT	[213]			0.1	1.8
DFT	[216]			0.04	1.09
TEM	[59]			≥ 0.4	≤ 1.2
TEM	[60]		1~1.2		1~1.2
HREM	[61]	0.8	1.55	0.74	1.55

average of the lowest values for two left (LK, LK') and two right (RK, RK') kinks separately, giving $E_k = 0.52\text{eV}$ (EDIP) and 0.80eV (TB). For W_m we choose the lower value from the maximum of (LK, LK') and of (RK, RK'), giving $W_m = 0.89\text{eV}$ (EDIP) and 1.52eV (TB).

As will be seen in the next section, the different kink energies from EDIP and TB calculations leads to a discrepancy on dislocation velocity up to four orders of magnitude, indicating that kMC predictions for dislocation velocity depend sensitively on the atomistic input. Simple analysis shows that to achieve reasonable agreement in the absolute values of dislocation velocity, the kink energy calculations has to reach

the accuracy of 0.1eV, which is only attainable for the first principles methods. However, as shown in Table I, even density functional theory (DFT) calculations available for the partial dislocations in Si [224, 213, 216] have neither converged nor agreed with the experimental estimates which themselves show considerable scatter [59, 60, 61]. Based on various calculated and experimental values available at present, our best estimates for the energetics of the “generic” kink on 30° partial are $E_k = 0.7\text{eV}$ and $W_m = 1.2\text{eV}$.

7.3 Dislocation Mobility

7.3.1 Extracting Dislocation Velocity

Figure 7-5 shows the evolution of the profile for the leading partial of a moving screw dislocation. The simulation is carried out at resolved shear stress of $\sigma_{yz} = 50\text{MPa}$ and temperature of $T = 1000\text{K}$. The energy parameters we use are $E_k = 0.52\text{eV}$, $W_m = 0.89\text{eV}$, based on EDIP calculations. The stacking fault energy is chosen to be $\gamma_{SF} = 0.004\text{eV}/\text{\AA}^2$, so that the separation between the two partials is around $10h$. The simulation starts at $t = 0$ with a straight dislocation. Shortly after, a double-kink is nucleated in the middle of the dislocation shortly after that. The two kinks begin to drift in opposite directions and finally annihilate with neighboring kinks. As more double-kinks are nucleated and more kink pairs annihilated, the motion reaches a steady state, with about 10 kinks on the $2\mu\text{m}$ long dislocation at any instant. At $t = 2\text{ms}$, the dislocation has glided a distance of 6 kink heights in the x direction, which is about 20\AA .

To extract dislocation velocity, instantaneous average positions of the leading and trailing partials along the dislocation line is plotted as a function of time, as shown in Fig. 7-6 corresponding to $T = 1000\text{K}$, $\sigma_{yz} = 10\text{MPa}$. During the 0.15s interval of simulation the two partials are seen to maintain roughly constant separation as they advance a distance of some $5.7 \times 10^{-6}\text{cm}$. The dislocation velocity is obtained from the average slope of the curve which yields $3.8 \times 10^{-5}\text{cm/s}$ in this example.

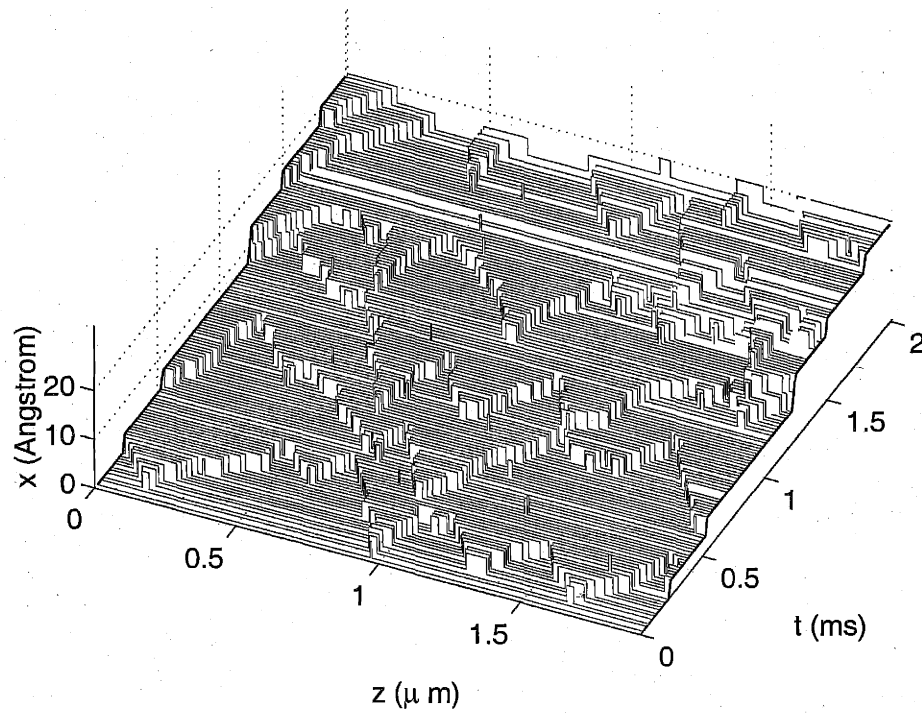


Figure 7-5: Profile of the leading 30° partial dislocation during the motion at $T = 1000K$, $\sigma_{yz} = 50MPa$. The dislocation length is $5000b = 1.92\mu m$. Kink energies are $E_k = 0.52eV$, $W_m = 0.89eV$.

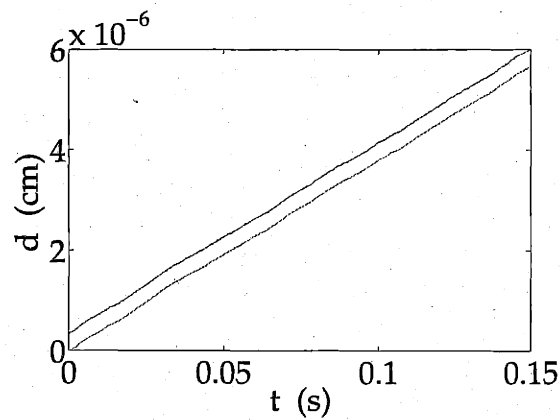


Figure 7-6: Simulated instantaneous positions of the two partials at $T = 1000K$, $\sigma_{yz} = 10MPa$.

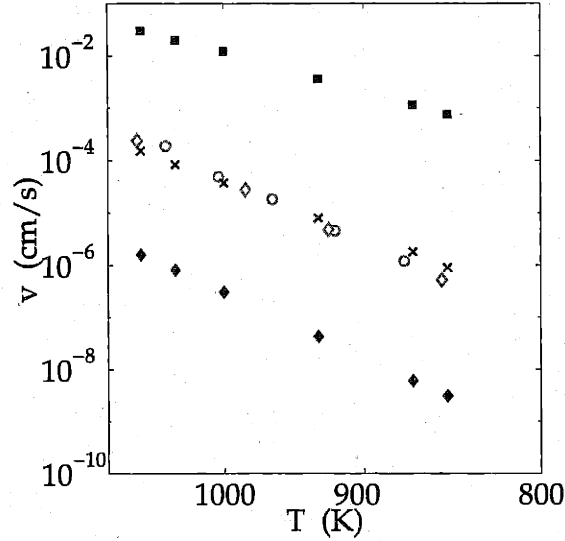


Figure 7-7: Temperature-dependent velocities of screw dislocations at stress $\tau = 10\text{MPa}$. Experiments are denoted by \diamond [43] and \circ [54] respectively. \blacksquare and \blacklozenge are kMC predictions using EDIP and TB kink energetics. KMC predictions for the optimized kink parameters, $E_k = 0.7\text{eV}$ and $W_m = 1.2\text{eV}$, are also shown in \times .

7.3.2 Temperature Dependence

Fig. 7-7 shows a kMC prediction for the dislocation velocity as a function of temperature at 10MPa shear stress, along with two sets of relevant experimental data [43, 54]. Kink energies from EDIP and TB calculations were used in kMC simulations. The predicted velocities based on these two sets of atomistic inputs are seen to differ by some four orders of magnitude, bracketing the experiments. An Arrhenius fit of the simulated and the experimental velocity data produces an overall activation energy $Q=1.31\text{eV}$ (EDIP), 2.23eV (TB), and 2.20 (exp't). Dislocation velocities calculated based on the “optimal” set of kink parameters ($E_k = 0.7\text{eV}$ and $W_m = 1.2\text{eV}$) are also shown in Fig. 7-7. Although the result looks reasonably good, we would like to emphasize that quantitative agreement between the predicted velocities and the experimental data is not significant at this stage. This is because some other parameters, such as the sampling frequency ω_0 or the vibrational entropy S in Eq. (7.1), can easily shift the entire velocity curve by one to two orders of magnitude. Despite these

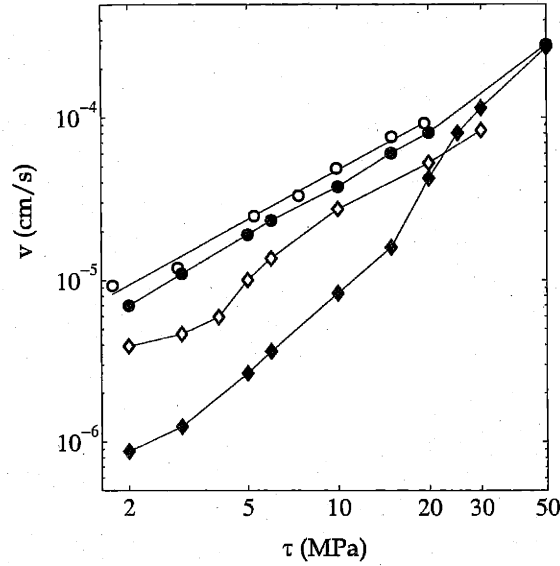


Figure 7-8: Velocity of a screw dislocation in Si as a function of stress, at temperature $T = 1000^\circ\text{K}$. kMC prediction for a commensurate case ($X_0 = 10.0h$) is shown as \blacklozenge , with a “starting stress” at about 20MPa. Experimental data from [43] shows similar velocity variation, plotted as \diamond . kMC results for a non-commensurate case ($X_0 = 10.5h$) are plotted as \bullet , demonstrating linear stress-velocity relationship, in agreement with other experiments [54], plotted as \circ .

uncertainties, the fact that the simulated dislocation velocities bracket the experimental data, and that they have similar temperature dependence with experiments are significant, indicating that our kMC model is adequate but the accuracy is limited by the quality of its atomistic input. If and when a more reliable set of atomistic parameters becomes available, the model will be ready to incorporate the new data for more accurate prediction of the intrinsic dislocation mobility in Si.

7.3.3 Stress Dependence

The stress dependence of dislocation velocity is examined using the “optimal” set of kink energies ($E_k = 0.7\text{eV}$ and $W_m = 1.2\text{eV}$). kMC predictions and experimental results are plotted together in Fig. 7-8, which shows two distinct behaviors which warrant detailed analysis. In the first case, dislocation velocity remains linear with

stress in the entire regime, while in the second case, a threshold behavior is observed where the dislocation velocity is initially low at low stress but increases markedly beyond a certain critical stress τ_c .

The most common interpretation of the threshold stress variation, long observed, invokes the existence of “weak obstacles”, assumed to be randomly distributed along the dislocation and having the effect of impeding the kink mobility [225, 8, 43]. The physical origin of these obstacles has been a longstanding unresolved issue, especially since fitting such models to the experimental data results in rather unreasonable magnitudes for the density of these obstacles [55, 8]. Möller was the first to recognize the importance of interaction between the dissociated partials. In his model [55] he attempted to do without *ad hoc* obstacles, but in the end was forced to re-introduce them to account for the low stress mobility variations in Si. In addition to this inconsistency, Möller’s model could not resolve another hotly debated experimental controversy. While some researchers have observed very pronounced starting stress behavior [43], others report perfectly linear velocity-stress behavior even down to a very low stress [54] (also shown in Fig. 7-8).

On the other hand, both these two mobility behaviors appear naturally as a result of underlying kink processes in our simulations, in which no *ad hoc* assumptions such as “weak obstacles” were ever introduced. For interpretation purposes we follow a simple mechanistic picture proposed in [226] and further developed in [227, 228]. We first consider what would be the ideal separation between the two partials if the Peierls barrier were not present. This separation, which we denote as X_0 , is given by the expression

$$X_0 = \mu b^2 \alpha / (\gamma_{SF} - \sigma_{xy} b_x), \quad (7.14)$$

where μ is the shear modulus, $\alpha = (1/4 - 1/12(1 - \nu))/2\pi$, $b_x = b\sqrt{3}/6$, and ν is the Poisson ratio. An analogy can be made between the effect of Peierls potential on the coupling partials and the act of putting two balls connected with a spring having original length X_0 onto a periodic landscape, as shown in Fig. 7-9(a). Depending on the commensurability of X_0 with the periodicity of the Peierls potential, two extreme

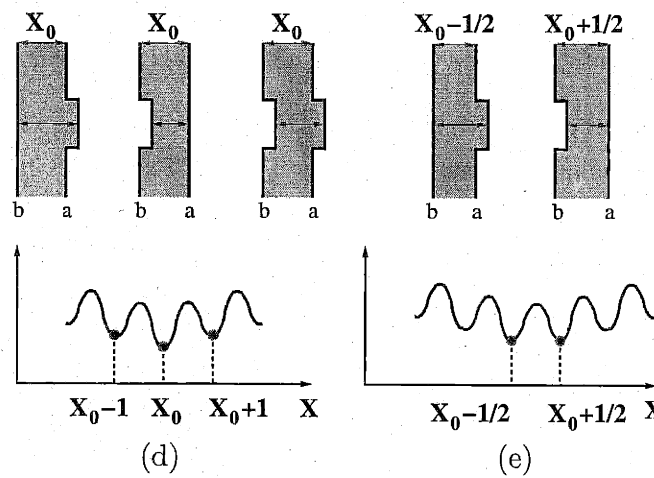
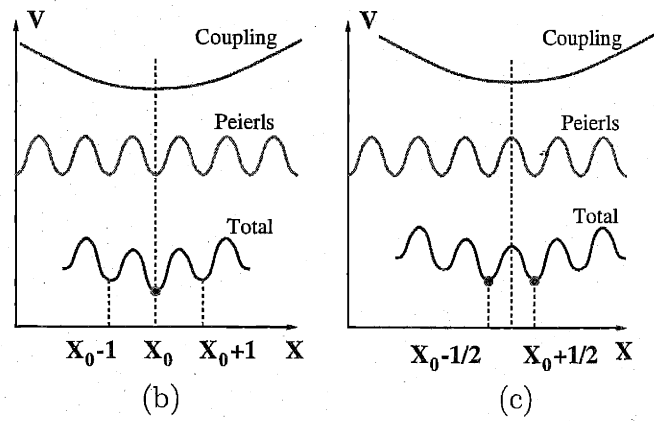
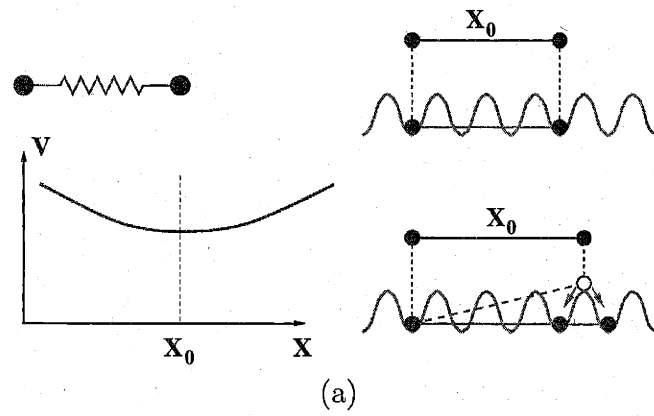


Figure 7-9: Commensurability between the ideal separation X_0 and the periodicity of Peierls barrier gives rise to two distinct mechanisms of dislocation motion at low stresses (see text).

situations can occur. If the two are commensurate, i.e. X_0 is an integer in unit of kink height h , the total energy of system as the superposition of the elastic coupling and the Peierls barrier has a single minimum at $X = X_0$, as shown in Fig. 7-9(b). If the two are non-commensurate, i.e. X_0 is a half-integer, as shown in Fig. 7-9(c), the total energy as a function of partial separation X has two (degenerate) minimum energy states. This two extreme cases will lead to very different low stress mechanisms of dislocation motion, as illustrated in Fig. 7-9(d) and (e). In the commensurate case, double-kink nucleation on either partial will move the system away from the ground state $X = X_0$, and is hence energetically unfavorable at low stresses. Therefore, the only way that the dislocation can move forward is by correlated double-kink nucleation on both partials, so that the lowest-energy state of $X = 0$ is preserved everywhere. This additional constraint at low stress reduces the dislocation mobility. In the non-commensurate case, because there are two states both having the minimum energy, i.e. $X = X_0 + 1/2, X = X_0 - 1/2$, double-kink nucleation is possible on one partial without having to be correlated with the other partial. In the case of $X = X_0 + 1/2$, double-kink nucleation on the leading partial is favored. After the leading partials has advanced on lattice period, double-kink nucleation on the trailing partial is favored. Hence the two partials can move in the sequential manner, with the stacking fault expanding and contracting alternatively. This mechanism preserves the linearity between stress and velocity down to very low stresses. Therefore, the commensurability mechanism originally proposed in FCC metals, i.e. in the limit of low Peierls barrier, is found to be also operative in the high Peierls barrier limit, where dislocations move via kinks.

The two curves in Fig. 7-8 from kMC simulations with and without the threshold behavior corresponds to the cases of $X_0 = 10h$ and $X_0 = 10.5h$, respectively. A somewhat weaker threshold behavior is observed experimentally, as indicated also in Fig. 7-8. This is not unreasonable given that the measurements average over a distribution of local conditions, whereas the prediction is strictly for the case of commensurate barrier (X_0/h is integral). The threshold condition is expected to become ineffective when applied stress becomes high enough for its work to compensate the

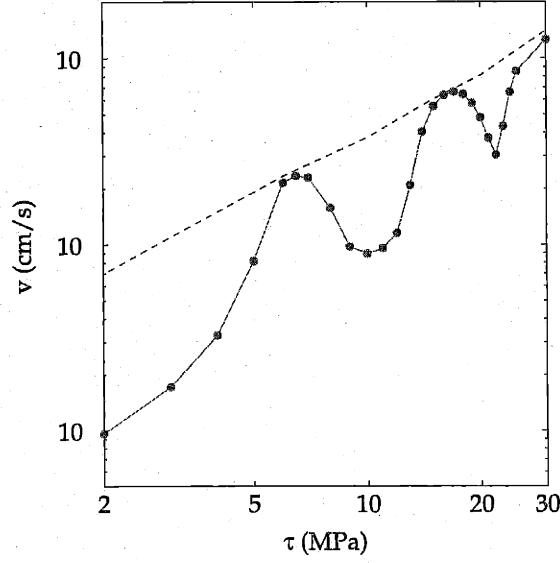


Figure.7-10: Dislocation velocity plotted against glide stress σ_{yz} , as \bullet , predicted for a special case when the ratio of the glide stress σ_{yz} to the non-glide stress σ_{xy} is fixed at -0.16 . For comparison, dislocation velocity for a non-commensurate case ($X_0 = 10.5h$) and zero non-glide stress is also shown as the dashed line.

“commensurate” energy barrier to moving a single partial to the next valley. Based on the numerical parameters used in our simulation we estimate this critical stress to be $\tau_c = 16.8\text{MPa}$, in agreement with our present kMC simulations and another estimate given in [8] (p. 167).

For the simulations discussed above, the variation of X_0 was induced by a 5% change in the stacking fault energy, but a similar effect will manifest by an equivalent variation in the elastic constant, or any other local factor which will influence the dissociation width. As shown in Eq. (7.14), X_0 depends on the so-called non-glide stress, or σ_{xy} in our notation, because it exerts opposite forces on the two partials. For an ideal dislocation, this stress component should have no effect on the glide velocity. However, in the context of our present model σ_{xy} can be used to manipulate the splitting width X_0 and to induce transitions between the “integral” and “half-integral” conditions. A striking illustration of such transitions is presented in Fig. 7-10, where simulated dislocation velocity is plotted against glide stress σ_{yz} for a special

loading condition chosen to maintain a constant ratio -0.16 of glide (σ_{yz}) to non-glide (σ_{xy}) stress components. With increasing stress amplitude, two effects counteract. The increasing glide stress makes both partials move faster while the increasing non-glide stress pushes the partials together making them pass through a sequence of “integral” and “half-integral” conditions. Accordingly, the dislocation velocity shows a non-monotonic oscillatory pattern, each dip corresponding to an “integral” situation and each hump to a “half-integral” one.

We conclude this Chapter by emphasizing that the present work is the first attempt to link the microscopic details being generated by electronic structure and atomistic calculations with dislocation mobility behavior that is directly experimentally accessible. We are collaborating with A. George in search of experimental verification of the predicted effect of non-monotonic velocity variations in the low stress regime.

Chapter 8

Mesoscale Study of Dislocation in BCC Metals

We have seen in the previous Chapter that the generic H-L model is insufficient to connect the atomistic kink calculations with experiments on dislocation glide in Si, because it ignores the coupling effect between the two partials. In this Chapter, we will discuss another situation in which a more detailed mechanistic treatment than H-L model is needed; the additional complexity here is introduced by cross slip, which occurs on screw dislocations in BCC metals.

We will present in Section 1 the kinetic Monte Carlo (kMC) model that is generalized from our study on dislocation glide in Si, and now incorporates cross slip. We will discuss how the static calculations of double kink energies and Molecular Dynamics simulations of kink mobility are incorporated into the mesoscale dislocation model. In Section 2, we will see that several new mechanisms arise as the result of cross slip, generating super jogs (cusps) on the dislocation and leaving behind debris dislocation loops — a microstructure that resembles experimental observations. The orientation dependence of dislocation mobility introduced by these mechanisms will be discussed in Section 3.

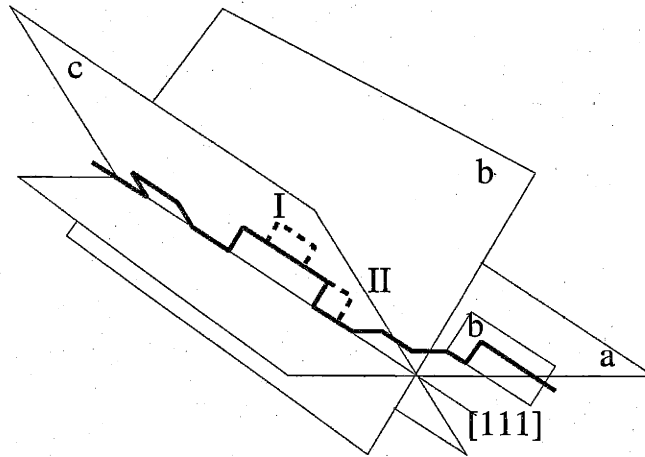


Figure 8-1: A schematic of dislocation motion in BCC metals examined in the kMC simulations. The dislocation line is mostly aligned along the $1/2\langle 111 \rangle$ Burgers vector. Kink pairs can nucleate on either of the three (110) planes a, b and c , after which kink migration is constrained to the glide plane selected by kink pair nucleation. A kink pair nucleation event is shown at position I, and a kink migration event is shown at position II, both in dashed lines.

8.1 KMC Model with Cross Slip

8.1.1 General Settings

As discussed in Chapter 3, the microstructure of BCC metals deformed at low temperature mainly consists of long screw dislocations. This is because non-screw dislocations have much higher mobility and have already moved out of the crystal. Therefore, low temperature plasticity of BCC metals is mainly controlled by screw dislocations. In this Chapter, we study the motion of a dislocation mainly aligned along the screw direction, i.e. along its Burgers vector $1/2[111]$, as shown in Fig 8-1. The dislocation line consists of horizontal (H) and vertical (V) segments, with H-segments being pure screw and V-segments being pure edge, representing kinks.¹ V-segments all have the same length h , the unit kink height, while H-segments can be of any length. This edge-screw representation of a dislocation is similar to edge-screw discretization

¹It is only an approximation to represent kinks as pure edge segments. Kinks in BCC metals usually have a finite width of $5 \sim 10b$, so that it can be represented more accurately as a tilted mixed dislocation segment. This approximation is introduced here only for the sake of simplicity.

employed in some Dislocation Dynamics (DD) simulations [229], although the edge segments are used in the latter case solely for the purpose of discretization.

To account for cross slip, kink pairs are allowed to nucleate on H-segments in any of the three (110) slip planes (a , b , c) intersecting the [111] direction. Once nucleated, a kink (V-segment) can move in its glide plane along the dislocation line until it recombines with another kink with the opposite sign. Similar to the previous Chapter, periodic boundary conditions are applied along the dislocation line. However, due to their difference in underlying atomistic mechanisms, the kMC algorithm for BCC metals here is somewhat different from that for Si, as will be discussed in more detail in following sections.

8.1.2 Double-kink Nucleation

Atomistic simulations using empirical many-body potential MGPT [162] have calculated kink pair nucleation energy barrier on screw dislocations in Mo to be around 2eV, in the absence of external stress. When the resolved shear stress reaches the Peierls stress $\tau_p = 2\text{GPa}$, screw dislocations can move as a whole, hence the double kink nucleation energy is zero. While no similar atomistic data are available for stress values in between², Edagawa's line tension model [212] provides a reasonable description of the variations of the double-kink nucleation energy as a function of loading stress. Combining Edagawa's model with the atomistic data [162], Bulatov [230] calculated and tabulated the double-kink nucleation energy H_{dk} as a function of the magnitude τ of and loading angle χ , which is the angle between the maximum resolved shear stress (M.R.S.S.) plane and the corresponding (110) glide plane. The tabulated data was then fitted to a simple functional form of $H_{dk}(\tau, \chi)$, which is then used to calculate the kink pair nucleation rates,

$$j_{dk} = \omega_0 \exp \left(-\frac{H_{dk}(\tau, \chi)}{k_B T} \right), \quad (8.1)$$

²Recently, atomistic calculations using embedded-atom method (EAM) potentials on screw dislocations in Fe have obtained double-kink nucleation energy on screw at finite shear stress [70]. We are currently performing similar calculations for Mo.

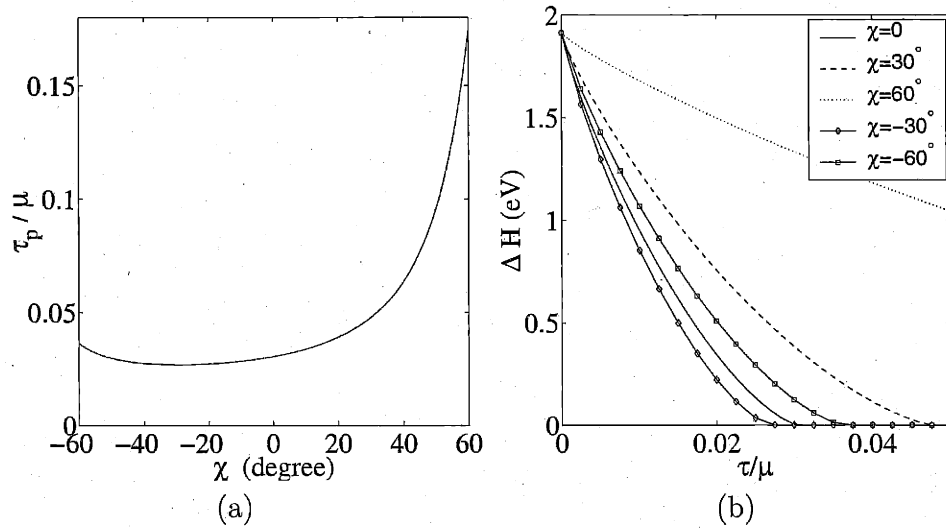


Figure 8-2: (a) Peierls stress τ_p as a function of loading angle χ (see text). (b) Double kink nucleation energy ΔH as a function of loading stress τ at different angle χ . Both predicted by the line tension model [212] taking only a single energy parameter from atomistic calculations, i.e. the core energy difference between hard and easy cores.

where ω_0 is an attempt frequency factor, and is set equal to the *Debye frequency* ($\omega_0 = 9.3768 \times 10^{12} \text{Hz}$) of Mo in this work. It needs to be emphasized that Eq. (8.1) is only an approximation. The effect of core polarization (see Chapter 6) and the effect of non-glide stresses (non-Schmid effect) are ignored, due to the lack of accurate atomistic data.

The double-kink nucleation energy takes the functional form of

$$H_{dk}(\tau, \chi) = H_0 \left[1 - \left(\frac{\tau}{\tau_p(\chi)} \right)^p \right]^q, \quad (8.2)$$

where $\tau_p(\chi)$ is the orientation dependent Peierls stress and is plotted in Fig. 8-2(a). Fig. 8-2(b) shows H_{dk} as a function of M.R.S.S. τ at several loading angles. It should be emphasized that only a single energy parameter is taken as input in this line tension model, which is the hard and easy core energy difference [162]. We observe that the line tension predicts $H_{dk} = 1.91 \text{eV}$ at zero shear stress, in good agreement with atomistic result of 2eV [162]. However, the predicted Peierls stress seems to be larger

than 2GPa as from atomistic calculations. In Fig. 8-2(a) the minimum Peierls stress is around 0.025μ which is around 3GPa if we take $\mu = 123\text{GPa}$ for Mo. On the other hand, the line tension model does capture the twinning-antitwining asymmetry of the host BCC lattice, in that the $\tau_p(\chi)$ plot in Fig. 8-2(a) is asymmetric with respect to $\chi = 0$, and is smaller in the $\chi < 0$ region (in favor of twinning). However, whether or not the minimum Peierls stress occurs at $\chi = -30^\circ$ as predicted by the line tension model is worth checking by direct atomistic simulations. In conclusion, the line tension model provides a reasonable description of stress assisted double-kink nucleation energy. But it should be replaced by the more accurate atomistic simulation data whenever they become available.

8.1.3 Kink Migration and KMC Algorithm

In contrast to the high Peierls barrier for kink pair nucleation, kink motion along screw dislocations in Mo is extremely easy, as manifested in the low kink (or secondary) Peierls barrier ($\sim 0.0005\text{eV}$), given by atomistic calculations [231] using the Finnis-Sinclair empirical potential. Such a low energy barrier means that kink migration along the screw dislocation does not require thermal activation and its speed is only limited by its interaction with phonons. Because the kinks on a screw dislocation can be viewed as short segments with non-screw component, their high mobility is consistent with recent Molecular Dynamics (MD) simulations of edge dislocations motion [179] in Mo using the same potential. Therefore, we model the kink velocity as proportional to the local stress, i.e.

$$v_k = \tau_g b / B , \quad (8.3)$$

where τ_g is the glide component of the resolved shear stress, b is the Burgers vector, and B is defined as the phonon drag coefficient. Our preliminary MD simulations have lead to the prediction of the drag coefficient $B = 4.5 \times 10^{-5}\text{Pa}\cdot\text{s}$.

Kink migration as described by Eq. (8.3) is deterministic, so that it cannot be treated in the same way as in Si (see Chapter 7). A new kMC algorithm is then

needed, which is briefly described below.

1. At the beginning of each kMC step, stress is calculated along the entire dislocation line, which determines double-kink nucleation rate on H-segments and kink velocity of V-segments through Eqs.(8.1) and (8.3) respectively.
2. Assuming that all the kinks move with constant velocity calculated at this moment, a migration time t_{mig} is then computed as the upper limit of the time before any kink has moved for more than a prescribed distance, and before any kink pair annihilation or debris dislocation loop formation (see next Section).
3. A nucleation time t_{nuc} is generated as a random number from the exponential distribution defined by the total nucleation rate. The latter is calculated by summing up kink pair nucleation rates on all H-segments.
4. If $t_{mig} < t_{nuc}$, then all kinks move with the current velocity for a time period t_{mig} . If any kink pair recombination or debris loop formation events are detected, they are carried out and the algorithm returns to step 1. Otherwise, the kinks move with their current velocities for a time period t_{nuc} , followed by a kink pair nucleation on an H-segment. The nucleation site is chosen according to the local nucleation rates by a standard kMC algorithm [222]. Return to 1.

8.2 Super Jog and Debris Loop

Because double-kink nucleation is now allowed on three different planes, an immediate consequence that need to be handled during the simulation is the formation of super jogs on the screw dislocation and debris loops left behind the moving dislocation (as mentioned in step 2 of the kMC algorithm in the previous Section). This process starts when two kink pairs form spontaneously on two different (110) planes. As illustrated in Fig. 8-3(a), when these two kinks move towards each other and collide, they cannot recombine. Because they are pushed towards each other by external stress the kinks are now constrained to move together, forming a super jog. In such

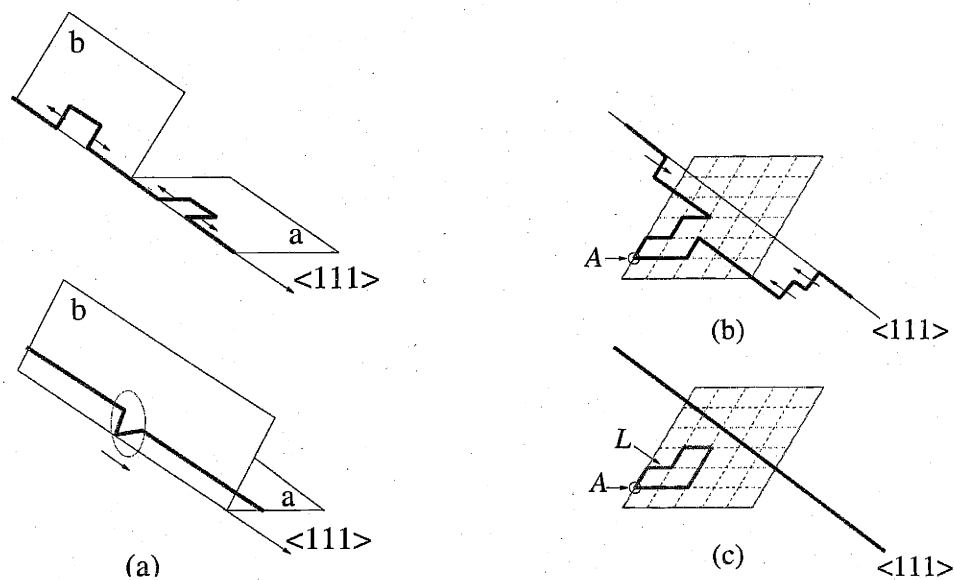


Figure 8-3: Schematic representation of the formation of (a) two kinks forming an elementary super jog (or cross-kink), (b) more kinks joining the super jog, and (c) debris loop L formation with the primary dislocation breaking away from the self-pinning point A .

cases the forces on the two cross kinks act in the opposite directions along the line and the cross kinks can slow down or halt their coupled motion altogether. Such elementary super jog will grow in size when more kinks pile up on either sides of the initial pinning point (A) forming super jogs [30] (p. 261), as shown in Fig. 8-3(b). Again, due to the easy cross-slip, the kinks in the pile-ups on two sides of the pinning point may belong to different planes. Consequently, projections of the two developing pile-ups on the $[111]$ plane appear similar to two random walk trajectories originating from the same point (initial cross kink) on a two-dimensional lattice. If and when two such trajectories cross each other again, the dislocation line may reconnect by recombination of kink pairs. As a result, the two pile-ups are now reduced in size leaving behind a prismatic (debris) loop L , shown in Fig. 2(c).

Fig. 8-4 shows the continuous formation of debris dislocation loops in the wake of the moving dislocation. In this plot, the H segments are significantly shrunk compared to the V segments in order to show the entire dislocation line; the total

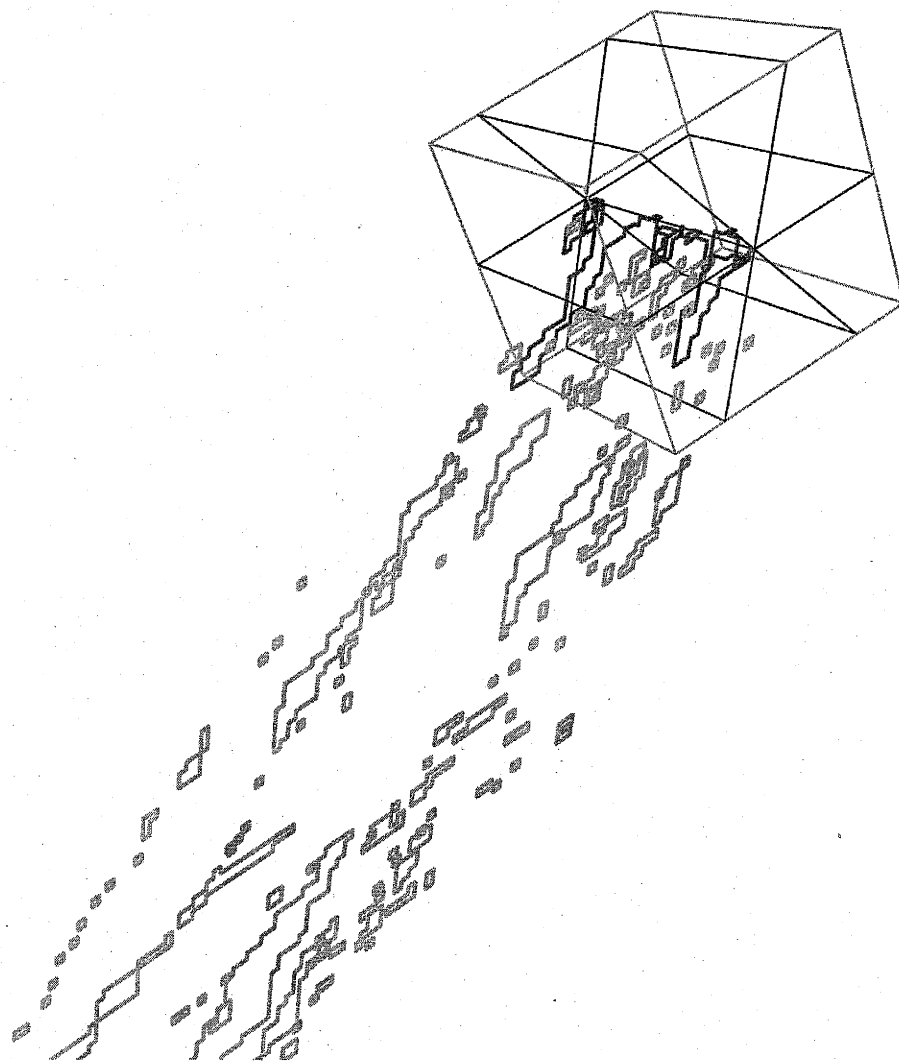


Figure 8-4: Snapshot of kMC simulation showing debris loops left in the wake of the moving screw dislocation. segments are significantly shrunken compared to the V segments in order to show the entire dislocation line; the total length of the H segments are in fact $27\mu m$ while each V segment is only 2.5\AA . Linear elastic interactions were ignored in this simulation.

length of the H segments are in fact $27\mu m$ while each V segment is only 2.5\AA . Linear elastic interaction between kinks were ignored in this particular simulation, so that it corresponds to an "ideal gas" model. An even more simplified model for the size distribution of debris loops is presented in Appendix C.4, in which the growth of two arms of the super jog is treated as 2-dimensional random walks. Although elastic interactions between kinks are also ignored in this model, it nonetheless leads to some interesting results, such as the slow decay of the distribution function in the large loop size limit. This means that there is always appreciable probability of finding very large sized loops, in apparent agreement of experimental observations (see Fig.3-15).

The occurrence of the above mentioned mechanism depends most critically on the loading stress, and also on temperature and the length of the dislocation. At low temperature and low stress, there is always at most one kink pair on the entire dislocation, which quickly moves apart and annihilate with its PBC images. In this case, the dislocation velocity is double-kink nucleation controlled, and is proportional to dislocation length, in agreement with earlier theories [71].

At a higher stress and/or higher temperature, kink pair nucleation rates increase dramatically. Consequently, a large number of kinks may be simultaneously present on the dislocation line in which case dislocation velocity becomes length-independent. In this case, the super jog and debris loop mechanism could operate. It is observed that this process would also occur even at lower stresses, if the simulation runs long enough, given the stochastic nature of the double-kink nucleation process. Recent TEM experiments [232] in Mo seems to agree with this analysis, showing loop formation at higher strain rate ($1s^{-1}$) but not at lower strain rate ($10^{-3}s^{-1}$). It is also observed that the rate of loop formation is material dependent, with loops forming more easily in Ta than in Mo. This is apparently related with the large shear modulus in Mo, giving rise to a higher energy barrier for the two arms of the super jog to form a closed loop.

The occurrence of the pinning points and kink pile-ups significantly affects the dislocation mobility. They act as intrinsic obstacles which can be overcome only by

slow side-way migration of the super jogs along the line leading to possible partial recombination with other super jogs, or by formation of prismatic debris loops left in the wake of the moving dislocation. In either case, a large amount of work is absorbed to help the screw dislocation overcome the linear elastic interactions of these microstructures. Not surprisingly, it has been proposed [116] that the cusps (super jogs) on the screw dislocation contribute a major part of the observed macroscopic yield strength, in comparison with the intrinsic lattice resistance. This mechanism was also postulated to explain the yield stress anomaly in γ -TiAl alloy [233].

At the same time, super jog formation also creates technical difficulty for kMC simulations. The kinks in these pile-ups tend to oscillate frequently between neighboring positions on the dislocation line, making no contribution to the overall dislocation displacement. This is similar to the fast processes of kink pair nucleation and recombination in the case of Si. Unless some sort of special treatment of such uninteresting events is applied, the simulation will become progressively less efficient as the kink pile-ups grow larger. Current work in progress involves approximating all the kinks in a pile-up as a single dislocation segment, in order to speed up the simulation.

8.3 Orientation Dependence of Dislocation Mobility

In this section, we discuss the effect of the shear stress orientation on super jog and debris loop formation and consequently on the dislocation mobility. Fig. 8-5 shows two snapshots of kMC simulations of screw dislocation motion at 373K under 320MPa shear stress with different orientations of the M.R.S.S. plane. In these plots, the H segments are significantly shrunk compared to the V segments in order to show the entire dislocation line; the total length of the H segments are in fact $27\mu m$ while each V segment is only 2.5\AA . In Fig. 8-5(a), the M.R.S.S. plane bisects two glide planes a and b , making kink pair nucleation equally probable on both planes. Cross-kinks and debris loops are readily observed in this case. In Fig. 8-5(b), the M.R.S.S.

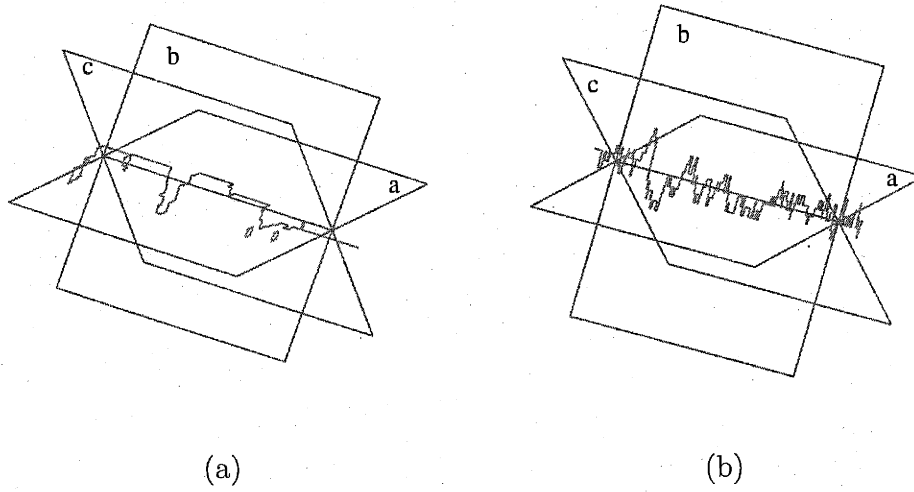


Figure 8-5: Snapshots of kMC simulations of screw dislocation motion at 373K under 320MPa resolved shear stress with different orientations. (a) M.R.S.S. plane bisects the glide plane a and b , with super jogs and debris loops readily observed. (b) M.R.S.S. plane is parallel to glide plane b . The dislocation moves only in this plane. The larger resolved shear stress on the glide plane results in a much higher kink density.

plane is parallel to glide plane b and double-kinks mostly nucleate on this plane. In addition, the resolved shear stress on the glide plane (b) is much larger than that in the previous case, resulting in a much higher kink density.

Similar to Chapter 7, dislocation velocity is extracted from the simulation by fitting the slope of the curve for the instantaneous average dislocation position as a function of time. We find that the above two different orientations of M.R.S.S plane lead to two different dislocation mobility behaviors. In case (a), the averaged double-kink nucleation rate per lattice site on plane a is $j_{dk} = 1.5 \times 10^5 b^{-1} s^{-1}$, and the averaged kink velocity is $v_k = 6.2 \times 10^{12} b \cdot s^{-1}$, where b is the Burgers vector. The overall dislocation velocity along plane a is found to be $v = 6.8 \text{ cm} \cdot s^{-1}$, which would be about half of what the kink diffusion model of Hirth and Lothe would predict [30], $v_{HL} = \sqrt{2} h (J v_k)^{1/2} = 11 \text{ cm} \cdot s^{-1}$. On the other hand, in case (b), $j_{dk} = 1.3 \times 10^7 b^{-1} s^{-1}$, $v_k = 7.1 \times 10^{12} b \cdot s^{-1}$, dislocation velocity of $v = 343 \text{ cm} \cdot s^{-1}$ obtained in the kMC simulation is in agreement with the kink diffusion model prediction of

$v_{HL} = 349 \text{ cm} \cdot \text{s}^{-1}$. The reason for such a considerable difference between the two models in the case (a) is that, in our model, spreading of kink pairs is constrained by pile-ups formed at cross kinks. In the presence of such pinning points many kink pairs eventually recombine with themselves and do not contribute to the overall dislocation motion.

Compared with the previous Chapter on Si, the kMC study in BCC metals is still in the beginning stage. Current work involves improving the efficiency of simulation algorithm when kink pile-up occurs and a systematic study of dislocation velocity at different temperature and stresses. The mobility data obtained from this model can serve as inputs for larger scale dislocation dynamics (DD) simulations, which study the behavior of a large collection of dislocations to model the deformation strength of a single crystal.

Chapter 9

Nodal Dislocation Dynamics

9.1 Introduction

While so far we have only discussed mobility of a single dislocation, in this Chapter we will address some problems concerning dislocation dynamics (DD), which was developed [234] to model the collective behavior of an assembly of dislocations, and has been envisioned as the link between single dislocation behavior and the plasticity strength of a single crystal [235, 236].

To date, several formulations for DD simulations have been proposed and implemented, with different discretization approaches and hence the governing equations of motion. These include representing a continuous dislocation line by pure edge and screw segments [234]¹, by a string of connected segments with arbitrary orientation [237, 238], or by a series of cubic splines [239]. However, there seems to be some controversy on how to calculate the dislocation driving force. It was found that when dislocations are discretized into straight segments, the stress diverges at the end points of each segment, creating problems if the driving force on each segment is defined as the average stress on them. An cut-off radius was introduced around segment ends to remove this singularity [240]; however, this approach was not satisfactory due to the arbitrariness of the cut-off radius. In this Chapter, we will show

¹Recently, mixed dislocation segments with a particular orientation is added for a better representation of dislocation loops.

that such a cut-off radius is unnecessary and the equation of motion for a system consisting of straight dislocation segments is well defined. We will show that the stress singularity problem can be regularized systematically by considering the interaction energy between adjacent segments.

Generally speaking, the current approaches for DD simulations can be classified into two categories. In the first case, one focuses on dislocation segments [237, 238], and the forces on the segments are calculated through the average stress on them, as mentioned above. At every timestep, the segments are displaced according to these forces. However, after displacing the segments, they are no longer connected, if their lengths are kept fixed, so that the dislocation becomes “broken”. Therefore, one will have to use some *ad hoc* technique to “glue” the segments back together again. The violation of the dislocation continuity in this approach is connected with the driving force divergence problem mentioned above.

In the second approach, the continuity of the dislocation is preserved at all times during the simulation. One focuses on generalized coordinates (such as nodes) describing a continuous dislocation line and compute the generalized forces on these coordinates. For example, when dislocations are represented as splines [239], it has been shown that no driving force singularity problem arises, if the driving force is defined as the derivative of the total (free) energy with respect to the spline parameters. In this Chapter, we will show that this is also the case if dislocations are discretized into peicewise straight segments, and that the driving force remains well defined even though the dislocations have sharp corners. The robustness of our method in handling sharp corners is advantageous, because they do exist on real dislocations, such as at the intersection between two slip planes, and at the junction node where three dislocations meet.

This approach is illustrated in Fig. 9-1, where the dislocations are represented as a set of nodes $(\vec{r}_1, \vec{r}_2, \dots, \vec{r}_n)$, connected by straight segments. If we ignore the kinetic energy for simplicity, the total energy of the system H is only the elastic interaction between the segments, plus their self energies. When inertia effects are ignored, we

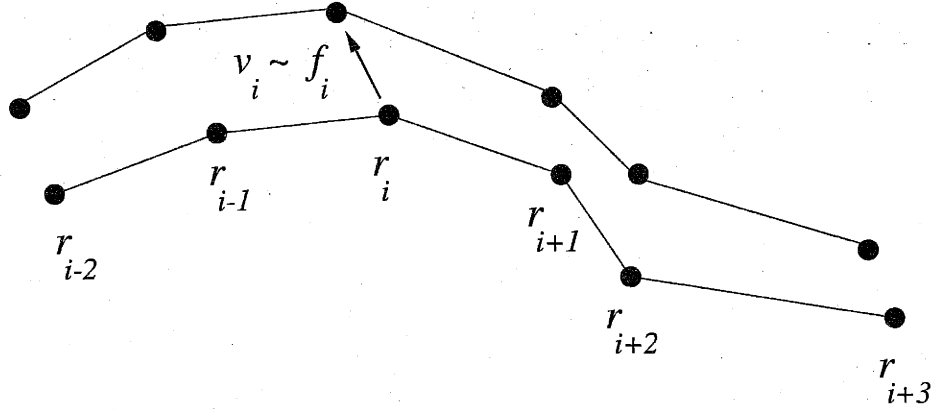


Figure 9-1: Representation of dislocation as linked nodes. The motion of nodes after each times step gives the dislocation motion.

can write down an equation of motion for the nodes as

$$\vec{f}_i = -\frac{\partial}{\partial \vec{r}_i} H(\{\vec{r}_j\}), \quad (9.1)$$

$$\vec{v}_i = D\vec{f}_i, \quad (9.2)$$

where f_i and v_i are nodal force and velocity respectively, and D is a damping ratio. Eq. (9.2) is only empirical and is helpful to relax a certain dislocation structure to a minimum energy configuration. However, it does not necessarily describe the true dynamics of the dislocation, especially when the segments do not have the same length. We will give a more rigorous derivation of the nodal equation of motion in Section 1.

Interestingly, this method has already been implemented by Ramirez et al. [241] to simulate dislocation glide in 2-dimension. However, when applying this approach directly to 3-dimension DD simulations, one is confronted with great technical difficulties. The form of the interaction energy between two generally oriented dislocation segments is very complicated, let alone its derivatives. To make things worse, the general formula becomes numerically unstable when the two segments become close to coplanar or parallel and different formulas have to be used in these special cases. This is probably the reason that most 3-dimensional DD simulations use stresses,

instead of the energy derivatives, as the dislocation driving force. The purpose of this Chapter is to develop an energy based DD formulation that is also practical enough to implement. As we will show in Section 3, the evaluation of the segment interaction energies is only necessary for segments that are adjacent to each other, which is coplanar by definition. The interaction energies between well separated segments can be rewritten in the form of stresses.

9.2 Equation of Motion

In this section, the equation of motion for a set of nodes r_1, r_2, \dots, r_n is derived, assuming that the dislocation velocity is limited by phonon drag, and that the dislocation inertia effect (kinetic energy) is negligible. The basis of this derivation is that the decrease total elastic energy is all dissipated into heat, through the dislocation-phonon interactions². The decrease rate of the total elastic energy can be written as a summation of nodal contributions,

$$-\frac{d}{dt}H = -\sum_i \frac{\partial H}{\partial \vec{r}_i} \cdot \frac{d\vec{r}_i}{dt} \quad (9.3)$$

$$\equiv \sum_i \vec{f}_i \cdot \vec{v}_i. \quad (9.4)$$

The phonon dissipation energy, on the other hand, has to be summed over segment contributions. For the sake of simplicity, we constrain the motion of every node i along a pre-specified direction \vec{t}_i , so that $\vec{v}_i = v_i \vec{t}_i$. Also define $f_i = \vec{f}_i \cdot \vec{t}_i$. This constraint is not unreasonable, because the motion of dislocation is usually confined to its glide plane and the drift of a node along the dislocation line does not change the dislocation at all. Therefore, there is only meaningful direction of motion for each node. The directions of \vec{t}_i can also change during the simulation, corresponding to the change of topological constraint of the dislocation. This is a generalization of the “abacus” model of Li [199], in which \vec{t}_i is the same for all nodes and does not

²Dr. Ju Li has expressed the same idea in our discussions.

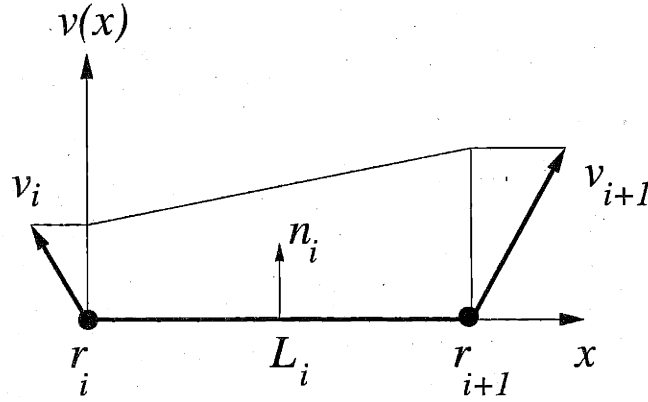


Figure 9-2: Velocity distribution on dislocation segment r_i-r_{i+1} .

change during the simulation. As the direction of motion can be calculated at each simulation step from topological constraints, the remaining task is to determine the scalar velocity v_i for each node.

Define L_i as the length of the segment r_i-r_{i+1} , and \vec{n}_i as the vector orthogonal to the segment and within the same plane as \vec{t}_i and \vec{t}_{i+1} , as shown in Fig. 9-2. The energy dissipation rate of this segment is then,

$$\dot{E}_{\text{diss}}(i) = B \cdot L_i \int_0^1 dx [v_i(\vec{t}_i \cdot \vec{n}_i)(1-x) + v_{i+1}(\vec{t}_{i+1} \cdot \vec{n}_i)x]^2 \quad (9.5)$$

$$= B \cdot L_i \frac{1}{3} [v_i^2(\vec{t}_i \cdot \vec{n}_i)^2 + v_{i+1}^2(\vec{t}_{i+1} \cdot \vec{n}_i)^2 + v_i v_{i+1}(\vec{t}_i \cdot \vec{n}_i)(\vec{t}_{i+1} \cdot \vec{n}_i)] \quad (9.6)$$

$$= B \cdot L_i \frac{1}{3} [v_i^2 \alpha_i^2 + v_{i+1}^2 \beta_{i+1}^2 + v_i v_{i+1} \alpha_i \beta_{i+1}] \quad (9.7)$$

where B is the phonon drag coefficient, $\alpha_i = (\vec{t}_i \cdot \vec{n}_i)$, $\beta_i = (\vec{t}_i \cdot \vec{n}_{i-1})$. The total energy dissipation rate is then

$$\begin{aligned} \dot{E}_{\text{diss}} &= \sum_i \dot{E}_{\text{diss}}(i) \\ &= \sum_i B \left[\frac{1}{3} (L_i \alpha_i^2 + L_{i-1} \beta_i^2) v_i^2 \right. \\ &\quad \left. + \frac{1}{6} L_i \alpha_i \beta_{i+1} v_i v_{i+1} + \frac{1}{6} L_{i-1} \beta_i \alpha_{i-1} v_{i-1} v_i \right] \end{aligned} \quad (9.8)$$

Equating \dot{E}_{diss} in Eq. (9.8) with $-dH/dt$ in Eq.(9.4), we construct the equation of motion for each node,

$$\frac{1}{3}(L_i\alpha_i^2 + L_{i-1}\beta_i^2)v_i + \frac{1}{6}L_i\alpha_i\beta_{i+1}v_{i+1} + \frac{1}{6}L_{i-1}\beta_i\alpha_{i-1}v_{i-1} = f_i/B \quad (9.9)$$

In other words, in order to obtain nodal velocity v_i , one needs to solve a set of linear equations

$$\sum_j A_{ij}v_j = f_i/B, \quad (9.10)$$

where the elements of matrix A are

$$A_{ij} = \begin{cases} \frac{1}{3}(L_i\alpha_i^2 + L_{i-1}\beta_i^2), & j = i \\ \frac{1}{6}L_i\alpha_i\beta_{i+1}, & j = i + 1 \\ \frac{1}{6}L_{i-1}\beta_i\alpha_{i-1}, & j = i - 1 \\ 0, & \text{otherwise} \end{cases} \quad (9.11)$$

In the limit of $L_i \approx L_{i+1} \approx L$ and $\alpha_i \approx \beta_i \approx 1$, matrix A becomes

$$A = \frac{L}{6} \begin{bmatrix} 1 & 4 & 1 & \dots \\ & 1 & 4 & 1 & \dots \\ & & 1 & 4 & \dots \\ & & & \dots \end{bmatrix} \quad (9.12)$$

A first order approximation of v_i would be

$$v_i = \frac{f_i}{BL}, \quad (9.13)$$

which is equivalent to Eq. (9.2) with $D = (BL)^{-1}$. However, it is only an approximate solution of Eq. (9.10) and (9.11).

To avoid solving the linear system Eq. (9.10) directly, one can calculate v_i itera-

tively. First, assuming $v_i \approx v_{i+1} \approx v_{i-1}$, one has the zeroth order approximation,

$$v_i^0 = fB^{-1} \left[\frac{1}{3}(L_i\alpha_i^2 + L_{i-1}\beta_i^2) + \frac{1}{6}L_i\alpha_i\beta_{i+1} + \frac{1}{6}L_{i-1}\beta_i\alpha_{i-1} \right]^{-1} \quad (9.14)$$

This solution can be improved by the following iteration, till satisfactory accuracy is reached,

$$v_i^{k+1} = \left[fB^{-1} - \frac{1}{6}L_i\alpha_i\beta_{i+1}v_{i+1}^k - \frac{1}{6}L_{i-1}\beta_i\alpha_{i-1}v_{i-1}^k \right] \left[\frac{1}{3}(L_i\alpha_i^2 + L_{i-1}\beta_i^2) \right]^{-1} \quad (9.15)$$

In conclusion, the nodal equation of motion is

$$\sum_j A_{ij}v_j = \frac{f_i}{B} = -\frac{1}{B} \frac{\partial}{\partial \vec{r}_i} H(\{\vec{r}_j\}) \cdot \vec{t}_i, \quad (9.16)$$

with matrix elements A_{ij} specified in Eq. (9.11).

9.3 Nodal Driving Force

In this section we develop a practical approach of calculating nodal driving force in 3-dimension. We show that for two segments that are well separated, their interaction can be represented in terms of stress fields. For two segments sharing a common node and for self interactions, explicit derivative of the elastic energy is needed. Special care need to be taken when combining these two methods, because both are meaningful only for complete dislocation loops.

For a dislocation consisting of straight segments as shown in Fig. 9-3, the driving force on node P is,

$$F_P = -\frac{\partial H}{\partial x_P}, \quad (9.17)$$

where H is the total elastic energy of the dislocation, which is the summation of self energies of all segments and interaction energies between them, i.e.

$$H = W_A + W_B + W_C + W_D + W_E$$

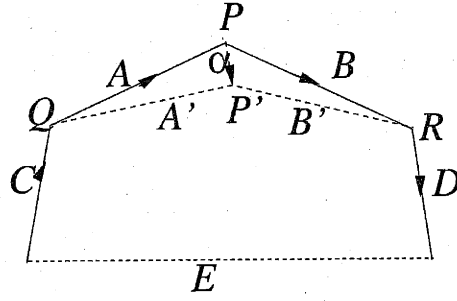


Figure 9-3: Dislocation discretization into segments.

$$\begin{aligned}
 & + W_{AB} + W_{AC} + W_{AD} + W_{AE} \\
 & + W_{BC} + W_{BD} + W_{BE} \\
 & + W_{CD} + W_{CE} \\
 & + W_{DE} ,
 \end{aligned} \tag{9.18}$$

where W_A is the self energy of segment A and W_{AB} is the interaction energy between A and B , etc. Therefore,

$$\begin{aligned}
 \frac{\partial H}{\partial x_P} &= \frac{\partial}{\partial x_P} (W_A + W_B + W_{AB} + W_{AC} + W_{BD} \\
 & + W_{AD} + W_{AE} + W_{BC} + W_{BE}) .
 \end{aligned} \tag{9.19}$$

For dislocation segments that are not adjacent each other, their interaction change can be written as the integration of the stress field over the area swept by the dislocation,

$$\frac{\partial}{\partial x_P} [(W_{A,C+D+E}) - (W_{\alpha,C+D+E})] = \frac{\partial}{\partial x_P} \oint_{QP'P} dS \tau_{C+D+E} \tag{9.20}$$

$$\frac{\partial}{\partial x_P} [(W_{B,C+D+E}) + (W_{\alpha,C+D+E})] = \frac{\partial}{\partial x_P} \oint_{PP'R} dS \tau_{C+D+E} , \tag{9.21}$$

where α is the differential segment PP' introduced to complete the dislocation loops $PP'Q$ and $PP'R$. τ_{C+D+E} represent the superposition of the stress fields of C , D , E

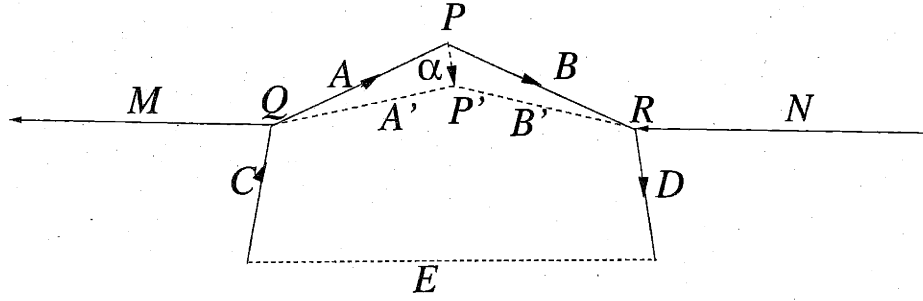


Figure 9-4: Introducing semi-infinite segments M and N for nodal force calculation.

segments. Therefore,

$$\frac{\partial H}{\partial x_P} = \frac{\partial}{\partial x_P} \left[W_A + W_B + W_{AB} + \oint_{QP'P+PP'R} dS \tau_{C+D+E} \right] \quad (9.22)$$

The prominent feature of Eq. (9.22) is that the contributions from segments shearing node P is treated with explicit energy formula, while far away segments are treated with stress fields. As will be shown later, the interaction energy for two segments with a common node takes a much simpler form than segments with general orientations. At the same time, stress fields of far away segments does not lead to singular nodal forces. Therefore, Eq. (9.22) provides a practical approach of computing nodal forces that is free from singularities. Unfortunately, Eq. (9.22) is not rigorously correct, because both energy and stress formula for dislocation segments are meaningful only when contributions of all segments forming a complete loop is summed together. In Eq. (9.22), neither the energy nor the stress terms form complete loops by themselves, which will lead to uncontrollable error.

Fortunately, this problem can be easily fixed, by introducing semi-infinite dislocation segments M and N to complete both loops, as shown in Fig. 9-4, which leads to

$$\begin{aligned} \frac{\partial H}{\partial x_P} = & \frac{\partial}{\partial x_P} [W_A + W_B + W_{AB} - W_{A+B,M+N} \\ & + \oint_{QP'P+PP'R} dS \tau_{M+C+D+E+N}] , \end{aligned} \quad (9.23)$$

where $W_{A+B,M+N} = W_{AM} + W_{AN} + W_{BM} + W_{BN}$. Segments M and N are co-linear with line QR , so that all the interaction energy terms in Eq. (9.23) are for co-planar segments, which have a very simplified form. As mentioned above, W_{AM} is infinite because of the infinite length of M . However, the derivative of W_{AM} with respect to x_P can be shown to be finite. The derivations of several terms in Eq. (9.23) are given in Appendix D.

9.4 Prismatic Loop and Super Jog

As a proof of principle, we compute the nodal driving force for a circular prismatic dislocation loop, as shown in Fig. 9-5. The Burgers vector is out of the plane. The total energy and nodal driving force at different number of nodes (N) are compared with analytical solutions [30] in Fig. 9-6. Both energy and driving force are converging to analytic solutions (solid lines) for large N . This result is clearly better than that of the stress approach using a cut-off radius [240], which reported divergence at large N and dependence of driving force on the choice of cut-off radius.

The development on Nodal Dynamics is still in progress. Current work involves using it to study the process of super jog growth and debris loop formation on screw dislocations in BCC metals, as illustrated in Fig. 9-7. The objective here is to determine the critical stress at which debris loops is formed, which will serve as an input for mesoscale dislocation mobility models (see Chapter 8).

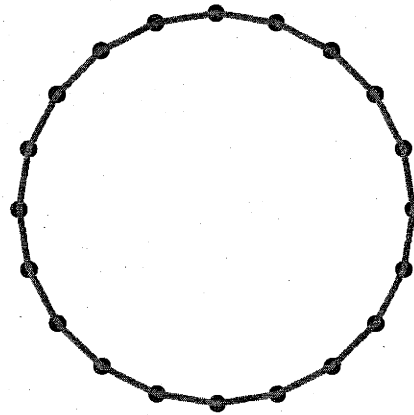


Figure 9-5: A circular prismatic dislocation loop discretized into linear segments connecting a set of equally spaced nodes. Number of nodes $N = 20$.

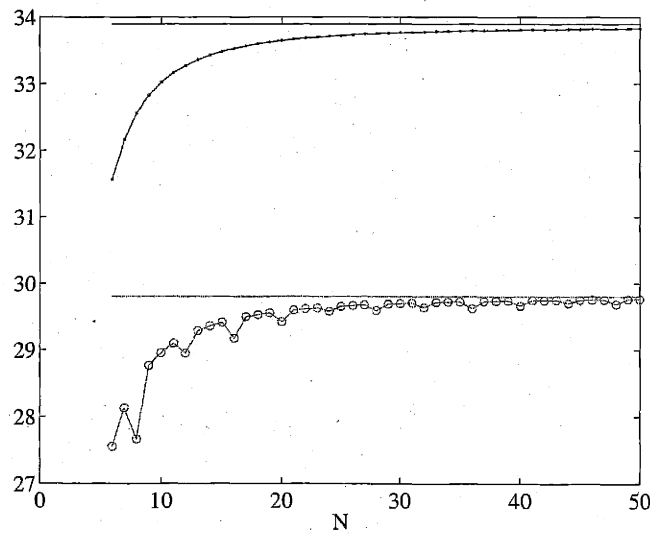


Figure 9-6: Total energy (○) and nodal driving force (●) of prismatic dislocation loop, as a function of node number N . Both energy and driving force are converging to analytic solutions (solid lines) for large N .

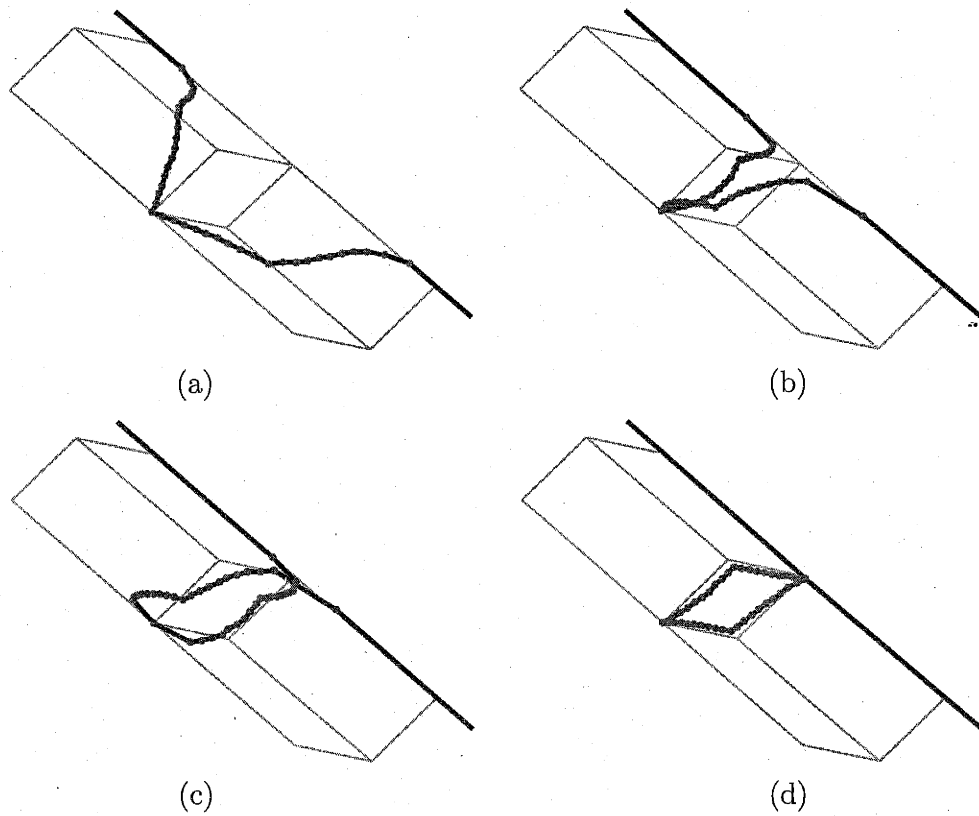


Figure 9-7: Super jog on screw dislocations in BCC metals represented by Nodal Dynamics. (a), (b) and (c) are equilibrium configurations under progressively larger shear stress. In (d) a prismatic loop is formed by joining the two arms of the super jog. Shear stress is removed after the loop forms.

Chapter 10

Summary and Outlook

This Thesis has presented five studies in dislocation mobility modeling to highlight the particular challenge of linking atomistic and meso scales. Each represents a specific contribution where only one scale is treated explicitly while the effects of the other are taken into account through a coupling of type (a) or (b). It is noteworthy that the energy of interaction, whether atomistic or elastic in nature, plays a central role in the proper treatment of the coupling effects.

As we have illustrated, proper coupling of an atomistic region to its larger surrounding can resolve effects that are not physical in origin or become important for avoiding simulation artifacts associated with unphysical constraints. For atomistic simulation of dislocations in a periodic cell, we have derived a rigorous method for calculating the anisotropic elastic energy due to the artificial effect of the periodic boundary conditions. This allows the extraction of dislocation core energy that is manifestly invariant with atomistic simulation cell sizes. This method also leads to the design of atomistic cell geometries for which the artificial image stress on dislocations can be completely canceled.

An even more clear-cut case of type (a) coupling is the simulation of an atomistic region embedded in an elastic continuum surrounding. Through a systematic study of linear response theory, we have derived a boundary condition for dynamically coupling the two domains for which the spurious reflection of elastic waves across the domain boundary is minimized. This method provides a rigorous solution in atomistic

simulations of dynamic processes where interactions with phonons are important, such as crack propagation and dislocation motion. While so far we have focused on the atomistic simulation domain only, opportunities exist in combining this method with the quasi-continuum method [242], or coarse grain MD [191], so that an atomistic simulation can be coupled with a coarse grained method while still maintaining the correct dynamics in the former.

In type (b) coupling, on the other hand, the emphasis is on combining atomistic mechanisms and a mesoscale mechanistic description in modeling dislocation motion. We have presented several recent results on the dislocation core and kink mechanisms in Si and BCC Mo. Our calculations on the kink energies have shed new light on the interpretation of the long standing shuffle-glide controversy in Si. And a better treatment of boundary condition has allow us to determine the “true” Peierls stress of edge dislocation in Mo, which is much smaller than previously reported. This result leads to a deeper understanding of the mechanism of motion of edge dislocations and naturally explains their high mobility.

The atomistic-mesoscale coupling becomes most apparent when the atomistic kink mechanisms are used as the basis to construct our mesoscale kinetic Monte Carlo (kMC) model of dislocation motion. In the case of Si, where the dislocation dissociation into partials has been taken into account, our approach leads to a qualitative agreement between the predicted mobility data and experimental results. While previous explanation of the low stress dislocation mobility behavior has relied on *ad hoc* assumptions such as “weak obstacles”, our results suggests that they are not necessary, and that the coupling effect between the partials is enough to give either a linear or a sublinear behavior of stress dependence, depending on the commensurability between partial separation and the lattice periodicity. This has also leads to a new prediction of non-monotonic stress-velocity dependence for a given loading condition. Evidently, an experimental verification or invalidation of this prediction would be highly informative towards a definitive understanding on the modes of dislocation motion in Si.

We have generalized our kMC model for Si and incorporated the effect of cross

slip for studying the motion of screw dislocations in BCC metals. We found that cross slip of these dislocations automatically leads to several new mechanisms that generates cusps and debris loops from an initially straight dislocation, which produces a marked effect on dislocation mobility, and a microstructure that resembles experiment observations. While these results are still preliminary, further study along this direction would need to include the interaction between the dislocation and debris loops, which could be left behind by a previous dislocation.

In our last contribution, we developed a new formulation of dislocation dynamics (DD) simulations focusing on dislocation nodes. The conventional stress singularity problem was removed by using the concept of local interaction energies. This leads to a convergence behavior when a dislocation line is represented into progressively more segments, while an previous artificial cutoff scheme has resulted in divergence.

Now at the end of this Thesis, which so far has been focused on single dislocation mobilities, it is natural to raise the question: what is coming next? Evidently, more studies towards clarifying the atomistic details of dislocation motion are still needed. However, it seems now critical to start connecting the understandings about single dislocations with materials behavior at an even larger scale. In Chapter 1 we have discussed that there is an opportunity to predict macroscopic plastic deformation behavior of a single crystal, base on underlying physics that focuses primarily on dislocations. This opportunity now becomes more realistic as we can start to develop large scale dislocation dynamics (DD) simulations that will benefit from our recent formulation in Chapter 9, and incorporate understandings on single dislocations in other Chapters. In order for the DD model to be able to make meaningful predictions, the challenges here are, whether we can afford to simulate enough number of dislocation segments, and whether we can reproduce experimentally observed dislocation microstructures. Regarding the size limitation on current DD simulation efforts, it is reasonable to expect that at least in studying large strain deformations, we would need to transfer the information generated by discrete DD simulations to a field theory of dislocations that describes the lattice deformation at a more coarse grained level. Further developments on dislocation field theories are also needed, to go beyond a

mean-field type approach [243] and to include spatial gradients and dislocation flux.

That would get us to single crystals. But to resolve the discrepancy between experiments and theoretical models such as shown in Fig. 1-1, which is on polycrystal Ta, we will need to incorporate the effects of multiple grains and grain boundary activities. While all of these looks pretty straightforward, at least in principle, we have to remind ourselves that we are still within a small corner of reality. Even if we succeed in obtaining a detailed understanding on the strength of a crystal, there is still a long way to go before we can comprehend and start mimicking the microstructural effects on the strength of a living biological system, let it be a tree or a bone [244]. The coalescence between computation and materials science is only at its beginning. With more years to come, we would have a better understanding than today on what computations can and cannot do. Yet there are already ample reasons now for us to believe that it is worthwhile to pay more attention to the coupling across different scales and the connection between strength and microstructure.

Appendix A

Dislocation Dipole Energy in PBC

A.1 Cut-off Radius and Core Energy

The linear elastic theory of dislocations has singularities at both the small and the large scale limit. It is the purpose of this section and the next to address them separately in reasonable detail, and our hope is to provide some clarification on certain commonly raised confusions. For the sake of simplicity, isotropic elasticity is assumed in these two sections.

Let's start with the energy of an infinitely long straight dislocation. This is essentially a two-dimensional problem since the system is invariant along the dislocation line. For a straight screw dislocation with Burgers vector b at the center of a cylindrical medium with radius R , as shown in Fig. A-1, the self energy of the dislocation per unit length is [30]

$$E_{\text{el}}(r_c) = \frac{\mu b^2}{4\pi} \ln \frac{R}{r_c}, \quad (\text{A.1})$$

where r_c is an artificial cut-off radius around the dislocation, which is usually referred to as the core radius. Here we insist on calling it cut-off radius in order to differentiate it from a *physical* core radius of dislocations, which will be discussed later. We use $E_{\text{el}}(r_c)$ to emphasize that the elasticity theory prediction is explicitly dependent on the choice of r_c . Eq. (A.1) diverges both at the small scale limit, i.e. $r_c \rightarrow 0$ and at the large scale limit, i.e. $R \rightarrow \infty$. We will discuss the origins and consequences of

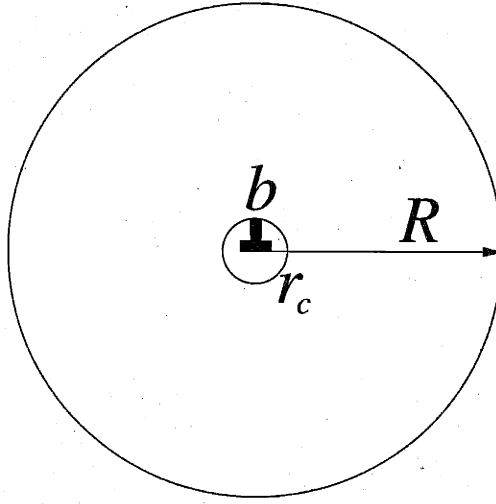


Figure A-1: An isolated screw dislocation within a cylinder of radius R . The dislocation line and Burgers vector b are out of the plane. The material within cut-off radius r_c around the dislocation is removed to avoid singularity.

these two singularities separately.

The need to introduce a cut-off radius r_c is because linear elastic solution of dislocation stress and strain field diverges on the dislocation line. Common practice in linear elasticity theory is to assume the medium to be hollow within a radius r_c around the dislocation, so as to “cut out” the singular region. The choice of r_c is completely arbitrary, but the total elastic energy differs for different choice of r_c . In order to compare results from different people, one has make sure the same cut-off radius is applied. Confusion will arise if some researcher uses a constant r_c for all dislocations while others choose r_c to be dependent on the dislocation character angle.¹

The small scale divergence is merely an artifact of the linear elastic theory, which assumes the existence of mathematically smooth fields of stress and strain. The fact that this is only an approximation can be easily appreciated since all materials are made up of atoms, i.e. they are all fundamentally discrete. The arbitrariness of dislocation self energy due to the choice of r_c can be fixed by comparing E_{el} with

¹angle between dislocation line direction and Burgers vector

direct atomistic simulation results E_{atm} [245], which is free from the cut-off problem. A dislocation core energy $E_{\text{core}}(r_c)$ is defined as their difference,

$$E_{\text{atm}} = E_{\text{el}}(r_c) + E_{\text{core}}(r_c) . \quad (\text{A.2})$$

Since dislocation core energy is introduced to cancel the r_c dependence of the elastic energy, it obviously has to have r_c dependence as well. Therefore, to compare dislocation core energies, one has to specify the choice of cut-off radius as well.

As mentioned above, the choice is r_c is arbitrary; it can be either 1\AA or $1b$. On the other hand, a dislocation also has a *physical* core radius, r_p , which is one half of the minimum separation between two dislocations where their interaction energy can still be described by linear elasticity theory. One can choose r_c to be r_p , but this is not mandatory.

One can also choose r_c such that $E_{\text{core}} = 0$ [30]. In this case, the linear elasticity theory exactly matches the atomistic calculation. The r_c that makes E_{core} vanishes is usually expressed in terms of a dimensionless parameter α , for which $r_c = b/\alpha$. One can show that α is related with the core energy at $r_c = 1b$ through,

$$\alpha = \exp \left[\frac{4\pi E_{\text{core}}(r_c = 1b)}{Kb^2} \right] , \quad (\text{A.3})$$

where K is the self energy prefactor in anisotropic elasticity, which equals to μ in isotropic elasticity.

A.2 Line Energy Divergence at Large Scale Limit

According to the last section, the small scale divergence of Eq.(A.1) is only a mathematical artifact, which can be completely removed by introducing an r_c -dependent core energy. However, the large scale divergence over R is not an artifact at all, contrary to some common beliefs. This is in accordance with the fact that linear elastic theory only becomes more and more accurate as one goes to larger length scales. Therefore, the logarithmic divergence of dislocation self energy over the medium ra-

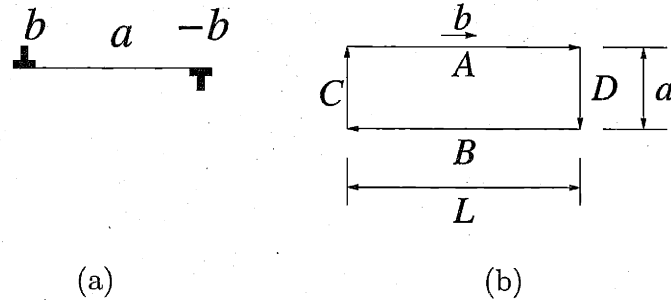


Figure A-2: (a) A screw dislocation dipole separated by a . (b) An elongated dislocation loop consisting of two screw segments of length L and two edge segments of length a .

dius R is physical, as can be seen from direct atomistic simulations in Mo by Xu et al. [245].

It may seem counter-intuitive if one is not allowed to take the size of the elastic medium to infinity when it contains dislocations, an idealization that is usually assumed when discussing lattice defects such as vacancies. However, we can still work with an infinite elastic medium if it contains two dislocations in the form of a dipole, or if it contains a dislocation loop, as shown in Fig. A-2. For a screw dislocation dipole separated by a , its elastic energy (per unit length) is [30]

$$E_{\text{el}}(r_c) = \frac{\mu b^2}{2\pi} \ln \frac{a}{r_c}, \quad (\text{A.4})$$

which is very similar to Eq.(A.1). Again, the elastic energy diverges if their separation a goes to infinity. This is similar to the quark confinement in Quantum Chromodynamics (QCD), in that no “free dislocation” or free quark could exist. The fact that the line energy² of an isolated straight dislocation goes to infinity was sometime used to arrive at the following conclusion, that “no dislocation should exist in perfect

²The energy per unit length, also called line tension.

thermodynamic equilibrium”³. While it is probably true that the notion of thermal equilibrium may not be very helpful in the discussion of plasticity processes, in which the system is driven far away from equilibrium, the above claim is not exactly correct. This is because the line tension only diverges for isolated straight dislocation that is infinitely long. For dislocation dipoles or dislocation loops, which appear frequently in real materials, their line energy is finite. Therefore, the equilibrium concentration of dislocation loops would be non-zero in principle, although in practice this value could still be vanishingly small. Under an applied shear stress, the energy of dislocation loops could decrease and homogeneous dislocation loop nucleation is then possible with the aid of thermal activation [246].

Before closing this section, let's study the energy of an elongated dislocation loop, shown in Fig. A-2(b), as another path towards the divergence of dislocation self energy. The loop consists of two screw segments having length L and the two edge segments having length a , with $L \gg a$.⁴ As $L \rightarrow \infty$, we approach the limit of Fig. A-2(a). The total elastic energy of the system can be expressed as the self energy of dislocation segments A, B, C, D and the interaction energy between them [30]. When $L \gg a$, only the contributions from segments A and B are dominant, i.e.

$$\frac{W_s(A)}{L} = \frac{W_s(B)}{L} = \frac{\mu b^2}{4\pi} \ln \frac{L}{r_c}, \quad (\text{A.5})$$

$$\frac{W_{\text{int}}(AB)}{L} = \frac{\mu b^2}{2\pi} \ln \frac{a}{L}, \quad (\text{A.6})$$

$$E_{\text{el}} \approx \frac{W_s(A)}{L} + \frac{W_s(B)}{L} + \frac{W_{\text{int}}(AB)}{L} \quad (\text{A.7})$$

$$= \frac{\mu b^2}{2\pi} \ln \frac{a}{r_c}. \quad (\text{A.8})$$

Therefore we obtain the same result as Eq. (A.4). At the same time, Eq.(A.5) shows that the self energy (per unit length) of a dislocation segment diverges as its length goes to infinity. The total energy of the system is still finite, if there exists an anti-dislocation nearby, with the divergent term exactly canceled by their interaction

³At least I have made similar claims to my fellow colleagues occasionally.

⁴This type of microstructure is very common in BCC metals due to the much higher velocity of edge segments than the screws.

energy Eq (A.6).

In summary, Eq. (A.1),(A.4) and (A.5) illustrate the divergence of dislocation energy (per unit length) as the size of elastic medium, the separation of a dislocation dipole and the dislocation length goes to infinity, respectively. These effects are not artifacts at all, but is due to the long range stress-strain field of dislocations, the same reason that gives rise to the conditional convergence problem as discussed in Chapter 4.2 and in the next two sections.

A.3 Derivation of Dipole Energy in PBC

This section derives Eq. (4.32), which expresses the elastic energy of a periodic cell containing a dislocation dipole in terms of its stress field. This is accomplished by evaluating the reversible work done when creating a dislocation dipole in a defect free medium.

We start out with a defect free and stress free system, with energy E_0 , which serves as the energy reference state. For generality, we construct a reversible path from E_0 to the final state E_2 in two steps. First, system E_0 is given a shear deformation so that it has a homogeneous stress σ^1 and reaches energy E_1 ,

$$E_1 = E_0 + \frac{1}{2}S(\sigma^1)^2V \equiv E_0 + \frac{1}{2}S_{ijkl}\sigma_{ij}^1\sigma_{kl}^1V, \quad (\text{A.9})$$

where S is the elastic compliant tensor and V is the volume of the PBC cell. Following Hirth and Lothe [30], the dislocation dipole is then created in system E_1 by making a cut at surface A and displace the surface on the positive side of the cut by \vec{b} with respect to the negative side, as shown in Fig. A.3.

Define the stress field of E_2 as $\sigma(\vec{r})$, its volume average as $\bar{\sigma} = \langle \sigma(\vec{r}) \rangle$, and spatial variation as $\sigma^0(\vec{r}) = \sigma(\vec{r}) - \bar{\sigma}$, respectively. Due to the internal stress, external force has to be applied to balance the internal force at the cut surface. During the transformation, the stress in the medium changes continuously from σ_{ij}^1 to $\sigma_{ij}(\vec{r})$, so

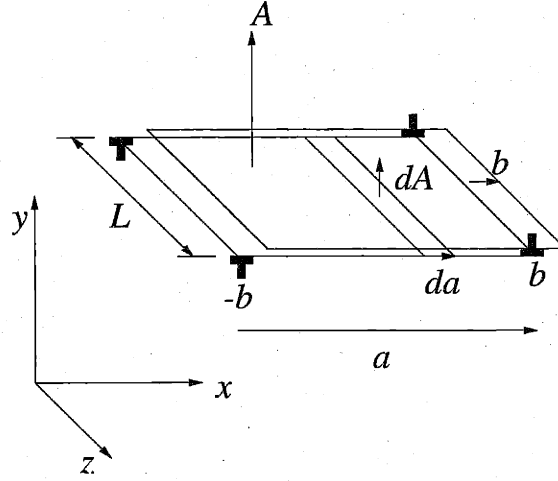


Figure A-3: Introducing a cut in a perfect lattice at surface \vec{A} and displacing the positive side of \vec{A} by \vec{b} relative to the negative side, to create a dislocation dipole separated by \vec{a} .

that the work done in displacing the surface is,

$$\begin{aligned}
 E_2 - E_1 &= \Delta W \\
 &= -\frac{1}{2} \int dA_j b_i (\sigma_{ij}(\vec{r}) + \sigma_{ij}^1) \\
 &= -\frac{1}{2} \int dA_j b_i \sigma_{ij}^0(\vec{r}) - \frac{1}{2} A_j b_i (\bar{\sigma}_{ij} + \sigma_{ij}^1) \quad (\text{A.10})
 \end{aligned}$$

In order to express E_2 solely in terms of $\sigma(\vec{r})$, we need to evaluate σ^1 . We note that the transformation from E_1 to E_2 introduces a finite plastic strain to the system,

$$\epsilon_{ij}^p = \left[\frac{b_i A_j}{V} \right]_s, \quad (\text{A.11})$$

where $[\cdot]_s$ represent the symmetritization operation, i.e. $[a_{ij}]_s = (a_{ij} + a_{ji})/2$. At the same time, since the transformation from E_1 to E_2 only operates on the internal surface, the total strain change is zero. This means that the internal plastic strain ϵ_{ij}^p is balanced by an internal elastic strain ϵ_{ij}^e ,

$$\epsilon_{ij} = \epsilon_{ij}^e + \epsilon_{ij}^p = 0, \quad (\text{A.12})$$

$$\epsilon_{ij}^e = -\epsilon_{ij}^p = -\left[\frac{b_i A_j}{V}\right]_s \quad (\text{A.13})$$

The elastic strain leads to the change of the average stress in the system, so that

$$\begin{aligned} \bar{\sigma}_{ij} - \sigma_{ij}^1 &= C_{ijkl} \epsilon_{kl}^e \\ &= -C_{ijkl} \frac{b_k A_l}{V} \\ \sigma_{ij}^1 &= \bar{\sigma}_{ij} + C_{ijkl} \frac{b_k A_l}{V}, \end{aligned} \quad (\text{A.14})$$

where C is the elastic constant tensor. Combining Eq. (A.9), (A.10) and (A.14), we obtain

$$E_2 - E_0 = -\frac{1}{2} \int dA_j b_i \sigma_{ij}^0(\vec{r}) + \frac{1}{2} S \bar{\sigma}^2 V, \quad (\text{A.15})$$

If we regard $\sigma_{ij}^0(\vec{r})$ as the intrinsic stress field of the dislocation microstructure, and the homogeneous $\bar{\sigma}_{ij}$ as an external stress field, Eq. (A.15) is then a verification of the statement that “there is no cross term between the external and internal stress fields in the total elastic energy.” by Hirth-Lothe [30] (p. 53, Theorem 2-1).

Before closing this section, we give the proof that $-\int dA_j b_i \sigma_{ij}(\vec{r})$ is the interaction energy between the primary dislocation dipole and the stress field σ_{ij} . This proposition is used in Chapter 4.2 to separate E_{img} from the total elastic energy $E_{\text{el}} = E_2 - E_0$. Because

$$d\vec{A} = L(\hat{e}_z \times d\vec{a}), \quad (\text{A.16})$$

it follows that,

$$\begin{aligned} -\int d\vec{A} \cdot (\vec{b} \cdot \sigma(\vec{r})) &= -L \int (\hat{e}_z \times d\vec{a}) \cdot (\vec{b} \cdot \sigma(\vec{r})) \\ &= -L \int (\vec{b} \cdot \sigma(\vec{r}) \times \hat{e}_z) \\ &= -L \int \vec{f}(\vec{r}) \cdot d\vec{a}, \end{aligned} \quad (\text{A.17})$$

where $\vec{f}(\vec{r})$ is the force per unit length exerted by σ_{ij} onto a dislocation with Burgers

vector \vec{b} at position \vec{r} . Therefore, $-\int dA_j b_i \sigma_{ij}(\vec{r})$ is the work done to move dislocation b for a distance a , which is equivalent to what we intended to prove.

A.4 Ghost Dipole Correction Term

Instead of giving a rigorous proof, this section will use a highly simplified model, i.e. screw dislocations in isotropic medium, as an example to demonstrate the effect of “ghost” dislocation dipoles in correcting the σ^{err} term in Eq. (4.35).

In analogy to the electrostatic potential field, we define a 2-dimensional *potential field* of dislocations, as the work to be done to move a “test” dislocation, i.e. with unit Burgers vector, from a reference point to the specified position. For example, the potential field of a screw dislocation b at origin in isotropic linear elasticity is

$$\phi_m(\vec{r}) = -\frac{\mu b}{2\pi} \ln \frac{r}{r_c}, \quad (\text{A.18})$$

where we use the subscript “m” to indicate dislocation “monopole”, or a single dislocation. The potential field of a dislocation dipole consisting of a screw b at $\vec{R} + \vec{a}/2$ and a screw $-b$ at $\vec{R} - \vec{a}/2$ is then

$$\phi_d(\vec{r}) = -\frac{\mu b}{2\pi} \ln \frac{|\vec{r} - \vec{R} - \vec{a}/2|}{|\vec{r} - \vec{R} + \vec{a}/2|} \quad (\text{A.19})$$

where we use “d” to indicate dislocation “dipole”. By superimposing the potential fields of primary and image dislocation dipoles, one can construct the potential field in a simulation cell containing a dislocation dipole under Periodic Boundary Conditions,

$$\tilde{\phi}^{\text{PBC}}(\vec{r}) = \sum_{\vec{R}}^{\text{all dipoles}} \phi_d(\vec{r} - \vec{R}), \quad (\text{A.20})$$

where \vec{R} runs through the offset vector of all dipoles with respect to the primary dipole ($\vec{R} = 0$ for the primary dipole). Of course, this summation is not *absolutely convergent*. Similar to Eq. (4.29), we use a “ \sim ” sign here to indicate that this sum-

mation can be problematic, and define the “true” potential field as $\phi^{\text{PBC}}(\vec{r})$. By definition, $\phi^{\text{PBC}}(\vec{r})$ is periodic, i.e.

$$\phi^{\text{PBC}}(\vec{r} + \vec{c}_i) - \phi^{\text{PBC}}(\vec{r}) = 0, \quad i = 1, 2. \quad (\text{A.21})$$

Now let's study the convergence property of $\tilde{\phi}^{\text{PBC}}(\vec{r})$. From Eq. (A.19) it follows that the dipole potential field and its derivatives have different decay rates as $R \rightarrow \infty$,

$$|\phi_d(\vec{r} - \vec{R})| \sim R^{-1}, \quad (\text{A.22})$$

$$|\partial_i \phi_d(\vec{r} - \vec{R})| \sim R^{-2}, \quad (\text{A.23})$$

$$|\partial_i \partial_j \phi_d(\vec{r} - \vec{R})| \sim R^{-3}, \quad (\text{A.24})$$

where $\partial_i \equiv \partial/\partial x_i$, $i = 1, 2$, $R = \sqrt{x_1^2 + x_2^2}$. It then follows that $\partial_i \partial_j \tilde{\phi}^{\text{PBC}}(\vec{r})$ is absolutely convergent, while $\partial_i \tilde{\phi}^{\text{PBC}}(\vec{r})$ is conditionally convergent, and $\tilde{\phi}^{\text{PBC}}(\vec{r})$ is not convergent at all.

Since the second derivatives $\partial_i \partial_j \tilde{\phi}^{\text{PBC}}(\vec{r})$ of the potential field is absolutely convergent, it means that different summation sequences will converge to the same result, i.e.

$$\partial_i \partial_j \tilde{\phi}^{\text{PBC}}(\vec{r}) = \partial_i \partial_j \phi^{\text{PBC}}(\vec{r}). \quad (\text{A.25})$$

By integration we obtain

$$\begin{aligned} \partial_j \tilde{\phi}^{\text{PBC}}(\vec{r}) &= \partial_j \phi^{\text{PBC}}(\vec{r}) - E_j, \\ \tilde{\phi}^{\text{PBC}}(\vec{r}) &= \phi^{\text{PBC}}(\vec{r}) - E_j r_j + \phi^0, \end{aligned} \quad (\text{A.26})$$

where E_j and ϕ^0 are integration constants, and summation over $j = 1, 2$ is implied when it appears twice in a multiplication. Eq. (A.26) is an important result we have obtained, stating that although different summation schemes will converge to different potential fields, they are essentially the same up to a constant term (ϕ^0) and a constant slope term ($E_j r_j$).

The constant ϕ^0 is irrelevant since we can always redefine the reference (zero)

potential point. The constant vector \vec{E} on the other hand, corresponds to the force on a dislocation with unit Burgers vector $(\vec{b}/|\vec{b}|)$ due to the residual constant stress σ^{err} , i.e.

$$\vec{E} = \left(\sigma^{\text{err}} \cdot \vec{b}/|\vec{b}| \right) \times \hat{e}_z, \quad (\text{A.27})$$

If we define α, β such that $\vec{a} = \alpha \vec{c}_1 + \beta \vec{c}_2$, then

$$-A_j b_i \sigma_{ij}^{\text{err}} = - \left(\alpha \vec{E} \cdot \vec{c}_1 + \beta \vec{E} \cdot \vec{c}_2 \right) b. \quad (\text{A.28})$$

From Eq. (A.21) and (A.26) we have

$$\tilde{\phi}^{\text{PBC}}(\vec{r} + \vec{c}_i) - \tilde{\phi}^{\text{PBC}}(\vec{r}) = -\vec{E} \cdot \vec{c}_i. \quad (\text{A.29})$$

Therefore,

$$\begin{aligned} -A_j b_i \sigma_{ij}^{\text{err}} &= \alpha b \left(\tilde{\phi}^{\text{PBC}}(\vec{r} + \vec{c}_1) - \tilde{\phi}^{\text{PBC}}(\vec{r}) \right) \\ &\quad + \beta b \left(\tilde{\phi}^{\text{PBC}}(\vec{r} + \vec{c}_2) - \tilde{\phi}^{\text{PBC}}(\vec{r}) \right) \end{aligned} \quad (\text{A.30})$$

$$= \sum_{\vec{R}}^{\text{all dipoles}} E_{\text{dg}}(\vec{R}), \quad (\text{A.31})$$

$$= \sum_{\vec{R}}^{\text{all images}} E_{\text{dg}}(\vec{R}) + E_{\text{dg}}(\vec{R} = 0), \quad (\text{A.32})$$

where $E_{\text{dg}}(\vec{R})$ is the interaction energy between the dipole at offset \vec{R} (w.r.t the primary dipole) with the “ghost” dipoles, consisting of dislocations αb at $\vec{c}_1/2$, $-\alpha b$ at $-\vec{c}_1/2$, βb at $\vec{c}_2/2$, and $-\beta b$ at $-\vec{c}_2/2$.

Appendix B

More on Dynamic Coupling

B.1 Derivation of Generalized Langevin Equation

In this section, the derivation of the Generalized Langevin Equation, Eq. (4.37) is presented. The two domains P and Q are as defined in Section 4.3.2 and Fig. 4-11. The only assumption is the linearity in P - Q and Q - Q interactions. No assumption on P - P interactions is needed. Therefore, it is more general than that given in [188]. Mathematically, the linearity assumptions can be written as

$$\frac{\partial^2}{\partial x_P \partial x_Q} V(x_P, x_Q) = \text{const} \quad (\text{B.1})$$

$$\frac{\partial^2}{\partial x_Q \partial x_Q} V(x_P, x_Q) = \text{const} \quad (\text{B.2})$$

where V is the total potential energy of the system. Here we use a vector notation where x_P and x_Q represent the displacements of P and Q atoms respectively, measured from their equilibrium positions.

Taylor expand the potential function $V(x_P, x_Q)$ around $x_Q = 0$,

$$V(x_P, x_Q) = V(x_P, 0) + \sum_{n=1}^{\infty} a_n(x_P) x_Q^n \quad (\text{B.3})$$

and then expand the coefficients $a_n(x_P)$ around $x_P = 0$,

$$V(x_P, x_Q) = V(x_P, 0) + \sum_{m=0}^{\infty} \sum_{n=1}^{\infty} a_{mn} x_P^m x_Q^n \quad (\text{B.4})$$

$$= V(x_P, 0) + a_{11} x_P x_Q + a_{02} x_Q^2 \quad (\text{B.5})$$

$$= V(x_P, 0) + x_P^T \Phi_{PQ} x_Q + \frac{1}{2} x_Q^T \Phi_{QQ} x_Q \quad (\text{B.6})$$

Eq.(B.5) is valid because the higher order terms vanish due to Eq. (B.1) and (B.2), and the lower order terms disappear because x_P and x_Q are defined relative to the equilibrium positions. In Eq.(B.6) we redefine the symbols to be consistent with the notation of Moseler, where Φ_{PQ} and Φ_{QQ} are constant matrices. The equation of motion for both P and Q atoms now reads,

$$m\ddot{x}_P = -\frac{\partial}{\partial x_P} V(x_P, x_Q) = -\frac{\partial}{\partial x_P} V(x_P, 0) - \Phi_{PQ} x_Q \quad (\text{B.7})$$

$$= -\frac{\partial}{\partial x_P} V(x_P, 0) + F_{PQ}, \quad (\text{B.8})$$

$$m\ddot{x}_Q = -\frac{\partial}{\partial x_Q} V(x_P, x_Q) = -\Phi_{QP} x_P - \Phi_{QQ} x_Q, \quad (\text{B.9})$$

where $\Phi_{QP} = \Phi_{PQ}^T$, and double-dot represents second order time derivative. F_{PQ} is defined as $F_{PQ} \equiv -\Phi_{PQ} x_Q$. After Fourier transform of Eq.(B.9),

$$-m\omega^2 \tilde{x}_Q = -\Phi_{QP} \tilde{x}_P - \Phi_{QQ} \tilde{x}_Q, \quad (\text{B.10})$$

x_Q can be symbolically solved as

$$\tilde{x}_Q(\omega) = (m\omega^2 I + \Phi_{QQ})^{-1} \Phi_{QP} \tilde{x}_P(\omega). \quad (\text{B.11})$$

Therefore, the force from Q to P atoms can be solved as,

$$\tilde{F}_{PQ}(\omega) = -\Phi_{PQ} (m\omega^2 I + \Phi_{QQ})^{-1} \Phi_{QP} \tilde{x}_P(\omega) \quad (\text{B.12})$$

$$\equiv \tilde{\Theta}_{PP}(\omega) \tilde{x}_P(\omega) \quad (\text{B.13})$$

$$F_{PQ}(t) = \int_0^t \Theta_{PP}(\tau) \tilde{x}_P(t - \tau) d\tau \quad (\text{B.14})$$

Hence follows the equation of motion for P atoms, commonly known as the Generalized Langevin Equation (GLE),

$$m\ddot{x}_P = -\frac{\partial}{\partial x_P}V(x_P, 0) + \int_0^t \Theta_{PP}(\tau)x_P(t-\tau)d\tau \quad (\text{B.15})$$

After integrating by part, we arrive at form similar to Eq. (4.37), which relates the boundary force with P atom velocities instead of positions,

$$m\ddot{x}_P = -\frac{\partial}{\partial x_P}V(x_P, 0) + \int_0^t \beta_{PP}(\tau)\dot{x}_P(t-\tau)d\tau + \beta_{PP}(t)x(0) + R(t), \quad (\text{B.16})$$

where $\Theta_{PP}(t) = d\beta(t)_{PP}/dt$ and $R(t)$ is a complex functional of the initial condition in Q .

B.2 Symmetry between GLE and Green's Function

Suppose the entire system is divided into two parts, a finite region P for MD simulations and a much larger surrounding Q treated as the boundary condition. In principle, there are two ways to establish a dynamic coupling between P and Q within the linear response theory. One is the *Generalized Langevin Equation* (GLE) type as discussed above and in Chapter 4, and the other is *Time-dependent Green's Function* (TGF) type. The notion of Green's function is perhaps more widely used than the GLE. The newly developed GFBC [247] (stands for Green's Function Boundary Condition) uses static Green's function for structural relaxation purposes. We find it interesting as well as instructive to think about the symmetry between GLE and TGF, and to make analogies between MD and linear systems (circuits), which opens up new opportunities for improving both types of boundary conditions.

Let's start with the Generalized Langevin equation written in the following way,

$$m\frac{d^2x_P}{dt^2} = F_{PP}(x_P) + F_{PQ}, \quad (\text{B.17})$$

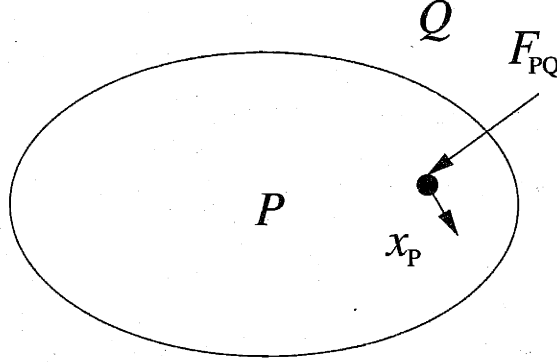


Figure B-1: MD region P is the region enclosed by the solid line, surrounded by region Q , which is perfect lattice. The effect of Q is to exert a force $F_{PQ}(t)$ on atoms in P , as a boundary condition. This boundary is of the Generalized Langevin Equation (GLE) type.

where F_{PP} is the force on P atoms due to other P atoms, and F_{PQ} is the force on P atoms due to Q atoms. Neglecting the effect of initial condition in Q , $F_{PQ}(t)$ should depend on the trajectory of P atoms $x_P(t)$. This dependence is the property of Q , and can be formally written as a functional,

$$F_{PQ}(t) = Q[x_P(t)]. \quad (\text{B.18})$$

If functional $Q[\cdot]$ is linear, it can be expressed as a convolution of $x_P(t)$ with the so called Memory Kernel matrix $\Theta_{PP}(t)$, i.e.

$$F_{PQ}(t) = \int_0^\infty \Theta_{PP}(\tau) x_P(t - \tau) d\tau. \quad (\text{B.19})$$

One can then regard domain Q as a (linear) system, whose input is the displacement $x_P(t)$ of P atoms, whose output is the force $F_{PQ}(t)$ from Q on P atoms, as illustrated in Fig. B-2(a). Following this analogy, we can also represent domain P as a (usually nonlinear) system, i.e.,

$$x_P(t) = P[F_{PQ}(t)]. \quad (\text{B.20})$$

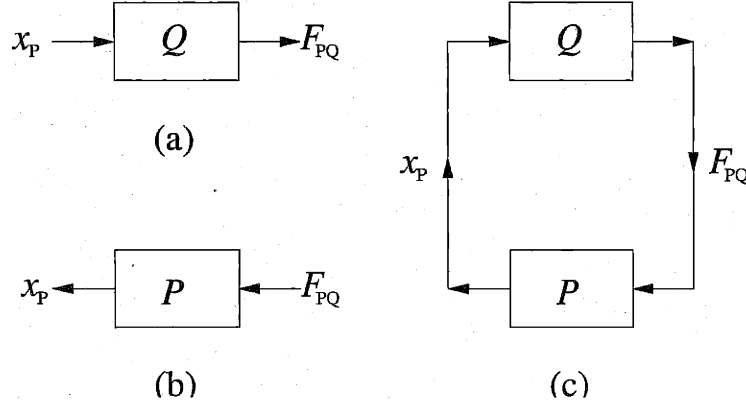


Figure B-2: Domain P and Q as systems. (a) $F_{PQ}(t) = Q[x_P(t)]$. (b) $x_P(t) = P[F_{PQ}(t)]$. (c) Coupling between P and Q .

The input of system P is the forces $F_{PQ}(t)$ from region Q , and its output is the displacements of P atoms, $x_P(t)$, as illustrated in Fig. B-2(b). The dynamics of the entire domain is then represented by the coupled PQ system, formed by directing the output of Q into the input of P and vice versa, as illustrated in Fig. B-2(c).

There is no obvious reason for the choice of atomic forces as the input of P and atomic positions as its output, and conversely for Q . By symmetry, the interface of P and Q can be interchanged. As shown in Fig. B-3, we can set up a layer of atoms x_Q as the boundary condition for P . P will exert forces F_{QP} on Q , and Q will respond to these forces by moving atoms x_Q accordingly. Mathematically, we can also express P and Q as functionals,

$$x_Q(t) = Q[F_{QP}(t)], \quad (\text{B.21})$$

$$F_{QP}(t) = P[x_Q(t)]. \quad (\text{B.22})$$

When the functional $Q[\cdot]$ in Eq. (B.21) is linear, $x_Q(t)$ can be expressed as a convolution of F_{QP} with the so called Time-dependent Green's Function matrix $G_{QQ}(t)$, i.e.

$$x_Q(t) = \int_0^\infty G_{QQ}(\tau) F_{QP}(x_Q(t-\tau), x_P(t-\tau)) d\tau. \quad (\text{B.23})$$

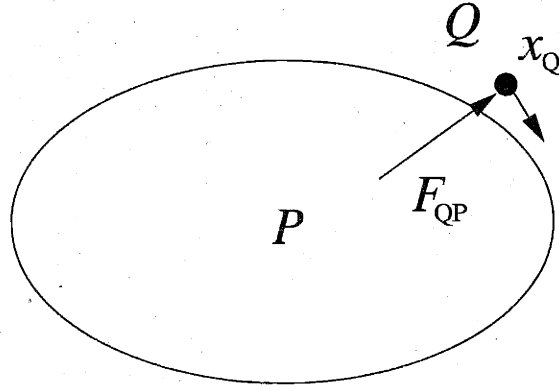


Figure B-3: MD region P is the region enclosed by the solid line, surrounded by region Q , which is perfect lattice. P will exert forces $F_{QP}(t)$ on atoms in Q , while Q responds to these forces accordingly by moving its atoms $x_Q(t)$. This boundary is of the Time-dependent Green's Function (TGF) type.

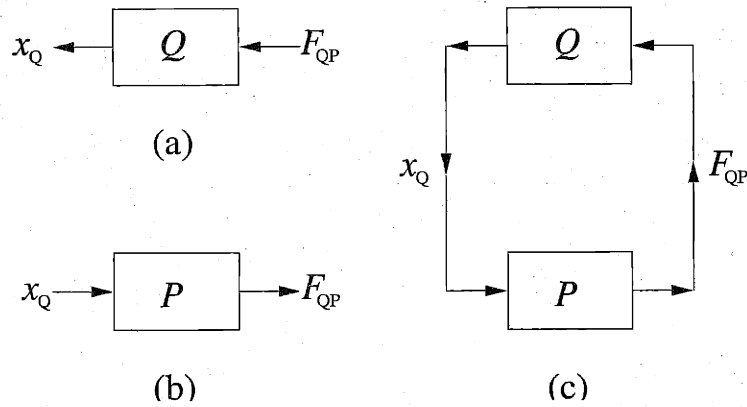


Figure B-4: Domain P and Q as systems. (a) $x_Q(t) = Q[F_{QP}(t)]$. (b) $F_{QP}(t) = P[x_Q(t)]$. (c) Coupling between P and Q .

In analogy with the GLE type coupling, the TGF type coupling represented as circuits is illustrated in Fig. B-4. A Time-dependent Green's Function (TGF) boundary condition for MD simulation in P can be implemented if we obtain the Green's function $G_{QQ}(t)$ and use Eq. (B.23) to update the displacement $x_Q(t)$ during the simulation. The Time-dependent Green's Function $G_{QQ}(t)$ can be calculated before the MD simulation in P by performing a series of "test" simulations in region Q . In principle, for atoms i, j in Q , if we exert an external force $F_j(t) = \delta(t)$ on one atom j , the displacement $x_i(t)$ of atom i equals to the matrix element $G_{ij}(t)$. This is to say that, each of these "test" simulations in Q will provide one column of the Green's function matrix. The entire procedure here would be completely analogous with the GLE type boundary conditions discussed previously.

B.3 Translational Invariance in GLE Approach

Both the GLE and TGF boundaries discussed in the last section have the same requirement, i.e. one needs to compute and store a time-dependent large dimension matrix, which may create technical difficulty for large scale simulations. It is natural to pose the following question: Is it necessary to store all these data? The numerical results on the memory kernel functions in some model systems (see Chapter 4) indicate two reasons for which technical improvement should be possible. Firstly, all matrix elements have similar time dependence. They all take some negative value at $t = 0$ and then oscillate around its long-time limit. Secondly, all matrix elements are *smooth* functions. In this section and the next, we explore the possibilities of reducing the size of the kernel matrix by the translational invariance of the crystal lattice. In the last section, we propose a method to take advantage of the smoothness of the memory functions by studying their Fourier transform.

For a general shape P region, each matrix column of the memory kernel matrix β_{PP} is different, except for some accidental symmetries. This is because the translational invariance of the perfect lattice is destroyed in the very definition of β_{PP} . Note that each column of β_{PP} is defined as the force coming from Q atoms due to a perturbation

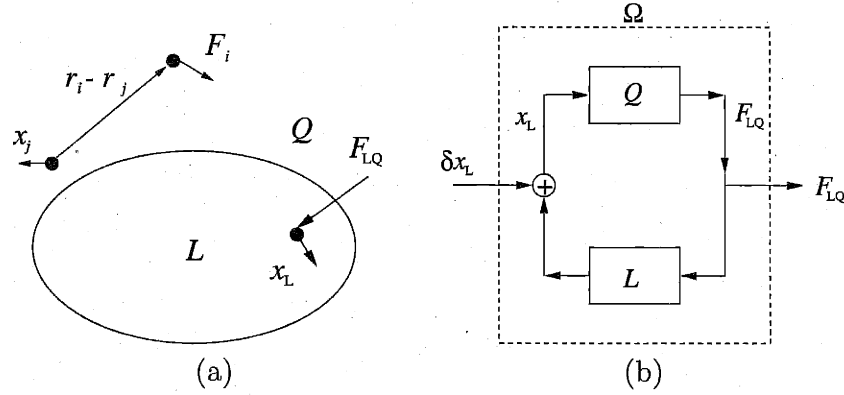


Figure B-5: (a) Replace MD region P with a perfect lattice region L . Define the total region L plus Q to be Ω , which is translationally invariant. Define a Memory Kernel matrix $\hat{\beta}_{\Omega\Omega}(t)$ for Ω , whose element $\hat{\beta}_{ij}(t)$ is the *total* force $F_i(t)$ on atom i , if atom j is displaced to $x_j = 1$, while $x_i = 0$ for all the other atoms $i \neq j$ in Q (and $v_i = 0$ for all i). $\hat{\beta}_{\Omega\Omega}(t)$ is translationally invariant, i.e. $\hat{\beta}_{ij}(t) = \hat{\beta}(\vec{r}_i - \vec{r}_j, t)$. (b) Representation of Q, L and Ω as systems.

on a specific P atom, with *all* other P atoms *kept fixed*. Therefore, each column corresponds to a distinct scenario defined as the relative position of the perturbed atoms with respect to the remaining fixed domain.

As region P may contain local defects disrupting the lattice translational invariance, we can only restore the latter by replacing P with a perfect lattice named L which is coherent with the surrounding lattice domain Q , as shown in Fig. B-5(a). The entire system $\Omega = Q + L$ is then an infinitely large perfect lattice. A new definition of the memory function $\hat{\beta}_{\Omega\Omega}$ is also necessary in order to restore translational invariance. We define matrix element $\hat{\beta}_{ij}$ as the *total* force $F_i(t)$ on atom i if atom j is displaced to $x_j = 1$ at $t = 0$. Initial conditions of all other atoms are $x = 0$ and *all* atoms (including j) are allowed to relax at $t > 0$. Under this definition, $\hat{\beta}_{\Omega\Omega}(t)$ is translationally invariant, i.e.

$$\hat{\beta}_{ij}(t) = \hat{\beta}(\vec{r}_i - \vec{r}_j, t), \quad (\text{B.24})$$

where \vec{r}_i refers to the perfect lattice position of atom i . Using $\hat{\beta}_{\Omega\Omega}$, one can construct a linear system as shown in Fig. B-5(b), which responds to external perturbations

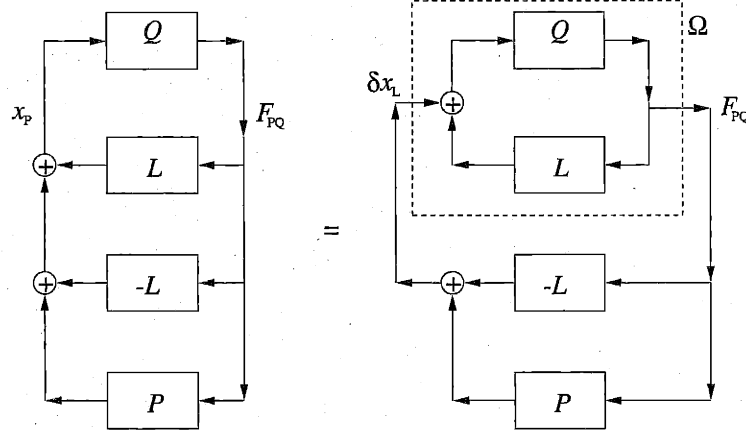


Figure B-6: Representing P - Q system in terms of the L - Q system in GLE formulation.

on L atoms by exerting a time dependent force F_{QL} on L . Although $\hat{\beta}_{\Omega\Omega}$ only gives the total forces on L atoms, F_{QL} can be computed by subtracting off forces due to L atoms themselves, thus without the knowledge of Q atoms. In other words, $\hat{\beta}_{\Omega\Omega}$ is equivalent to a linear system $F_{LQ} = \Omega[\delta x_L]$.

Comparing system Q - P in Fig. B-2(c) with system Q - L in Fig. B-5(b), we are now in the position to construct a dynamic boundary for P using the translational invariant memory function $\hat{\beta}_{\Omega\Omega}$. As shown in Fig. B-6, we can decompose the P - Q system and represent it in terms of Ω , L and P . Mathematically, this coupling can be written as

$$F_{PQ} = \Omega[\delta x_L], \quad (\text{B.25})$$

$$\delta x_L = P[F_{PQ}] - L[F_{PQ}]. \quad (\text{B.26})$$

Even though we do not give an rigorous proof here, we hope that Fig. B-6 and Eq.(B.26) describe a reasonable picture of how this alternative way of coupling is possible. At this point, we want to emphasize that difference between this new coupling and the one presented in Chapter 4 is that a *translationally invariant* memory kernel ($\hat{\beta}_{\Omega\Omega}$) now suffices to replace the Q region, saving the effort to compute and store a much larger matrix (β_{PP}).

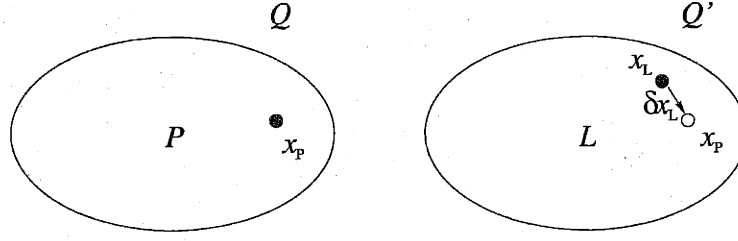


Figure B-7: Molecular Dynamics on two sets of coupled systems, P - Q and L - Q' , where Q' behaves the same as Q . We interpret the physical meaning of δx_L , as the amount of external disturbance needed to maintain system Q' the same as Q .

We close this section by pointing out the physical interpretation of the newly introduced variable δx_L . Imagine doing MD on two sets of coupled systems, P - Q and L - Q' . Q' and Q are two subsystems having the same Hamiltonian and initial conditions, but are coupled to L and P respectively, see Fig. B-7. Because P and L behave differently (either in their Hamiltonians or initial conditions), the trajectories of atoms in L would be different from those in P , so would Q' behave differently from Q . However, if we add external disturbance δx_L to make the atoms in L to have the same trajectory as P , i.e. $x_L + \delta x_L = x_P$, (actually this is necessary only for a layer of atoms in L which couples directly to Q), then the trajectories of atoms in Q will be no different from those in Q' . On the other hand, the trajectory of Q' (and hence Q) atoms can be calculated using the memory function $\hat{\beta}_{\Omega\Omega}$. Therefore by introducing L and then subtracting it off again P , we arrived at a method of providing a dynamic boundary for P using a translationally invariant memory kernel. Unfortunately this method has not been implemented at this moment, so that we will need to wait a little longer to see how it works in real applications.

B.4 Translational Invariance in Greens' Function Approach

Due to the symmetry between GLE and TGF coupling methods as discussed in Section 2, the translational invariance approach for GLE discussed in the last section

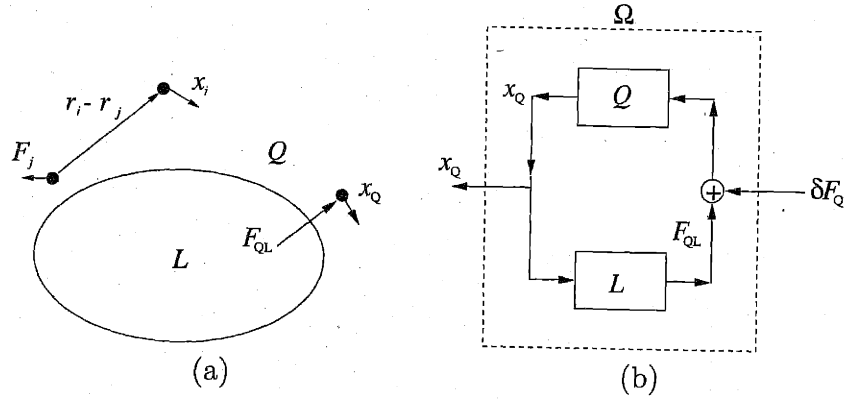


Figure B-8: (a) Replace MD region P with a perfect lattice region L . Define the total region L plus Q to be Ω , which is translationally invariant. Define a Time-dependent Green's Function matrix $\hat{G}_{\Omega\Omega}(t)$ for Ω , whose element $\hat{G}_{ij}(t)$ is the displacement x_i of atom i in response to an external force $\delta F_j(t) = \delta(t)$ exerted on atom j , while $x_i = 0$ for all atoms at $t = 0$. $\hat{G}_{\Omega\Omega}(t)$ is translationally invariant, i.e. $\hat{G}_{ij}(t) = \hat{\beta}(\vec{r}_i - \vec{r}_j, t)$. (b) Representation of Q, L and Ω as systems.

can be directly generalized to TGF method.

Following the treatment in the last section, we replace P with a perfect lattice region L and introduce a new Green's function matrix $\hat{G}_{\Omega\Omega}$ defined on system $\Omega = Q + L$. The matrix element \hat{G}_{ij} is the displacement x_i of atom i in response to an additional external force $\delta F_j(t) = \delta(t)$ exerted on atom j , with $x_i = 0$ for all atoms at $t = 0$. With this definition, $\hat{G}_{\Omega\Omega}$ is translationally invariant, i.e.

$$\hat{G}_{ij}(t) = \hat{G}(\vec{r}_i - \vec{r}_j, t). \quad (\text{B.27})$$

The coupled Q - L system together with the external forces are represented in Fig. B-8. With $\hat{G}_{\Omega\Omega}$ we can construct a linear system taking external forces on Q atoms as inputs and outputting trajectories of Q atoms.¹ Denote this system as $x_Q = \Omega[\delta F_Q]$, we have

$$x_Q = \int_0^\infty \hat{G}_{QQ}(\tau) \delta F_Q(t - \tau) d\tau, \quad (\text{B.28})$$

¹The reader may find this definition of Green's function more "physical" than the corresponding definition for the Memory Kernel function $\hat{\beta}_{\Omega\Omega}$. Mathematically, they are symmetric.

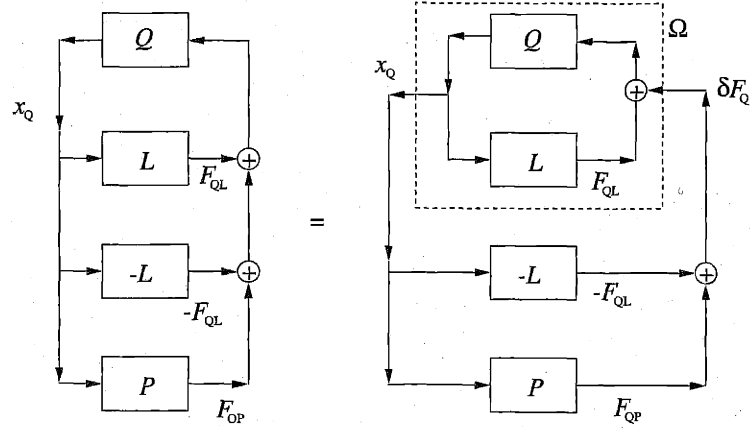


Figure B-9: Representing P - Q system in terms of the L - Q system in TGF formulation.

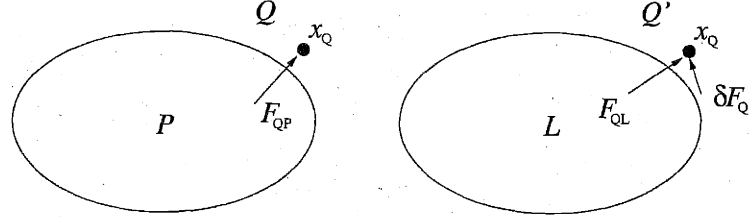


Figure B-10: Molecular Dynamics on two sets of coupled systems, P - Q and L - Q' , where Q' behaves the same as Q . We interpret the physical meaning of δF_Q , as the amount of external force on Q' needed to maintain system Q' the same as Q .

where \hat{G}_{QQ} is a sub-matrix of the $\hat{G}_{\Omega\Omega}$ matrix.

Comparing system Q - P in Fig. B-4(c) with Fig. B-8(b), we are now in the position of representing the Q - P system in terms of the Q - L system, as shown in Fig. B-9. Mathematically, this coupling can be written as

$$x_Q = \Omega[\delta F_Q], \quad (\text{B.29})$$

$$\delta F_Q = P[x_Q] - L[x_Q]. \quad (\text{B.30})$$

Eq. (B.30) and Fig. B-9 illustrates the recipe of using a translationally invariant Green's function for dynamic coupling of P and Q regions.

We close this section by pointing out the physical interpretation of the newly

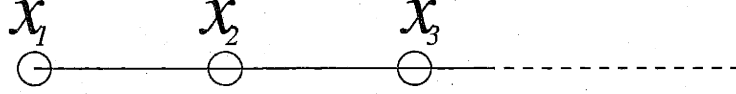


Figure B-11: One dimensional semi-infinite chain of harmonic oscillators x_1, x_2, x_3, \dots .

introduced variable δF_Q . Imagine doing MD on two sets of coupled systems, P - Q and L - Q' , see Fig. B-10. The trajectory of atoms in Q and Q' will naturally be different, because they couple to different systems. However, if we exert an external forces δF_Q on atoms in Q' , such that $\delta F_Q + F_{QL} = F_{QP}$, then the trajectories of atoms in Q' will be no different from those in Q , because now they have exactly the same input — $F_{QL} + \delta F_Q$ for Q' and F_{QP} for Q . Because the $x_{Q'}$ ($= x_Q$) due to external forces δF_Q can be calculated from the Green's function $\hat{G}_{\Omega\Omega}$ instead of performing simulations in Q , we obtain the time-dependent boundary condition for P based on linear response theory.

B.5 GLE Type Coupling in Fourier Space

In principle, the computational and storage cost of the memory kernel function matrix could be further reduced (after using a translationally invariant formalism) by exploiting the smoothness of their time-dependence. In this context, an analysis of the memory functions in Fourier space would be useful. In fact, the analytic solution for the memory function of the one-dimensional harmonic oscillator was derived [196] in the Fourier space. This derivation is reproduced below, which serves as a basis for our further discussions.

Following in Section 1, the force on oscillator x_1 due to the infinite chain to its right is related with the memory function $\tilde{\Theta}(\omega)$ through

$$\tilde{F}_{21}(\omega) = \tilde{\Theta}(\omega)\tilde{x}_1(\omega). \quad (\text{B.31})$$

At the same time, this force is exerted solely through oscillator x_2 , so that we have,

$$\tilde{x}_2(\omega) - \tilde{x}_1(\omega) = \Theta(\omega)\tilde{x}_2(\omega) \quad (\text{B.32})$$

Similarly, the force on x_2 due to x_3 can also be written as

$$F_{32} = -\tilde{\Theta}(\omega)\tilde{x}_2(\omega) \quad (\text{B.33})$$

The equation of motion for x_2 can be written as

$$-\omega^2\tilde{x}_2(\omega) = F_{12} + F_{32} \quad (\text{B.34})$$

$$= -\tilde{\Theta}(\omega)\tilde{x}_1(\omega) + \tilde{\Theta}(\omega)\tilde{x}_2(\omega), \quad (\text{B.35})$$

where the identity $F_{12} = -F_{21}$ is used. Combining Eq. (B.32) and (B.35) yields an equation for $\tilde{\Theta}(\omega)$,

$$\frac{\tilde{\Theta}}{\tilde{\Theta} + \omega^2} - 1 = \tilde{\Theta} \quad (\text{B.36})$$

$$\tilde{\Theta}^2 + \omega^2\tilde{\Theta} + \omega^2 = 0, \quad (\text{B.37})$$

which leads to,

$$\tilde{\Theta}(\omega) = \frac{\omega\sqrt{\omega^2 - 4} - \omega^2}{2} \quad (\text{B.38})$$

$$\tilde{\beta}(\omega) = \frac{\tilde{\Theta}(\omega)}{i\omega} = \sqrt{1 - \left(\frac{\omega}{2}\right)^2} + \frac{i\omega}{2} \quad (\text{B.39})$$

$$\beta(t) = -J_0(2t) - J_2(2t) \quad (\text{B.40})$$

Fig. B-12(a) shows the real part of $\tilde{\beta}(\omega)$, which has a semicircular shape. The reason that it is bounded within $\omega \in [-2, 2]$ can be seen from the phonon dispersion curve. As shown in Fig. B-12(b), $\omega = 2$ is the maximum frequency in this lattice. Since any physical lattice has a natural upper bound in its frequency spectrum, it explains the smoothness of all the matrix elements for a general system. Because $\tilde{\beta}(\omega)$ is nonzero only within a finite region of ω , it appears to be more economic to

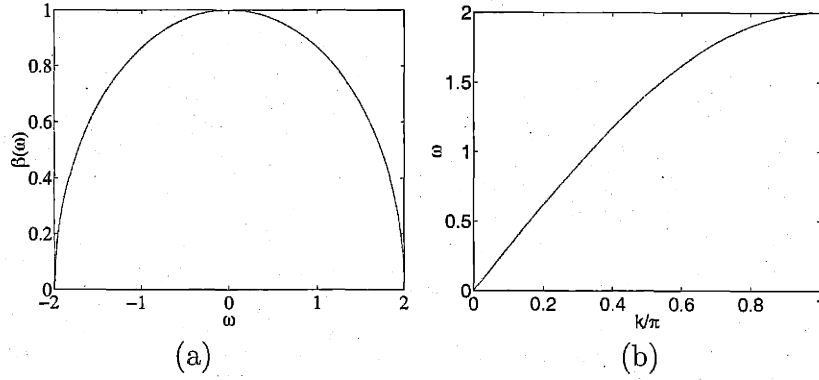


Figure B-12: (a) Real part of the memory kernel function in Fourier space. (b) Phonon dispersion relation of the one-dimensional harmonic oscillator.

store the memory kernel functions in Fourier space, instead of tabulating it in real space, for which the time axis is unbounded:

In a Fourier space implementation of dynamic boundary, the Fourier transform $\tilde{x}_P(\omega)$ of the velocity history $x_P(t)$ would be maintained. It is updated at every timestep as

$$\tilde{x}_P(\omega) \leftarrow \tilde{x}_P(\omega) \exp(i\omega\Delta t) + x_P(t), \quad (\text{B.41})$$

where Δt is the simulation timestep and $x_P(t)$ is the atom position at the current timestep. The Fourier transform of the boundary force is then calculated as

$$\tilde{F}_{PQ}(\omega) = \tilde{\Theta}_{PP}(\omega) \tilde{x}_P(\omega), \quad (\text{B.42})$$

and the boundary force at current timestep can be calculated as

$$F_{PQ}(t) = \int d\omega \tilde{F}_{PQ}(\omega). \quad (\text{B.43})$$

Appendix C

Markovian Models for Dislocation Motion

C.1 Hirth-Lothe Model

In the Hirth-Lothe (H-L) model [30], the dislocation velocity is calculated from the double-kink nucleation rate J and the kink drift velocity v_k . It is a mean field theory in that it calculates the average kink migration distance X by equating the double-kink nucleation rate with the kink annihilation rate. The arguments of the H-L model is outlined below. Let τ be the mean life time of a kink pair, so that

$$X = v_k \tau. \quad (\text{C.1})$$

At the same time, τ must equal to the average waiting time for a double-kink nucleation,

$$\tau = \frac{1}{JX}, \quad (\text{C.2})$$

so that

$$X = \sqrt{\frac{v_k}{J}}, \quad (\text{C.3})$$

and dislocation velocity is then

$$v = 2hXJ = 2h\sqrt{Jv_k}, \quad (\text{C.4})$$

where h is the kink height. A more detailed analysis of Bertocci [248] incorporating the effect of statistical fluctuations gives similar results, but with different numerical constants,

$$\tau = \frac{1}{2JX}, \quad (\text{C.5})$$

$$X = \sqrt{\frac{v_k}{2J}}, \quad (\text{C.6})$$

$$v = h\sqrt{2Jv_k}. \quad (\text{C.7})$$

For completeness, we reproduce Bertocci's development here. The Bertocci's model was designed for surface growth but it can be translated into the language of dislocation motion without any change in its mathematical content. Define the density for left and right kink as ρ_+ and ρ_- respectively. Let $\zeta = \rho_+ - \rho_-$ and total kink density $\rho = \rho_+ + \rho_-$. Let l be the distance between two left kinks and $n(l)$ be the normalized statistical distribution,

$$\int_0^\infty n(l)l dl = 1, \quad (\text{C.8})$$

$$\int_0^\infty n(l) dl = \rho_+. \quad (\text{C.9})$$

The average lifetime for a right kink (–) nucleated on a segment l is

$$\tau_-(l) = \frac{l}{4v_k}. \quad (\text{C.10})$$

The density of right kink ρ_- is then the product of life time $\tau_-(l)$ and the rate of production on segment l , $Jn(l)l$, integrated over all l 's,

$$\rho_- = \int_0^\infty J\tau_-(l)n(l)l dl = \frac{J}{4v_k} \int_0^\infty n(l)l^2 dl. \quad (\text{C.11})$$

If one assumes no correlation between individual events, i.e.

$$n(l) = n_0 \exp(-al) = \rho_+^2 \exp(-\rho_+ l), \quad (\text{C.12})$$

then

$$\rho^2 - \zeta^2 = 4\rho_+\rho_- = 2J/v_k, \quad (\text{C.13})$$

$$\rho = \sqrt{\frac{2J}{v_k} + \zeta^2}, \quad (\text{C.14})$$

$$v = \rho h v_k = h \sqrt{2J v_k + \zeta^2 v_k^2}. \quad (\text{C.15})$$

In the case of non-tilted dislocations, $\zeta = \rho_+ - \rho_- = 0$, Eq. (C.15) reduces to Eq. (C.7). Although Bertocchi' model includes statistical fluctuations, it is still not a rigorous proof of Eq. (C.7), due to the approximation made in Eq. (C.10), (C.12). On the other hand, if one assumes uniform double-kink nucleation rate J and kink velocity v_k , the dislocation velocity has to take the form

$$v = \alpha h \sqrt{J v_k}, \quad (\text{C.16})$$

from dimensional analysis. The argument goes as the following. Define $X_s = 1/\rho$, which is the average separation between kinks, then

$$v = h \frac{v_k}{X_s} = 2hXJ, \quad (\text{C.17})$$

$$XX_s = \frac{v_k}{2J}. \quad (\text{C.18})$$

Note that X (average kink migration distance) and X_s (average kink separation) are different entities, the former being more related with dynamics (kink life time) and the latter more with statics (instantaneous kink distribution). The Bertocchi's model is equivalent to the approximation of $X = X_s$, while the original H-L model is equivalent to $X = 2X_s$. If one neglects the discreteness of elementary kink jump distance, there will be no intrinsic length scale of the system and X must be proportional with X_s ,

which will lead to Eq. (C.16). Although no rigorous proof exists for $\alpha = \sqrt{2}$ in Eq. (C.16), it was confirmed by Monte Carlo simulations [248].

A detailed derivation of double kink nucleation rate J and kink drift velocity v_k , based on stochastic jumps of kinks are given in the next section. Here we simply quote the result of H-L model based on continuous kink diffusion,

$$J = \frac{\sigma b h}{a^2 k_B T} D_k \exp\left(-\frac{2E_k}{k_B T}\right), \quad (\text{C.19})$$

$$v_k = D_k \frac{\sigma b h}{k_B T}, \quad (\text{C.20})$$

$$(\text{C.21})$$

where a is the elementary kink jump distance, E_k is the kink formation energy and D_k is the kink diffusivity,

$$D_k = \omega_0 a^2 \exp\left(-\frac{W_m}{k_B T}\right). \quad (\text{C.22})$$

Here W_m is the kink migration energy barrier and ω_0 is the attempt frequency and is usually taken as the *Debye* frequency of the lattice. Therefore,

$$J = \omega_0 \frac{\sigma b h}{k_B T} \exp\left(-\frac{2E_k + W_m}{k_B T}\right), \quad (\text{C.23})$$

$$v_k = \omega_0 \frac{a^2 \sigma b h}{k_B T} \exp\left(-\frac{W_m}{k_B T}\right), \quad (\text{C.24})$$

$$v = \omega_0 \sqrt{2} h \frac{\sigma b h a}{k_B T} \exp\left(-\frac{E_k + W_m}{k_B T}\right). \quad (\text{C.25})$$

Eq. (C.25) is valid for infinitely long dislocations. It shows that the temperature dependence of dislocation velocity is governed by the effective activation energy $Q = E_k + W_m$. For dislocation segments with finite length L , the dislocation velocity becomes modified to

$$v = h \sqrt{2Jv_k} \frac{L}{L + X}. \quad (\text{C.26})$$

In the limit of $L \ll x$, the dislocation velocity becomes nucleation controlled,

$$\begin{aligned} v &= hLJ = \frac{\sigma b h^2 L}{a^2 k_B T} D_k \exp\left(-\frac{2E_k}{k_B T}\right) \\ &= \omega_0 \frac{\sigma b h^2 L}{k_B T} \exp\left(-\frac{2E_k + W_m}{k_B T}\right). \end{aligned} \quad (\text{C.27})$$

Therefore, in the limit of short dislocation segments, their temperature dependence of dislocation velocity is governed by a higher activation energy $Q = 2E_k + W_m$.

C.2 H-L Model with Discrete Kink Jump

In the previous section, we quoted the expressions for J and v_k from H-L theory [30]. They were derived by assuming kink diffusion on a continuous landscape. In this section, we present a rigorous derivation of J and v_k based on discrete kink jumps. The discrete approach is more physical in the limit of high Peierls barrier such as in Si. We will show that most of the predictions of H-L theory can be rederived in the language of discrete kink jumps. However, in low stress limit, prediction of H-L model should be modified.

In this section, we still ignore the elastic interaction between kinks, leaving the most complete treatment to the kinetic Monte Carlo simulations in Chapter 7 and 8. In this case, the kink pair energy E_{dk} as a function of width w takes the form as shown in Fig. C-1.

The nucleation rate of embryonic double-kink (width $w = 1$) is then

$$j_{dk}(1) = \omega_0 \exp\left(-\frac{2E_k + W_m}{k_B T}\right). \quad (\text{C.28})$$

Following Chapter 7, the nucleation rate of double-kink with finite width $w = N$ can be calculated as

$$j_{dk}(N) = j_{dk}(1) \cdot p_s(1 \rightarrow N), \quad (\text{C.29})$$

where p_s is the survival probability. Because the kink elastic energy is ignored, we

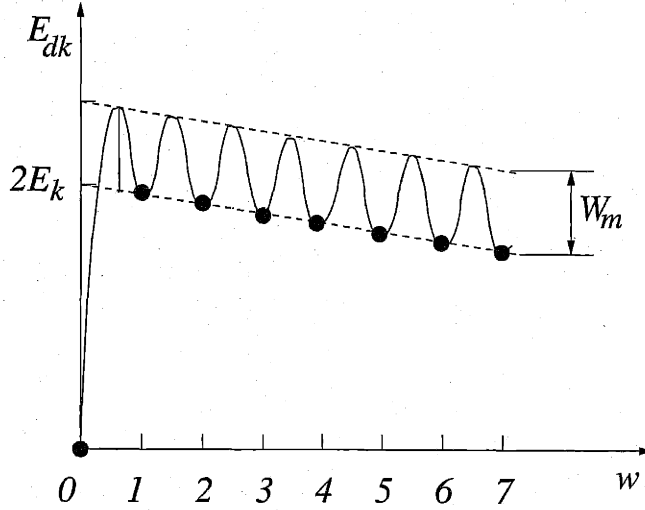


Figure C-1: Kink pair energy E_{dk} as a function of width w , shown as dots. Elastic interactions of between kinks are ignored. The applied stress creates a tilt in the energy landscape.

can derive the explicit form of p_s . As shown in Fig. C-1, the kink pair energy E_{dk} as well as energy barriers are the following,

$$E_{dk}(w) = 2E_k - \sigma abhw, \quad (\text{C.30})$$

$$W^+ = W_m - \frac{1}{2}\sigma abh, \quad (\text{C.31})$$

$$W^- = W_m + \frac{1}{2}\sigma abh \quad (\text{C.32})$$

The forward and backward probability are the same for each state ($i \leq 1$),

$$F(i) = \left[1 + \exp\left(-\frac{\sigma abh}{k_B T}\right) \right]^{-1} \equiv F, \quad (\text{C.33})$$

$$B(i) = 1 - F(i) = \left[1 + \exp\left(\frac{\sigma abh}{k_B T}\right) \right]^{-1} \equiv B \quad (\text{C.34})$$

Following Eq. (7.9), (7.11), the general solution for the survival probability is

$$p_s(m, n) = \frac{1 - (B/F)^m}{1 - (B/F)^n} \quad (\text{C.35})$$

Let $B = 1/2 - \alpha$, $F = 1/2 + \alpha$. In the limit of $\alpha \ll 1$,

$$\alpha = \frac{\sigma abh}{4k_B T}, \quad (\text{C.36})$$

$$\frac{B}{F} = 1 - 4\alpha, \quad (\text{C.37})$$

$$p_s(m, n) = \frac{1 - (1 - 4\alpha)^m}{1 - (1 - 4\alpha)^n} = \frac{m}{n} \quad (\text{C.38})$$

However, if $\alpha \ll 1$ but with $n \rightarrow \infty$ and $\alpha n > 1$, then

$$\alpha = \frac{\sigma abh}{4k_B T}, \quad (\text{C.39})$$

$$\frac{B}{F} = 1 - 4\alpha, \quad (\text{C.40})$$

$$p_s(m, \infty) = 1 - \left(\frac{B}{F}\right)^m = 4\alpha m, \quad (\text{C.41})$$

$$p_s(1, \infty) = 4\alpha = \frac{\sigma abh}{k_B T}. \quad (\text{C.42})$$

Therefore the double-kink nucleation rate J is

$$J = j_{dk}(1) \cdot p_s(1, \infty)/a = \omega_0 \frac{\sigma b h}{k_B T} \exp\left(-\frac{2E_k + W_m}{k_B T}\right). \quad (\text{C.43})$$

Thus we reproduce Eq. (C.23).

Next we study how Eq. (C.24) can be reproduced, by calculating the elastic average time for a “successful” double-kink to expand to a given width N , in the limit of $N \gg 1$. Define *forward time* of state i , $t_f(i)$ as the average time it takes for the double-kink to reach width $i + 1$, starting from width i , under the condition that it never reaches state with width 0. Define average waiting time for elementary kink jump

$$\tau \equiv \frac{1}{2} \omega_0^{-1} \exp\left(\frac{W_m}{k_B T}\right), \quad (\text{C.44})$$

then

$$t_f(1) = \tau, \quad (C.45)$$

$$\begin{aligned} t_f(2) &= \tau F + B(\tau + t_f(1) + t_f(2)) \\ &= \frac{\tau}{F} + \frac{B}{F} t_f(1) \end{aligned} \quad (C.46)$$

Define $g \equiv F/B = 1 - 4\alpha = 1 - \sigma abh/k_B T$, then

$$t_f(1) = \tau, \quad (C.47)$$

$$t_f(2) = (F^{-1} + g)\tau, \quad (C.48)$$

$$t_f(3) = (F^{-1}(1 + g) + g^2)\tau, \quad (C.49)$$

$$t_f(4) = (F^{-1}(1 + g + g^2) + g^3)\tau. \quad (C.50)$$

$$(C.51)$$

The total time $t(1, N)$ it takes to reach state N from state 1, under the condition that state 0 is never reached is

$$\begin{aligned} t(1, N) &= \sum_{i=1}^N t_f(i) \\ &= \tau \left\{ F^{-1} \left[\frac{N-1}{1-g} - g \frac{1-g^{N-1}}{(1-g)^2} \right] + \frac{1-g^N}{1-g} \right\} \\ &\approx \frac{\tau}{1-g} \left[(2N-1) - 2g \frac{1-g^{N-1}}{1-g} - g^N \right], \end{aligned} \quad (C.52)$$

where in the last step $F \approx 1/2$ is used. A plot of $t(1, N)$ as a function of N at different value of $\alpha = (1-g)/4$ is given in Fig. C-2.

In the limit of $N \rightarrow 0$, $\alpha \ll 1$,

$$t(1, N) \approx \tau(3N - 2), \quad (C.53)$$

$$(C.54)$$

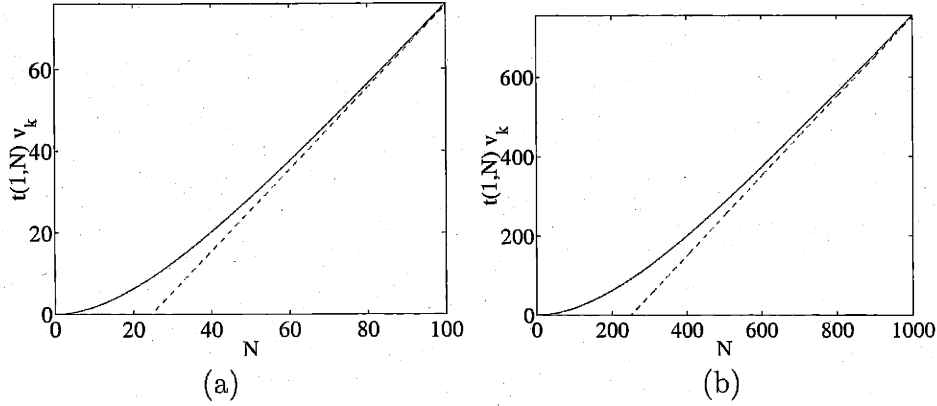


Figure C-2: Expansion time $t(1, N)$ for successful double-kinks (see text). Kink jump step is set to $a = 1$. (a) $\alpha = 0.01$, $x_d = 24.5$, $v_k = 0.02$. (b) $\alpha = 0.001$, $x_d = 249.5$, $v_k = 0.002$.

In the limit of $N \rightarrow \infty$, $g^N \rightarrow 0$,

$$\begin{aligned} t(1, N) &\approx \frac{2\tau}{1-g} \left(N - \frac{1+g}{2(1-g)} \right) \\ &\equiv \frac{(N - n_D)a}{v_k}, \end{aligned} \quad (\text{C.55})$$

where

$$n_D \equiv (1+g)/2(1-g) = 1/4\alpha - 1/2 = \frac{k_B T}{\sigma a b h} - \frac{1}{2}, \quad (\text{C.56})$$

$$v_k \equiv \frac{a(1-g)}{2\tau} = \frac{2a\alpha}{\tau} = \omega_0 \frac{\sigma a^2 b h}{k_B T} \exp\left(-\frac{W_m}{k_B T}\right) \quad (\text{C.57})$$

Therefore, we reproduce the expression for v_k in Eq. (C.24). Moreover, n_D in Eq. (C.56) correspond to the critical separation x^* in H-L theory [30] (p. 538) through $\Delta x \equiv n_D a \approx x^*$. The physical meaning of Eq. (C.55) is that, kinks belonging to successful kink pairs¹ have an apparent velocity higher than v_k when their anti-kink is within a distance Δx away. This apparent “repulsion” between kinks is completely statistical in nature. It is simply because those kink pairs which do not move fast away from each other has a larger probability of annihilating with themselves and will not become a “successful” pair. To incorporate this effect, the H-L model for dislocation

¹Those who do not annihilate with themselves.

velocity should be modified in the following way.

$$v = 2hXJ \approx h \frac{v_k}{X - \Delta x}, \quad (\text{C.58})$$

which lead to

$$X^2 - \Delta x X - X_{HL}^2 = 0, \quad (\text{C.59})$$

where $X_{HL} = \sqrt{v_k/2J}$. The solution is

$$X = \frac{\Delta x}{2} + \sqrt{\left(\frac{\Delta x}{2}\right)^2 + X_{HL}^2}, \quad (\text{C.60})$$

$$v = v_0 + \sqrt{v_0^2 + v_{HL}^2} \quad (\text{C.61})$$

where $v_{HL} = 2hJX = \sqrt{2Jv_k}$ and

$$v_0 = hJ\Delta x \quad (\text{C.62})$$

$$\approx \frac{k_B T J}{\sigma b} \quad (\text{C.63})$$

$$= \omega_0 h \exp\left(-\frac{2E_k + W_m}{k_B T}\right) \quad (\text{C.64})$$

Eq. (C.61) provides a correction term (v_0) for the dislocation velocity in H-L model, due to the effect of lattice discreteness. The correction is always positive and becomes more significant in the limit of high temperature, low stress and low kink formation energy E_k . However, as shown in Fig. C-2, Eq. (C.55) and hence Eq. (C.61) are valid only if $X \geq 2\Delta x$, or $v_{HL} \geq 4v_0$.

C.3 Correlated Double Kink Nucleation in Si

In Chapter 7.2.2 we studied double-kink nucleation and expansion as a one-dimensional random walk process on a semi-infinite lattice. It has been postulated [55] that double-kink nucleation on two partial dislocations in Si at low stress could be correlated. In

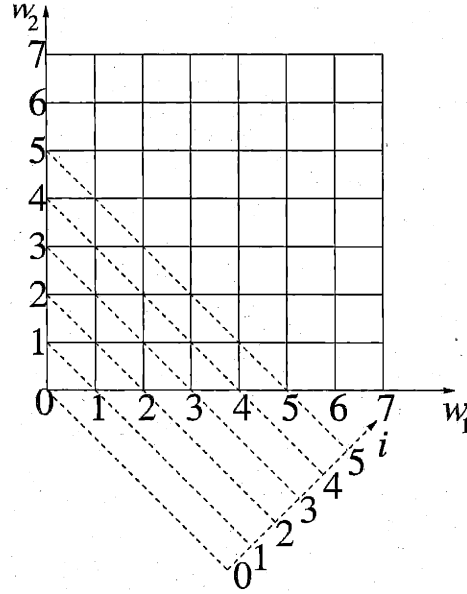


Figure C-3: Two-dimensional lattice representing the width of the double-kinks on the coupled partials.

Chapter 7.3.3, it is shown that this correlation may or may not exist depending on whether the ideal partial separation X_0 is commensurate or not with the periodicity of the Peierls barrier. In this section, we investigate this correlation by isolating the double-kink nucleation on two partials from other kink events and model it as a Markov process, similar to the treatment of kink nucleation on a single partial in Chapter 7.2.2. This is the first detailed study of correlated double-kink nucleation by discrete stochastic processes, and it is supposed to be more rigorous than previous investigations [55].

The system of double-kinks on two coupled partial dislocations can be mapped on to a discrete 3-dimensional lattice, with each lattice point (w_1, w_2, L) specifying the width of the two double-kinks (w_1 and w_2) and the offset between their centers (L). For simplicity, we assume $L = 0$ in following discussions, so that the system corresponds to the first quadrant of a 2-dimensional square lattice, as shown in Fig. C-3. The double-kink nucleation and growth process then corresponds to the random walk on this 2-dimensional lattice. Due to the elastic interaction between kinks and the randomness of their motion, kink pairs with small widths are prone to annihilate with themselves. In this section, we calculate the rate for nucleating kink pairs with

width larger than one lattice spacing.

Define sets of states

$$\hat{i} = \{(w_1, w_2) | w_1 + w_2 = i, w_1 \geq 0, w_2 \geq 0\}. \quad (\text{C.65})$$

In the following discussion, we simply call \hat{i} a state, which contains $i+1$ sub-states with $w_1 = 0, \dots, i$. Due to the connectivity of the lattice, the system cannot reach state \hat{i} without go to $(\hat{i} - 1)$. Therefore, a recursive formula similar to that in Chapter 7.2.2 can be developed. It follows that all the definitions and derivations in Chapter 7.2.2 can be directly applied here, provided the variables are now interpreted as matrices.

The double-kink nucleation rate for state \hat{N} is related with the survival probability $p_s(\hat{1} \rightarrow \hat{N})$ through,

$$j_{dk}(\hat{N}) = j_{dk}(\hat{1}) \cdot p_s(\hat{1} \rightarrow \hat{N}), \quad (\text{C.66})$$

where $j_{dk}(\hat{N})$, $j_{dk}(\hat{1})$, $p_s(\hat{1} \rightarrow \hat{N})$ are $1 \times (N+1)$, 1×2 and $2 \times (N+1)$ matrices, respectively. The survival probability matrix can be calculated as

$$p_s(\hat{1} \rightarrow \hat{N}) = \prod_{i=1}^{N-1} p_s(\hat{i} \rightarrow (\hat{i} + 1)), \quad (\text{C.67})$$

$$p_s(\hat{i} \rightarrow (\hat{i} + 1)) = \left[I - B(\hat{i}) p_s((\hat{i} - 1) \rightarrow \hat{i}) \right]^{-1} \cdot F(\hat{i}), \quad (\text{C.68})$$

$$(\text{C.69})$$

where $F(\hat{i})$ and $B(\hat{i})$ forward and backward probability matrices with dimension $i \times (i+1)$ and $i \times (i-1)$ respectively. $F(\hat{i})$ and $B(\hat{i})$ can be calculated from the energy difference between state \hat{i} and its neighboring states. They are band matrices due to the connectivity of the square lattice. The explicit form of $F(\hat{i})$ and $B(\hat{i})$ is omitted here for brevity.

Fig. C-4 shows the energy landscape on the square lattice (w_1, w_2) , in the case of commensurate ($X_0 = 5.0$) and incommensurate ($X_0 = 5.5$) partial separations, calculated using linear elasticity (more details in Appendix D). From the energy

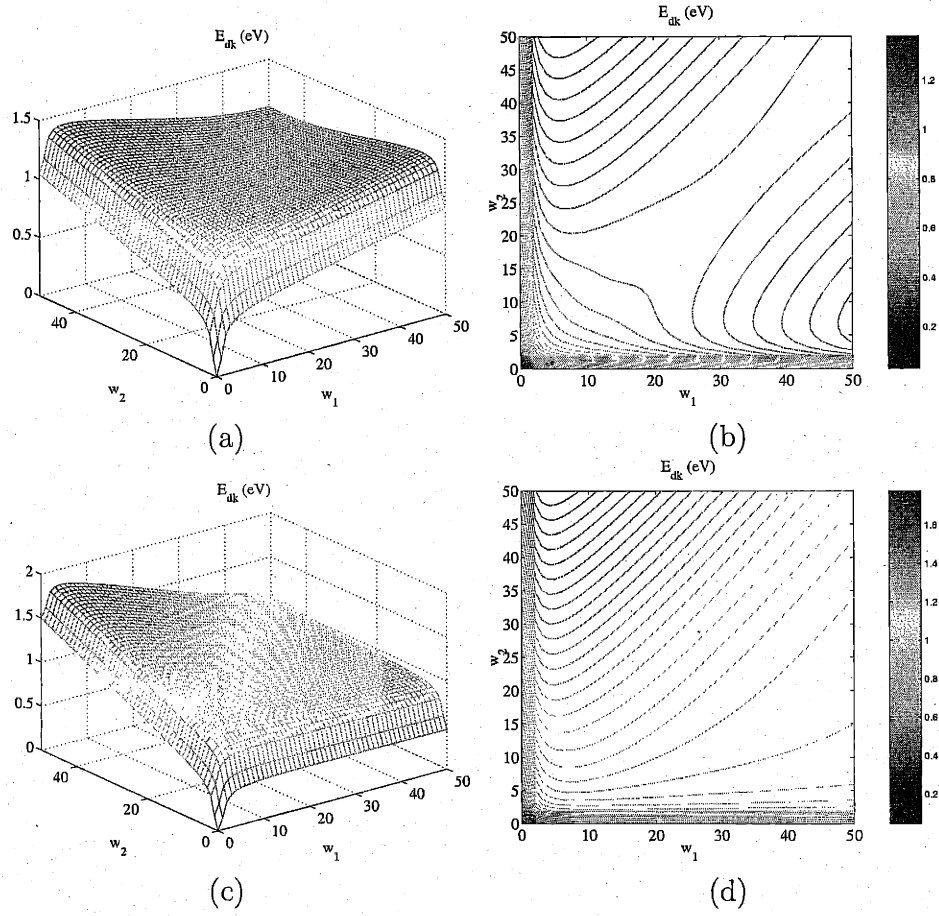


Figure C-4: Energy landscape and contour for double-kinks on the two coupling partials as a function of their width w_1 and w_2 . (a), (b) $X_0 = 5.0$. (c), (d) $X_0 = 5.5$. Kink energy $E_k = 0.25\text{eV}$. Stress $\sigma = 4\text{MPa}$.

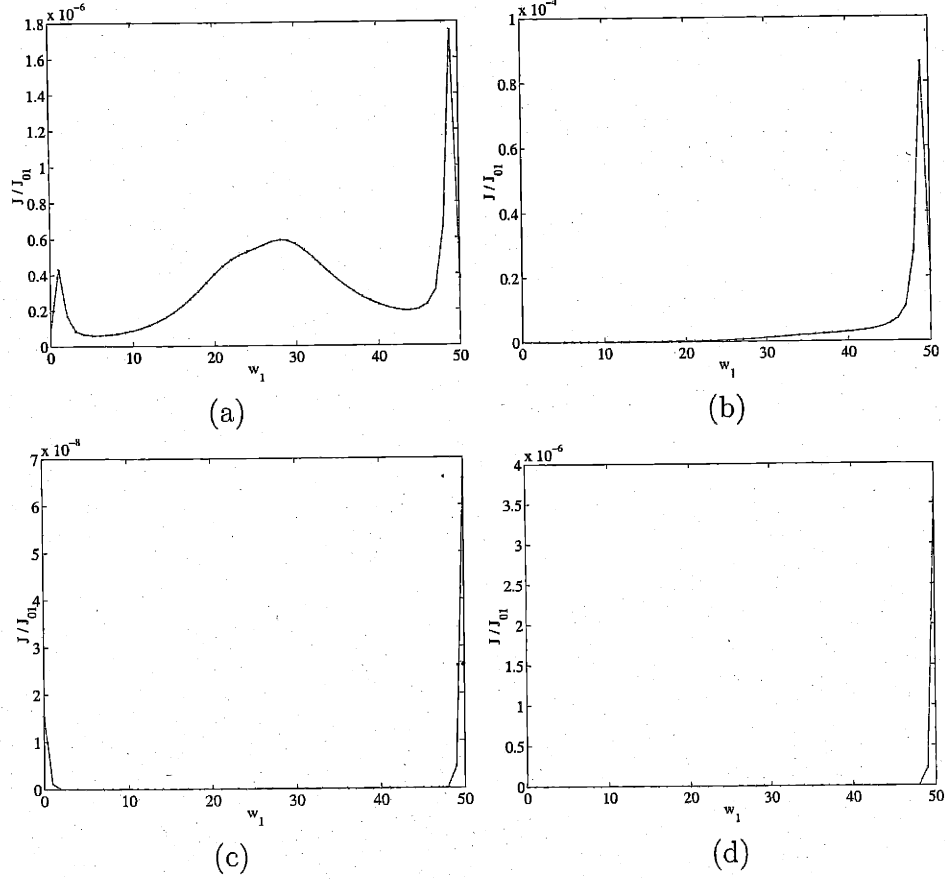


Figure C-5: Rate distribution of double-kink nucleation on two partials with $w_1 + w_2 = w = 50$ at stress $\sigma = 4\text{MPa}$. (a) $X_0 = 5.0$, $E_k = 0.25\text{eV}$. (b) $X_0 = 5.5$, $E_k = 0.25\text{eV}$. (c) $X_0 = 5.0$, $E_k = 0.5\text{eV}$. (d) $X_0 = 5.5$, $E_k = 0.5\text{eV}$.

landscape in (a) and (b), one can anticipate that correlated nucleation on two partials ($w_1 \approx w_2$) is the only way to nucleate kink pairs at small stresses that is energetically favorable, for $X_0 = 5.0$. In Fig. C-4(c) and (d), $X_0 = 5.5$ while the actual separation of the partials is $X = 5$. The energy landscape shows that double-kink nucleation on the leading partial ($w_1 > 0, w_2 = 0$) is favored. This observation is largely consistent with the detailed rate calculation using the recursive formula above. However, it is found that the kink energy E_k also play an important role on the nucleation correlations.

Fig. C-5 shows the distribution of double-kink nucleation rates in state $\tilde{50}$, i.e. $w_1 + w_2 = 50$, among the 51 individual substates. For $E_k = 0.25\text{eV}$, the difference in the commensurate and incommensurate case is clearly observed. At $X_0 = 5.0$, a peak exists for $w_1 \approx w_2$ indicating a large contribution from correlated nucleation. At

$X_0 = 5.5$, only a single peak exists around $w_1 = 49$, so that double-kink nucleation on the leading partial is the main contribution. In the case of $E_k = 0.5\text{eV}$, the peak at $w_1 \approx w_2$ ceased to exist even for the commensurate case. However, two peaks are observed for $X_0 = 5.0$ indicating kink nucleation on both partials are both possible. When $X_0 = 5.5$, only nucleation on the leading partial is favored. For both small and large values of E_k , the double-kink nucleation rate is always larger in the incommensurate case ($X_0 = 5.5$) than that in the commensurate case ($X_0 = 5.5$), in agreement with Chapter 7.3.3.

C.4 Debris Loop Distribution

In this section we derive the size distribution of the remnant (debris) dislocation loops in the wake of a moving screw dislocation, under the assumption that double-kink nucleations occur randomly and uncorrelated on two slip planes.

Consider the growth of the two arms of a kink cluster, also called cross kink, or super jog on screw dislocations in BCC metals. According to the kMC model in Chapter 8, double kink nucleation on three (110) planes are possible. When the maximum resolved shear stress (MRSS) plane bisects two (110) planes, double-kink nucleation rates on these two planes are equal, and super jog are most likely to grow. In this section, we only consider double kink nucleation on two slip planes for simplicity. In this case, the growth of two arms of the super jog is equivalent to two random walkers in two dimensional lattice, as shown in Fig. C-6.

For simplicity, we only consider kink formation in the forward direction, i.e. the random walkers only moves upward or to the right. Define p as the probability of choosing upward, and $1 - p$ for moving to the right. Let the meeting point to be $X(m, n)$, then the length of the loop is $2L = 2(m + n)$. Define the area of the loop as A . In this section, we calculate the distribution functions of L and A in terms of p .

This problem can be simplified into the process of one random walker on a one dimensional lattice. Define coordination transformation $i = m + n$, $j = n - m$ and $k(i) = j_1(i) - j_2(i)$ as the offset of the two walker along j direction for a given i .

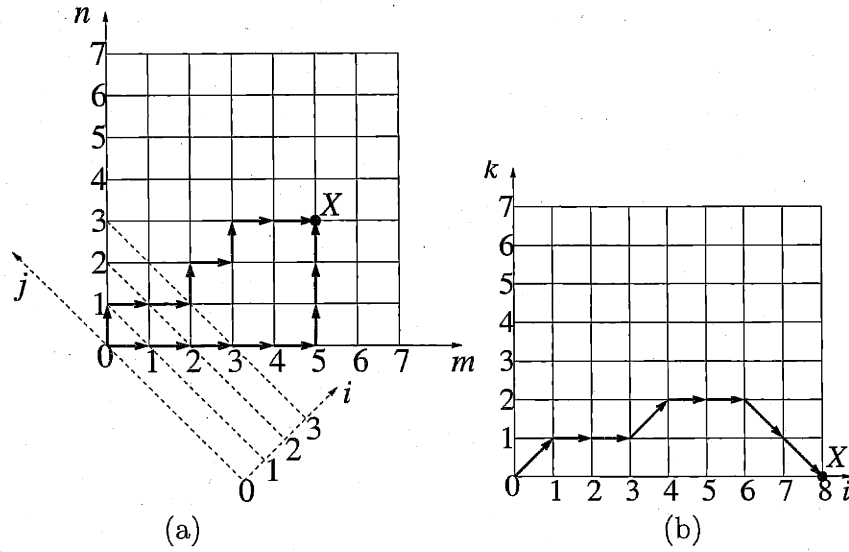


Figure C-6: (a) Two random walkers on two dimensional lattice representing the growth of the two arms of the super jog. (b) Coordinate transformation of (a) into a one-dimensional random walk.

Then the loop formation process can be regarded as a one-dimensional random walk along k axis, with i playing the role of time. The initial condition is $k(i = 0) = 0$, $k(i = 1) = 1$ and the random walk terminates, i.e. loop forms at $k(i) = 0$ again. At each step, the walker can either go up, or down, or stay at the same level with probabilities p_1, p_2, p_3 , respectively i.e.

$$k(i+1) = \begin{cases} k(i) + 1, & p_1 = p(1-p) \\ k(i), & p_2 = p^2 + (1-p)^2 \\ k(i) - 1, & p_3 = p(1-p) \end{cases} \quad (\text{C.70})$$

The probability of a given path is then the product of L number of p_i terms, $i = 1, 2, 3$. For example, the probability of the path shown in Fig. C-6(b) is $p_1 p_2 p_2 p_1 p_2 p_2 p_3 p_3$. Define $F(L, A)$ as the summation of probabilities for all paths with length L and area A , for which only the starting and ending point has $k = 0$, while all other points satisfies $k > 0$. Since all such paths must choose p_1 in the first step and p_3 in the last step, the probability distribution function $f(L, A)$ that we are after is $f(L, A) = p_1^{-1} p_3^{-1} F(L, A)$. Also define $G(L, A)$ as the summation of probabilities

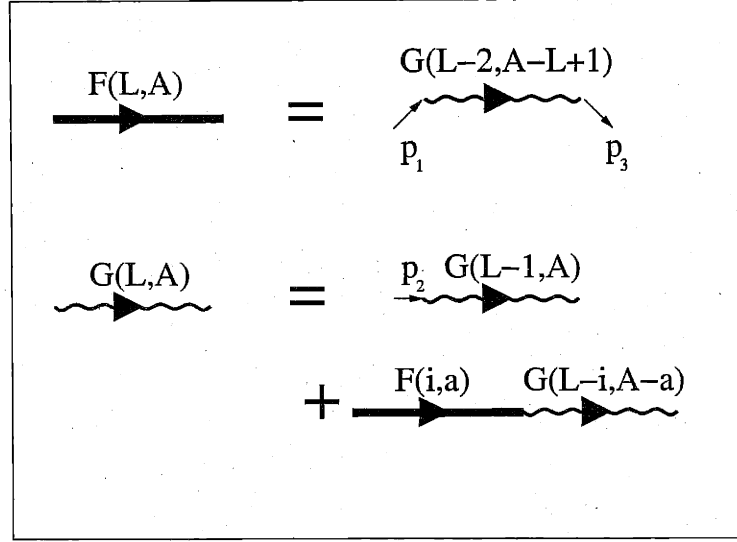


Figure C-7: Diagram for $F(L, A)$ (solid path) and $G(L, A)$ (wavy path) and their recursive relationships.

for all paths with all points satisfies $k \geq 0$. We can develop recursive relations for $F(L, A)$ and $G(L, A)$.

As shown in Fig. C-7, we can represent $F(L, A)$ as a solid path, and $G(L, A)$ as a wavy path, and they satisfy the recursive relationship,

$$F(L, A) = p_1 p_3 G(L-2, A-L+1), \quad (\text{C.71})$$

$$G(L, A) = p_2 G(L-1, A) + \sum_{i=1}^L \sum_{a=1}^A F(i, a) G(L-i, A-a), \quad (\text{C.72})$$

$$(\text{C.73})$$

with initial conditions

$$F(1, A) = 0, \quad (\text{C.74})$$

$$F(2, 1) = p_1 p_3, \quad (\text{C.75})$$

$$G(0, A) = 0, \quad (\text{C.76})$$

$$G(1, 0) = p_2 \quad (\text{C.77})$$

Similar relations also exist for the distribution function for loop half length L alone,

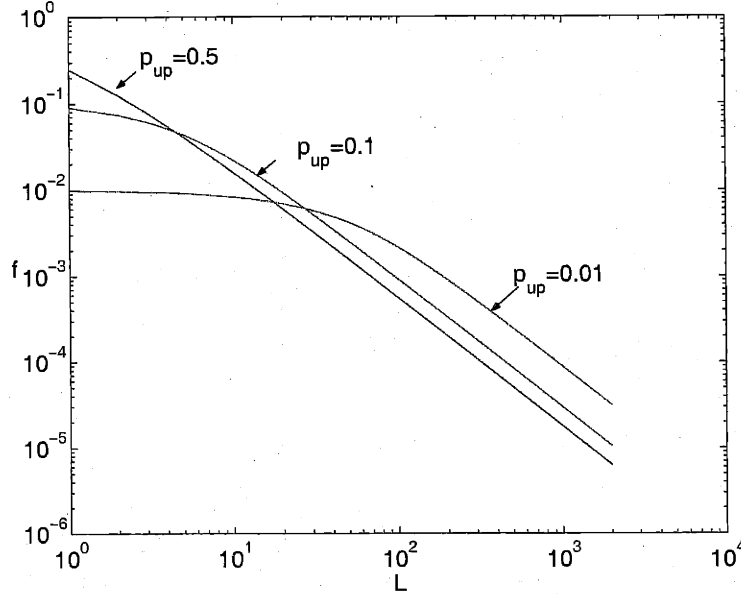


Figure C-8: Loop half length distribution function $f(L)$ for different values of p .

i.e.

$$f(L) = p_2 f(L-1) + \sum_{i=2}^L f(i-2) f(L-i), \quad (\text{C.78})$$

$$f(0) = 1, \quad (\text{C.79})$$

$$f(1) = p_2 \quad (\text{C.80})$$

Fig. C-8 shows the numerical solution of loop half length distribution function $f(L)$ for different p . The distribution function has a slow decaying tail $\sim L^{-3/2}$, regardless of the value of p . Therefore, the average loop half length $\langle L \rangle$ diverges, meaning that there exist appreciable probability of finding arbitrarily large loops. The distribution function $f(L, A)$ for fixed L and fixed A are plotted in Fig. C-9 and a contour plot of $f(L, A)$ is shown in Fig. C-10. The dislocation function is nonzero only for $L^2/4 \leq A \leq L-1$, and are most prominent along the ridge $A = L^{1.5}/2.3$, indicating a “fractal” loop dimension of $D = 1.5$.

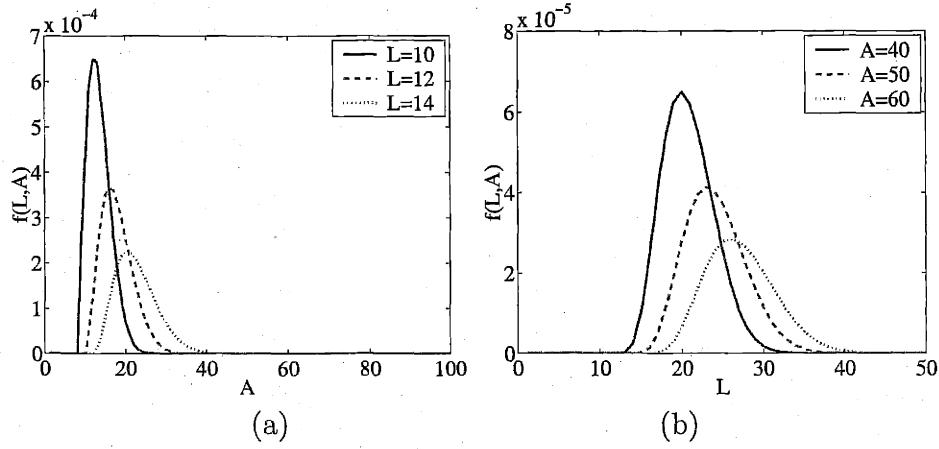


Figure C-9: Distribution function $f(L, A)$ for (a) fixed L and (b) fixed A at $p = 0.5$.

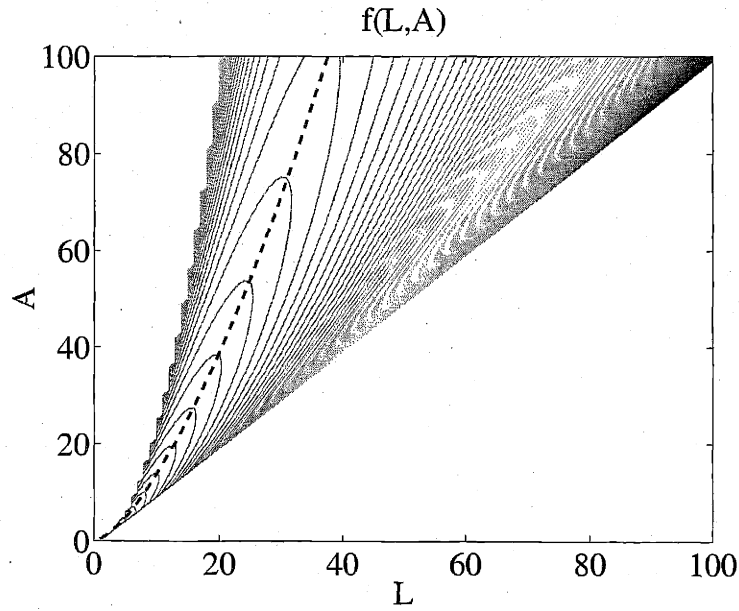


Figure C-10: Contour plot of $f(L, A)$ for $p = 0.5$. $f(L, A)$ is nonzero only for $L^2/4 \leq A \leq L-1$, and are most prominent along the ridge $A = L^{1.5}/2.3$ (dash line), indicating a "fractal" loop dimension of $D = 1.5$.

C.5 Lattice Spin Model of Dislocation Motion

C.5.1 System Description

In this section we discuss an alternative approach for kinetic Monte Carlo (kMC) modeling of dislocation motion, different from that described in Chapter 7. The model development and numerical results presented in this section are the consequences of the author's collaboration with C. Deo ² [249]. Although the ultimate goal of this work is to study dislocation solute interaction, we only discuss dislocation motion in this section.

In this approach, the system is similar to Ising model, and the kMC simulation resembles *cellular automata*. The system is specified by a set of integer values on a 2-dimensional square lattice. For simplicity, assume the lattice values can only be 0 or 1. This 2-dimensional lattice represents a slip plane of the crystal, with value 0 representing the original state of the crystal and value 1 representing the occurrence of slip by one Burgers vector. The dislocation line is then the boundary between the domain of all 0's and that of all 1's, i.e. the boundary between the slipped and unslipped region, as shown in Fig. C-11. This representation is similar to the newly proposed *Phase Field* method for dislocation simulations [250, 251]. Comparing with the method in Chapter 7 and 8, this approach has the advantage that multiple dislocations and dislocation loops can be represented naturally, but the necessity to store a 2-dimensional matrix limits the size of the system.

The kinetic Monte Carlo simulation of dislocation motion then corresponds to flip of lattice values (spins) between 0 and 1. Similar to Chapter 7, an *event list* is generated at each step, which lists the rate of spin flip for every lattice point. A kMC algorithm is then applied to select a particular spin, whose value is then flipped and the simulation continues. The rate of spin flip is then the central aspect of the simulation, which consists of contribution from double-kink nucleation and kink migration mechanisms.

²The original simulation code was implemented by C. Deo (Princeton), whose collaboration with the author during his visit to MIT (during 1/8-1/11/2000) are summarized in [249].

1	1	1	1	1	1	1
1	1	1	1	1	1	1
0	0	0	0	0	0	0
0	0	0	0	0	0	0

Figure C-11: Lattice points next to a dislocation segment

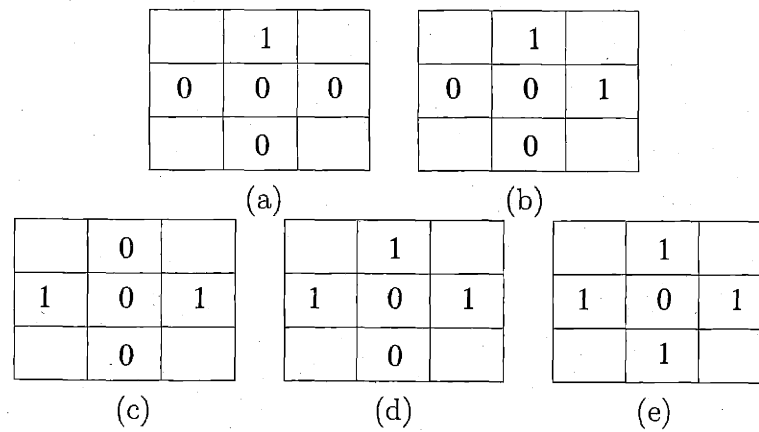


Figure C-12: Local environment of a lattice spin determining whether (a) double-kink nucleation, (b) kink migration, or (c),(d),(e) annihilation is controlling the spin flip.

Because spontaneous dislocation loops is not allowed in this model, a lattice spin cannot flip unless one of its four neighbors has opposite spin values. Furthermore, we use the values of the four neighboring spins to identify whether the spin flip is due to double-kink nucleation and kink migration. As shown in Fig C-12(a), if only one neighbor has opposite spin value, the spin would flip as a double-kink nucleation. If neighbors that are not facing each other have opposite spins, as in (b), kink migration is then possible.. For all other cases, as in (c),(d),(e), the spin would flip as kink annihilation. Different from the treatment in Chapter 7, we specify an annihilation energy barrier E_{ann} and compute the annihilate rate by,

$$j_{\text{ann}} = \omega_0 \exp(-(E_{\text{ann}} + \tau_{yz} b_z A/2)/k_B T) . \quad (\text{C.81})$$

C.5.2 Verify H-L Model

As a check on the validity of the model, simulations with constant double-kink nucleation rate J and kink migration velocity v_k is carried out, whose predictions of dislocation velocity v are compared with that of Hirth-Lothe (HL) model, i.e. $v_{HL} = \sqrt{2Jv_k}$ (see Appendix C.1 for more detail).

The simulation cell consists of 100×100 lattice points s_i . Initially the lattice values s_i in the lower half of the cell are all set to 1 and those in the upper half all set to 0. The average displacement d of the dislocation is simply the number of lattice points that has flipped from (0 to 1), divided by the cell width, i.e. $d = (\sum_i s_i - 5000)/100$. Because every kMC step, one and only one lattice point flips from 0 to 1, a plot of d against kMC steps would always give a straight line with slope 0.01, regardless of the values of J and v_k . On the other hand, dislocation velocity is obtained by plotting d against physical (real) time, and it depends on J and v_k because they determine the relative proportions of nucleation and migration contributions to a spin flip rate.

Fig. C-13(a) shows a snapshot of the simulation with $J = 1$ and $v_k = 50$, (in arbitrary units). Only the lattice sites adjacent to the dislocation are plotted. Fig. C-13(b) shows the average dislocation displacement as a function of the physical time. The average dislocation velocity extracted from the slope of the curve is $v = 10.306$,

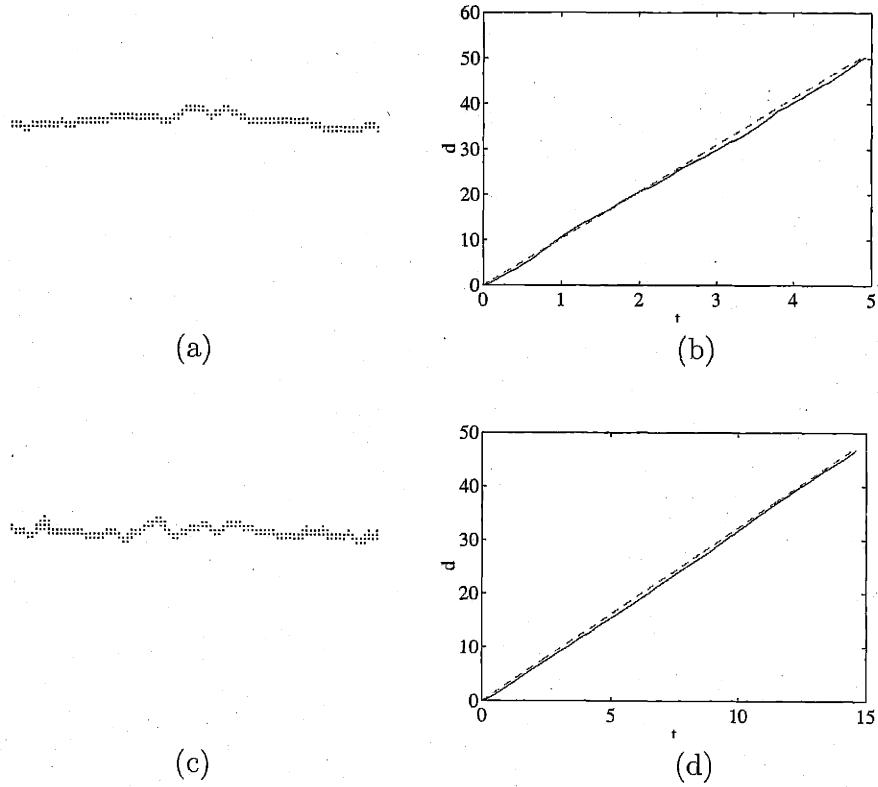


Figure C-13: KMC simulation of dislocation motion with constant double kink nucleation rate J and kink migration rate v_k , only lattice sites neighboring the dislocation are shown. (a) simulation snapshot with $J = 1$, $v_k = 50$. (b) average dislocation displacement as a function of physical time, parameters as in (a). (c) simulation snapshot with $J = 1$, $v_k = 5$, (d) average dislocation displacement, parameters as in (c).

which is in good agreement with the theoretical value of $v_{HL} = 10$. Fig. C-13(c) shows a snapshot of the simulation with $J = 1$ and $v_k = 5$, (in arbitrary units). Fig. C-13(d) shows the average dislocation displacement as a function of the physical time. The average dislocation velocity extracted from the slope of Fig. C-13(d) is $v = 3.23$, in good agreement with the theoretical value of $v_{HL} = 3.16$.

C.5.3 Dislocation Loops and Pinning Points

To demonstrate the robustness of the model in treating multiple dislocations and dislocation loops, simulations with an initial dislocation loop are carried out. Pinning points are also introduced simply by specifying a spin (0) that are not allowed to flip (to 1).

Fig. C-14 shows snapshots of such a simulation with constant J and v_k and ignoring linear elastic interactions. Fig. C-14(a) shows the initial condition of a rectangular dislocation loop with 4 pinning points. Periodic boundary condition is applied so that dislocation can annihilate with itself across the cell border. As shown in Fig. C-14(e), (f), (k), the dislocations is temporarily impeded when it encounters the pinning point. The dislocation then bows around it, eventually leaving behind a small dislocation loop surrounding the pinning point. Since this model does not include linear elastic interactions, i.e. dislocation has no line tension, this bowing-out process occurs rather rapidly, and the pinning point is therefore not a strong obstacle to the dislocation motion in this case. In Fig. C-14(l) and (m), for example, as the dislocation reaches the edge of the simulation cell, it recombines with itself due to the periodic boundary conditions. The recombination occurs quite naturally, with no special rules necessary, showing the robustness of this method.

Fig. C-15 shows snapshots of a similar simulation when the stress field effect is included. In this case, the dislocation appears more straight, due to the effective line tension. As a result, the dragging effect of the pinning point is more pronounced. Eventually, the dislocation annihilates with itself across the periodic boundary, leaving behind four loops surrounding the pinning points.

As a conclusion, we discuss the limitation and future generalizations of the lattice kMC model. The system sizes, i.e. dislocation length and its range of motion are currently limited by the size of the two dimensional array (on the order of 100×100) for the lattice values. This limit can be removed by representing the lattice array as a sparse matrix. As discussed in Chapter 7.3.3, a special treatment for double-kink nucleations is needed to prevent rapid nucleation and annihilation of embryonic

double-kinks. The lattice spins can be generalized to take multiple values, even vectors, to represent multiple dislocations, partial dislocations and stacking faults. It is also possible to apply a Fast Fourier Transform (FFT) method to calculate stresses, similar to the Phase Field approach of Wang et al. [250, 251], which may increase computational efficiency.

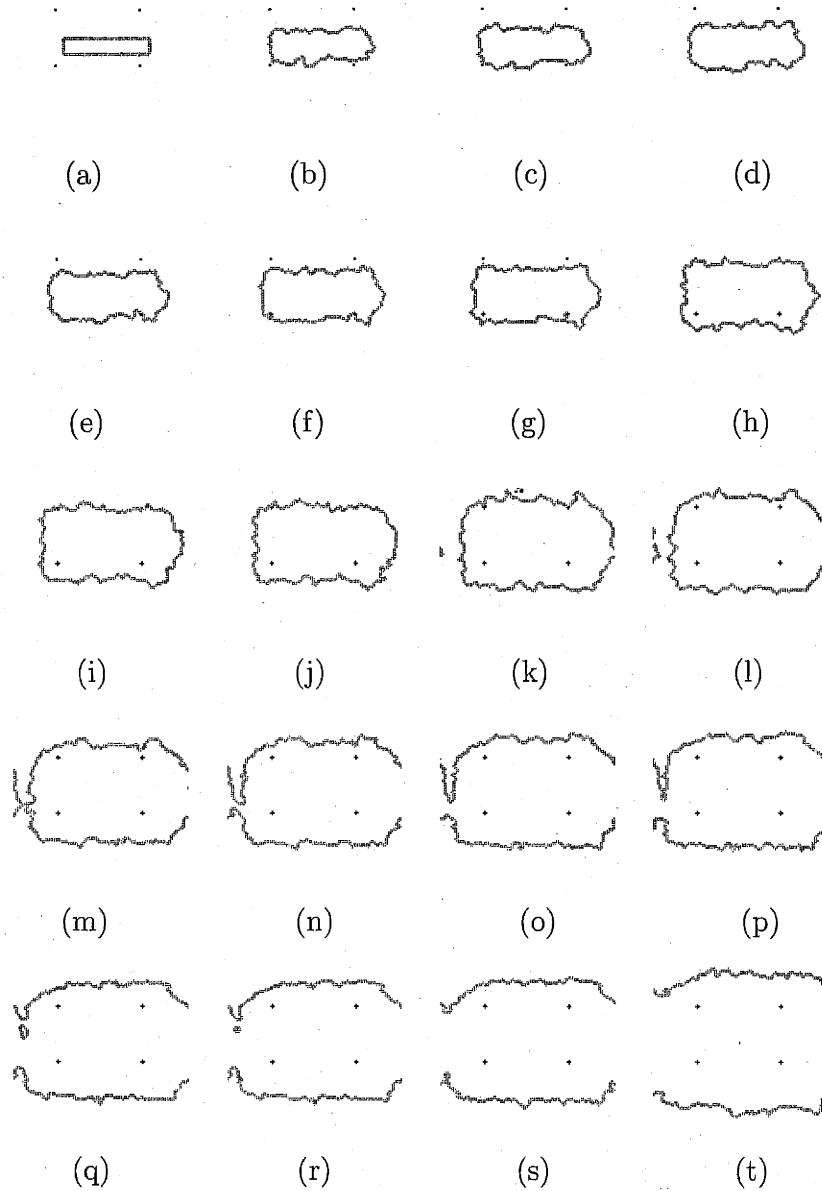


Figure C-14: KMC simulation of dislocation motion with constant double kink nucleation rate J and kink migration rate v_k . The dislocation loop overcomes four pinning points during expansion. (a) initial condition containing a dislocation loop. (b-t) snapshots of subsequent simulation steps.

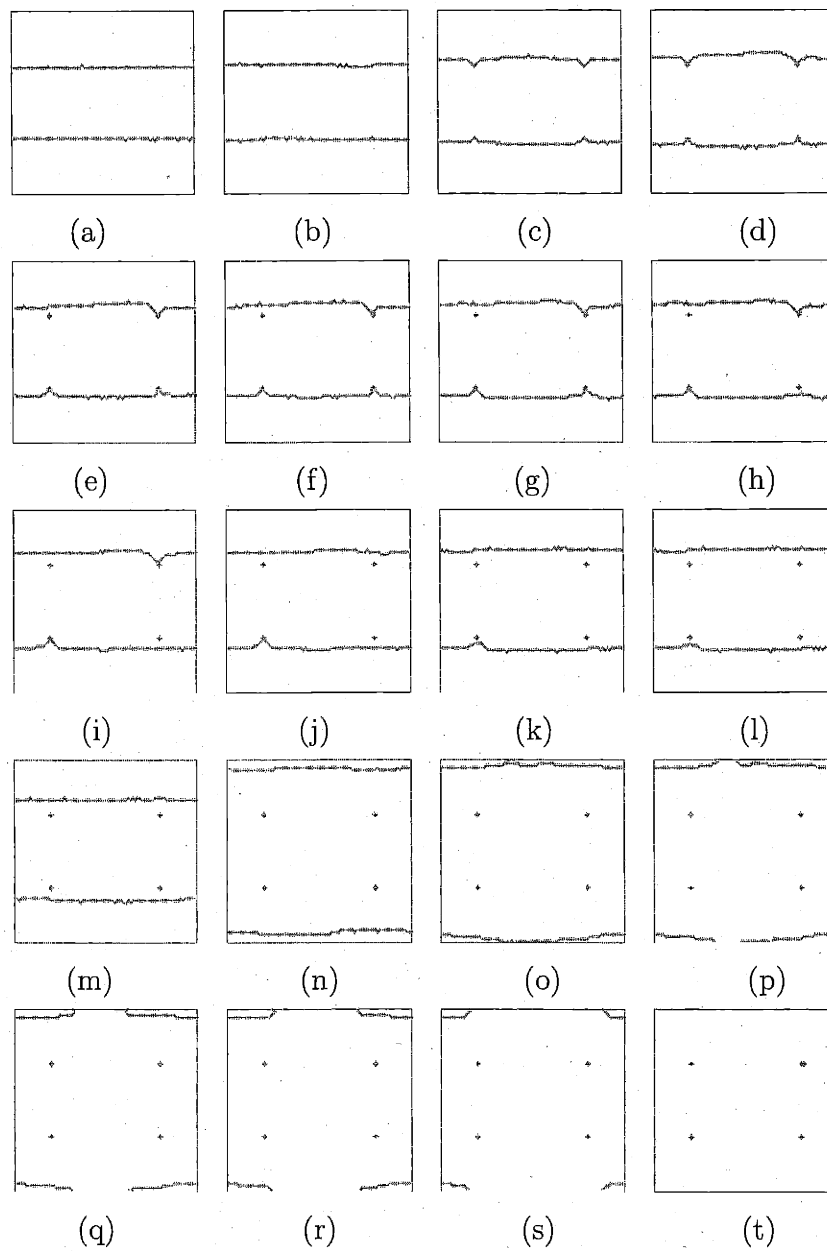


Figure C-15: KMC simulation snapshots of dislocation motion and interaction with pinning points. The effect of dislocation self stress is included.

Appendix D

Linear Elasticity Theory of Dislocations

D.1 Stress in Two-Dimension

In this section, we give the explicit formulas for the stress fields of a dislocation on its glide plane, which are used in kinetic Monte Carlo simulations in Chapter 7. With the coordinate system shown in Fig. D-1, the dislocation Burgers vector is specified by (b_z, b_x) . We have $b_y = 0$ because plane x - z is chosen as the dislocation glide plane.

The formulas below are simplified from those given in [30] for a general case. Only two stress components $(\sigma_{xy}, \sigma_{yz})$ are listed here because they are the only ones that are exert forces back to the dislocation itself. The stress at point (z, x) is given as

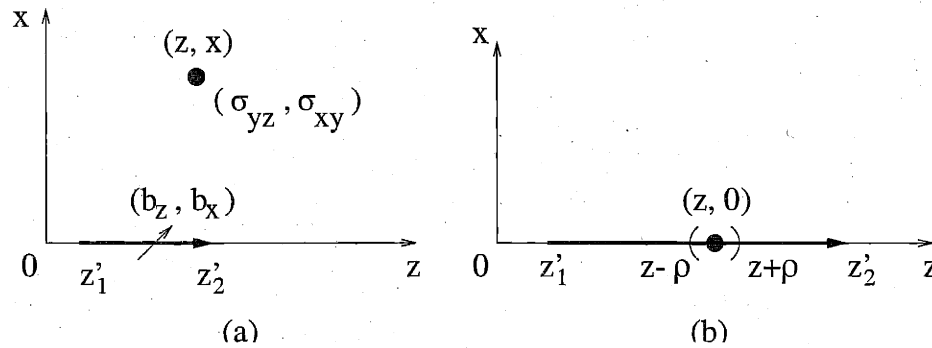


Figure D-1: Stress calculation of dislocation segment for the points on the glide plane.

the difference between functions evaluated at two end points of the segment,

$$\sigma_{xy} = \sigma_{xy}(z'_2) - \sigma_{xy}(z'_1) , \quad (\text{D.1})$$

$$\sigma_{yz} = \sigma_{yz}(z'_2) - \sigma_{yz}(z'_1) , \quad (\text{D.2})$$

where

$$\frac{\sigma_{xy}(z')}{\sigma_0} = \begin{cases} -b_x \frac{x}{R(R+\lambda)} & z < z'_1 < z'_2 \\ b_x \frac{\lambda}{xR} & z'_1 < z < z'_2 \\ b_x \frac{x}{R(R-\lambda)} & z'_1 < z'_2 < z \end{cases} \quad (\text{D.3})$$

$$\frac{\sigma_{yz}(z')}{\sigma_0} = \begin{cases} \nu b_x \frac{1}{R} - (1-\nu) \frac{b_z x}{R(R+\lambda)} & z < z'_1 < z'_2 \\ \nu b_x \frac{1}{R} + (1-\nu) \frac{b_z \lambda}{xR} & z'_1 < z < z'_2 \\ \nu b_x \frac{1}{R} + (1-\nu) \frac{b_z x}{R(R-\lambda)} & z < z'_1 < z'_2 \end{cases} \quad (\text{D.4})$$

$$\sigma_0 = \mu/4\pi(1-\nu) , \quad (\text{D.5})$$

$$\lambda = z' - z , \quad (\text{D.6})$$

$$R^2 = x^2 + (z - z')^2 \quad (\text{D.7})$$

The three forms of stress formula yield are mathematically equivalent results, but each one should be applied at different situations as specified to ensure numerical stability. For example, for infinitely long dislocation, $z'_1 \rightarrow -\infty$, $z'_2 \rightarrow \infty$, one should use the second form and will get,

$$\sigma_{xy} = \frac{2b_x}{x} \sigma_0 = \frac{\mu b_x}{2\pi(1-\nu)x} , \quad (\text{D.8})$$

$$\sigma_{yz} = (1-\nu) \frac{2b_z}{z} \sigma_0 = \frac{\mu b_z}{2\pi x} , \quad (\text{D.9})$$

which agrees with the stress field for infinitely long edge and screw dislocations [30].

To calculate the stress at a point on the dislocation segment, as shown in Fig. D-1(b), we use the “principal value”. This is to say that we will attribute the stress at point $(z, 0)$ due to the segment z'_1, z'_2 as the superposition of the stress due to two segments $z'_1, z - \rho$ and $z + \rho, z'_2$, and take the limit of $\rho \rightarrow 0$. Specifically, when $x = 0$,

$z'_1 < z < z'_2$, we have $\sigma_{xy} = 0$ and $\sigma_{yz} = \sigma_{yz}(z'_2) - \sigma_{yz}(z'_1)$, with

$$\frac{\sigma_{yz}(z')}{\sigma_0} = \nu b_x \frac{1}{R}. \quad (\text{D.10})$$

D.2 Energy in Two-Dimension

In this section, we give the explicit formulas for elastic energies of dislocation segments on the glide plane. For simplicity, only horizontal (H) and vertical (V) segments are considered. This is sufficient to calculate the double-kink nucleation energy landscape on coupled partial dislocations in Si (see Appendix C.3).

The interaction energy between two dislocations is given by [30],

$$\begin{aligned} W_{12} = & -\frac{\mu}{2\pi} \oint_{C_1} \oint_{C_2} \frac{(\vec{b}_1 \times \vec{b}_2) \cdot (d\vec{l}_1 \times d\vec{l}_2)}{R} + \frac{\mu}{4\pi} \oint_{C_1} \oint_{C_2} \frac{(\vec{b}_1 \cdot d\vec{l}_1)(\vec{b}_2 \cdot d\vec{l}_2)}{R} \\ & + \frac{\mu}{4\pi(1-\nu)} \oint_{C_1} \oint_{C_2} (\vec{b}_1 \times d\vec{l}_1) \cdot \nabla \nabla R \cdot (\vec{b}_2 \times d\vec{l}_2), \end{aligned} \quad (\text{D.11})$$

where b_1, b_2 are Burgers vectors, $R = ((x_1 - x_2)^2 + (y_1 - y_2)^2 + (z_1 - z_2)^2)^{-1/2}$, and the integrations are along the two dislocation lines.

If all the dislocations are on the glide plane $z = 0$, then $b_{1z} = b_{2z} = 0$, $z_1 = z_2 = 0$. $\vec{b}_1 \times d\vec{l}_1 \sim \hat{e}_z$, $\vec{b}_2 \times d\vec{l}_2 \sim \hat{e}_z$. Also notice that,

$$\frac{\partial}{\partial z_1} R = \frac{z_1 - z_2}{R}, \quad (\text{D.12})$$

$$\frac{\partial^2}{\partial z_1 \partial z_2} R = \frac{1}{R} - \frac{(z_1 - z_2)^2}{R^3} = \frac{1}{R}. \quad (\text{D.13})$$

$$(\text{D.14})$$

Therefore,

$$\begin{aligned} W_{12} = & \frac{\mu}{4\pi} \oint_{C_1} \oint_{C_2} \left[-2(\vec{b}_1 \times \vec{b}_2) \cdot (d\vec{l}_1 \times d\vec{l}_2) + (\vec{b}_1 \cdot d\vec{l}_1)(\vec{b}_2 \cdot d\vec{l}_2) \right] \frac{1}{R} \\ & + \frac{\mu}{4\pi(1-\nu)} \oint_{C_1} \oint_{C_2} \left[(\vec{b}_1 \times d\vec{l}_1) \cdot \hat{e}_z \right] \left[(\vec{b}_2 \times d\vec{l}_2) \cdot \hat{e}_z \right] \frac{1}{R} \end{aligned} \quad (\text{D.15})$$

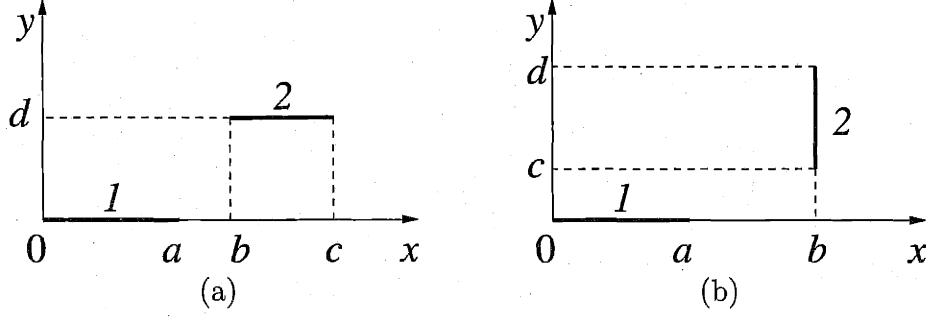


Figure D-2: Dislocation segment interactions (a) between horizontal (H) segments, (b) between horizontal (H) and vertical (V) segments.

For interactions between H-H segments, as shown in Fig. D-2(a),

$$W_{HH} = \frac{\mu}{4\pi(1-\nu)} \left(b_{1x}b_{2x} + \frac{b_{1y}b_{2y}}{1-\nu} \right) \int \tilde{d}x_1 \int dx_2 \frac{1}{R} \quad (D.16)$$

$$= E_{HH} \int_0^a dx_1 \int_b^c dx_2 \frac{1}{\sqrt{(x_1 - x_2)^2 + d^2}} \quad (D.17)$$

$$= E_{HH}(f(c, d) - f(c - a, d) - f(b, d) + f(b - a, d)) , \quad (D.18)$$

$$\text{where} \quad (D.19)$$

$$E_{HH} = \frac{\mu}{4\pi(1-\nu)} \left(b_{1x}b_{2x} + \frac{b_{1y}b_{2y}}{1-\nu} \right) \quad (D.20)$$

$$f(x, y) = x \ln(\sqrt{x^2 + y^2} + x) - \sqrt{x^2 + y^2} . \quad (D.21)$$

For interactions between H-V segments, as shown in Fig. D-2(b),

$$W_{HV} = \frac{\mu}{4\pi(1-\nu)} \left(-b_{1x}b_{2y} + \frac{1-2\nu}{1-\nu} b_{1y}b_{2x} \right) \int dx_1 \int dy_2 \frac{1}{R} \quad (D.22)$$

$$= E_{HV} \int_0^a dx_1 \int_c^d dx_2 \frac{1}{\sqrt{(x_1 - b)^2 + y_2^2}} \quad (D.23)$$

$$= E_{HV}(g(b, d) - g(b - a, d) - g(b, c) + g(b - a, c)) , \quad (D.24)$$

$$\text{where} \quad (D.25)$$

$$E_{HV} = \frac{\mu}{4\pi(1-\nu)} \left(-b_{1x}b_{2y} + \frac{1-2\nu}{1-\nu} b_{1y}b_{2x} \right) \quad (D.26)$$

$$g(x, y) = x \ln(\sqrt{x^2 + y^2} + y) + y \ln(\sqrt{x^2 + y^2} + x) . \quad (D.27)$$

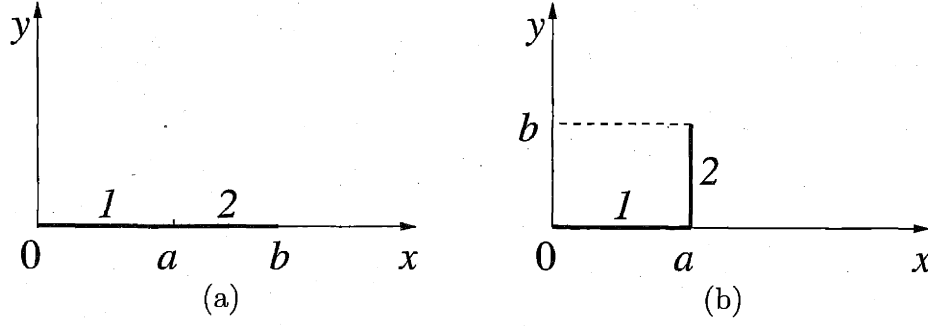


Figure D-3: Dislocation segment interactions (a) between horizontal (H) segments, (b) between horizontal (H) and vertical (V) segments, when two segments share a common node.

If two H segment share a common node, as shown in Fig. D-3(a), then

$$W_{HH} = E_{HH}(f(b,0) - f(b-a,0) - f(a,0) + f(0,0)) , \quad (D.28)$$

$$f(x,0) = x(\ln(|x| + x) - |x|) = x \ln 2x - x , (x > 0) \quad (D.29)$$

$$f(0,0) = 0 , \quad (D.30)$$

$$W_{HH} = E_{HH}(b \ln b - (b-a) \ln(b-a) - a \ln a) . \quad (D.31)$$

One can check that in this case, W_{HH} equals to the self energy of segment with length b minus the self energies of segments with length a and $b-a$, where the self energy of a segment with length L is [30],

$$W_s(L) = \frac{\mu}{4\pi(1-\nu)} \left(b_{1x}b_{2x} + \frac{b_{1y}b_{2y}}{1-\nu} \right) L \left(\ln \frac{L}{r_c} - 1 \right) , \quad (D.32)$$

with r_c being a cut-off radius (see Appendix A.1). In the limit of $a \rightarrow \infty$,

$$W_{HH} \rightarrow E_{HH}(b + b \ln \frac{a}{b}) \rightarrow \infty \quad (D.33)$$

If an H and a V segment share a common node, as shown in Fig. D-3(b), then

$$W_{HV} = E_{HV}(g(a,b) - g(0,b) - g(a,0) + g(0,0)) , \quad (D.34)$$

$$g(x,0) = g(0,x) = x \ln(|x|) = x \ln x , (x > 0) \quad (D.35)$$

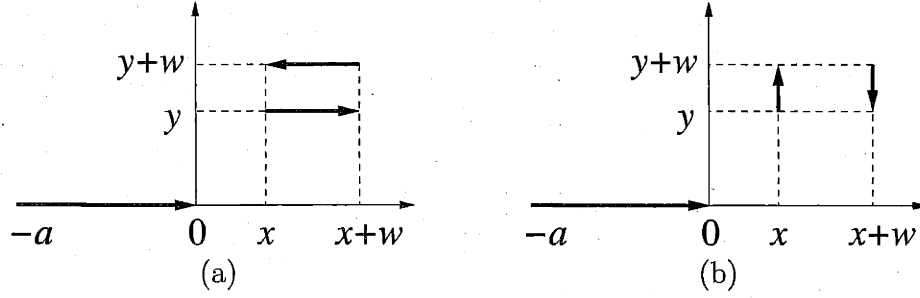


Figure D-4: Interaction between an infinitely long H segment ($a \rightarrow \infty$) with (a) an H dipole, (b) a V dipole.

$$g(0,0) = 0, \quad (\text{D.36})$$

$$W_{\text{HV}} = E_{\text{HV}} \left\{ a \ln(\sqrt{a^2 + b^2} + b) + b \ln(\sqrt{a^2 + b^2} + a) - a \ln a - b \ln b \right\} \quad (\text{D.37})$$

In the limit of $a \rightarrow \infty$,

$$W_{\text{HV}} \rightarrow E_{\text{HV}}(b + b \ln \frac{2a}{b}) \rightarrow \infty \quad (\text{D.38})$$

The interaction energy between an infinitely long H segment with a H segment dipole, as shown in Fig. D-4, is

$$W = \lim_{a \rightarrow \infty} E_{\text{HH}} \{ [f(x+w+a, y) - f(x+w, y) - f(x+a, y) + f(x, y)] - [f(x+w+a, y+h) - f(x+w, y+h) - f(x+a, y+h) + f(x, y+h)] \} \quad (\text{D.39})$$

$$= E_{\text{HH}} [f(x+w, y+h) - f(x+w, y) - f(x, y+h) + f(x, y)], \quad (\text{D.40})$$

$$\text{because} \quad (\text{D.41})$$

$$\lim_{a \rightarrow \infty} f(x+a, y) - f(x+a, y+h) \sim O(\frac{1}{a}) \rightarrow 0 \quad (\text{D.42})$$

The interaction energy between an infinitely long H segment with a V segment dipole, as shown in Fig. D-4, is

$$W = \lim_{a \rightarrow \infty} E_{\text{HV}} \{ [g(x+a, y+h) - g(x, y+h) - g(x+a, y) + g(x, y)]$$

$$\begin{aligned}
& -[g(x+w+a, y+h) - g(x+w, y+h) \\
& -g(x+w+a, y) + g(x+w, y)] \} \quad (D.43)
\end{aligned}$$

$$= E_{\text{HV}}[g(x+w, y+h) - g(x+w, y) - g(x, y+h) + g(x, y)], \quad (D.44)$$

$$\text{because} \quad (D.45)$$

$$\lim_{a \rightarrow \infty} g(x+a, y) - g(x+a, y+h) \sim O\left(\frac{1}{a}\right) \rightarrow 0 \quad (D.46)$$

D.3 Nodal Driving Force

In this section we give the formulas that will be essential to calculate nodal driving force in a Nodal Dislocation Dynamics simulation (for more details see Chapter 9). These include interaction energy for two dislocation segments sharing a common node (i.e. a hinge), and the interaction energy between a finite and an differential dislocation segment.

D.3.1 Hinge Interaction

According to [30], the interaction energy between the two dislocation segment forming a hinge, as shown in Fig. D-5, is

$$\begin{aligned}
W_{12} = & \frac{\mu}{4\pi} \left\{ (\vec{b}_1 \cdot \vec{\xi}_1)(\vec{b}_2 \cdot \vec{\xi}_2) - 2 [(\vec{b}_1 \times \vec{b}_2) \cdot (\vec{\xi}_1 \times \vec{\xi}_2)] \right. \\
& + \frac{1}{1-\nu} [\vec{b}_1 \cdot (\vec{\xi}_1 \times \vec{e}_3)] [\vec{b}_2 \cdot (\vec{\xi}_2 \times \vec{e}_3)] \left. \right\} \\
& \times I(x_\alpha, y_\beta) + \frac{\mu}{4\pi(1-\nu)} [\vec{b}_1 \cdot \vec{e}_3](\vec{b}_2 \cdot \vec{e}_3) \\
& \times \{R(x_\alpha, y_\beta) - \cos \theta [x_\alpha \ln t(x_\alpha, y_\beta) + y_\beta \ln s(x_\alpha, y_\beta)]\} , \quad (D.47)
\end{aligned}$$

where $\vec{\xi}_1$ and $\vec{\xi}_2$ are the line directions of the two segments, $I(x_\alpha, y_\beta) = I(x, y) - I(x, 0) - I(0, y) + I(0, 0)$, etc. The functions I, R, s and t are given below,

$$I(x, y) = x \ln \frac{R+y-x \cos \theta}{x} + y \ln \frac{R+x-y \cos \theta}{y} , \quad (D.48)$$

$$I(0, y) = y \ln \left(2 \sin^2 \frac{\theta}{2} \right) , \quad (D.49)$$

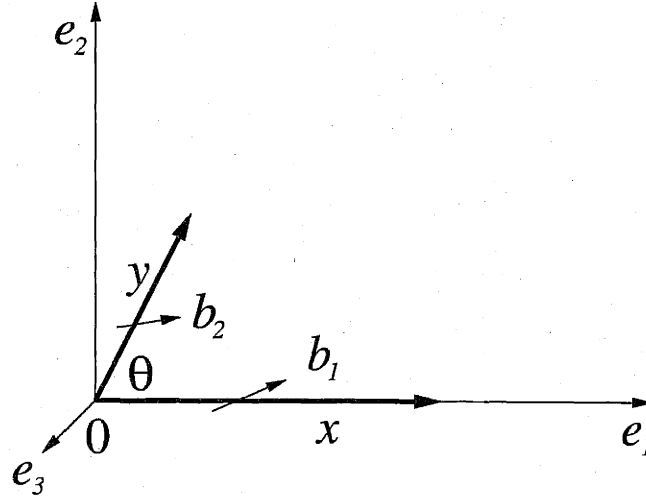


Figure D-5: Two dislocation segments sharing a common node form a hinge structure.

$$I(x, 0) = x \ln \left(2 \sin^2 \frac{\theta}{2} \right), \quad (\text{D.50})$$

$$I(0, 0) = 0, \quad (\text{D.51})$$

$$R(x, y) = (x^2 + y^2 - 2xy \cos \theta)^{-1/2}, \quad (\text{D.52})$$

$$s(x, y) = y \cos \theta - x + R(x, y), \quad (\text{D.53})$$

$$t(x, y) = x \sin \theta - y + R(x, y). \quad (\text{D.54})$$

If the two dislocation segments belong to the same dislocation, then $\vec{b}_1 = \vec{b}_2 = \vec{b}$, and W_{12} simplifies to,

$$\begin{aligned} W_{12} = & \frac{\mu}{4\pi} \left\{ (\vec{b} \cdot \vec{\xi}_1)(\vec{b} \cdot \vec{\xi}_2) + \frac{1}{1-\nu} \left[\vec{b} \cdot (\vec{\xi}_1 \times \vec{e}_3) \right] \left[\vec{b} \cdot (\vec{\xi}_2 \times \vec{e}_3) \right] \right\} \\ & \times I(x_\alpha, y_\beta) + \frac{\mu}{4\pi(1-\nu)} \left[(\vec{b} \cdot \vec{e}_3)(\vec{b} \cdot \vec{e}_3) \right] \\ & \times \{ R(x_\alpha, y_\beta) - \cos \theta [x_\alpha \ln t(x_\alpha, y_\beta) + y_\beta \ln s(x_\alpha, y_\beta)] \}. \end{aligned} \quad (\text{D.55})$$

Let $\vec{b} = (b_x, b_y, b_z)$, $\vec{\xi}_1 = (1, 0, 0)$, $\vec{\xi}_2 = (\cos \theta, \sin \theta, 0)$, then,

$$\vec{b} \cdot \vec{\xi}_1 = b_x \quad (\text{D.56})$$

$$\vec{b} \cdot \vec{\xi}_2 = b_x \cos \theta + b_y \sin \theta \quad (\text{D.57})$$

$$\vec{b} \cdot (\vec{\xi}_1 \times \vec{e}_3) = -b_y \quad (\text{D.58})$$

$$\vec{b} \cdot (\vec{\xi}_2 \times \vec{e}_3) = b_x \sin \theta - b_y \cos \theta \quad (\text{D.59})$$

$$I(x_\alpha, y_\beta) = x \ln \frac{R + y - x \cos \theta}{x} + y \ln \frac{R + x - y \cos \theta}{y} - y \ln \left(2 \sin^2 \frac{\theta}{2} \right) - x \ln \left(2 \sin^2 \frac{\theta}{2} \right) \quad (\text{D.60})$$

$$R(x_\alpha, y_\beta) = R - x - y \quad (\text{D.61})$$

$$x_\alpha \ln t(x_\alpha, y_\beta) = x \ln(x \cos \theta - y + R) - x \ln(x \cos \theta + x) \quad (\text{D.62})$$

$$y_\beta \ln s(x_\alpha, y_\beta) = y \ln(y \cos \theta - x + R) - y \ln(y \cos \theta + y) \quad (\text{D.63})$$

Several terms in Eq. (D.62-D.63) becomes singular when $\theta \rightarrow \pi$, i.e. $\cos \theta \rightarrow -1$, while the energy itself remains finite. When this is the case, the energy should be calculated using a different formula. Define $\epsilon = 1 + \cos \theta$, then

$$x_\alpha \ln t(x_\alpha, y_\beta) = x \ln \left(1 + \frac{x+y}{x} \delta \right) \quad (\text{D.64})$$

$$y_\beta \ln s(x_\alpha, y_\beta) = y \ln \left(1 + \frac{x+y}{y} \delta \right), \quad (\text{D.65})$$

where,

$$\delta = -\frac{1}{2}a - \frac{1}{8}a^2\epsilon - \frac{1}{16}a^3\epsilon^2 - \frac{5}{128}a^4\epsilon^3 - \frac{7}{256}a^5\epsilon^4 + O(\epsilon^5), \quad (\text{D.66})$$

$$a = \frac{2xy}{(x+y)^2}. \quad (\text{D.67})$$

For two dislocation segments oriented in different directions, we transform the coordinate system into geometries shown in Fig .D-5 and use Eq. (D.55-D.67) to calculate their interaction energy. Contribution to nodal driving force due to this interaction can be obtained by differentiating W_{12} against x, y, θ etc. The explicit forms of the driving force will not be given here.

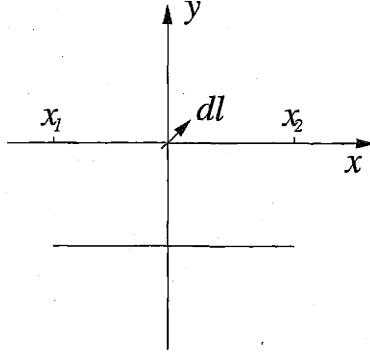


Figure D-6: Interaction between a finite and a differential dislocation segment.

D.3.2 Interaction Energy between a Finite and a Differential Dislocation Segment

In this section, we assume that the two dislocation segments have the same Burgers vector, i.e. $\vec{b}_1 = \vec{b}_2 = \vec{b}$. Then Eq. (D.47) becomes,

$$W_{12} = \frac{\mu}{4\pi} \oint_{C_1} \oint_{C_2} \frac{(\vec{b} \cdot d\vec{l}_1)(\vec{b} \cdot d\vec{l}_2)}{R} + \frac{\mu}{4\pi(1-\nu)} \oint_{C_1} \oint_{C_2} (\vec{b} \times d\vec{l}_1) \cdot \nabla \nabla R \cdot (\vec{b} \times d\vec{l}_2) \quad (D.68)$$

When one of the dislocation is a differential segment ($d\vec{l}$), as shown in Fig. D-6, their interaction becomes,

$$W_{12} = \frac{\mu}{4\pi} \int_{x_1}^{x_2} dx \frac{1}{R} (\vec{b} \cdot \vec{e}_x) (\vec{b} \cdot d\vec{l}) + \frac{\mu}{4\pi(1-\nu)} \int_{x_1}^{x_2} dx (\vec{b} \times \vec{e}_x) \cdot \nabla \nabla R \cdot (\vec{b} \times d\vec{l}) \quad (D.69)$$

In the geometry of Fig. D-6, $R = \sqrt{x^2 + y^2}$. Therefore,

$$\begin{aligned} \int_{x_1}^{x_2} dx \frac{1}{\sqrt{x^2 + y^2}} &= \ln(R + x) \Big|_{x_1}^{x_2} \\ &= -\ln(R - x) \Big|_{x_1}^{x_2} \end{aligned}$$

$$\begin{aligned}
&= \ln \frac{\sqrt{x_2^2 + y^2} + x_2}{\sqrt{x_1^2 + y^2} + x_1} \\
&= \ln \frac{\sqrt{x_1^2 + y^2} - x_1}{\sqrt{x_2^2 + y^2} - x_2}
\end{aligned} \tag{D.70}$$

The components of $\nabla\nabla R$ are, e.g.

$$\frac{\partial^2}{\partial x^2} R = \frac{\partial}{\partial x} \left(\frac{x}{R} \right) = \frac{1}{R} - \frac{x^2}{R^3} = \frac{y^2}{R^3} \tag{D.71}$$

$$\frac{\partial^2}{\partial x \partial y} R = \frac{\partial}{\partial x} \left(\frac{y}{R} \right) = -\frac{xy}{R^3} \tag{D.72}$$

The integration of $\nabla\nabla R$ will use the following integrals,

$$\int_{x_1}^{x_2} dx \frac{x}{R^3} = -\frac{1}{R} \Big|_{x_1}^{x_2} = -\left(\frac{1}{\sqrt{x_2^2 + y^2}} - \frac{1}{\sqrt{x_1^2 + y^2}} \right) \tag{D.73}$$

$$\begin{aligned}
\int_{x_1}^{x_2} dx \frac{x^2}{R^3} &= \left(-\frac{x}{R} + \ln(R+x) \right)_{x_1}^{x_2} \\
&= \left(-\frac{x}{R} - \ln(R+x) \right)_{x_1}^{x_2}
\end{aligned} \tag{D.74}$$

$$\int_{x_1}^{x_2} dx \frac{y^2}{R^3} = \frac{x}{R} \tag{D.75}$$

Therefore,

$$\int_{x_1}^{x_2} dx \nabla\nabla R = \int_{x_1}^{x_2} dx \begin{bmatrix} \frac{1}{R} - \frac{x^2}{R^3} & -\frac{xy}{R^3} & 0 \\ -\frac{xy}{R} & \frac{1}{R} - \frac{y^2}{R^3} & 0 \\ 0 & 0 & \frac{1}{R} \end{bmatrix} \tag{D.76}$$

$$= \begin{bmatrix} \frac{x}{R} & -\frac{y}{R} & 0 \\ -\frac{y}{R} & \ln(R+x) - \frac{x}{R} & 0 \\ 0 & 0 & \ln(R+x) \end{bmatrix}_{x_1}^{x_2} \tag{D.77}$$

The interaction energy can be calculated as,

$$W_{12} = \frac{\mu}{4\pi} (\vec{b} \cdot \vec{e}_x) (\vec{b} \cdot d\vec{l}) \ln(R+x) \Big|_{x_1}^{x_2} + \frac{\mu}{4\pi(1-\nu)} (\vec{b} \times \vec{e}_x) \cdot$$

$$\left[\begin{array}{ccc} \frac{x}{R} & -\frac{y}{R} & 0 \\ -\frac{y}{R} & \ln(R+x) - \frac{x}{R} & 0 \\ 0 & 0 & \ln(R+x) \end{array} \right]_{x_1}^{x_2} \cdot (\vec{b} \times d\vec{l}) \quad (D.78)$$

D.4 Anisotropic Elasticity

There are two forms [30] of anisotropic elasticity theory for straight dislocations. One is the Stroh's classical sextic theory, which involves a solution of a six order polynomial equation. The other is the Integral Method, where the sextic problem is reformulated into evaluating a set of integrals. In the limit of isotropic elasticity, the Stroh's sextic theory fails as the roots of the sextic equation becomes degenerate. In comparison, the Integral Method is more robust, but is also more complicated to implement. In this section, we use integrate the dislocation stress field given by Stroh's sextic formalism [30] to derive the interaction energy between two dislocations in an anisotropic medium, which is used in Chapter 4.2.

For completeness, we give a short summary of the Stroh's sextic formalism [30] below. Let us start with the standard elasticity relationships, between stress σ_{ij} and strain ϵ_{kl} , strain and displacement field u_k , and on force equilibrium,

$$\sigma_{ij} = C_{ijkl}\epsilon_{kl} \quad (D.79)$$

$$\epsilon_{kl} = \frac{1}{2} \left(\frac{\partial u_k}{\partial x_l} + \frac{\partial u_l}{\partial x_k} \right) \quad (D.80)$$

$$\frac{\partial \sigma_{ij}}{\partial x_j} = 0 \quad (D.81)$$

where C_{ijkl} is the elastic constant tensor, and $i, j, k = 1, 2, 3$. Let the dislocation line be along \hat{e}_3 , the stress and strain fields are then invariant along \hat{e}_3 . The force equilibrium conditions now reduce to,

$$\frac{\partial \sigma_{i\alpha}}{\partial x_\alpha} = 0 \quad (D.82)$$

$$\frac{\partial}{\partial x_3} = 0 \quad (D.83)$$

$$\sigma_{i\alpha} = C_{i\alpha k\beta} \frac{\partial u_k}{\partial x_\beta} \quad (\text{D.84})$$

$$C_{i\alpha k\beta} \frac{\partial^2 u_k}{\partial x_\alpha \partial x_\beta} = 0, \quad (\text{D.85})$$

where $\alpha, \beta = 1, 2$. The solution of Eq (D.85) is

$$u_k = A_k f(\eta) \quad (\text{D.86})$$

$$\eta = x_1 + p x_2 \quad (\text{D.87})$$

where A_k is the solution of,

$$[C_{i1k1} + (C_{i1k2} + C_{i2k1})p + C_{i2k2}p^2] A_k \frac{\partial^2 f}{\partial \eta^2} = 0, \quad (\text{D.88})$$

or equivalently,

$$a_{ik} A_k = 0 \quad (\text{D.89})$$

$$\text{where,} \quad (\text{D.90})$$

$$a_{ik} = C_{i1k1} + (C_{i1k2} + C_{i2k1})p + C_{i2k2}p^2 \quad (\text{D.91})$$

For Eq. (D.89) to have solution, matrix a_{ik} has to satisfy

$$\det\{a_{ik}\} = 0 \quad (\text{D.92})$$

Eq.(D.92) is a sixth order equation for p . Let $p_n, n = 1, 2, 3, 4, 5, 6$ be its six roots, and one can show that they are complex conjugate of each another, i.e.

$$p_4 = p_1^*, p_5 = p_2^*, p_6 = p_3^* \quad (\text{D.93})$$

The solution for the displacement field is then

$$u_k = \text{Re} \sum_{n=1}^3 [A_k(n) f_n(\eta_n)] , \quad (\text{D.94})$$

$$f_n(\eta_n) = -\frac{D(n)}{2\pi i} \ln \eta_n, \quad (\text{D.95})$$

where $D(n)$ satisfies,

$$\text{Re} \left[\sum_{n=1}^3 \pm A_k(n) D(n) \right] = b_k, k = 1, 2, 3. \quad (\text{D.96})$$

Here, b_k is the Burgers vector and the \pm sign takes $+$ for $\text{Im}(p) > 0$ and $-$ for $\text{Im}(p) < 0$. Eq (D.96) only provide three equations for the 6 unknowns of $D(n)$, since $D(n)$ are complex numbers. The other three equation are supplied by demanding zero self force on the dislocation core, which yields

$$\text{Re} \left[\sum_{n=1}^3 B_{i2k}(n) A_k(n) D(n) \right] = 0, i = 1, 2, 3, \quad (\text{D.97})$$

where

$$B_{ijk}(n) = C_{ijk1} + C_{ijk2} p_n \quad (\text{D.98})$$

The final form for the solution of displacement and stress field is then

$$u_k = \text{Re} \left[\frac{-1}{2\pi i} \sum_{n=1}^3 A_k(n) D(n) \ln \eta_n \right] \quad (\text{D.99})$$

$$\sigma_{ij} = \text{Re} \left[\frac{-1}{2\pi i} \sum_{n=1}^3 B_{ijk}(n) A_k(n) D(n) \eta_n^{-1} \right] \quad (\text{D.100})$$

$$(\text{D.101})$$

One can calculate the dislocation self energy by measuring the work done to displace the two sides of a cut surface with respect to each other by \vec{b} against the self stress of the dislocation, which yields

$$\frac{W}{L} = -\frac{1}{2} \int_{r_c}^R \sigma_{i2} b_i dx_1 \quad (\text{D.102})$$

$$= \frac{b_i}{4\pi} \ln \frac{R}{r_c} \text{Im} \left[\sum_{n=1}^3 B_{i2k}(n) A_k(n) D(n) \right]. \quad (\text{D.103})$$

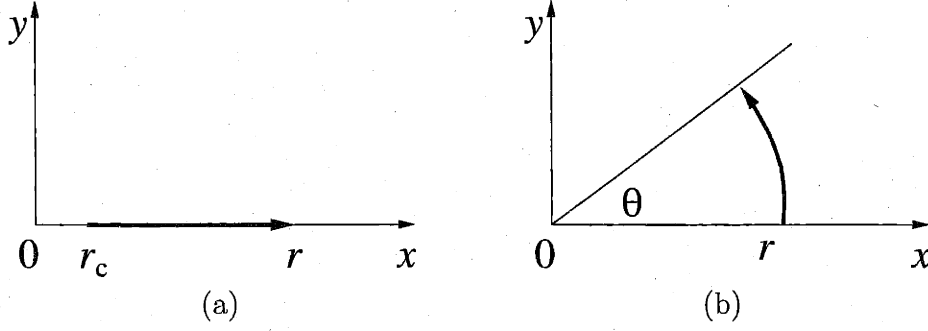


Figure D-7: Integration path of the second dislocation in the stress field of the first dislocation at the origin to compute interaction energy . (a) The second dislocation moves along x axis. (b) The second dislocation moves along a circle.

$$\equiv \frac{Kb^2}{4\pi} \ln \frac{R}{r_c} \quad (\text{D.104})$$

where r_c is the cut-off radius and R is the size of the elastic medium (see Appendix A.1 for more details). K is the so called energy coefficient, which is defined through

$$Kb^2 = b_i \text{Im} \left[\sum_{n=1}^3 B_{i2k}(n) A_k(n) D(n) \right] \quad (\text{D.105})$$

Eqs. (D.79)-(D.105) are already given in [30]. In the remaining part of this section, we will use these equations to derive the general form of the interaction energies between two straight dislocations in anisotropic medium.

First, we study the case where the two dislocations are both on x_1 axis, as shown in Fig. D-7(a). Let dislocation 1 be at origin and move dislocation 2 along x axis. For simplicity assume the two dislocation form a dipole, i.e. $\vec{b}^{(1)} = -\vec{b}^{(2)} \equiv \vec{b}$. Let r_c be the separation where the energy of the system is defined as 0. Then the energy of the two dislocation system as a function of their separation is

$$\frac{W}{L} = \int_{r_c}^r \sigma_{i2}^{(1)} b_i^{(2)} dx_1 \quad (\text{D.106})$$

$$= \frac{Kb^2}{2\pi} \ln \frac{r}{r_c} \quad (\text{D.107})$$

Eq (D.107) is similar to Eq (A.4), with only μ in isotropic elasticity replaced by

the anisotropic energy coefficient K . However, Eq (D.107) does NOT mean that the interaction energy between two dislocations depends only on their separation r . Remember that Eq (D.107) is derived with dislocation 2 constrained along the x axis. To obtain a general formula for the interaction energy, we need to measure the work done to move dislocation 2 around a circle, as shown in Fig. D-7(b). Define

$$h_\beta(n) = \epsilon_{j3\beta} B_{ijk}(n) b_i A_k(n) D(n) , \quad (\text{D.108})$$

we have,

$$Kb^2 = \sum_{n=1}^3 \text{Im} [h_1(n)] . \quad (\text{D.109})$$

The interaction energy as a function of the position of dislocation 2 is found as,

$$\begin{aligned} \frac{W(r, \theta)}{L} &= \sum_{n=1}^3 \text{Re} \left[\frac{h_1(n)}{2\pi i} \right] \ln \frac{r}{r_c} \\ &+ \sum_{n=1}^3 \text{Re} \left[\frac{h_1(n)}{2\pi i} \ln(\cos \theta + p_n \sin \theta) \right] \end{aligned} \quad (\text{D.110})$$

$$\frac{W(x, y)}{L} = \sum_{n=1}^3 \text{Re} \left[\frac{h_1(n)}{2\pi i} \ln \frac{x + p_n y}{r_c} \right] \quad (\text{D.111})$$

In the limit of isotropic elasticity, $p_{1,2,3} \rightarrow i$ and $p_{4,5,6} \rightarrow -i$, the sextic theory breaks down for dislocations with edge components, because Eq. (D.111) (D.111) will fail to describe any angular dependence. However, for screw dislocations they will naturally reduce to the form of Eq. (A.4).

Bibliography

- [1] I. Prigogine and I. Stengers, *Order out of chaos : man's new dialogue with nature*, Bantam Books, New York, 1984.
- [2] W. E. King, G. Campbell, T. Gonis, G. Henshall, D. Lesuer, E. Zywiec, and S. Foiles *Mater. Sci. Eng. A*, vol. 191, pp. 1–16, 1995.
- [3] D. J. Steinberg, S. G. Cochran, and M. W. Guinan, "A constitutive model of metals applicable at high-strain rate," *J. Appl. Phys.*, vol. 51, no. 3, p. 1498, 1980.
- [4] D. J. Steinberg and C. M. Lund, "A constitutive model for strain rates from 10^{-4}s^{-1} ," *J. Appl. Phys.*, vol. 65, no. 4, p. 1528, 1989.
- [5] S. T. Weir, J. Akella, C. Ruddle, T. Goodwin, and L. Hsiung, "Static strengths of Ta and U under ultrahigh pressures," *Phys. Rev. B*, vol. 58, p. 11258, 1998.
- [6] S. Mil'shtein, "Dislocations in microelectronics," *Phys. Stat. Solidi A*, vol. 171, p. 377, 1999.
- [7] F. Louchet and A. George, "Dislocation mobility measurements: an essential tool for understanding the atomic and electronic core structures of dislocations in semiconductors," *J. Phys. (Paris)*, vol. C4, p. 44, 1983.
- [8] H. Alexander, "Dislocations in covalent crystals," in *Dislocation in Solids* (F. R. N. Nabarro, ed.), vol. 7, p. 113, North-Holland, Amsterdam, 1986.

- [9] A. George and J. Rabier, "Dislocations and plasticity in semiconductors. (i). dislocation structures and dynamics," *Revue Phys. Appl.*, vol. 22, pp. 941–966, 1987.
- [10] J. Rabier and A. George, "Dislocations and plasticity in semiconductors. (ii). the relation between dislocation dynamics and plastic deformation," *Revue Phys. Appl.*, vol. 22, pp. 1327–1351, 1987.
- [11] M. S. Duesbery and G. Y. Richardson, "The dislocation core in crystalline materials," *Critical Reviews in Solid State and Materials Sciences*, vol. 17(1), pp. 1–46, 1991.
- [12] E. Kaxiras and M. S. Duesbery, "Free energies of generalized stacking faults in Si and implications for the brittle-ductile transition," *Phys. Rev. Lett.*, vol. 70, p. 3752, 1993.
- [13] H. Balamane, T. Halicioglu, and W. A. Tiller, "Comparative study of silicon empirical interatomic potentials," *Phys. Rev. B*, vol. 46, p. 2250, 1992.
- [14] I. Yonenaga and K. Sumino, "Dislocation dynamics in the plastic deformation of silicon crystals," *Phys. Stat. Solidi A*, vol. 50, p. 685, 1978.
- [15] H. G. Brion, H. Siethoff, and W. Schröter, "New stages in stress-strain curves of germanium at high temperatures," *Phil. Mag. A*, vol. 43, pp. 1505–1503, 1981.
- [16] H. Siethoff, H. G. Brion, and W. Schroter, "A regime of the yield point of silicon at high temperatures," *Appl. Phys. Lett.*, vol. 43, p. 1505, 1999.
- [17] M. Tang, L. Colombo, J. Zhu, and T. D. de la Rubia, "Intrinsic point defects in crystalline silicon: Tight-binding molecular dynamics studies of self-diffusion, interstitial-vacancy recombination, and formation," *Phys. Rev. B*, vol. 55, p. 14279, 1999.
- [18] J. Rabier and J. L. Demenet, "Low temperature, high stress plastic deformation of semiconductors: The silicon case," *Phys. Stat. Solidi B*, vol. 222, p. 63, 2000.

- [19] T. Suzuki, T. Yasutomi, T. Tokuoka, and I. Yonenaga, "Plasticity of III-V compounds at low temperature," *Phys. Stat. Solidi A*, vol. 171, p. 47, 1999.
- [20] T. Suzuki, T. Nishisako, T. Taru, and T. Yasutomi, "Plastic deformation of InP at temperature between 77K and 500K," *Phil. Mag. Lett.*, vol. 77, no. 4, pp. 173–180, 1998.
- [21] T. Suzuki, T. Yasutomi, and T. Tokuoka, "Plasticity deformation of GaAs at low temperature," *Phil. Mag. A*, vol. 79, no. 11, pp. 2637–2654, 1999.
- [22] M. S. Duesbery and B. Joos, "Dislocation motion in silicon: the shuffle-glide controversy," *Phil. Mag. Lett.*, vol. 74, pp. 253–258, 1996.
- [23] K. Wessel and H. Alexander, "On the mobility of partial dislocations in silicon," *Phil. Mag.*, vol. 35, p. 1523, 1977.
- [24] D. J. H. Cockayne, I. L. F. Ray, and M. J. Whelman, "Investigations of dislocation strain fields using weak beams," *Phil. Mag. A*, vol. 20, p. 1265, 1969.
- [25] A. Gomez, D. J. H. Cockayne, P. B. Hirsch, and V. Vitek, "Dissociation of near-screw dislocations in germanium and silicon," *Phil. Mag.*, vol. 31, p. 105, 1975.
- [26] F. Häussermann and D. Schaumburg, "Extended dislocations in germanium," *Phil. Mag.*, vol. 27, p. 745, 1973.
- [27] I. L. F. Ray and D. J. H. Cockayne, "The observation of dissociated dislocations in silicon," *Phil. Mag. A*, vol. 22, p. 853, 1970.
- [28] R. Meingast and H. Alexander, "Dissociated dislocations in germanium," *Phys. Stat. Solidi A*, vol. 17, p. 229, 1973.
- [29] S. Takeuchi and K. Suzuki, "Stacking fault energies of tetrahedrally coordinated crystals," *Phys. Stat. Solidi A*, vol. 171, p. 99, 1999.
- [30] J. P. Hirth and J. Lothe, *Theory of Dislocations*. Wiley, New York, 1982.

- [31] F. Louchet and J. Thibault-Desseaux, "Dislocation cores in semiconductors. from the "shuffle or glide" dispute to the "glide and shuffle" partnership," *Revue Phys. Appl.*, vol. 22, pp. 207–219, 1987.
- [32] E. Weber and H. Alexander, "Electron paramagnetic resonance of point defects in deformed silicon," *Inst. Phys. Conf. Ser.*, vol. 31, p. 266, 1977.
- [33] L. C. Kimerling and J. R. Patel, "Defect states associated with dislocations in silicon," *Appl. Phys. Lett.*, vol. 34, p. 73, 1979.
- [34] C. Kisielowski-Kemmerich, "Vacancies and their complexes in the core of screw dislocations: Models which account for esr investigations of deformed silicon," *Phys. Stat. Solidi B*, vol. 161, p. 11, 1990.
- [35] J. Weber, "Correlation of structural and electronic properties from dislocations in semiconductors," *Solid State Phenomena*, vol. 37-38, pp. 13–24, 1994.
- [36] H. Alexander, "Models of the dislocation structure," *J. Phys. (Paris)*, vol. 40, 1979.
- [37] J. F. Justo, M. de Koning, W. Cai, and V. V. Bulatov, "Vacancy interaction with dislocations in silicon: The shuffle-glide competition," *Phys. Rev. Lett.*, vol. 84, p. 2172, 2000.
- [38] R. Jones, "Do we really understand dislocations in semiconductors," *Mater. Sci. Eng. B*, vol. 71, p. 24, 2000.
- [39] J. Rabier, P. Cordier, T. Tondellier, J. L. Demenet, and H. Garem, "Dislocation microstructures in Si plastically deformed at RT," *J. Phys. Condens. Matter*, vol. 12, pp. 10059–10064, 2000.
- [40] J. Castaing, P. Veyssi re, L. P. Kubin, and J. Rabier, "The plastic deformation of silicon between 300 degrees C and 600 degrees C," *Phil. Mag. A*, vol. 44, p. 1407, 1981.

- [41] A. George, C. Escaravage, G. Champier, and W. Schröter, "Velocities of screw and 60°-dislocations in silicon," *Phys. Stat. Solidi B*, vol. 53, p. 483, 1972.
- [42] V. N. Erofeev, V. I. Nikitenko, and V. B. Osvenskii, "Effect of impurities on the individual dislocation mobility in silicon," *Phys. Stat. Solidi*, vol. 35, p. 79, 1969.
- [43] A. George, "Measurements of the dislocation velocities in silicon," *J. Phys. (Paris)*, vol. 40 C-6, p. 133, 1979.
- [44] A. George and G. Champier, "Velocities of screw and 60°-dislocations in n and p-type silicon," *Phys. Stat. Solidi A*, vol. 53, p. 529, 1979.
- [45] A. George, C. Escaravage, W. Schröter, and G. Champier, "X-ray topographic observation of single dislocation mobility in silicon," *Cryst. Latt. Def.*, vol. 4, pp. 29-36, 1973.
- [46] K. E. Puttick, M. A. Shahid, and M. M. Hosseini, "Size effects in abrasion of brittle materials," *J. Phys. D Appl. Phys.*, vol. 12, no. 2, pp. 195-202, 1979.
- [47] A. S. T. Badrick and K. E. Puttick, "Annealing of scratches on near (111) silicon slices," *J. Phys. D Appl. Phys.*, vol. 12, no. 6, pp. 909-918, 1979.
- [48] K. E. Puttick and M. A. Shadid, "Dislocation movement at annealed scratches on near (111) silicon," *Phys. Stat. Solidi A*, vol. 54, no. 2, pp. K95-98, 1979.
- [49] P. Tu and H. Yizhen, "Motion of dislocations from an indentation rosette on silicon crystals," *Phys. Stat. Solidi A*, vol. 59, p. 195, 1980.
- [50] F. Louchet, "On the mobility of dislocations in silicon by in situ straining in a high-voltage electron microscope," *Phil. Mag. A*, vol. 43, p. 1289, 1981.
- [51] B. Y. Farber and V. I. Nikitenko, "Change of dislocation mobility characteristics in silicon single crystals at elevated temperature," *Phys. Stat. Solidi A*, vol. 73, p. K141, 1982.

- [52] J. Chikawa, I. Fujimoto, and T. Abe, "X-ray topographic observation of moving dislocations in silicon crystals," *Appl. Phys. Lett.*, vol. 21, no. 6, pp. 295-298, 1972.
- [53] B. Y. Farber, I. E. Bondarenko, and V. I. Nikitenko, "High-temperature mobility of isolated dislocations in germanium single crystals," *Fizika Tverdogo Tela*, vol. 23, no. 7, pp. 2192-2194, 1981.
- [54] M. Imai and K. Sumino, "In situ x-ray topographic study of the dislocation mobility in high-purity and impurity-doped silicon crystals," *Phil. Mag. A*, vol. 47, p. 599, 1983.
- [55] H. J. Möller, "The movement of dissociated dislocations in the diamond-cubic structure," *Acta Metall.*, vol. 26, p. 963, 1978.
- [56] H. Alexander, C. Kisielowski-Kemmerich, and E. R. Weber, "Investigations of well defined dislocations in silicon," *Physica B & C*, vol. 116B+C, no. 1-3, pp. 583-593, 1983.
- [57] V. I. Nikitenko, B. Y. Farber, and E. B. Yakimov, "Asymmetry of isolated dislocation mobility in silicon single crystals," *Cryst. Res. & Technol.*, vol. 19, p. 295, 1984.
- [58] B. Y. Farber and Y. L. Iunin, "On the nature of the asymmetry effect in dislocation mobility in Si single crystals," in *Structure and Properties of Dislocations in Semiconductors 1989. Proceedings of the Sixth International Symposium. IOP*, pp. 297-302, Bristol, UK, 1989.
- [59] P. B. Hirsch, A. Ourmazd, and P. Pirouz, "Relaxation of dislocations in deformed silicon," *Inst. Phys. Conf. Ser.*, vol. 60, p. 29, 1981.
- [60] H. Gottschalk, H. Alexander, and V. Dietz, "The fine structure of dislocations in silicon," *Inst. Phys. Conf. Ser.*, vol. 87, p. 339, 1987.

- [61] H. R. Kolar, J. C. H. Spence, and H. Alexander, "Observation of moving dislocation kinks and unpinning," *Phys. Rev. Lett.*, vol. 77, p. 4031, 1996.
- [62] H. Alexander, H. R. Kolar, and J. C. H. Spence, "Kinks on partials of 60° dislocations silicon as revealed by a novel TEM technique," *Phys. Stat. Solidi A*, vol. 171, p. 5, 1999.
- [63] B. Y. Farber, Y. L. Iunin, and V. I. Nikitenko, "Experimental study of the double kink formation kinetics and kink mobility on the dislocation line in Si single crystals," *Phys. Stat. Solidi A*, vol. 97, p. 469, 1986.
- [64] H.-J. Möller and J. Buchholz, "Low-temperature internal friction of deformed germanium and silicon," *Phys. Stat. Solidi A*, vol. 20, p. 545, 1973.
- [65] V. I. Nikitenko, B. Y. Farber, Y. L. Iunin, and V. I. Orlov, "Gettering phenomena and dislocation kink mobility," in *Springer Proceedings in Physics* (J. H. Werner and H. P. Strunk, eds.), vol. 54, Springer-Verlag Berlin, Heidelberg, 1991.
- [66] Y. L. Iunin and V. I. Nikitenko, "Dislocation kink dynamics in crystals with deep peierls potential relief," *Phys. Stat. Solidi A*, vol. 171, p. 17, 1999.
- [67] A. W. Cramb, "A short history of metals," 4/4/2001. URL: <http://neon.mems.cmu.edu/cramb/Processing/history.html>.
- [68] M. S. Duesbery and V. Vitek, "Plastic anisotropy in b.c.c. transition metals," *Acta Mater.*, vol. 46, pp. 1481–1492, 1998.
- [69] 3/6/2001. URL: <http://library.thinkquest.org/3659/pertable/42.html>.
- [70] M. Wen and A. H. W. Ngan, "Atomistic simulation of kink-pairs of screw dislocations in body-centred cubic iron," vol. 48, pp. 4255–4265, 2000.
- [71] M. S. Duesbery, "The influence of core structure on dislocation mobility," *Phil. Mag.*, vol. 19, p. 501, 1969.

- [72] M. S. Duesbery, V. V. Vitek, and D. K. Bowen, "The effect of shear stress on the screw dislocation core structure in body-centered cubic lattices," *Proc. R. Soc. Lond.*, vol. A 332, pp. 85–111, 1973.
- [73] V. Vitek, "Theory of the core structures of dislocations in body-centered-cubic metals," *Cryst. Latt. Def.*, vol. 5, pp. 1–34, 1974.
- [74] V. Vitek, "Computer simulation of the screw dislocation motion in bcc metals under the effect of the external shear and uniaxial stresses," *Proc. R. Soc. Lond.*, vol. A 352, pp. 109–124, 1976.
- [75] M. S. Duesbery, "On kinked screw dislocations in the b.c.c. lattice — i. the structure and peierls stress of isolated kinks," *Acta Metall.*, vol. 31, pp. 1747–1758, 1983.
- [76] M. S. Duesbery, "On kinked screw dislocations in the b.c.c. lattice — ii. kink energies and double kinks," *Acta Metall.*, vol. 31, pp. 1759–1770, 1983.
- [77] L. P. Kubin, "unknown," *Rev. Deform. Behav. Mater.*, vol. 4, p. 181, 1982.
- [78] F. A. McClintock and A. S. Argon, *Mechanical Behavior of Materials*. Addison-Wesley, Massachusetts, 1966.
- [79] A. Luft and L. Kaun, "Electron microscopic investigation of the dislocation structure in molybdenum single crystals deformed in tension at 293 and 493°K," *Phys. Stat. Solidi*, vol. 37, p. 781, 1970.
- [80] C. V. Kopetskii and A. I. Pashkovskii, "Plastic deformation and dislocation structure of molybdenum single crystals upon extending along $\langle 110 \rangle$ and $\langle 100 \rangle$ axes in the range from 77 to 573°K," *Phys. Stat. Solidi A*, vol. 21, p. 714, 1974.
- [81] G. J. Irwin, F. Guiu, and P. L. Pratt, "The influence of orientation on slip and strain hardening of molybdenum single crystals," *Phys. Stat. Solidi A*, vol. 22, p. 685, 1974.

- [82] H.-J. Kaufmann, A. Luft, and D. Schulze, "Deformation mechanism and dislocation structure of high-purity molybdenum single crystals at low temperatures," *Cryst. Res. Technol.*, vol. 19, p. 357, 1984.
- [83] S. Takeuchi and K. Maeda, "Slip in high purity tantalum between 0.7 and 40 k," *Acta Metall.*, vol. 25, p. 1485, 1977.
- [84] R. M. Rose, D. P. Ferris, and J. Wulff, "Yielding and plastic flow in single crystals of tungsten," *Trans. AIME*, vol. 224, p. 981, 1962.
- [85] A. S. Argon and S. R. Maloof, "Plastic deformation of tungsten single crystals at low temperatures," *Acta Metall.*, vol. 14, p. 1449, 1966.
- [86] P. J. Sherwood, F. Guiu, H. C. Kim, and P. L. Pratt, "Plastic anisotropy of tantalum, niobium and molybdenum," *Can. J. Phys.*, vol. 45, p. 1075, 1967.
- [87] D. Hull, J. F. Byron, and F. W. Noble, "Orientation dependence of yield in body-centered cubic metals," *Can. J. Phys.*, vol. 45, p. 1091, 1967.
- [88] D. P. Ferris, R. M. Rose, and J. Wulff, "Deformation of tantalum single crystals," *Trans. AIME*, vol. 224, p. 975, 1962.
- [89] J. F. Byron *J. Less-Common Met.*, vol. 14, p. 201, 1968.
- [90] A. S. Keh and Y. Nakada, "Plasticity of iron single crystals," *Can. J. Phys.*, vol. 45, p. 1001, 1967.
- [91] D. F. Stein, "The effect of orientation and impurities on the mechanical properties of molybdenum single crystals," *Can. J. Phys.*, vol. 45, p. 1063, 1967.
- [92] F. Guiu and P. L. Pratt, "The effect of orientation on the yielding and flow of molybdenum single crystals," *Phys. Stat. Solidi*, vol. 15, p. 539, 1966.
- [93] M. S. Duesbery and R. A. Foxall, "A detailed study of the deformation of high purity niobium single crystals," *Phil. Mag.*, vol. 20, p. 719, 1969.

- [94] W. A. Spitzig and A. S. Keh, "The effect of orientation and temperature on the plastic flow properties of iron single crystals," *Acta Metall.*, vol. 18, pp. 611–622, 1970.
- [95] D. Veselý, "The study of slip bands on the surface of Mo single crystals," *Phys. Stat. Solidi*, vol. 29, pp. 657, 685, 1968.
- [96] F. Guiu, "Slip asymmetry in molybdenum single crystals deformed in direct shear," *Script. Metall.*, vol. 3, p. 449, 1969.
- [97] H. D. Nine, "Asymmetric deformation in fatigue of body-centered cubic single crystals," *J. Appl. Phys.*, vol. 44, pp. 4875–4881, 1973.
- [98] H. Mughrabi and C. Wüthrich, "Asymmetry of slip and shape changes during cyclic deformation of α -iron single crystals," *Phil. Mag. A*, vol. 33, pp. 963–984, 1976.
- [99] F. Guiu and M. Anglada, "Irreversible glide and shape changes in the cyclic deformation of b.c.c. crystals," *Phil. Mag. A*, vol. 42, pp. 271–276, 1980.
- [100] M. Anglada, B. Etemad, J. A. Planell, and F. Guiu, "Stress asymmetry and shape changes in cyclically deformed Mo single crystals," *Script. Metall.*, vol. 14, p. 1319, 1980.
- [101] J. A. Planell and F. Guiu, "Cyclic deformation of molybdenum single crystals i. mechanical behavior," *Phil. Mag. A*, vol. 54, p. 325, 1986.
- [102] S. Suresh, *Fatigue of Materials*. Cambridge University Press, 1992.
- [103] H. Matsui and H. Kimura, "Anomalous (110) slip in high-purity molybdenum single crystals and its comparison with that in V(a) metals," *Mater. Sci. Eng.*, vol. 24, no. 2, pp. 247–256, 1976.
- [104] H. Saka, K. Noda, T. Imura, H. Matsui, and H. Kimura, "Hvem in-situ observation of anomalous (101) slip in molybdenum," *Phil. Mag.*, vol. 34, no. 1, pp. 33–48, 1976.

- [105] C. J. Bolton and G. Taylor, "Anomalous slip in high purity niobium single crystals deformed at 77°K in tension," *Phil. Mag.*, vol. 26, pp. 1359–1376, 1972.
- [106] A. J. Garratt-Reed and G. Taylor, "Optical and electron microscopy of niobium crystals deformed below room temperature," *Phil. Mag. A*, vol. 39, pp. 597–646, 1979.
- [107] M. H. A. Nawaz and B. L. Mordike, "Slip geometry of tantalum and tantalum alloys," *Phys. Stat. Solidi A*, vol. 32, p. 449, 1975.
- [108] S. Takeuchi and E. Kuramoto, "Anomalous slip in a b.c.c. crystal observed in computer simulation of screw dislocation motion," *Script. Metall.*, vol. 8, no. 7, pp. 785–790, 1974.
- [109] V. Vitek and G. Taylor, "Comment on 'anomalous slip in b.c.c. crystals observed in computer simulation of screw dislocation motion'," *Script. Metall.*, vol. 8, no. 11, pp. 1283–1285, 1974.
- [110] H. Matsui and H. Kimura, "A mechanism of the 'unexpected (110) slip' observed in bcc metals deformed at low temperatures," *Script. Metall.*, vol. 7, no. 9, pp. 905–913, 1973.
- [111] H. Matsui and H. Kimura, "Reply to comments on 'a mechanism of the unexpected (110) slip observed in b.c.c. metals deformed at low temperatures'," *Script. Metall.*, vol. 8, no. 5, pp. 463–466, 1974.
- [112] H. Matsui, H. Kimura, H. Saka, K. Noda, and T. Imura, "Direct observation of active 'unexpected slip' in molybdenum by HVEM," *Script. Metall.*, vol. 8, no. 5, pp. 467–474, 1974.
- [113] H. Matsui and H. Kimura, "Anomalous (110) slip and the role of co-planar double slip in bcc metals," *Script. Metall.*, vol. 9, no. 9, pp. 971–978, 1975.
- [114] A. Lawley and H. L. Gaigher, "Observations on prismatic and grown-in dislocations in zone-melted molybdenum," *Phil. Mag.*, vol. 8, p. 1713, 1963.

- [115] J. A. Planell and F. Guiu, "Cyclic deformation of molybdenum single crystals ii. dislocation substructures and cyclic hardening in crystals deformed at 400 k," *Phil. Mag. A*, vol. 54, p. 343, 1986.
- [116] A. Lawley and H. L. Gaigher, "Deformation structure in zone-melted molybdenum," *Phil. Mag.*, vol. 10, 1964.
- [117] A. Luft, "The correlation between dislocation structure and work-hardening behavior of molybdenum single crystal deformed at 293°K," *Phys. Stat. Solidi*, vol. 42, p. 429, 1970.
- [118] I. I. Novikov, V. A. Yermishkin, M. M. Kantor, and V. N. Timofeev, "The free surface effect on the dislocation mobility in molybdenum single crystals," *Kristall und Technik*, vol. 14, p. 1288, 1979.
- [119] T. Imura, K. Noda, H. Matsui, H. Saka, and H. Kimura, "Direct measurement of mobility of dislocations in high-purity molybdenum," in *Dislocations in Solids*, p. 287, University of Tokyo Press, 1985.
- [120] D. H. Lassila, 2000. private communication.
- [121] H. L. Prekel, A. Lawley, and H. Conrad, "Dislocation velocity measurements in high purity molybdenum," *Acta Metall.*, vol. 16, p. 337, 1968.
- [122] S. S. Lau and J. T. Vreeland, "The introduction of dislocations and slip bands in molybdenum single crystals," *Phys. Stat. Solidi A*, vol. 20, p. 337, 1973.
- [123] D. F. Stein, "Comment on "dislocation velocity measurements in high purity-molybdenum"," *Script. Metall.*, vol. 2, p. 555, 1968.
- [124] E. Nadgornyi, "Dislocation dynamics and mechanical properties of crystals," *Prog. Mater. Sci.*, vol. 31, p. 1, 1988.
- [125] E. B. Leiko and E. M. Nadgornyi, "Dislocation dynamics of molybdenum single crystals in the microplasticity region," *Kristallografiya*, vol. 19, p. 584, 1974.

- [126] E. B. Leiko, D. V. Lotsko, E. M. Nadgornyi, and V. I. Trefilov, "Temperature dependence of the mobility of dislocations in molybdenum single crystals," *Sov. Phys. Solid State*, vol. 17, p. 1814, 1975.
- [127] E. B. Leiko, A. Luft, and E. M. Nadgornyi, "Slip rosettes and dislocation structure formed by microindentation in molybdenum single crystals," *Phys. Stat. Solidi A*, vol. 44, p. 285, 1977.
- [128] E. B. Leiko and A. Luft, "A combined study of the dynamical properties of dislocations in molybdenum single crystals by etch pitting and interference contrast techniques," *Phys. Stat. Solidi A*, vol. 67, p. 435, 1981.
- [129] W. Sigle, "High-resolution electron microscopy and molecular dynamics study of the $(a/2)[111]$ screw dislocation in molybdenum," *Phil. Mag. A*, vol. 79, pp. 1009–1020, 1999.
- [130] P. B. Hirsch in *5th International Conference on Crystallography*, p. 139, Cambridge University, 1960.
- [131] M. P. Allen and D. J. Tildesley, *Computer Simulation of Liquids*. Clarendon, Oxford, 1989.
- [132] D. Frenkel and B. Smit, *Understanding Molecular Simulation From Algorithm to Application*. Academic, San Diego, 1996.
- [133] K. Binder, *Monte Carlo Methods in Statistical Physics, 4th ed.* Springer-Verlag, Berlin, 1979.
- [134] M. E. J. Newman and G. T. Barkema, *Monte Carlo Methods in Statistical Physics*. Oxford University Press, Oxford, 1999.
- [135] F. H. Stillinger and T. A. Weber, "Computer simulation of local order in condensed phases of silicon," *Phys. Rev. B*, vol. 31, p. 5262, 1985.

- [136] J. F. Justo, M. Z. Bazant, E. Kaxiras, V. V. Bulatov, and S. Yip, "Interatomic potential for silicon defects and disordered phases," *Phys. Rev. B*, vol. 58, p. 2539, 1998.
- [137] J. Tersoff, "New empirical model for the structural properties of silicon," *Phys. Rev. Lett.*, vol. 56, p. 632, 1986.
- [138] M. W. Finnis and J. E. Sinclair, "A simple empirical N-body potential for transition metals," *Phil. Mag. A*, vol. 50, pp. 45–55, 1984.
- [139] J. E. Lennard-Jones, "The determination of molecular fields I. From the variation of the viscosity of a gas with temperature," *Proc. R. Soc. Lond.*, vol. 106A, p. 441, 1924.
- [140] J. E. Lennard-Jones, "The determination of molecular fields II. From the equation of state of a gas," *Proc. R. Soc. Lond.*, vol. 106A, p. 463, 1924.
- [141] P. N. Keating *Phys. Rev.*, vol. 145, p. 637, 1966.
- [142] J. Q. Broughton and X. P. Li, "Phase diagram of silicon by molecular dynamics," *Phys. Rev. B*, vol. 35, p. 9120, 1987.
- [143] J. Tersoff, "New empirical approach for the structural and energy of covalent systems," *Phys. Rev. B*, vol. 37, p. 6991, 1988.
- [144] A. P. Sutton, *Electronic Structure of Materials*. Clarendon Press, Oxford, 1993.
- [145] J. Tersoff, "Empirical interatomic potential for silicon with improved elastic properties," *Phys. Rev. B*, vol. 38, p. 9902, 1988.
- [146] J. Tersoff, "Empirical interatomic potential for carbon, with applications to amorphous carbon," *Phys. Rev. Lett.*, vol. 61, p. 2879, 1988.
- [147] J. Tersoff, "Modeling solid-state chemistry: Interatomic potentials for multi-component systems," *Phys. Rev. B*, vol. 39, p. 5566, 1989.

- [148] M. Z. Bazant and E. Kaxiras, "Modeling of covalent bonding in solids by inversion of cohesive energy curves," *Phys. Rev. Lett.*, vol. 77, p. 4370, 1996.
- [149] M. Z. Bazant, E. Kaxiras, and J. F. Justo, "Environment-dependent interatomic potential for bulk silicon," *Phys. Rev. B*, vol. 56, p. 8542, 1997.
- [150] A. Y. Belov, K. Scheerschmidt, and U. Gosele, "Extended point defect structures at intersections of screw dislocations in si: a molecular dynamics study," *Phys. Stat. Solidi A*, vol. 171, pp. 159–166, 1999.
- [151] J. R. K. Bigger, D. A. McInnes, A. P. Sutton, M. C. Payne, I. Stich, R. D. King-Smith, D. M. Bird, and L. J. Clarke, "Atomic and electronic structures of the 90° partial dislocations in silicon," *Phys. Rev. Lett.*, vol. 69, p. 2224, 1992.
- [152] J. F. Justo, M. Z. Bazant, E. Kaxiras, V. V. Bulatov, and S. Yip, "Interatomic potential for condensed phases and bulk defects in silicon," *Mater. Res. Soc. Symp. Proc.*, vol. 469, p. 217, 1997.
- [153] M. S. Duesbery, B. Joos, and D. J. Michel, "Dislocation core studies in empirical silicon models," *Phys. Rev. B*, vol. 43, p. 5143, 1991.
- [154] G. J. Ackland, M. W. Finnis, and V. Vitek, "Validity of the second moment tight-binding model," *J. Phys. F Metal Phys.*, vol. 18, pp. L153–157, 1988.
- [155] G. J. Ackland and R. Thetford, "An improved N-body semi-empirical model for body-centered cubic transition metals," *Phil. Mag. A*, vol. 56, pp. 15–30, 1987.
- [156] W. Xu and J. B. Adams, "Fourth moment approximation to tight binding: application to bcc transition metals," *Surface Science*, vol. 301, pp. 371–385, 1994.
- [157] A. E. Carlsson, "Angular forces in group-vi transition metals: Application to w(100)," *Phys. Rev. B*, vol. 44, p. 6590, 1991.

- [158] J. A. Moriarty, "Angular forces and melting-in bcc transition metals: a case study of molybdenum," *Phys. Rev. B*, vol. 49, p. 12431, 1994.
- [159] J. A. Moriarty, "Analytic representation of multi-ion interatomic potentials in transition metals," *Phys. Rev. B*, vol. 42, p. 1609, 1990.
- [160] J. A. Moriarty and R. Phillips, "First-principles interatomic potentials for transition-metal surfaces," *Phys. Rev. Lett.*, vol. 66, p. 3036, 1991.
- [161] J. A. Moriarty, "Ultrahigh-pressure structural phase transitions in cr, mo, and w," *Phys. Rev. B*, vol. 45, p. 2004, 1992.
- [162] W. Xu and J. Moriarty, "Accurate atomistic simulations of the peierls barrier and kink-pair formation energy for $\langle 111 \rangle$ screw dislocations in bcc mo," *Comput. Mater. Sci.*, vol. 9, p. 348, 1998.
- [163] M. S. Duesbery and W. Xu, "The motion of edge dislocations in body-center cubic metals," *Script. Metall.*, vol. 39, p. 283, 1998.
- [164] A. N. Gulluoglu, D. J. Srolovitz, R. LeSar, and P. S. Lomdahl, "Dislocation distributions in two dimensions," *Script. Metall.*, vol. 23, p. 1347, 1989.
- [165] H. Y. Wang and R. LeSar, "O(N) algorithm for dislocation dynamics," *Phil. Mag. A*, vol. 71, p. 149, 1995.
- [166] X. Blase, K. L. A. Canning, S. G. Louie, and D. C. Chrzan, "Structure and energy of the 90° partial dislocation in diamond: A combined ab initio and elasticity theory analysis," *Phys. Rev. Lett.*, vol. 84, p. 5780, 2000.
- [167] S. Ismail-Beigi and T. A. Arias, "Ab initio study of screw dislocations in Mo and Ta: A new picture of plasticity in bcc transition metals," *Phys. Rev. Lett.*, vol. 84, p. 1499, 2000.
- [168] W. Cai, V. V. Bulatov, J. Chang, J. Li, and S. Yip, "Anisotropic elastic interactions of a periodic dislocation array." *Phys. Rev. Lett.* (in press), 2001.

- [169] T. A. Arias and J. D. Joannopoulos, "Ab initio theory of dislocation interactions: From close-range spontaneous annihilation to the long-range continuum limit," *Phys. Rev. Lett.*, vol. 73, p. 680, 1994.
- [170] L. B. Hansen, K. Stokbro, B. I. Lundqvist, K. W. Jacobsen, and D. M. Deaven, "Nature of dislocations in silicon," *Phys. Rev. Lett.*, vol. 75, p. 4444, 1995.
- [171] D. Borwein, J. M. Borwein, and K. F. Taylor, "Convergence of lattice sums and Madelung's constant," *J. Math. Phys.*, vol. 26, p. 2999, 1985.
- [172] K. F. Taylor, "On Madelung's constant," *J. Comput. Chem.*, vol. 8, p. 291, 1987.
- [173] S. W. de Leeuw, J. W. Perram, and E. R. Smith, "Simulation of electrostatic systems in periodic boundary conditions. I. lattice sums and dielectric constants," *Proc. R. Soc. Lond.*, vol. A 373, p. 27, 1980.
- [174] S. W. de Leeuw, J. W. Perram, and E. R. Smith, "Simulation of electrostatic systems in periodic boundary conditions. II. equivalence of boundary conditions," *Proc. R. Soc. Lond.*, vol. A 373, p. 57, 1980.
- [175] V. V. Bulatov, 2000. private communication.
- [176] D. Wolf, "Reconstruction of NaCl surfaces from a dipolar solution to the Madelung problem," *Phys. Rev. Lett.*, vol. 68, p. 3315, 1992.
- [177] E. R. Smith, "Electrostatic energy in ionic crystals," *Proc. R. Soc. Lond.*, vol. A 375, p. 475, 1981.
- [178] K. N. Kudin and G. E. Scuseria, "A fast multipole method for periodic systems with arbitrary unit cell geometries," *Chem. Phys. Lett.*, vol. 283, p. 61, 1998.
- [179] J. Chang, V. V. Bulatov, and S. Yip, "Molecular dynamics study of edge dislocation motion in bcc metal," *J. Computer-Aided Materials Design*, vol. 6, p. 165, 1999.

- [180] J. Chang. unpublished.
- [181] W. Cai, M. de Koning, V. V. Bulatov, and S. Yip, "Minimizing boundary reflections in coupled-domain simulations," *Phys. Rev. Lett.*, vol. 85, p. 3213, 2000.
- [182] B. L. Holian and R. Ravelo, "Fracture simulations using large-scale molecular dynamics," *Phys. Rev. B*, vol. 51, p. 11275, 1995.
- [183] K. Ohsawa and E. Kuramoto, "Flexible boundary condition for a moving dislocation," *J. Appl. Phys.*, vol. 86, p. 179, 1999.
- [184] F. F. Abraham and H. Gao, "How fast can cracks propagate?," *Phys. Rev. Lett.*, vol. 84, p. 3113, 2000.
- [185] S. J. Zhou, P. S. Lomdahl, R. Thomson, and B. L. Holian, "Dynamic crack processes via molecular dynamics," *Phys. Rev. Lett.*, vol. 76, p. 2318, 1996.
- [186] P. Gumbsch, S. J. Zhou, and B. L. Holian, "Molecular dynamics investigation of dynamic crack stability," *Phys. Rev. B*, vol. 55, p. 3445, 1997.
- [187] S. J. Carroll, P. D. Nellist, R. E. Palmer, S. Hobday, and R. Smith, "Shallow implantation of "size-selected" ag clusters into graphite," *Phys. Rev. Lett.*, vol. 84, p. 2654, 2000.
- [188] M. Moseler, J. Nordiek, and H. Haberland, "Reduction of the reflected pressure wave in the molecular-dynamics simulation of energetic particle-solid collisions," *Phys. Rev. B*, vol. 56, p. 15439, 1997.
- [189] F. F. Abraham, J. Q. Broughton, N. Bernstein, and E. Kaxiras, "Spanning the length scales in dynamic simulation," *Comput. Phys.*, vol. 12, p. 538, 1998.
- [190] J. Q. Broughton, F. F. Abraham, N. Bernstein, and E. Kaxiras, "Concurrent coupling of length scales: Methodology and applicatoin," *Phys. Rev. B*, vol. 60, p. 2391, 1999.

- [191] R. E. Rudd and J. Q. Broughton, "Coarse-grained molecular dynamics and the atomic limit of finite elements," *Phys. Rev. B*, vol. 58, p. R5893, 1998.
- [192] J. A. Smirnova, L. Zhigilei, and B. Garrison, "A combined molecular dynamics and finite element method technique applied to laser induced pressure wave propagation," *Comp. Phys. Comm.*, vol. 118, p. 11, 1999.
- [193] S. A. Adelman and J. D. Doll, "Generalised langevin equation approach for atom/solid-surface scattering: Collinear atom/harmonic chain model," *J. Chem. Phys.*, vol. 61, p. 4242, 1974.
- [194] J. D. Doll, L. E. Myers, and S. A. Adelman, "Generalized langevin equation approach for atom/solid-surface scattering: inelastic studies," *J. Chem. Phys.*, vol. 63, p. 4908, 1975.
- [195] D. Chandler, *Introduction to Modern Statistical Mechanics*. Oxford University Press, New York, 1987.
- [196] F. O. Goodman *J. Phys. Chem. Solids*, vol. 23, p. 1269, 1962.
- [197] Q. Ren, B. Joos, and M. S. Duesbery, "Test of peierls-nabarro model for dislocations in si," *Phys. Rev. B*, vol. 52, p. 13223, 1995.
- [198] H. Koizumi, Y. Kamimura, and T. Suzuki, "Core structure of a screw dislocation in a diamond-like structure," *Phil. Mag. A*, vol. 80, pp. 609–620, 2000.
- [199] J. Li, *Modeling Microstructural Effects on Deformation Resistance and Thermal Conductivity*. PhD thesis, Massachusetts Institute of Technology, August 2000.
- [200] K. S. Cheung and S. Yip, "Atomic-level stress in an inhomogeneous system," *J. Appl. Phys.*, vol. 70, pp. 5688–5690, 1991.
- [201] H. Jónsson, G. Mills, and G. K. Schenter, "Reversible work transition state theory: Application to dissociative adsorption of hydrogen," *Surface Science*, vol. 324, p. 305, 1995.

- [202] G. Henkelman, B. P. Uberuaga, and H. Jónsson, "A climbing image nudged elastic band method for finding saddle points and minimum energy paths," *J. Chem. Phys.*, vol. 113, pp. 9901–9904, 2000.
- [203] G. Henkelman and H. Jónsson, "A climbing image nudged elastic band method for finding saddle points and minimum energy paths," *J. Chem. Phys.*, vol. 113, pp. 9978–9985, 2000.
- [204] V. V. Bulatov, S. Yip, and A. S. Argon, "Atomic modes of dislocation mobility in silicon," *Phil. Mag. A*, vol. 72, p. 453, 1995.
- [205] V. V. Bulatov, J. F. Justo, W. Cai, S. Yip, A. S. Argon, T. Lenosky, M. de Koninck, and T. D. de la Rubia, "Parameter-free modeling of dislocation motion: the case of silicon," *Phil. Mag. A*, 2000, in press.
- [206] V. V. Bulatov, J. F. Justo, W. Cai, and S. Yip, "Kink asymmetry and multiplicity in dislocation cores," *Phys. Rev. Lett.*, vol. 79, p. 5042, 1997.
- [207] S. Melchionna, G. Ciccotti, and B. L. Holian, "Hoover npt dynamics for systems varying in shape and size," *Molec. Phys.*, vol. 78, no. 3, 1993.
- [208] J. Chang, W. Cai, V. V. Bulatov, and S. Yip. unpublished.
- [209] S. V. Franklin, F. Mertens, and M. Marder, "Portevin-le chatelier effect," *Phys. Rev. E*, vol. 62, no. 6, p. 8195, 2000.
- [210] A. Portevin and F. L. Chatelier *C. R. Hebd. Seances Acad. Sci*, vol. 176, p. 507, 1923.
- [211] M. Khantha, D. P. Pope, and V. Vitek, "Dislocation screening and the brittle-to-ductile transition: A kosterlitz-thouless type instability," *Phys. Rev. Lett.*, vol. 73, p. 684, 1994.
- [212] K. Edagawa, T. Suzuki, and S. Takeuchi, "Motion of a screw dislocation in a two-dimensional peierls potential," *Phys. Rev. B*, vol. 55, p. 6180, 1997.

- [213] S. Oberg, P. K. Sitch, R. Jones, and M. I. Heggie, "First-principles calculations of the energy barrier to dislocation motion in Si and GaAs," *Phys. Rev. B*, vol. 51, p. 13138, 1995.
- [214] R. W. Nunes, J. Bennetto, and D. Vanderbilt, "Structure, barriers, and relaxation mechanisms of kinks in the 90° partial dislocation in silicon," *Phys. Rev. Lett.*, vol. 77, p. 1516, 1996.
- [215] R. W. Nunes, J. Bennetto, and D. Vanderbilt, "Atomic structure of dislocation kinks in silicon," *Phys. Rev. B*, vol. 57, p. 10388, 1998.
- [216] A. Valladares, J. A. White, and A. P. Sutton, "First principles simulations of the structure, formation, and migration energies of kinks on the 90° partial dislocation in silicon," *Phys. Rev. Lett.*, vol. 81, p. 4903, 1998.
- [217] K. A. Fichthorn and W. H. Weinberg, "Theoretical foundations of dynamical Monte Carlo simulations," *J. Chem. Phys.*, vol. 95, p. 1090, 1991.
- [218] B. Lehner, M. Hohage, and P. Zeppenfeld, "Kinetic Monte Carlo simulation scheme for studying desorption processes," *Surf. Sci.*, vol. 454-456, p. 251, 2000.
- [219] A. B. Bortz, M. H. Kalos, and J. L. Lebowitz, "A new algorithm for Monte Carlo simulation of ising spin systems," *J. Comput. Phys.*, vol. 17, p. 10, 1975.
- [220] S. Glasstone, K. J. Laidler, and H. Eyring, *The Theory of Rate Processes*. McGraw-Hill, New York, 1941.
- [221] S. Marklund, "The entropy factor involved in the hirth and lothe theory of dislocation velocity in silicon," *Solid State Communications*, vol. 54, p. 555, 1985.
- [222] W. Cai, V. V. Bulatov, and S. Yip, "Kinetic Monte Carlo simulation for dislocation glide in si," *J. Computer-Aided Materials Design*, vol. 6, no. 2/3, pp. 175-183, 1999.

- [223] J. F. Justo, V. V. Bulatov, and S. Yip, "Dislocation core reconstruction and its effect on dislocation mobility in silicon," *J. Appl. Phys.*, vol. 86, p. 4249, 1999.
- [224] Y. M. Huang, J. C. H. Spence, and O. F. Sankey, "Dislocation kink motion in silicon," *Phys. Rev. Lett.*, vol. 74, p. 3392, 1995.
- [225] V. Celli, M. Kabler, T. Ninomiya, and R. Thomson *Phys. Rev.*, vol. 131, p. 58, 1963.
- [226] W. Benoit, M. Bujard, and G. Gremaud, "Kink dynamics in f.c.c. metals," *Phys. Stat. Solidi A*, vol. 104, p. 427, 1987.
- [227] G. Schoeck, "The peierls stress and the flow stress in fcc metals," *Script. Metall. Mater.*, vol. 30, p. 611, 1994.
- [228] F. R. N. Nabarro, "Theoretical and experimental estimates of the peierls stress," *Philos. Mag. A*, vol. 75, p. 703, 1997.
- [229] M. Tang, L. P. Kubin, and G. R. Canova, "Dislocation mobility and the mechanical response of bcc single crystals: A mesoscopic approach," *Acta Mater.*, vol. 9, p. 3221, 1998.
- [230] V. V. Bulatov. unpublished.
- [231] J. Moriarty, 2000. private communication.
- [232] L. Hsuing, 2000. private communication.
- [233] F. Louchet and B. Viguier, "Ordinary dislocations in γ -TiAl: cups unzipping, jog dragging and stress anomaly," *Phil. Mag. A*, vol. 80, pp. 765–779, 2000.
- [234] B. Devincre and L. P. Kubin, "Mesoscopic simulations of dislocations and plasticity," *Mater. Sci. Eng. A*, vol. 8, pp. 234–236, 1997.
- [235] V. V. Bulatov, F. F. Abraham, L. Kubin, B. Devincre, and S. Yip, "Connecting atomistic and mesoscale simulations of crystal plasticity," *Nature*, vol. 391, p. 669, 1998.

- [236] V. V. Bulatov and L. P. Kubin, "Dislocation modeling at atomistic and mesoscopic scales," *Current Opinion in Solid State and Materials Science*, vol. 3, pp. 558–561, 1998.
- [237] K. W. Schwarz, "Simulation of dislocations on the mesoscopic scale. i. methods and examples," *J. Appl. Phys.*, vol. 85, p. 108, 1999.
- [238] K. W. Schwarz, "Simulation of dislocations on the mesoscopic scale. ii. application to strained-layer relaxation," *J. Appl. Phys.*, vol. 85, p. 120, 1999.
- [239] N. M. Ghoniem, S.-H. Tong, and L. Z. Sun, "Parametric dislocation dynamics: A thermodynamics-based approach to investigations of mesoscopic plastic deformation," *Phys. Rev. B*, vol. 61, p. 913, 2000.
- [240] H. M. Zbib, M. Rhee, and J. P. Hirth, "On plastic deformation and the dynamics of 3d dislocation," *Int. J. Mech. Sci.*, vol. 40, p. 113, 1998.
- [241] L. B. Freund, A. Bower, and J. C. Ramirez, "Mechanics of elastic dislocations in strained layer structures," in *Thin Films: Stresses and Mechanical Properties Symposium, Mater. Res. Soc.*, vol. 130, pp. 139–152, 1989.
- [242] E. B. Tadmor, M. Ortiz, and R. Phillips, "Quasicontinuum analysis of defects in solids," *Phil. Mag. A*, vol. 73, p. 1529, 1996.
- [243] A. Arsenlis, *Modeling Dislocation Density Evolution in Continuum Crystal Plasticity*. PhD thesis, Massachusetts Institute of Technology, 2001.
- [244] M. Marder and J. Fineberg, "How things break," *Physics Today*, p. 24, September 1996.
- [245] W. Xu and J. Moriarty, "Atomistic simulation of ideal shear strength, point defects, and screw dislocations in bcc transition metals: Mo as a prototype," *Phys. Rev. B*, vol. 54, p. 6941, 1996.
- [246] G. Xu and A. S. Argon, "Homogeneous nucleation of dislocation loops under stress in perfect crystals," *Phil. Mag. Lett.*, vol. 80, pp. 605–611, 2000.

- [247] S. Rao, C. Hernandez, J. P. Simmons, T. A. Parthasarathy, and C. Woodward, "Green's function boundary conditions in two-dimensional and three-dimensional atomistic simulations of dislocations," *Phil. Mag. A*, vol. 77, p. 231, 1998.
- [248] U. Bertocci, "The influence of step motion and two-dimensional nucleation on the rate of crystal growth: Some computer simulated experiments," *Surface Science*, vol. 15, pp. 286–302, 1969.
- [249] C. Deo and W. Cai, "Lattice kinetic Monte Carlo model of dislocation solute interactions." unpublished.
- [250] Y. U. Wang, Y. M. Jin, A. M. Cuitino, and A. G. Khachaturyan, "Nanoscale phase field theory of dislocations: Model and 3d simulations," 2000. submitted to *Acta. Mater.*
- [251] Y. U. Wang, Y. M. Jin, A. M. Cuitino, and A. G. Khachaturyan, "Phase field microelasticity theory and modeling of multiple dislocation dynamics," *Appl. Phys. Lett.*, vol. 78, pp. 2324–2326, 2001.

About the Author

Mr. Wei Cai was born in Wuhan, P. R. China in 1977. He obtained his B.S. in Huazhong University of Science and Technology majoring Optoelectronic Engineering in 1995. He joined the Nuclear Engineering department of Massachusetts Institute of Technology in 1996 and started his Ph.D. thesis research on atomistic modeling of materials strength with Professor Sidney Yip and Dr. Vasily Bulatov. Mr. Cai was awarded the Manson Benedict Fellowship of Nuclear Engineering Department and Silver Medal of the Materials Research Society Graduate Student Award. He is a member of Sigma Xi, American Nuclear Society, American Physical Society and Materials Research Society. He is offered the Lawrence Livermore Post Doctoral Fellowship by the Lawrence Livermore National Laboratory, where he will continue his research on computational materials science.